

Advancing macro and microalgal valorisation via green technologies

Ewan Ward

PhD

University of York

Chemistry

November 2024

Abstract

This research explores the valorisation of renewable algal biomass feedstocks into materials and chemicals via green technologies in the context of a zero-waste biorefinery. The work reported in this thesis is divided into two areas corresponding to the two algal feedstocks explored: namely i) the production and characterisation of naturally-inherent sulfur-containing porous carbons derived from unrefined carrageenan extracts obtained from Irish Moss macroalgae; and their novel application to copper(II) remediation, and ii) the fractionation of commercial microalgae, ALG01, into antioxidant-rich lipids via supercritical CO₂ extraction, hydrogel forming defibrillated cellulose via hydrothermal microwave processing, and proteins via tandem cell disruption and ultrafiltration methodologies.

The pyrolysis of carrageenan aerogels afforded porous chars rich in sulfur (3.9-7.6 %). Low pyrolysis temperatures (250 °C) developed acidic, sulfate surface chemistry facilitating copper(II) adsorption (54 mg g⁻¹) under acidic conditions (pH 1) described well by Langmuir adsorption isotherm and pseudo-second order kinetic models. In contrast, high temperatures (800 °C) incorporated sulfur as organic thiol/thiophene functionalities and carbothermic reduction of deposited sulfate salts developed alkaline magnesium oxide composites which promoted basification and deposition of copper(II) (86 mg g⁻¹, pH 4). These results prompt future development of carrageenan-derived sulfur-containing carbons for metal adsorption.

Lipid extracts rich in PUFAs, pigments and phenolics with significant antioxidant activity were obtained from ALG01 via supercritical CO₂ extraction (300 bar, 35-50 °C). Supercritical CO₂ pretreatment perturbed hemicellulose hydrolysis, however, hydrogel forming defibrillated cellulose was still afforded following acid-free 220 °C hydrothermal microwave treatment of the deoiled ALG01. Cell disruption methods, ultrasonication and microwave treatment, were successfully implemented and evolved larger water-soluble proteins (100-150 kDa). A maximum yield of 3% and 12% purity was achieved following tandem ultrasonication and ultrafiltration. This research has contributed significant new knowledge to the concept of zero-waste algal biorefineries.

Author's Declaration

I declare that this thesis is a presentation of original work and I am the sole author. This work has not previously been presented for a degree or other qualification at this University or elsewhere. All sources are acknowledged as references.

Some of this research (section 4.3) has been published in peer-reviewed journals:

- I. Zitzmann, F.L.; Ward, E.; Meng, X.; Matharu, A.S. Microwave-Assisted Defibrillation of Microalgae. *Molecules*, 2021, **26**, 4972.

<https://doi.org/10.3390/molecules26164972>

For Terry Bell

Table of contents

Abstract	1
Author's Declaration	2
Table of contents	4
Table of figures	8
List of tables	18
List of abbreviations	19
Acknowledgements	20
Preface: How to navigate this thesis	21
Chapter 1. Introduction	22
1.1. Contextualisation: The biorefinery concept.....	23
1.2. Algae and algal biorefineries.....	24
1.3. Composition of algae.....	30
1.3.1. Lipids.....	30
1.3.2. Pigments.....	32
1.3.3. Phenolics.....	36
1.3.4. Carbohydrates.....	37
1.3.5. Proteins.....	39
1.4. Aims and green chemistry context.....	41
1.4.1. Aims.....	41
1.4.1.1. Macroalgae, Irish Moss (<i>Chondrus crispus</i>).....	41
1.4.1.1.1. Carrageenan.....	43
1.4.1.2. Biochars from macroalgal biomass: objectives.....	46
Objective I: Characterisation of Irish Moss, its carrageenan extract and residues.....	47
Objective II: Production and characterisation of Irish Moss porous carbons..	47
Objective III: Application of sulfur-containing chars for copper(II) adsorption	51
1.4.1.3. Commercially cultivated microalgae, ALG01.....	54
1.4.1.4. Microalgal valorisation objectives.....	59
Objective I: Characterisation of ALG01 and EPA-free ALG01.....	59
Objective II: Supercritical CO ₂ extraction of lipids.....	60
Objective III: Microalgal defibrillated cellulose via microwave hydrothermal treatment.....	62
Objective IV: Protein extraction and enrichment.....	64
1.4.2. Green Chemistry context.....	68
Chapter 2: Experimental	70
2.1 Materials.....	71
2.2 Instrumentation and Analysis.....	71
2.2.1. IR spectroscopy.....	71
2.2.2. Elemental analysis.....	72
2.2.2.1. CHN microanalysis.....	72
2.2.2.2. Sulfur content.....	72
2.2.2.3. ICP-MS.....	73
2.2.2.3.1. Sample Digestion.....	73

2.2.2.3.2. Calibration curve preparation.....	73
2.2.2.3.2. ICP-MS procedure.....	74
2.2.3. Differential scanning calorimetry (DSC).....	75
2.2.4. Gas chromatography-mass spectrometry (GC-MS).....	75
2.2.5. High-performance liquid chromatography (HPLC).....	76
2.2.6. High-resolution transmission electron microscopy (HRTEM).....	76
2.2.7. N ₂ Adsorption porosimetry.....	76
2.2.8. Scanning electron microscopy - energy dispersive spectroscopy (SEM / SEM-EDS).....	77
2.2.9. Solid-state nuclear magnetic resonance (SSNMR) spectroscopy.....	77
2.2.10. Thermogravimetric analysis (TGA).....	77
2.2.11. Thermogravimetric gas chromatography-mass spectrometry (TG-GCMS)....	78
2.2.12. Powder X-ray diffraction (pXRD).....	78
2.2.13. X-ray photoelectron spectroscopy (XPS).....	78
2.2.14. Klason lignin analysis.....	79
2.2.15. Boehm titration.....	80
2.2.16. PZC analysis by pH drift.....	80
2.2.17. Zeta potential.....	80
2.2.18. Antioxidant activity.....	81
2.2.18.1. Determination of total phenolic content (TPC).....	81
2.2.18.2. Determination of total flavonoid content (TFC).....	82
2.2.18.3. Ferrous reducing antioxidant power (FRAP) assay.....	82
2.2.19. Water holding capacity.....	83
2.2.20. Gel formation.....	83
2.2.21. Ultrafiltration.....	83
2.2.22. Protein analysis.....	84
2.2.22.1. Protein precipitation and SDS-PAGE analysis.....	84
2.2.22.2. Bradford-assay analysis:.....	85
2.3. Methods.....	86
2.3.1. Pyrolysis of Irish Moss and Irish Moss components.....	86
2.3.2. Copper(II) adsorption study.....	87
2.3.3. Supercritical CO ₂ extraction of microalgal lipids.....	89
2.3.4. Microwave hydrothermal treatment and cellulose isolation.....	90
2.3.5. Cell disruption and soluble-protein extraction methodologies.....	91
2.3.5.1. Mechanical grinding.....	91
2.3.5.2. High-speed homogenisation.....	91
2.3.5.3. Ultrasonication.....	92
2.3.5.4. Microwave-assisted extraction.....	92
Chapter 3. Biochars from macroalgal biomass.....	93
3.1. Characterisation of Irish Moss (IM), Irish Moss extract (IME), and residual biomass (RIM) (Objective I).....	94
3.1.1. Preliminary compositional analysis.....	94
3.1.2. Carbohydrate and sugar analysis.....	95
3.1.3. Elemental analysis (CHNS).....	97

3.1.4. Mineral analysis.....	99
3.1.5. Thermogravimetric analysis (TGA).....	100
3.1.5.1. TG-GCMS.....	102
3.1.6. Attenuated total reflection infrared spectroscopy (ATR-IR).....	107
3.3.7. Variable temperature ¹ H NMR (VT ¹ H NMR) of IME.....	109
3.3.8. Gel formation of IME.....	111
3.2. Production and characterisation of Irish Moss chars (Objective II).....	112
3.2.1. Char appearance and composition.....	112
3.2.1.1. Thermogravimetric analysis (TGA).....	113
3.2.1.2. Elemental analysis (CHNS).....	115
3.2.1.3. CPMAAS solid-state nuclear magnetic resonance (SSNMR) spectroscopy..	117
3.2.1.4. FT-IR spectroscopy.....	119
3.2.1.5. Powder X-ray diffraction (pXRD).....	121
3.2.2. Surface topography and elemental analysis.....	124
3.2.2.1. Scanning electron microscopy (SEM) and energy dispersive X-ray	
spectroscopy (EDS).....	124
3.2.2.1.1. Irish Moss chars (IMC).....	126
3.2.2.1.2. Irish Moss extract chars (IMEC).....	130
3.2.2.1.3. Residual Irish Moss chars (RIMC).....	135
3.2.2.2. Porosity.....	138
3.2.2.3. X-ray photoelectron spectroscopy (XPS).....	143
3.2.2.4. High-resolution transmission electron spectroscopy (HRTEM).....	149
3.2.2.5. Boehm titration, PZC analysis, and zeta potential.....	153
3.3. Copper (II) adsorption kinetics and mechanism (Objective III).....	159
3.3.1. Indirect copper(II) adsorption measurement (UV-vis).....	159
3.3.1.1. Effect of char dosage.....	160
3.3.1.2. Effect of initial copper(II) concentration.....	161
3.3.1.2.1. pH 4.0-4.5.....	162
3.3.1.2.2. pH 1.0.....	166
3.3.1.3. Effect of adsorption contact time.....	169
3.3.1.3.1. pH 4.0-4.5.....	170
3.3.1.3.2. pH 1.0.....	173
3.3.2. Direct copper(II) adsorption measurement.....	175
3.3.2.1. SEM-EDS.....	175
3.3.2.2. pXRD.....	177
3.4. Section summary.....	179
Chapter 4. Valorisation of commercial microalgae.....	182
4.1. Characterisation of spray dried and EPA-free ALG01 biomass (Objective 1).....	183
4.1.1. Preliminary compositional analysis.....	183
4.1.2. Carbohydrate and sugar analysis.....	184
4.1.3. Elemental analysis (CHN).....	186
4.1.4. Thermogravimetric analysis (TGA).....	187
4.1.5. Attenuated total reflection infrared spectroscopy (ATR-IR).....	189

4.2. Supercritical CO ₂ extraction of lipids (Objective II).....	190
4.2.1. UV-vis spectroscopy.....	192
4.2.2. Gas chromatography-mass spectrometry (GC-MS).....	195
4.2.3. ATR-IR spectroscopy.....	200
4.2.4. Antioxidant activity: TPC, TFC, and FRAP assay.....	201
4.2.5. Differential scanning calorimetry (DSC).....	204
4.3. Microwave hydrothermal defibrillation of microalgal cellulose (Objective III).....	207
4.3.1. Thermogravimetric analysis.....	209
4.3.2. X-ray diffraction.....	211
4.3.3. Solid state ¹³ C cross polarisation magic angle spinning NMR.....	213
4.3.4. Transmission electron microscopy.....	215
4.3.5. Water-holding capacity and gel formation.....	216
4.3.6. Hydrothermal microwave hydrolysate sugar content.....	218
4.4. Extraction of proteins from EPA-free spent ALG01 (Objective IV).....	220
4.4.1. Elemental analysis (CHN).....	224
4.4.2. Protein visualisation.....	225
4.4.3. Protein content via Bradford Assay.....	227
4.4.4. ATR-IR spectroscopy.....	230
4.4.5. HPLC analysis of ultrafiltration permeate.....	231
4.5. Chapter summary.....	233
Chapter 5. Future work & conclusions.....	235
5.1. Future work.....	236
5.1.1. Carbonisation of microwave-assisted carrageenan extracts.....	236
5.2.2. Optimisation and tuning the methodology of carrageenan-derived sulfur-containing porous carbons.....	239
5.2.3. Pyrolytic bio-oils from Irish Moss.....	242
5.2.4. Further metal adsorption onto inherent sulfur-containing porous carbons.....	242
5.2.5. Additional applications of inherent sulfur-containing porous carbons.....	243
5.2.6. Advancing microalgal supercritical CO ₂ extraction.....	243
5.2.7. Applications of microalgal lipid extracts.....	245
5.2.8. Oil/protein-depleted ALG01 processing for bio-oil and biochar using hydrothermal liquefaction and microwave pyrolysis.....	246
5.2. Conclusions.....	247
Appendices:.....	250
Chapter 1:.....	250
Chapter 3:.....	251
Chapter 4:.....	263
Chapter 5:.....	265
Chapter 6. References.....	267

Table of figures:

Figure 1: Light microscopy images of green microalgal species, <i>Chlorella vulgaris</i> (A) ¹⁷ and <i>Dunaliella salina</i> (B1) ¹⁸ . In contrast, carotenoid-enriched <i>Dunaliella salina</i> exhibits an orange/red colour (B2) ¹⁹ .	25
Figure 2: Examples of green (a), red (b), and brown (c) macroalgae ²⁰ .	26
Figure 3: Examples of Kelp products: Dashi flavour via glutamates (left) and NotPla Ooho packaging using alginates (right) ²⁶⁻²⁸	27
Figure 4: Chemical structure of some common lipid types. Highlighted is the typical steroid skeleton (green), fatty acids (yellow), sphingosine (lilac) and glycerol (orange) backbones, and phosphocholine (blue) polar head.	30
Figure 5: Chemical structures of essential omega-3 fatty acids, EPA, DHA, and ALA	31
Figure 6: Chemical structure of various pigments: chlorophylls (green), carotenoids (yellow), and phycobilin chromophores (blue/red).	33
Figure 7: BASF method of β -carotene synthesis via Wittig Condensation ^{61,66} . Problematic or hazardous reagents/waste have been highlighted.	35
Figure 8: Phenolics present in some algae, phenolic acids: tannic acid and caffeic acid, phlorotannin components: phloroglucinol and eckol, and mycosporine-like amino acids.	36
Figure 9: Typical celluloses found in the microalgae, <i>Nannochloropsis</i> . On the left, a polymer of β -glucose bound by 1,4-glycosidic bonds. On the right, a similar polymer but bound by 1,3-glycosidic bonds. β -(1,3) Glucans are often desired for their immunological effects ^{72,73} .	37
Figure 10: Common polysaccharides in green, brown, and red algae.	38
Figure 11: A comparison of microalgae EAA profile with common protein sources (A) and the fraction of the protein content EAAs account for (B). Plant based sources are coloured green. Data obtained by Gorissen et al and reproduced as a bar graph ⁸³ .	40
Figure 12: Irish Moss (<i>Chondrus crispus</i>) exhibiting a blue iridescence underwater ⁹² .	42
Figure 13: Forms of carrageenan (iota, kappa, and lambda). β -galactose and 3,6-anhydro- α -galactose or α -galactose units covalently bound by alternating β (1,4) and α (1,3) glycosidic bonding.	43
Figure 14: Rhein-Knudsen et al thermoreversible gelation mechanism of kappa-carrageenan in the presence of potassium ions ⁹⁶ .	44

Figure 15: Flow chart depicting the aims of Chapter 3: Biochars from macroalgal biomass.	46
Figure 16: A representation of the different types of heteroatomic doping of graphitic carbon. X1 = pyrrolic-like, X2 = pyridinic-like, X3 = graphitic (bulk), X4 = graphitic (edge), Y = intercalation, Z1 = surface functionalization, Z2 = edge functionalization, T = nanocomposite.	48
Figure 17: Fatty acid composition of Folch method lipid extracts from <i>Nannochloropsis gaditana</i> . Castejón and Marko data reproduced as a bar graph ¹⁴³ .	55
Figure 18: Scholz et al produced diagram of <i>Nannochloropsis</i> cell wall indicating algaenan and cellulose-based layers (A) based on quick freeze deep-etch electron microscopy (QFDE EM) images of a cell wall cross-section (B and C) ³⁹ .	57
Figure 19: Proposed algaenan structures from algae: <i>Tetraedon minimum</i> , <i>Scenedesmus communis</i> , and <i>Pediastrum boryanum</i> (A) ¹⁵⁷ , <i>Nannochloropsis</i> (B) ¹⁵⁴ , and <i>Botryococcus braunii</i> (C) ¹⁵⁵ .	58
Figure 20: Flow chart depicting the aims of Chapter 4: Valorisation of Commercial Microalgae	59
Figure 21: Phase transition diagram of carbon dioxide, indicating the critical point in which the material becomes a supercritical fluid ¹⁵⁹ .	60
Figure 22: Biorefinery approach for ALG01 microalgae and Irish Moss macroalgae feedstocks highlighting green principles addressed.	69
Figure 23: ICP-MS calibration curve of high concentration elements (data points are superimposed).	75
Figure 24: TPC Calibration Curve of Gallic Acid standards (0.000-0.005 mg/mL) determined via UV-vis absorbance at 730 nm.	81
Figure 25: TFC Calibration Curve of Quercetin standards (0.000-0.005 mg/mL) determined via UV-vis absorbance at 730 nm.	82
Figure 26: Simplified diagram of a typical micro/ultrafiltration set-up.	84
Figure 27: Zoomed region of Calibration curve illustrating the UV-vis absorbance at 595 nm of varying albumin concentrations in Coomassie Plus reagent. Inset is the full curve exhibiting poor repeatability at concentrations higher than 750 ug mL ⁻¹ .	85
Figure 28: Barnstead 6000 Muffle Furnace set-up	86
Figure 29: UV-vis Calibration curve indicating the effect of copper(II) concentration on the absorbance intensity at 810 nm.	88

Figure 30: Simplified diagram of a supercritical CO ₂ extractor.	89
Figure 31: Milestone Synthwave Reactor set-up.	90
Figure 32: Acid-hydrolysed profile of Irish Moss (IM), carrageenan (IME) and residual Irish Moss (RIM) carbohydrates.	96
Figure 33: CHNS content of Irish Moss (IM), Irish Moss extract (IME), and residual Irish Moss (RIM).	97
Figure 34: Mineral composition of Irish moss, Irish Moss extract and residual Irish Moss determined by ICP-MS analysis. Full analysis including trace metal quantities is available in appendix 3.1.	99
Figure 35: Thermogravimetric analysis of Irish Moss biomass (IM), the aqueous extract (IME) and residues (RIM), and a kappa-carrageenan standard and the respective DTG thermograms.	100
Figure 36: GC-MS spectra of flue gases produced at 220-240 °C and 320-350 °C from the pyrolysis of Irish Moss biomass under inert atmosphere (N ₂). Inset are assigned peaks to known polysaccharide decomposition products. The TG plots of IM, IME, and RIM have been included to show the regions by TG-GCMS.	103
Figure 37: Mechanisms for the pyrolysis of potassium/calcium carrageenan fibres adapted from the proposed Zhang et al mechanism ²⁰⁹ .	105
Figure 38: A suggested mechanism for the formation of levoglucosenone from carrageenan. Depolymerisation by transglycosylation (1) or ring-opening (2) ^{2,218} , and deposition of sulphate salts (3) ²⁰⁹ .	106
Figure 39: ATR-IR spectra of Irish Moss, Irish Moss extract (IME), residual biomass (RIM), and kappa-carrageenan.	107
Figure 40: Overlaid VT (20 to 90 °C) 500 MHz 1H NMR spectroscopy of conventionally extracted IME in D ₂ O. Assigned as κ-carrageenan (structure inset), specifically noting anomeric anhydrogalactose protons between 5.75 and 6.00 ppm of both iota and kappa carrageenan.	109
Figure 41: Varying concentrations of IME in water, depicting the gelling properties of carrageenan as the gels resist gravity.	111
Figure 42: Appearance of IM, IME, and RIM biomass materials and resulting chars following pyrolysis at 250, 400, and 800 °C.	112
Figure 43: TGA thermograms of Irish Moss biomass: IM, IME, and RIM (plot A), and their carbons: C250s (B), C400s (C), and C800s (D).	113
Figure 44: CHNS content charts for IM, IME, and RIM at various pyrolysis temperatures before and after washing with hot water and acetone, and HHV values determined by the Channiwala formula ²³⁰ .	115

Figure 45: ¹³ C SSNMR spectra of Irish Moss biochars (IM, IME, RIM)	117
Figure 46: FT-IR spectra of Irish Moss biochars (IMC, IMEC, RIMC) from carbonisation temperatures 250, 400, and 800 °C, alongside ATR-IR spectra of native non-carbonised biomasses, indicated by 0 °C.	119
Figure 47: pXRD diffractogram of IM, IME, and RIM materials carbonised at 250 °C , 400 °C , and 800 °C, phase identification of (Na,K) ₂ SO ₄ , CaS and MgO salts have also been included.	121
Figure 48: SEM images of IME and IMEC (250-800) at a magnification of x50,000. Indicating the change in surface porosity with temperature (red circles).	125
Figure 49: SEM/SEM-EDS images of IM and IMCs (250, 400, 800 °C) at magnifications of x10k (SEM) and x5k (SEM-EDS).	126
Figure 50: SEM-EDS elemental mapping of an area of unwashed IMC250 at a magnification of x5k. Individual calcium, sodium, sulfur, and oxygen element maps are included for clarification of the metal sulfates present.	127
Figure 51: SEM-EDS element maps of carbon, oxygen, sulfur, and nitrogen for IMC250-800. Inset are the %Wt values for each element.	128
Figure 52: SEM/SEM-EDS images of IME and IMECs (250, 400, 800 °C) at magnifications of x10k (SEM) and x5k (SEM-EDS).	130
Figure 53: SEM-EDS element maps of carbon, oxygen, sulfur, and nitrogen for IMEC250-800. Inset are the %wt values for each element.	131
Figure 54: SEM-EDS image of washed IMEC800 at x10k magnification. Elemental maps of magnesium, calcium, oxygen, and sulfur have been included to show the elemental composition of magnesium oxide ‘barnacles’.	133
Figure 55: A simple diagram showing the formation of IME porous structures, and SEM images of IMEC800WG at x1000 magnification exhibiting the porous internal structure and smooth flat external structure.	134
Figure 56: SEM/SEM-EDS images of RIM and RIMCs (250, 400, 800 °C) at magnifications of x10k (SEM) and x5k (SEM-EDS).	135
Figure 57: SEM-EDS element maps of carbon, oxygen, sulfur, and nitrogen for RIMC250-800. Inset are the %Wt values for each element.	137
Figure 58: The IUPAC classification of adsorption isotherm types (I-VI) (left) and the hysteresis shapes for different pore types (H1-4) (right) ¹⁰⁵ .	139
Figure 59: N ₂ adsorption porosimetry isotherms (A) and pore size distributions (B) for carbonised IM, IME, and RIM at temperatures of 250, 400, and 800 °C.	139
Figure 60: O:C, N:C, and S:C ratios at the surface of IMC, IMEC, and RIMC	145

biochars quantified by XPS analysis.

Figure 61: XPS spectra of IM and IMC(250-800) showing the carbon binding energy region C1s (280-300 eV) and identification of the deconvoluted spectral lines. 145

Figure 62: XPS spectra of IM, IME, and RIM biomass and chars from pyrolysis temperatures of 250 °C to 800 °C showing the sulfur binding energy region (280-300 eV) and identification of the deconvoluted spectral regions. 148

Figure 63: HRTEM images of washed IMC250, IMC400, and IMC800 chars at magnifications of x50k, x200k, and x500k. Circled areas indicate regions of porosity. 149

Figure 64: HRTEM images of washed IMEC250, IMEC400, and IMEC800 chars at magnifications of x50k, x200k, and x500k. Circled areas indicate regions of porosity. 150

Figure 65: HRTEM images of washed RIMC250, RIMC400, and RIMC800 chars at magnifications of x50k, x200k, and x500k. Circled areas indicate regions of porosity. 151

Figure 66: Magnesium hydroxide composite observed in IMEC800 using HRTEM imaging at magnifications of x200k (left) and x500k (middle). A zoomed in region of the middle image has been included to show the lattice structure (right). 152

Figure 67: pKa values of Boehm titration bases and common acidic sites present on chars²⁵². Included are common acidic sulfur functional groups. 153

Figure 68: pH Drift analysis for the determination of pH_{pzc} values of washed IMC250-800, IMEC250-800, and RIMC250-800 chars. 154

Figure 69: Total Acidity (and acidic breakdown) and Basicity determined via Boehm Titration of washed Irish Moss Chars, IMC, IMEC, and RIMC, carbonised at 250, 400, and 800 °C. 155

Figure 70: An illustration of zeta potential showing a charged particle and the layers of solvent counter ions at the particle-solvent interface, adapted from Yakasai et al.²⁵³ 156

Figure 71: The effect of pH on Zeta potential measurements of IMC (A), IMEC (B), and RIMC (C) materials suspended in aqueous KCl electrolyte solution. For comparison literature zeta potential values of carrageenan-derived hydrochars and activated carbons have been included (D)¹²⁸. 158

Figure 72: UV-vis spectra of aqueous copper(II) nitrate solutions at varying concentrations (500-5000 mg/L $Cu(NO_3)_2$). 159

Figure 73: Copper(II) adsorption capacity of IMC, IMEC, and RIMC (250-800) 160

materials, determined indirectly by UV-vis analysis of copper(II) nitrate solution (5000 mg/L, 10 mL, pH 4.5) after 24h dosed with 10, 50, or 100 mg of char material.

Figure 74: Copper(II) adsorption isotherm plots at pH 4.0-4.5 of IMC, IMEC, and RIMC (250-800). Freundlich (blue line) and Langmuir (orange line) isotherm models have been plotted for each material. Inset are zeta potential values for each char at pH 4.5 and the end pH after 24h. 163

Figure 75: The effect of pH on the adsorption intensity at 810 nm of the $[\text{Cu}(\text{H}_2\text{O})_6]^{2+}$ complex and expected transitions as the solution becomes alkaline^{257,258}. Inset is the change in the pH of the copper(II) solution plotted against the corresponding UV absorbance at 810 nm for IMEC adsorption experiments. Arrows indicate the first pH measurement (t = 0.5 h) and last (t = 24 h) of the adsorption experiments. 165

Figure 76: Copper(II) adsorption isotherm plots at pH 1.0 of IMC, IMEC, and RIMC (250-800). Freundlich (blue line) and Langmuir (orange line) isotherm models have been plotted for each material. Inset is the end pH after 24h. 168

Figure 77: Copper(II) adsorption kinetics at pH 4.0-4.5 of IMC, IMEC, and RIMC (250-800). Pseudo-first order (blue line) and pseudo-second order (orange line) kinetic models have been plotted for each material. 172

Figure 78: Copper(II) adsorption kinetics at pH 1.0 of IMC, IMEC, and RIMC (250-800). Pseudo-first order (blue line) and pseudo-second order (orange line) kinetic models have been plotted for each material. 174

Figure 79: SEM-EDS images of IMEC materials (C250-800) following the aqueous adsorption of copper(II) from a copper nitrate solution (5000 mg/L) at pH 4 and 1 after 24h. Overlaid element maps and individual element maps of copper, sulfur and oxygen have been included. Inset are element maps of IMEC800 'barnacles' post copper(II) adsorption. 176

Figure 80: pXRD diffractograms of IMC, IMEC, and RIMC materials (C250-C800) before and after copper(II) adsorption at pH 4 and pH 1. (001) and (002) phases of copper(II) hydroxy salts are highlighted. 177

Figure 81: Chemical structure of carrageenan (left) and the proposed structures for carrageenan low temperature chars (250-400 °C, centre) and high temperature chars (800 °C, right). 180

Figure 82: Acid-hydrolysed carbohydrate content of ALG01 and EPA-free spent ALG01 derived via Klason analysis. Component sugars and decomposition products are depicted and decomposition mechanism inset²⁶⁴. 184

Figure 83: TGA of the dried and spent microalgae ALG01, presenting the mass lost (TG/%) as the biomass is heated from 20 C to 800 C at 10 K min⁻¹ under a Nitrogen atmosphere (100 mL min⁻¹ flow rate). The rate of mass loss (DTG/% min⁻¹) has been included. The 3 decomposition stages are 187

highlighted.

- Figure 84: ATR-IR Spectroscopy of spray dried and spent ALG01. 189
- Figure 85: Variation in supercritical CO₂ extract yield from the microalgae, ALG01, at various temperature and pressure extraction conditions. 190
- Figure 86: The effect of supercritical CO₂ density on the extractive yield from a 2h extraction from the microalgae, ALG01. 191
- Figure 87: UV-vis absorption spectra of the supercritical extracts (200-400 bar and 35-50 °C) from ALG01 after a 2-hour extraction (focused specifically on the region 325-725 nm). The extracts are dissolved in ethanol at a concentration of 0.1 mg mL⁻¹. Intense characteristic Chlorophyll and Carotenoid absorption bands are visible in 400 bar and 300 bar extracts, respectively. 192
- Figure 88: Literature UV-vis spectra of chlorophyll a/b and their respective pheophytin ²⁷⁴. 193
- Figure 89: GC spectra of supercritical extracts SC(200-400)(35-50). Compounds with a high probability (>50%) MS match with NIST library data have been labelled. Major FFA and sterol components were identifiable by GC-MS. Sample concentrations vary between 10-25 mg mL⁻¹. 195
- Figure 90: Mass Spectrum of myristic acid (C14:0) from ALG01 extract (85.2% similarity with library fragmentation fingerprint). 196
- Figure 91: Mass Spectrum of palmitoleic acid (C16:1) and EPA (C20:5) from ALG01 extract (49.7% and 35.8% similarity with library fragmentation fingerprint). 197
- Figure 92: Chemical structure of identified steroids, terpenes and phenolics in supercritical CO₂ extracts. 198
- Figure 93: 300 MHz 1H NMR spectra of a supercritical CO₂ extract from ALG01 in Chloroform-d. Major signals have been labelled using HSQC and HMBC spectra. Highlighted are hydrogen environments and the corresponding proton in the fatty acid, EPA, these environments are also common in many other PUFAs. 199
- Figure 94: FT-IR spectra of the dried supercritical extracts (200-400 bar and 35-50 °C) from ALG01 after a 2-hour extraction. Inset shows zoomed carbonyl region. 200
- Figure 95: Antioxidant activity of supercritical CO₂ extracts from ALG01 using varying extraction conditions. Figures A and B show the effect of supercritical CO₂ density on the TPC and TFC of the supercritical extracts, respectively. Figure C and D show the ferrous reducing power of the supercritical CO₂ extractives in comparison with known strong antioxidants, BHT and Ascorbic 201

Acid.

- Figure 96: Chemical structure of TPC, TFC and FRAP standards, gallic acid, quercetin, ascorbic acid, and BHT. 202
- Figure 97: Reaction scheme for the formation of Prussian Blue from ferricyanide and iron(III) ²⁸³. 203
- Figure 98: Cropped 300MHz 1H NMR spectrograms of various supercritical CO₂ extracts in chloroform-d. Highlighted are weak aromatic proton signals at 6.70, 7.00-7.05, and 7.50-7.70 ppm. 204
- Figure 99: DSC spectra showing the 1st heat-cool cycle of supercritical extracts SC(200-400)(35-50). An irreproducible exothermic transition at 80-100 °C in SC30050 and SC40040, suggest the thermally labile presence of chlorophylls. 205
- Figure 100: DSC spectra showing the 2nd and 3rd heat-cool cycles of supercritical extracts SC(200-400)(35-50). Labelled are the main two melts and corresponding recrystallisations of the extracts at 0-10 °C and 20-40 °C. Also labelled is the third melt and recrystallisation present in the SC400 extracts. 206
- Figure 101: Defibrillated cellulose obtained via microwave treatment at the temperatures of 160, 180, 200 and 220 °C for a total of 30 minutes (50:50 ramp:hold). Brown colour potentially described by the Maillard reaction inset. 207
- Figure 102: Defibrillated cellulose yield (line chart) and carbohydrate yields (bar chart) of spray dried and supercritical treated microalgal biomass at different microwave temperatures. 208
- Figure 103: DTG thermograms of spray-dried biomass and scCO₂ deoiled biomass produced defibrillated celluloses. Spectra produced from TGA from 20-800 °C under a 100 mL min⁻¹ N₂ atmosphere. 209
- Figure 104: X-Ray diffractograms of defibrillated celluloses derived from (A) Spray Dried biomass and (B) scCO₂ deoiled biomass. Black numbers indicate crystalline cellulose I planes, red numbers indicate CaC₂O₄ planes. (C) Literature x-ray diffractograms of crystalline cellulose I and predominantly amorphous cotton cellulose. (D) Crystallinity index (CrI) of defibrillated celluloses against microwave temperatures calculated via Segal's method ²⁹³. 211
- Figure 105: Solid state ¹³C CPMAS NMR spectra of defibrillated celluloses derived from spray dried and scCO₂ deoiled biomasses using microwave hydrothermal treatment (160-220 °C) 213
- Figure 106: TEM images of defibrillated celluloses derived from spray dried biomass (160-200 °C). Defibrillated celluloses of both biomasses are shown at 220 °C to contrast the defibrillation resistance of the scCO₂ deoiled biomass. 215

Figure 107: Water holding capacities (WHC) of defibrillated celluloses derived from both spray dried and scCO ₂ deoiled biomass. Inset is the visual gelling properties of the high temperature MHT treatments at a concentration of 3.0% in water.	216
Figure 108: Hydrolysate carbohydrate content obtained from HPLC for spray dried biomass (left) and scCO ₂ deoiled biomass hydrolysates (right).	218
Figure 109: Yields of ultrafiltration obtained retentate and permeate extracted from spray dried and EPA-spent ALG01. Inset are images of the typical appearance of freeze-dried retentate and permeate samples.	220
Figure 110: Simplified diagram of a micelle formed from saponified fatty acids containing chlorophyll within a lipid droplet.	222
Figure 111: CHN microanalysis contents for spray dried and EPA spent ALG01 retentate and permeate samples following aqueous extraction and ultrafiltration, and variable cell disruption methods.	224
Figure 112: SDS-PAGE gel presenting the distribution of protein sizes, stained in blue, within ultrafiltration obtained retentate and permeate samples, extracted from ALG01 and EPA-spent ALG01 samples following different cell disruption methods: None (N), Grinding (G), Homogenisation (H), Ultrasonication (U), and Microwave assisted extraction (M).	225
Figure 113: ALG01 and EPA-spent ALG01 retentate yields and protein contents determined by CHN nitrogen-to-protein conversion (bar) and Bradford assay (line).	227
Figure 114: Chemical structure of amino acids that bind to the Coomassie dye and are recognised by Bradford Assay.	228
Figure 115: ATR-IR spectroscopy of ultrafiltration obtained retentate and permeates extracted ALG01 and EPA-spent ALG01 following various cell disruption methods.	230
Figure 116: HPLC determined carbohydrate content of ALG01 and EPA-spent ALG01 ultrafiltration permeates.	231
Figure 117: A zoomed region (3.5-6.0 ppm) comparing the 80 °C 1H NMR spectra of IME obtained using conventional and microwave assisted extraction methods. Labels are pyranose proton environments of kappa carrageenan and the ratio of kappa and iota carrageenan for each sample determined by the ratio of the anomeric protons. Yields of Irish Moss extract (IME) using microwave assisted extraction methods compared to conventional heating (timings indicate ramp:hold).	237
Figure 118: Thermogravimetric analysis of RIM biomass from conventional or microwave extraction processes.	238

Figure 119: Carrageenan aerogels produced from freeze-drying gels of different loadings (2.5%-25%)	239
Figure 120: SEM images of Carr300 materials (2.5-20.0% Gel loading) at x500 magnification and the size of material macropores. The relationship between gel loading and the N ₂ adsorption porosimetry measured surface area and pore volume is also included.	240
Figure 121: N ₂ adsorption porosimetry adsorption isotherms and pore distribution plots of unexpanded Carr300 (10%) vs expanded Carr300 (10%).	241
Figure 122: Supercritical CO ₂ extraction vessel containing microalgal extract following an extraction under 300 bar and 35 °C.	244
Figure 123: ALG01 supercritical CO ₂ extracts (300 bar, 50 °C) in ethanol, after 24h refrigerated (left) and at room temperature (right).	245
Figure 124: Proposed zero-waste biorefinery approaches for ALG01 microalgae and Irish Moss macroalgae including potential applications for all side products. Work completed in this thesis have been highlighted using *.	249

List of tables:

Table 1: Percentage polyunsaturated fatty acid (PUFA) content of some microalgal and macroalgal species (dry weight (DW)), highlighting the content of valued omega-3 oils, EPA and DHA.	32
Table 2: A comparison of the cell disruption efficiency and increases in the product yield for a variety of cell disruption methods.	67
Table 3: Elements in the environmental calibration fluid.	74
Table 4: Calibration concentrations for high and low concentration elements in the environmental standard	74
Table 5: Compositional analysis (%) of Irish Moss (IM) and its water-soluble (IMEC) and insoluble (RIM) fractions.	94
Table 6: Surface Characteristics of IMC, IMEC, RIMC washed Chars from temperatures of 250 °C, 400 °C, and 800 °C, and literature values comparable red seaweed chars.	141
Table 7: Elemental Composition of the surface of washed IMC, IMEC, and RIMC chars from pyrolysis at 250 °C and 800 °C.	144
Table 8: Isotherm model constants determined for the adsorption of copper(II) to IMC, IMEC, and RIMC chars (C250-800) at a pH of 4.0-4.5.	162
Table 9: Isotherm model constants determined for the adsorption of copper(II) to IMC, IMEC, and RIMC chars (C250-800) at a pH of 1.0.	166
Table 10: Kinetic parameters for pseudo-first and second order models determined for the adsorption of copper(II) to IMC, IMEC, and RIMC chars (C250-800) at a pH of 4.0-4.5.	170
Table 11: Kinetic parameters for pseudo-first and second order models determined for the adsorption of copper(II) to IMC, IMEC, and RIMC chars (C250-800) at a pH of 1.0.	173
Table 12: Summarised ALG01 composition.	183

List of abbreviations:

ALA	- α -linolenic acid	scCO ₂	- Supercritical carbon dioxide
ATP	- Atmospheric temperature & pressure	SDG	- Sustainable development goal
ATR	- Attenuated total reflectance	SDPC	- Sulfur-doped porous carbon
BET	- Brunauer-Emmett-Teller	SE	- Secondary electron
BHT	- Butylated hydroxytoluene	SEM	- Scanning electron microscopy
BJH	- Barrett-Joyner-Halenda	TAG	- Triacyl glycerides
BSE	- Back-scattered electron	TEM	- Transmission electron microscopy
DHA	- Docosahexaenoic Acid	TFC	- Total flavonoid content
DSC	- Differential scanning calorimetry	TGA	- Thermogravimetric analysis
DTG	- Differential thermogram	TMS	- Tetramethylsilane
DW	- Dry weight	TPC	- Total phenolic content
EAA	- Essential Amino Acids	VOC	- Volatile organic carbon
EDS	- Energy dispersive spectroscopy	WHC	- Water holding capacity
ELS	- Electrophoretic light scattering	XPS	- X-ray photoelectron spectroscopy
EPA	- Eicosapentaenoic Acid	pXRD	- (powder) X-ray diffraction
FAMES	- Fatty acid methyl esters		
FCR	- Folin-Ciocalteu reagent		
FFA	- Free Fatty Acids		
FRAP	- Ferric reducing antioxidant power		
FT	- Fourier transform		
GAE	- Gallic acid equivalent		
GC	- Gas chromatography		
HHV	- Higher heating value		
HPH	- High-pressure homogenisation		
HPLC	- High-pressure liquid chromatography		
HMF	- Hydroxymethylfurfural		
IM(C)	- Irish Moss (carbon)		
IME(C)	- Irish Moss extract (carbon)		
ISPC	- Inherent sulfur-containing porous carbon		
LGO	- Levoglucosenone		
MAAs	- Mycosporine-like Amino Acids		
MAE	- Microwave-assisted extraction		
MHT	- Microwave hydrothermal treatment		
MS	- Mass spectrometry		
MSG	- Monosodium glutamate		
NDPC	- Nitrogen-doped porous carbon		
NMR	- Nuclear magnetic resonance		
ORR	- Oxygen reduction reaction		
PUFAs	- Polyunsaturated Fatty Acids		
PZC	- Point of zero charge		
QE	- Quercetin equivalent		
RDI	- Recommended Daily Intake		
RIM(C)	- Residue Irish Moss (carbon)		

Acknowledgements

The work produced in this thesis could not have been achieved without the support of the chemistry department at York University, specifically the staff and students of the green chemistry centre of excellence (GCCE). I wish to offer a special thanks to Prof. Avtar Matharu. His support throughout my masters and PhD has been crucial for my development as a professional chemist and researcher and this research would not have been possible without his depth of knowledge and unwavering support throughout the ups and downs of this PhD.

The following people I wish to acknowledge for providing me analytical/instrumental training: Rob McElroy (Supercritical CO₂ extraction), Chris Taylor (SDS-PAGE analysis), Jon Barnard (SEM/SEM-EDS), Adam Kerrigan (HRTEM), Adrian Whitwood (pXRD), Richard Gammons, Suranjana Bose and Tabitha Petchey (various GCCE instruments). Also David Morgan at Cardiff University for providing XPS analysis, Jon Angus at the Biorenewables development centre (BDC) for providing ICP-MS analysis, and Ryan Barker for providing SSNMR analysis. I would also like to thank Suranjana Bose, and Nicholas Garland for their knowledge in porous carbon production and their support in the analysis of the novel chars produced in these works. Also, Frederik Zitzmann for his knowledge of microalgae and support producing defibrillated cellulose and proteins from them.

I would also like to thank my friends and family for their support, I love you all.

Preface: How to navigate this thesis

This thesis is composed of 6 chapters. The first chapter introduces the concept of algae, its composition, and provides context for the development of an algal biorefinery. After a brief instrumentation and methodology chapter, the third chapter entails the development of inherent sulfur-containing porous carbons (ISCPC) derived from macroalgal Irish Moss components, specifically the hydrocolloid, and porous aerogel-forming sulfated polysaccharide, carrageenan for copper(II) remediation. This chapter's contents include the extraction of carrageenan from Irish Moss, the detailed characterization of carrageenan-derived ISCPCs, and the novel application of these chars to copper(II) remediation via adsorption. The fourth chapter entails the application of green valorisation techniques to a microalgal stream (ALG01). This chapter's contents includes: supercritical CO₂ extraction to obtain high value lipid extracts, microwave hydrothermal treatment for novel defibrillated cellulose materials, and green cell disruption and ultrafiltration technologies to isolate protein-rich extracts. The thesis is concluded in the fifth chapter and proposes ideas for the future development of algal materials and their novel applications. The final pages contain the appendices and references of this research.

Chapter 1. Introduction

1.1. Contextualisation: The biorefinery concept

Many pharmaceuticals, cosmetics, and construction materials come from, or are made with, solvents and base platform molecules sourced from an oil refinery. The depletion of crude oil resources, and climate change, have pushed for sustainable alternatives ¹. Biomass feedstocks are inherently more renewable than crude oil. They offer reduced CO₂ emissions, offset by photosynthetic processes that occur during the growth of the biological material ². Also, they can be produced in various geographical locations, which enables individual nations to produce their own resources, reducing the emissions of overseas transportation.

A biorefinery is comparable to an oil or petroleum refinery. In an oil refinery, the crude oil resource is separated into its valuable fractions. A biorefinery follows the same concept. It takes organic matter (biomass) and implements a series of conversion processes to isolate valuable fractions for use in biofuels, nutraceuticals, pharmaceuticals, and many other industries ^{2,3}. In contrast to a crude oil refinery, biomass exhibits an increased complexity. It is typically oxidised and contains significant heteroatom content. This complexity introduces a wider range of products, but also complicates the processes required to refine them. Many of which are in their infancy and few are at an industrial or commercial scale ⁴.

Biomass is often subdivided into several categories. These were initially used in the context of biofuels, however, the pros and cons of each are still applicable in a biorefinery context. First generation biomass includes edible crops grown on arable land, often containing starchy carbohydrates. These feedstocks compete with food resources, however, the growth, production, and conversion of these materials is well-known and optimised ⁵. Similarly the production of second generation biomass is simple; and is often lignocellulosic waste from food industries. Lignocellulosic biomass, consisting of cellulose, hemicellulose and lignin, has a higher complexity to first generation sugars, starches and oils, leading to poorer efficiency in the conversion processes ⁵. These feedstocks, however, do not compete with food resources, but may compete for the same land. As populations continue to

increase, the demand for available arable land for food production increases, which drives research towards third generation biomasses. These feedstocks are non-edible and produced on non-arable land ². Fourth generation feedstocks encompass genetically modified second or third generation biomasses.

1.2. Algae and algal biorefineries

Algae is considered a third generation feedstock despite many species being edible. Algae occasionally finds itself in the public spotlight. Commonly, it is negatively associated with environmental pollution, such as toxic blue-green algal blooms that will give you rashes, make you sick, and kill your dog ⁶. Further, in Ruth Kassinger's *Slime*, they echo public opinion by initially characterising algae as an unpleasant, slimy, green pest ⁷. In 1978, following the 1973 oil crisis, algae was famed for the possible application of its oils in fuel industries. This has led to further algal biotechnologies, and more, positive algal-based news stories, for example AlgiKnit's kelp-based yarns ⁸, and Notpla's biodegradable plastics ⁹.

The term algae is not a taxonomy and is quite imprecise. They are described as polyphyly because they do not share an immediate, evolutionary ancestor. The collective similarities between these organisms is their ability to photosynthesise and their lack of multicellular vascular organs such as leaves, roots, or stems; in other words they are thallophytes ¹⁰. The classification of algae is still disputed. However, they are categorised in a range of different kingdoms and phylums. An example of this is the kingdom Plantae including phylums, Chlorophyta (green algae), and Rhodophyta (red algae), and the kingdom Chromista including phylums, Bacillariophyta (diatoms), and Ochrophyta (brown algae, yellow-green algae, and many others) ^{11,12}. Algae are typically aquatic, found in both freshwater and marine environments, although some are terrestrial. These terrestrial algae are found in soils, on rock surfaces, in snow and ice, and on animals and plants. Algae are truly ubiquitous, and incredibly important to healthy ecosystems.

Algae are found as unicellular microalgae, or as multicellular macroalgae. To note the term algae will be used to describe both microalgae and macroalgae, unless specified in these works. Both eukaryotic and prokaryotic microalgae exist, although the latter is often omitted from the definition of algae. Prokaryotic algae, typically cyanobacteria, include examples such as the well-known and frequently consumed spirulina (*Arthrospira*), and lesser-known *Prochlorococcus*; a prolific photosynthesizer responsible for much of the oxygen in the atmosphere ¹³. Eukaryotic algae include the aforementioned, Chlorophyta, Rhodophyta, and Ochrophyta. Many of these organisms have commercial applications: *Chlorella vulgaris* is a green algae cultivated as nutritional feed and for its polysaccharide content ^{12,14}. *Dunaliella salina* is another green algae, although when cultivated for β -carotene and other carotenoids it is bright red/orange in colour (Figure 1) ^{12,15}. *Nannochloropsis* is a Eustigmatophyte that accumulates polyunsaturated fatty acids (PUFAs) desirable in nutritional supplements ¹⁶. Even long-dead microalgae has commercial applications: Celite or diatomaceous earth is formed from the silica frustule of diatoms and has a multitude of filtration uses.

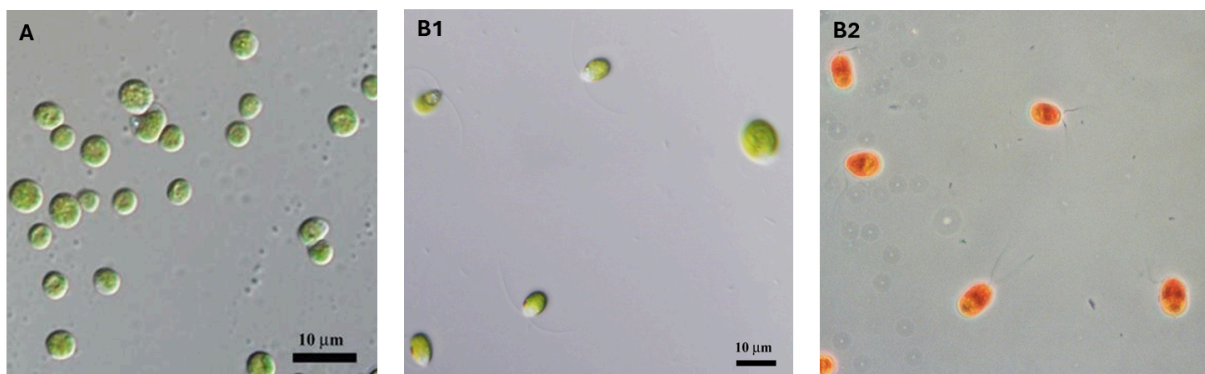


Figure 1: Light microscopy images of green microalgal species, *Chlorella vulgaris* (A) ¹⁷ and *Dunaliella salina* (B1) ¹⁸. In contrast, carotenoid-enriched *Dunaliella salina* exhibits an orange/red colour (B2) ¹⁹.

Macroalgae are commonly called seaweeds. These multicellular organisms have a similar morphology, body or thallus (Figure 2). Seaweed blades act like plant leaves, achieving light capture and are the main source of photosynthetic chemistry in the organism; although every algal cell is capable of photosynthesis. Many species have pneumatocysts that are gas-filled pockets that keep the blades of the organism buoyant and closer to the sun-rich surface. A holdfast secures the seaweed to ocean floor or rocky shore, while a hollow, buoyant, and sugar-channelling stipe connects the blades and holdfast together ⁷.



Figure 2: Examples of green (a), red (b), and brown (c) macroalgae ²⁰.

Macroalgae have been used in cuisine for millennia ²¹. Kelp or Kombu is a collection of brown macroalgal species in the *Laminaria* family. This edible macroalgae has influenced cuisine across the world. Two examples include monosodium glutamate (MSG) and Alginates (Figure 3, left and right respectively). *Dashi*, a Japanese broth produced from Kombu, has a rich umami flavour due to the combined effect of glutamic acids abundant in this seaweed and sodium salts from other ingredients ²¹. This inspired the production of

flavour enhancers such as glutamates like MSG (Figure 3, left), which are fundamental to some of the umami flavours of many East Asian dishes.

Alginates are a type of colloidal polysaccharide (Figure 3 right), others include agar or carrageenan. Alginates, agar, and carrageenan are all extracted from different macroalgal species. Alginates from species of brown algae, and agar and carrageenan from species of red algae. These colloidal polysaccharides are often used in dairy products such as ice creams and yoghurts, but they also have applications as gels, foams, emulsions, and films^{21,22}. Notpla's edible water capsules, Ooho (figure 3, right), composed of alginates²³, were used in the 2019 London marathon²⁴ and also the 2023 half marathon, Göteborgsvarvet in Sweden²⁵.



Figure 3: Examples of Kelp products: Dashi flavour via glutamates (left) and NotPla Ooho packaging using alginates (right)²⁶⁻²⁸

Algal biorefineries are typically designed in two parts: the growth and cultivation (upstream processing), and the harvesting, cell disruption, and extraction (downstream processing). However, due to the diversity in algae, one biorefinery approach will not necessarily fit all.

During the cultivation stage, the algae is grown on coastlines, in open-ponds, or photobioreactors ²⁹. The composition of the algal species can be manipulated to a certain extent by altering the light intensity, CO₂ availability, temperature, pH, salinity, or the nutrient availability in the medium ²⁹⁻³¹. Algae do not often require freshwater, and may utilise wastewater mediums. In some cases this can afford a biomass enriched in certain metabolites, for example phenolic-rich biomass from algae cultivated in spent cherry brine ³¹⁻³³. Algae are typically fast growing and can usually be harvested multiple times a year, which is a much shorter timescale than most plant-based biomasses ³⁴. These organisms are also excellent carbon fixers, and according to a study by Zhao and Su microalgae could theoretically sequester 1.66 tons of CO₂ for every ton of biomass produced each year ³⁵.

Harvesting can be relatively simple in the case of macroalgae, however, separating microalgae from its medium can be more difficult. Common methods of achieving this are filtration, centrifugation, and flocculation ^{36,37}. Each has their own advantages, however all are considered an additional costly step in the biorefinery. A further difficulty is caused by algae's hardiness. Many species have developed defences to enable survival in harsh environments. Complex cell wall structures consisting of layers of polysaccharides, peptides, lipid bilayers, and occasionally algaenan, resist osmotic lysis and other external stressors ³⁸⁻⁴⁰. Further, multicellular algae are typically bound together and coated with exopolysaccharides, which also protects the organism and prevents it drying out during changes in the tide. Some of these extracellular metabolites are valuable extracts ⁴¹, however, they cause difficulty in the extraction of intracellular metabolites. Introducing cell disruption aids in the extraction of these metabolites, but adds another step and cost to the biorefinery process. Cell disruption is a method of cracking open cells via the degradation of the cell wall and membrane. There are many methods of achieving this, each with varying degrees of effectiveness, costs, and selectivity, the choice of cell disruption method is dependent on the biomass and key product desired. Cell disruption methods are discussed further in chapter 4.

Due to high costs in the preparation of the biomass, valorisation of as many co-products as possible is necessary. This requires either a sequence of extraction processes that maximise metabolite yield while limiting the degradation of remaining co-products, or by implementing valorisation techniques (e.g. pyrolysis or fermentation) to transform waste byproducts into valuable materials ⁵.

1.3. Composition of algae

Algae have a plethora of commercial applications due to their complex composition of useful biological metabolites. This section includes some of the recognised valuable algal components and their uses. The detailed composition of the macroalgae (Irish Moss) and microalgae (ALG01) used in this thesis is given in section 1.4.1.1 and 1.4.1.2, respectively.

1.3.1. Lipids

Lipids are broadly defined as a collection of hydrophobic organic hydrocarbons, including fats, oils, steroids, waxes, and some vitamins. Although lipids are typically hydrophobic, they are often categorised as polar or nonpolar (Figure 4). Polar lipids typically have a polar phosphate, betaine, or sugar head attached to a glycerol or sphingosine backbone, with non-polar fatty acid tails. Non-polar lipids include free fatty acids (FFA), triacylglycerides (TAG), steroids, waxes, and hydrocarbons. Many lipids have bioactive properties, however, the fatty acid composition is of keen interest for their application in nutraceuticals.

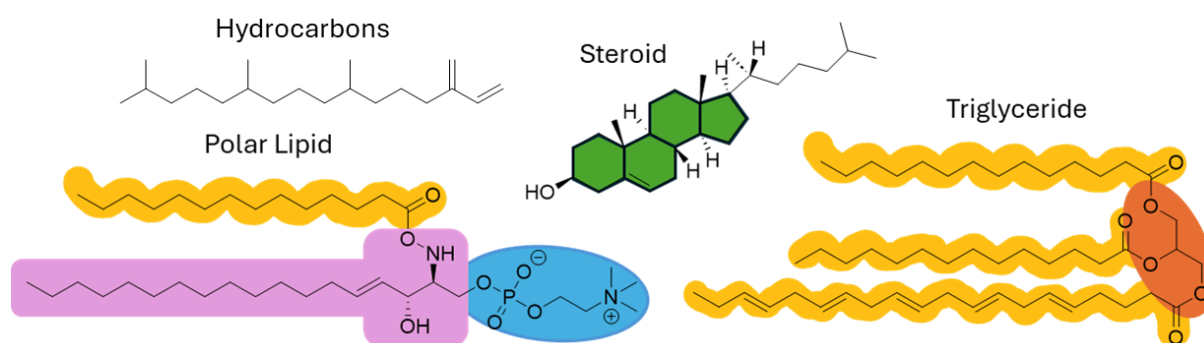


Figure 4: Chemical structure of some common lipid types. Highlighted is the typical steroid skeleton (green), fatty acids (yellow), sphingosine (lilac) and glycerol (orange) backbones, and phosphocholine (blue) polar head.

In eukaryotic cells, lipids are found in lipid droplets and lipid bilayers. Lipid droplets function as a storage of lipids for both energy and the replenishing of the lipid bilayer, which functions as a membrane for the cell and organelles within it ⁴². Lipids in algae are typically well researched, especially regarding the production of algal biodiesel ^{30,37,43–45}. The extraction and chemical conversion of lipids into biodiesel or fatty acid methyl esters (FAMES) by transesterification, and the biochemical and thermochemical conversion of carbohydrates and remaining biomass into bioethanol, biogas, bio-oils, or biochar, allow algae to be a potential source of bioenergy ⁴⁴. The lipid content of algae, however, also contains valuable components that would be wasted as a biofuel. PUFAs, steroids, and fat-soluble vitamins are desired in the nutraceutical and pharmaceutical industries ⁴⁶. Equally, the high PUFA content of algal lipids, affords biodiesel that is susceptible to oxidation and is unsuitable for long term storage ⁴³.

Omega-3 PUFAs such as eicosapentaenoic acid (EPA), docosahexaenoic acid (DHA), and α -linolenic acid (ALA) (Figure 5) are important for maintaining heart and brain health ¹⁶. The PUFA content in algae varies from species to species, but can be significantly enriched (Table 1). Commercial fish oils are the common source of omega-3 PUFAs. Algae, also rich in these oils, are a potential and suitable replacement when considering issues of overfishing, a dying ocean and the growing vegetarian/vegan population.

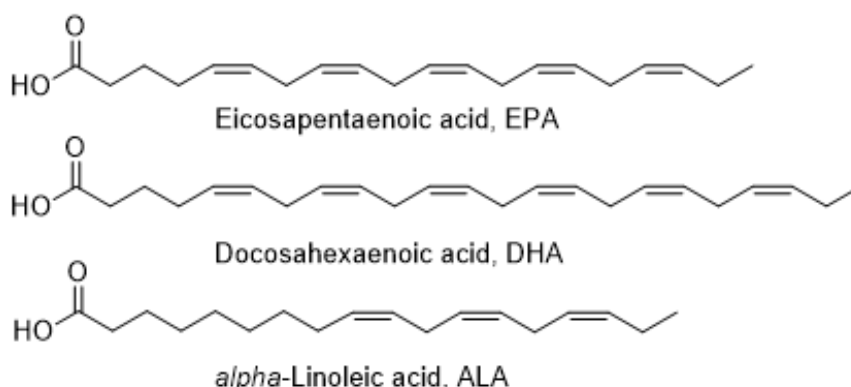


Figure 5: Chemical structures of essential omega-3 fatty acids, EPA, DHA, and ALA

Table 1: Percentage polyunsaturated fatty acid (PUFA) content of some microalgal and macroalgal species (dry weight (DW)), highlighting the content of valued omega-3 oils, EPA and DHA.

Algae Type*	Phylum (Kingdom)	Species	% PUFA Content			Refs
			EPA	DHA	Total	
Mi	Chlorophyta (Plantae)	<i>Pseudokirchnerilla subcapitata</i>	0.57	-	6.21	16
Mi	Chlorophyta (Plantae)	<i>Chlorella vulgaris</i>	2.26	-	26.49	47
Ma	Ochrophyta (Chromista)	<i>Lobophora sp.</i>	11.56	14.26	59.98	48
Mi	Bacillariophyta (Chromista)	<i>Odontella aurita</i>	10.96	1.89	19.37	49
Mi	Ochrophyta (Chromista)	<i>Nannochloropsis sp.</i>	18.94	-	20.79	16
Mi	Haptophyta (Chromista)	<i>Emiliania huxleyi</i>	-	17.20	40.00	50

* Mi = microalgae, Ma = macroalgae

1.3.2. Pigments

The pigments in algae are divided into three categories: chlorophylls, carotenoids, and phycobilins (Figure 6). The main function of these pigments is to improve or enhance light absorption for photosynthesis. Chlorophyll-a is the main photosynthetic pigment and is found in protein-pigment complexes within the cell's chloroplasts. The other chlorophylls act as accessory pigments and extend the wavelengths accessible for photosynthesis. Chlorophylls absorb blue (450-475 nm) and red (630-675 nm) light so consequently appear green⁵¹. Carotenoids and phycobilin chromophores are also bound in proteins and act as

accessory photosynthetic pigments absorbing a greater range of blue light (carotenoids: 400-550 nm) or green and yellow light (phycobilins: 500-650 nm) ⁵¹. Chlorophyll and carotenoid pigment-protein complexes are found within the thylakoid membrane in chloroplasts, and are therefore fat-soluble, whereas phycobiliproteins are water-soluble and are instead bound to the membrane via fat-soluble proteins ⁵¹. Carotenoids also have a secondary function protecting the cell from dangerous levels of excess light, and oxygenating species that are produced during photosynthesis ^{51,52}.

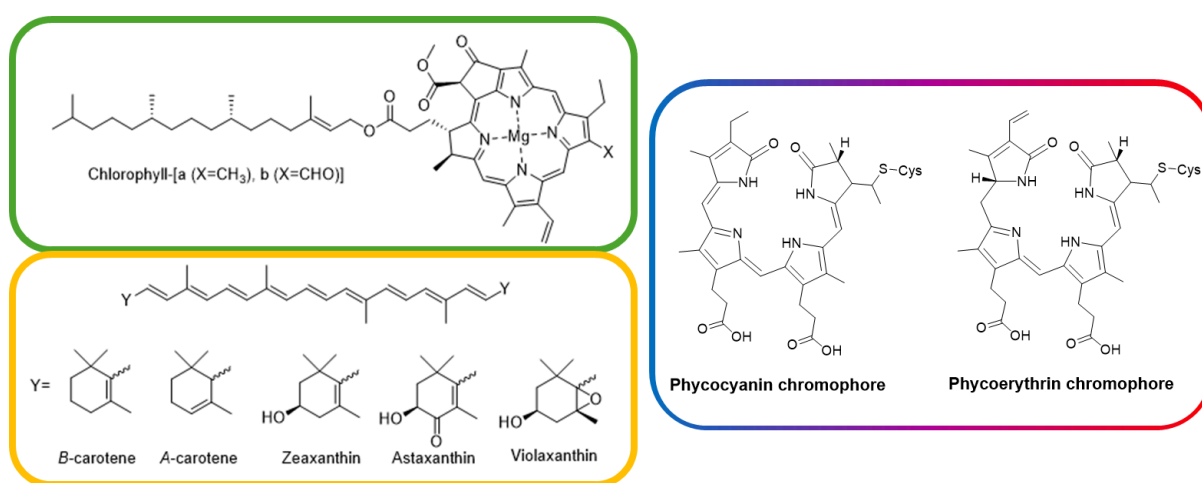


Figure 6: Chemical structure of various pigments: chlorophylls (green), carotenoids (yellow), and phycobilin chromophores (blue/red).

In algae, the chlorophyll content varies from species to species. Chen *et al.* reported green algae, *Ulva sp.* or Sea Lettuce, to contain almost 10 mg g⁻¹ (DW), brown algae, Laminariales or Kelp, 3 mg g⁻¹ (DW), and red algae, *Pyropia sp.* (Nori) 2.6 mg g⁻¹ (DW) ⁵³. Chlorophylls are a brilliant green colour and hydrophobic, and therefore have applications as food colourants and natural dyes ⁵⁴. Unfortunately, they also have poor stability and often degrade to pheophytin via dechelation of magnesium and thus, develop an unacceptable brown colour ⁵⁵. However, chlorophylls and pheophytins also have a potential in

pharmaceuticals with scientific research showing anti-inflammatory and anti-tumour effects^{54,56}.

Carotenoids are classified as either a carotene or a xanthophyll. They are both polyunsaturated hydrocarbons, however xanthophylls are oxygenated and contain functional groups such as alcohols, ethers, or aldehydes. All carotenoids are strong antioxidants and are highly valued in the food, nutraceutical, and pharmaceutical industries, resulting in a global carotenoid market projected to reach over £1.75 billion by 2032⁵⁷. In many microalgae, the most common carotene is β -carotene. It has applications as a food colourant, a protective antioxidant, and as a precursor to vitamin A⁵⁸. Like chlorophylls this pigment is highly sensitive to heat, light and oxygen, and will isomerize to various unstable *cis* forms of β -carotene⁵⁹. Extracting β -carotene from a natural and plentiful resource is far more sustainable than large-scale synthetic routes such as the BASF method (Figure 7)⁶⁰. These industrial approaches require hazardous reagents such as Grignard reagents and produce problematic byproducts⁶¹. *Dunaliella salina*, a green microalgae, is well known for its accumulation of β -carotene, which can account for up to 10% of its dry weight (100 mg g⁻¹) when grown under salinity stressed conditions¹⁵. Other algae such as *Nannochloropsis* and *Tetradismus* sp. are also known to accumulate β -carotene, but to a lesser degree^{58,62}.

Water-soluble phycobiliproteins are common in red algae and blue-green algae. Phycoerythrin is an intense, red, accessory pigment biosynthesised in red algae⁶³. This protein is used in a wide range of fields. Its therapeutic and fluorescent properties allow it to be used in immunology as an immunomodulator and fluorescent label, and in medicine to treat cancer^{63,64}. Given its applications, phycoerythrin is unsurprisingly high-valued, around £20-100 per mg⁶³ and an expected global market of £4.5 million by 2025⁶⁵. Algae of the genus: *Porphyra*, *Porphyridium*, *Rhodomonas*, and many others are potential sources of phycoerythrin⁶³⁻⁶⁵. In *Porphyridium* sp. this pigment accounts for 60-80% of the water-soluble proteins, and Ardiles et al. obtained a maximum of 33.85 mg g⁻¹ using modern extraction techniques, such as ultrasound⁶⁵.

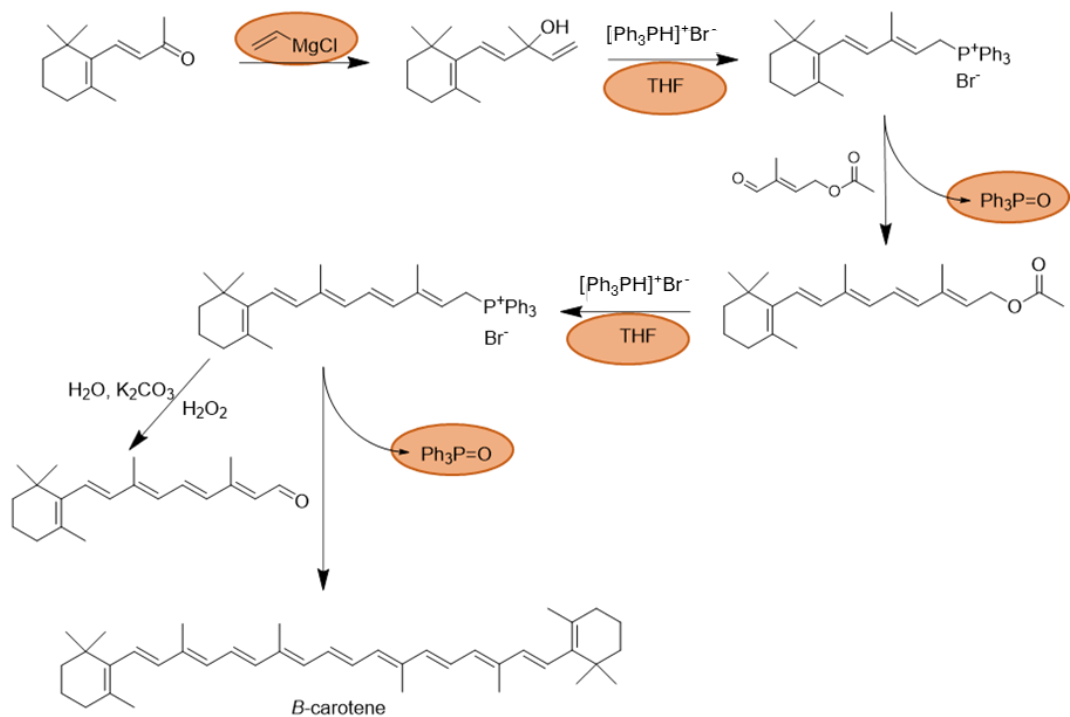


Figure 7: BASF method of β -carotene synthesis via Wittig Condensation ^{61,66}.

Problematic or hazardous reagents/waste have been highlighted.

1.3.3. Phenolics

Algae and seaweeds contain a large quantity of phenolic-based antioxidant metabolites. Phenolics are hydroxylated aromatic molecules. There is an abundance of different phenolics, from phenolic acids to phlorotannins to mycosporine-like amino acids (MAAs) (Figure 8). These compounds have a variety of functions in the cell, but some examples include oxidation protection, photo-protectants (MAAs), or chemical deterrents (bromophenols)⁶⁷⁻⁶⁹.

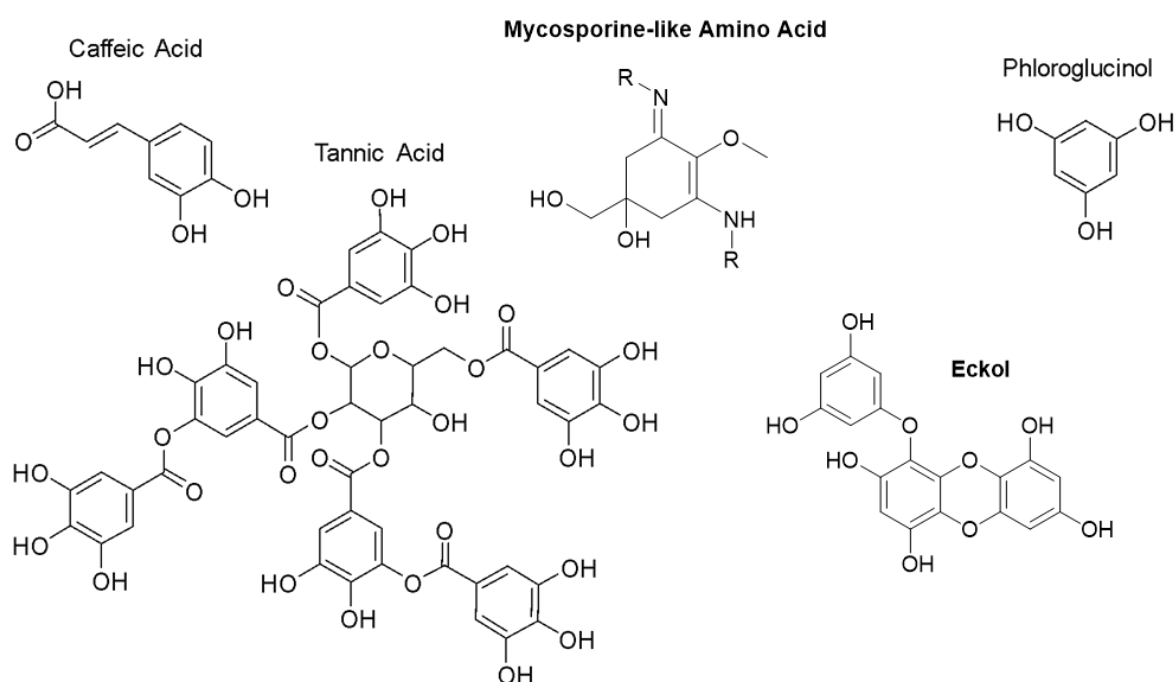


Figure 8: Phenolics present in some algae, phenolic acids: tannic acid and caffeic acid, phlorotannin components: phloroglucinol and eckol, and mycosporine-like amino acids.

Like most metabolites in algae the phenolic content varies from species to species. Phlorotannins dominate the phenolic content of brown algae, whereas phenolic acids, flavonoids, and MAAs account for the major fraction in red and green algae⁶⁷. Many of these phenols are desired because of their effect on human health. These molecules exhibit bioactive properties and are often desired as a neuroprotective, UV protectant, or simply as a health supplement, such as Vitamin E (α -tocopherol)^{68,69}.

1.3.4. Carbohydrates

In algae, the carbohydrate content varies from 4-76% (DW) depending on the species and the respective stressors of its cultivation environment ^{70,71}. Carbohydrates include sugar molecules like glucose, xylose, and other monosaccharides, but also chains of sugars bound through glycosidic bonds. These carbohydrates are found in the cell walls, usually as cellulose (β -(1,4) glucan), β -(1,3) glucans (Figure 9), and hemicelluloses, and as storage polysaccharides or starches ⁷².

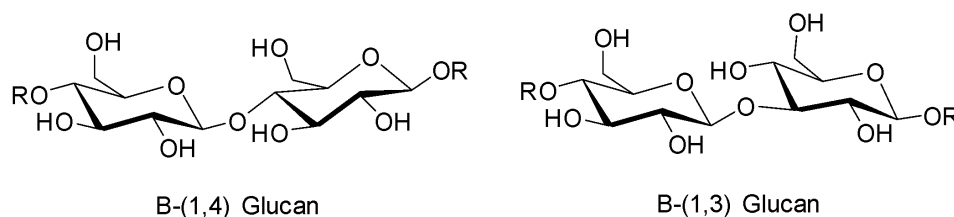


Figure 9: Typical celluloses found in the microalgae, *Nannochloropsis*. On the left, a polymer of β -glucose bound by 1,4-glycosidic bonds. On the right, a similar polymer but bound by 1,3-glycosidic bonds. β -(1,3) Glucans are often desired for their immunological effects ^{72,73}.

The types of polysaccharide found within macroalgae are often dependent on their taxonomy. In green macroalgae, there are typically sulfated polysaccharides, such as sulfated xylans, or ulvans ⁷⁰. In brown macroalgae, however, there is alginic acid, laminarin, and fucoidan ^{70,74}, whereas agars, carrageenan, and floridean starch (often called semi-amylopectin) are more common in red macroalgae ^{70,74}. These are just some examples of the species-specific polysaccharides in algae (Figure 10).

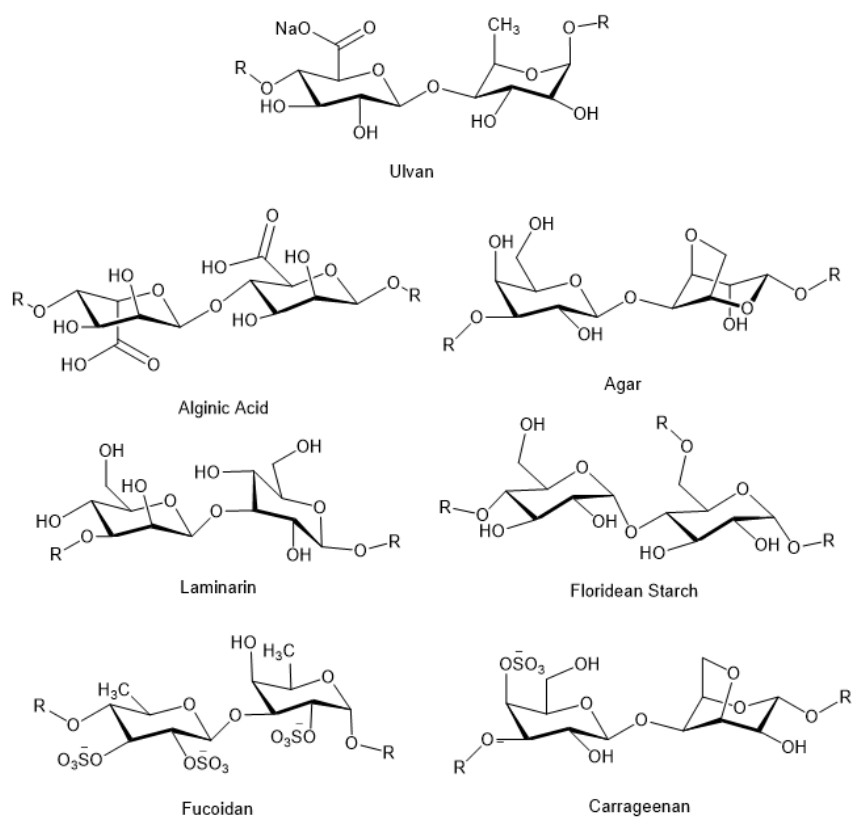


Figure 10: Common polysaccharides in green, brown, and red algae.

Sugar-rich biomass is often converted into biofuels, such as bioethanol. However, certain polysaccharides, such as the phycocolloids, carrageenan and agar, have better applications in food industries and pharmaceuticals. In these fields, they will have an estimated combined market value of £1.09 billion per annum by 2027 ^{75,76}. Many other polysaccharides are also bioactive and have antioxidant, antimicrobial, anti-inflammatory effects ⁷⁰. The low digestibility of some polysaccharides offer benefits for gut health and help contribute to the recommended daily intake (RDI) of dietary fibre ⁷⁷.

Properties of algal polysaccharides have also enabled applications of these materials in food packaging. A sustainable alternative to petroleum-based plastics, these polysaccharides are non-toxic, relatively low cost, and biodegradable. These features when combined with active ingredients, such as antioxidants or sensors, affords edible films that can extend shelf-life, or indicate when food spoilage has occurred ⁷⁸.

1.3.5. Proteins

Proteins are fundamental in all organisms. In algae, they have varying functionalities and are involved in almost all cellular activities, from carbon fixing to active transport. In macroalgae, proteins can make up to 47% of their dry weight ⁷⁹, and in microalgae, up to 70% of their dry weight ⁸⁰. These proteins are composed of amino acids and vary in size, some upwards of 200 kDa in weight.

The proteins from algae could have a range of commercial applications. Sport supplementation is a stable market. Many professional and amateur athletes consume food and drink with added protein. Typically, this protein comes from whey, a product of curdling cows' milk, however, animal agriculture is a stress on the environment and vegetable alternatives are rapidly becoming more common ⁸¹. These protein powders typically contain a mixture of denatured peptides and amino acids, which can be relatively easily obtained from algae ⁷⁹.

Many amino acids cannot be synthesised in the body, and therefore must be obtained from our food. These amino acids are known as essential amino acids (EAA), and many of them are present in algae. Red dulse, or *Palmaria palmata*, when cooked exhibited >10 mg g⁻¹ of leucine, lysine, and valine, and also indicated the presence of histidine, isoleucine, methionine, phenylalanine, and threonine ⁸². Further, other studies have compared microalgae to common protein sources, such as peas or eggs, and recognised a similarity in their amino acid profiles (figure 11) ⁸³.

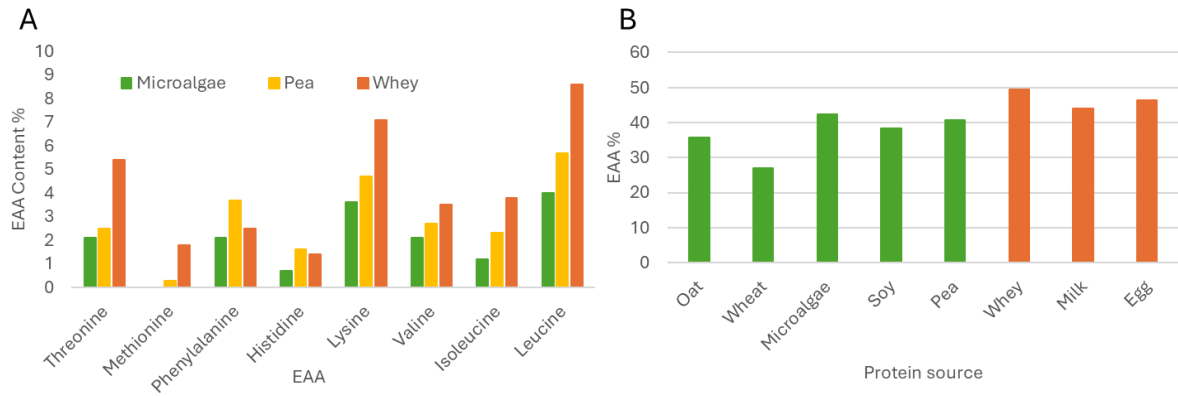


Figure 11: A comparison of microalgae EAA profile with common protein sources (A) and the fraction of the protein content EAAs account for (B). Plant based sources are coloured green. Data obtained by Gorissen et al and reproduced as a bar graph ⁸³.

1.4. Aims and green chemistry context

Algae is a proven biomass feedstock which should be capitalised on. Among other applications, aspects of their composition offer forgotten dietary benefits, replacements for petroleum-based additives in pharmaceuticals, and afford biodegradable materials for packaging. Developing several biorefinery approaches valorising the varied algal biomasses is a step towards renewable and sustainable industries, and ending the reliance on fossil fuels.

1.4.1. Aims

The primary aim of this research is to investigate the valorisation of specific macro- (Irish Moss) and micro-algal (ALG01) species via green methodologies to yield novel bio-based materials and chemical extracts within the context of a zero waste biorefinery. This research is divided into two key chapters according to the two algal feedstocks. A detailed account of the specific aims and objectives now follows including an initial brief overview of the composition of the feedstocks: Irish Moss and ALG01.

1.4.1.1. Macroalgae, Irish Moss (*Chondrus crispus*)

Irish Moss, *Chondrus crispus*, is an edible, red macroalgae of the family Gigartinales. Red algae or Rhodophyta are a classification of algae known for their florid complexion caused by a combination of chlorophyll and phycobiliproteins: phycoerythrin and phycocyanin. The majority of red algae are multicellular seaweeds and inhabit marine environments^{84,85}. They are often present in shallow waters on rocky shores and are therefore easy to harvest for coastal foragers. Red algae are rich in nutritional metabolites, vitamins, and minerals such as iodine, calcium, and magnesium. The consumption of red seaweeds such as laver (*Porphyra*) and dulse (*Palmaria palmata*) is common in east Asian countries and was once more prevalent in British and Irish coastal diets. This type of algae

has been recognised to contain proteins, polysaccharides, PUFA's, phenolics, and sterols which have anti-inflammatory, anti-diabetic, antioxidant, and antimicrobial effects ⁸⁴.

Irish Moss is an incredibly well researched red algal species. This algae has branching blades that form fan-like structures . It is found with varying complexions, such as reds, yellows, greens, and purples, but is recognisable by the blue iridescence appearing underwater at the tip of the fronds (see figure 12). It is abundant in the north east and north west of the Atlantic Ocean, and grows on rocky surfaces in marine waters. In regards to its composition, Irish Moss is primarily composed of carbohydrates, approximately 50% of its dry weight (DW) ⁸⁶. Protein content can make up around 20-40% (DW) ^{87,88}, a significant portion of which is often insoluble ⁸⁷. The lipid content of macroalgae is typically low 1-8% ⁸⁹. The fatty acid and sterol composition has been studied frequently and major fatty acids identified include: myristic (C14:0), palmitic (C16:0), ω -6 arachidonic (C20:4), and ω -3 EPA (C20:5), and the major sterol being cholesterol ⁸⁹⁻⁹¹. Although lipid yield is low, PUFAs make up a large proportion of the fatty acid content (68%) ⁸⁹. Further, phenolics, such as catechin, p-coumaric acid, and gallic acid, flavonoids, and MAAs have been found within extracts from this algae, all of which have been documented to have antioxidant activity ⁸⁴. Despite having a valuable lipid content this commercially grown algae is cultivated for one particular purpose, carrageenan.



Figure 12: Irish Moss (*Chondrus crispus*) exhibiting a blue iridescence underwater ⁹².

1.4.1.1.1. Carrageenan

Many macroalgal species are mucilaginous, meaning they excrete mucilage, a highly viscous substance composed of proteins and polysaccharides. This mucilage is often noticed by those who frequent the seaweed-covered rocky shores on the coasts of the UK. The slimy material excreted by these seaweeds contain jelly-like hydrocolloids, such as agar and carrageenan, that protect the algae. The polysaccharide, carrageenan, accounts for around 30-40% or sometimes upwards of 50% of dried Irish Moss biomass ⁹³, and was therefore heavily utilised for the production of commercial carrageenan. The carrageenan market shifted to eastern seaweed farms of *Eucheuma* and *Kappaphycus* as the material became more desired and larger scale farms were required ⁹⁴.

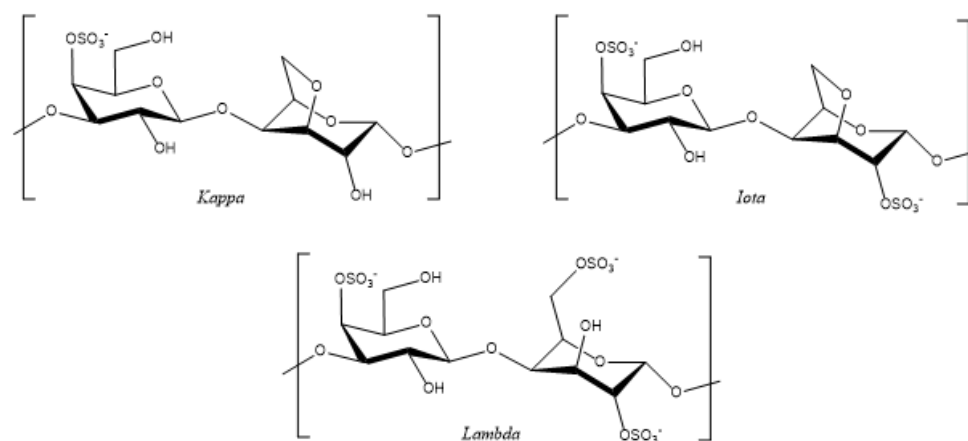


Figure 13: Forms of carrageenan (iota, kappa, and lambda). β -galactose and 3,6-anhydro- α -galactose or α -galactose units covalently bound by alternating $\beta(1,4)$ and $\alpha(1,3)$ glycosidic bonding.

Carrageenan is highly valued in the food industry due to its physical properties. Its current market value in 2024 is approximately £823 million and is expected to rise ⁷⁶. It is an additive to a variety of products such as non-dairy milks, fruit juices, and salad dressings due to its ability to be an effective stabilising, gelling, or thickening agent ⁷⁴. These properties originate from carrageenan's polymeric structure. Composed of alternating β -galactose and

3,6-anhydro- α -galactose or α -galactose units, this sulfated galactan exists in many different forms. These forms are classified by the number and location of the sulfate groups. The three most common forms are *iota* (ι), *kappa* (κ), and *lambda* (λ) carrageenan (Figure 13), and often hybrids of the different forms can exist in some algae⁹⁵. These varying chemical structures lead to variation in the physical properties of the material and consequently their gelling abilities. Gel formation begins upon cooling the viscous solution of carrageenan. Typically this initial cooling causes randomly oriented coils of polysaccharide to undergo a thermally reversible transition into a linked series of helices, cooling further results in an aggregation of helices around cationic species in solution⁷⁴, this results in a semi-solid matrix that can suspend micelles, in other words a very stable hydrogel (Figure 14).

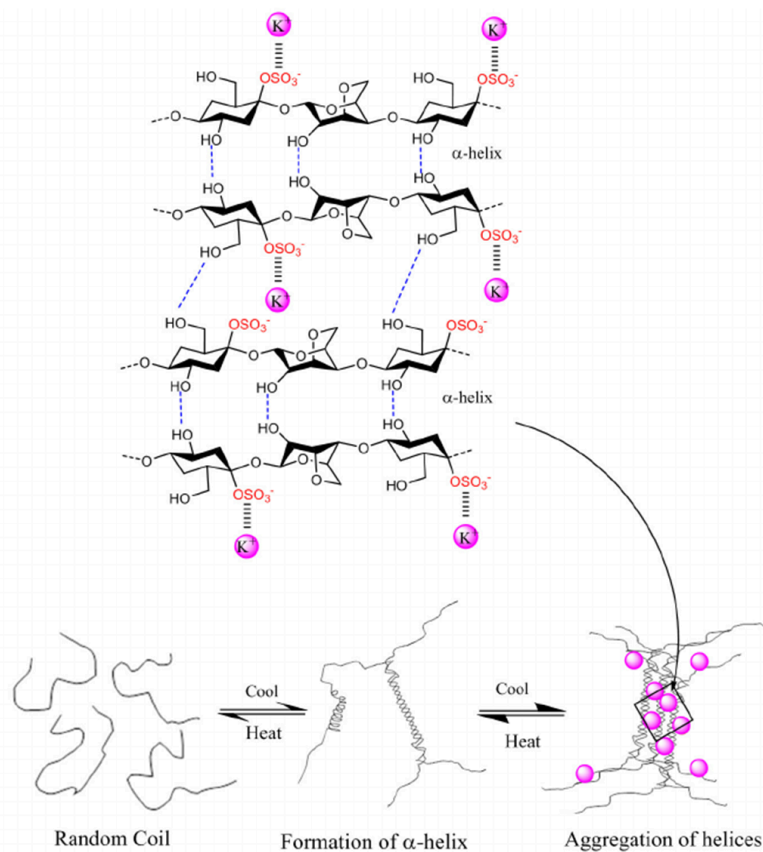


Figure 14: Rhein-Knudsen et al thermoreversible gelation mechanism of kappa-carrageenan in the presence of potassium ions⁹⁶.

Carrageenans are well researched, and they are not limited to food-based applications. Recent examples include carrageenan-based microgel delivery systems ^{97,98}, carrageenan-based films for packaging applications ⁹⁹, or utilising the antiviral activity of λ and ι -carrageenan against SARS-CoV-2 and Influenza ^{100,101}. Carrageenan extraction can be achieved using a simple aqueous extraction but to maximise yield a common industrial method is applied which utilises a high temperature alkaline digestion to break down algal tissue and dissolve carrageenan. This effectively cuts any potential branching side-streams as the residual biomass is macerated and unrecoverable ⁹⁵. The mucilaginous nature of Irish Moss, however, allows for the dissolution of carrageenan even in cold distilled water. Bahari et al. evaluated the effect of extraction temperature, duration and salinity on the yields of carrageenan from Irish Moss ⁹⁵. Carrageenan-rich precipitates were obtained from aqueous extracts using antisolvent precipitation (isopropyl alcohol) with the aid of potassium chloride. The authors recognised a linear increase in carrageenan yield from ~10 - 35 % (DW) between extraction temperatures 22 - 90 °C, respectively. Explained simply by the increased solubility of carrageenan in hot water. Extraction duration had limited effect on the precipitate yield after the first 30 minutes of extraction, the further 7.5 hours showed only minor increases in yield (+5%). The increase in extraction duration also had less impact the greater the extraction temperature ⁹⁵.

1.4.1.2. Biochars from macroalgal biomass: objectives

The aim of this section is the production and characterisation of naturally inherent sulfur-containing porous carbons derived from Irish Moss macroalgae and its carrageenan for their application in the remediation of copper(II) from aqueous solutions. The chapter is segmented into three objectives, which are also depicted pictorially in Figure 15:

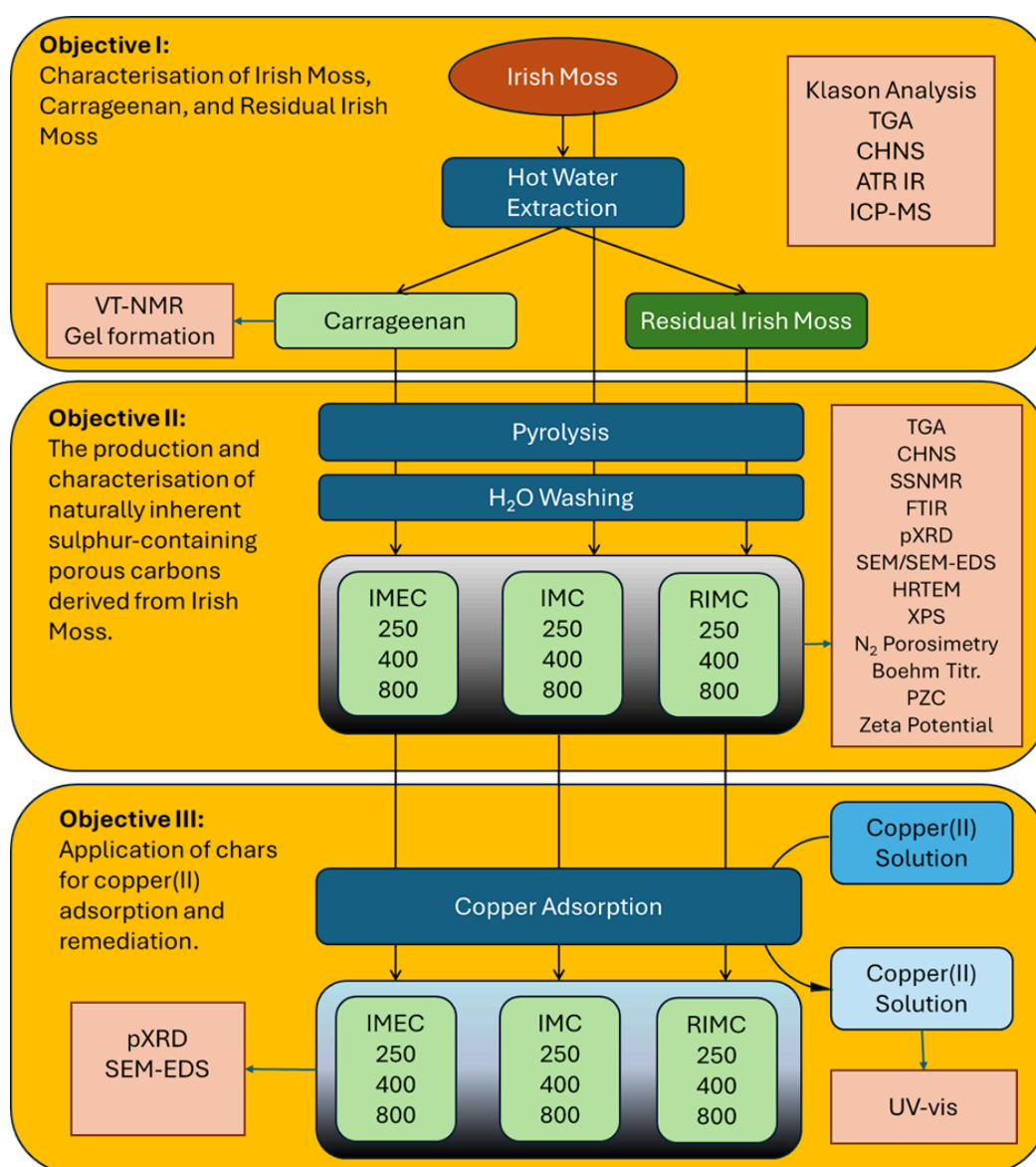


Figure 15: Flow chart depicting the aims of Chapter 3: Biochars from macroalgal biomass.

Objective I: Characterisation of Irish Moss, its carrageenan extract and residues

A carrageenan-rich extract will be obtained from Irish Moss via acid/alkaline-free hot water extraction. Although well characterised in literature, the variability in algal biomass composition due to cultivation conditions, geographical location, or lifecycle stage ^{102,103} indicates the need for an initial characterisation of this Irish Moss biomass and its carrageenan extract. This macroalgae and fractions (carrageenan and residue) will be characterised by elemental analysis, particularly CHNS microanalysis for sulfur content, ICP-MS analysis for mineral content, and lignocellulosic analysis for cellulose, hemicellulose, sugars and lignin content. Furthermore these analyses will be supported by TGA and ATR-IR spectroscopy. Additionally, variable temperature (VT) ¹H NMR spectroscopy will be applied to carrageenan extracts to determine the carrageenan form, and a simple gel formation test will be performed to determine its basic gelling capabilities.

Objective II: Production and characterisation of Irish Moss porous carbons

Porous carbons are frequently desired for and applied to a range of industrial and environmental applications, due to their adsorptive, catalytic, and electrical properties. Those derived from biomass materials, such as Starbons, are especially desired as a greener alternative to traditional activated carbons. Starbons, and other biomass-derived carbons, can have varying structural properties. The scale, temperature, rate of heating, and duration of biomass pyrolysis can affect the thermal decomposition of these materials and result in varying degrees of aromaticity, oxygen content, and chemical functionality in the graphitised carbon ¹⁰⁴. The pyrolysis of biomass or the biomass itself may also result in chars with varying degrees of porosity. Pore shape and size are important factors in the application of chars in adsorption, catalysis, electronics, or filtration ¹⁰⁵. Porous solids may be classified according to the IUPAC terminology: microporous (<2.0 nm pores), mesoporous (2.0-50.0 nm pores), and macroporous (>50.0 nm) ¹⁰⁵.

Doping graphitic carbon with heteroatoms influences the properties of the material and can broaden its functionality. The heteroatoms can act as binding sites, introduce

acidic/alkaline surfaces, or alter the electronic configuration by acting as a π -electron donor or acceptor. Common heteroatom dopants include nitrogen, oxygen, boron, and sulfur; however, other rarer dopants also include phosphorus and silicon^{106–109}. Heteroatoms can be inserted into various different locations in the graphitic carbon and result in complex structures. The location and state of the heteroatomic dopant in the porous carbon has a significant impact on the functional properties of the material. Some doping locations are depicted in Figure 16 and include¹¹⁰:

- Substitution: The covalent insertion of heteroatoms into the aromatic graphite sheets. Figure 16 shows that the heteroatoms can have different chemical environments within the sheets, ranging from ‘pyrrolic’-like to graphitic bulk and edge.
- Intercalation: The non-covalent insertion of the dopant as a salt or an organic compound between the graphite sheets.
- Surface Functionalization: This doping adds chemical functionality to the surface of the carbon by covalently bonding the heteroatom to the graphitic surface.
- Nanocomposites: The presence of nanosized clusters of dopants trapped in pores/defects on the surface or within the carbon material.

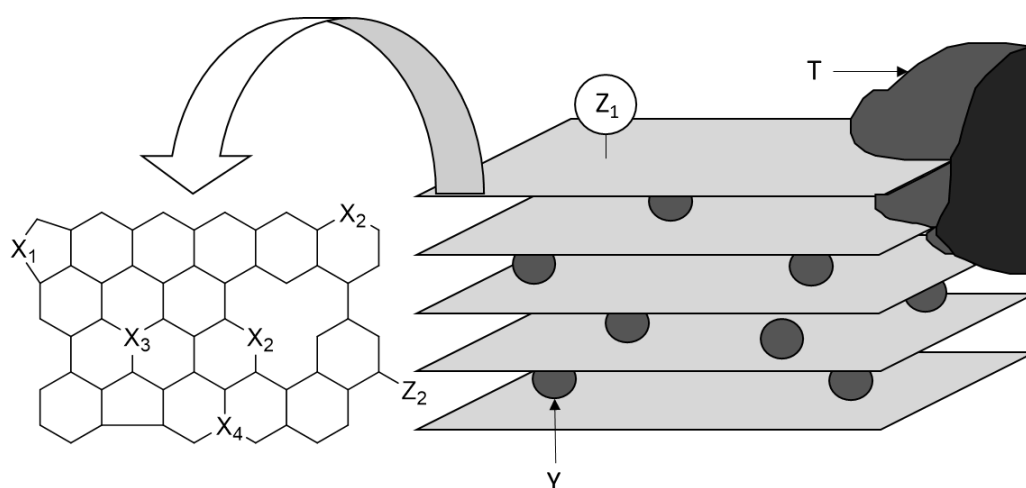


Figure 16: A representation of the different types of heteroatomic doping of graphitic carbon.

X_1 = pyrrolic-like, X_2 = pyridinic-like, X_3 = graphitic (bulk), X_4 = graphitic (edge), Y = intercalation, Z_1 = surface functionalization, Z_2 = edge functionalization, T = nanocomposite.

Recent publications have proposed that heteroatom-doped porous carbons have applications in areas such as electronics ¹¹¹, organic pollutant removal ¹¹² and greenhouse gas capture ¹⁰⁶. Doping can often be achieved *via* the addition of heteroatom containing compounds to the biomass material prior to pyrolysis, this allows the heteroatom to be included in the formation of graphite sheets. For example doping with urea or melamine introduced a nitrogen content of 0.5-30% in a series of nitrogen-doped porous carbons (NDPCs) ¹¹³⁻¹¹⁵. Even a minor heteroatom presence in porous carbons has a range of beneficial effects on the material. Substitution of an electron donor into aromatic carbon sheets enhances electron acceptor/donor interactions in the delocalised π -systems. This enables stronger π - π interactions between the carbon surface and aromatic pollutants, such as VOCs or dyes ^{112,113,116}.

Sulfur-doped porous carbons (SDPCs) are well reviewed by Kiciński *et al.* The stronger electronegativity of sulfur develops an increased surface polarity compared to that of pure graphitic carbon; aiding the adsorption of polar materials and improving surface wettability. The comparative size of sulfur atoms with carbon prevents the substitution of sulfur into the aromatic sheets without disrupting the planar structure. This results in a curvature of the sheets and protrudes the sulfur atoms out of the carbon layer. A benefit to this is an increase in reactivity at the sulfur sites, enabling rapid electron transfer and surface redox reactions to take place or for the binding of various materials, including nitrogen pollutants and precious metals ¹¹⁰. The increased electrical conductivity due to increased electron density, as well as redox potential and surface wettability enables SDPCs to be effective as electrode materials; more so than traditional activated carbons ^{114,117}. This kind of intrinsic doping also interrupts planar interactions between the sheets and results in the introduction of a semiconducting band gap, while also acting as an n-type dopant. The binding of a substance at sulfur sites in SDPCs, is expected to alter the electronic structure and result in a change in conductivity, which may allow SDPCs to act as a potential sensor

¹¹⁸.

Sulfur-doped carbons are typically synthesised from sulfur rich precursors, or by doping during pyrolysis with materials such as hydrogen sulfide, thiophenes, metal sulfates, or liquid or gaseous sulfur¹¹⁹. This may yield carbons with a few percent to almost 20% sulfur content¹¹⁰. These methods often result in the presence of sulfur containing nanocomposites or sulfur intercalation. This may be beneficial or detrimental depending on the application of the porous carbon. This method of doping often results in a decreased surface area and porosity due to the filling of pores with sulfur or metal sulfates/sulfides (often the presence of these salts can aid in conductivity).

Sulfur surface functionalization of porous carbons is typically achieved *via* sulfonation with concentrated sulfuric acid¹²⁰. This introduces various sulfur-containing functionalities such as thiols, sulfonic acids, disulfides, and thiophenes, the two former being most prevalent^{110,120}. These oxidising conditions also resulted in oxygenation of the surface¹²⁰. Thiol and sulfonic acid surface functionality enable these SDPCs to act as effective solid acid catalysts. Further, coordination of metal ions to both intrinsic and surface sulfur atoms enables even more catalytic activity, which is often easy due to the natural affinity of many metals such as gold, lead, and mercury to sulfur. These metal sulfide doped porous carbons are often also implemented in various zinc/lithium/sodium batteries as electrode or ORR catalytic materials^{121–123}. Unfortunately, the addition of toxic sulfur-containing dopants or the use of highly corrosive sulfuric acid is problematic, and greener alternatives are required. The chemistry of starch, pectin, and alginic acid-derived porous carbons (Starbons) is well established, however, carrageenan-derived porous carbons are somewhat less studied. NDPCs have been previously produced by doping with the nitrogen-rich polysaccharide, chitin, and therefore it would be reasonable to assume the same could be done with sulfated polysaccharides. The sulfated polysaccharide, carrageenan, can form stable hydrogels without additional gelling agents and upon drying form a macroporous aerogel. It also has a theoretical sulfur content of 8.30%, 13.8%, or 17.1% for kappa, iota, and lambda forms, respectively. Utilising carrageenan as a potential SDPC precursor, would eliminate the need for sulfur-based additives or unnecessary additional steps.

The aim of this section is to produce sulfur-containing porous carbons from unrefined carrageenan aerogels (IME) obtained from commercially available Irish Moss. This material is an effective green alternative to other sulfur-doped carbons, not only due to it being a non-toxic sulfur dopant source but also due to its sustainable sourcing from seaweed. Pyrolysis without any external dopants or activating agents will be performed at 250 °C, 400 °C, and 800 °C to produce chars with varying degrees of carbonisation and to better understand the pyrolysis mechanism. This mechanism will be monitored using TGA and TG-GCMS. The chars will be characterised using FT-IR, SSNMR, elemental analysis (CHNS and ICP-MS) and HRTEM to determine the compositional content of these materials and the degree of carbonisation. XRD will be performed to analyse the production of salts, as recognised in literature ¹²⁴. Surface characteristics will be determined as the material's surface will greatly impact its electrical, adsorption, and catalytic applications. Surface Topography and porosity will be determined using SEM-EDS and N₂ Adsorption Porosimetry, while surface functionality and acidity/basicity will be determined with XPS, Boehm Titration, Zeta potential and PZC analysis. For comparison, chars derived from Irish Moss (IM) biomass and carrageenan-depleted Irish Moss (RIM) biomass will be produced and characterised in an identical manner. Compiling char composition and surface characteristics should give a detailed understanding of these chars and suggest potential applications for these materials if any.

Objective III: Application of sulfur-containing chars for copper(II) adsorption

A typical application of carrageenan-derived sulfur-containing porous carbons is as a metal sulfide-doped carbon aerogel for metal ion storage in electrode materials ^{123,125,126}. Pyrolysis of iron-carrageenan at 800 °C leads to the presence of iron sulfide nanocomposites embedded into the porous carbon material. This provides a site for sodium ion storage through sodiation ($\text{FeS} + 2\text{Na}^+ + 2\text{e}^- \rightarrow \text{Na}_2\text{FeS}$) and subsequent desodiation with excellent cycling stability. The mesoporous aerogel also enables the storage of sodium

cations, decreasing the diffusion distance to embedded nanocomposites, while the graphitic carbon allows for rapid electron delivery and removal^{126,127}. This has also been achieved in literature using nickel-carrageenan, with both materials exhibiting high performance for use as sodium ion battery anodes^{123,126}.

There is some evidence of carrageenan-derived carbons being applied to adsorption. Nogueira *et al.* successfully adsorbed the antibiotic, ciprofloxacin, onto KOH activated, carrageenan-derived porous carbon¹²⁸. Antibiotic removal from wastewater streams is important to reduce antibiotic resistance. The 2300 m²/g highly graphitised surface area, enabled >99% removal of the antibiotic. However, this was achieved after submersion for 24h and required a 10 fold quantity of carbon to ciprofloxacin. It was determined that various molecular interactions were involved in the ciprofloxacin adsorption mechanism, including π - π interactions, hydrophobic interactions, and hydrogen bonding. The effect of pH also suggested cation- π interactions were favoured in acidic conditions but to a lesser degree¹²⁸. Similar interactions between aromatic carbon structures derived from carrageenan/sodium lignin sulfonate, and methylene-blue dye have also been recognised. In this case doping with sodium lignin sulfonate enabled the adsorption of approximately 400 mg/g of the aromatic dye, without the need to carbonise the carrageenan material to very high temperatures¹²⁹.

Many sulfur-doped carbons have been applied to heavy metal adsorption. For example, Saha *et al* explored the adsorption of metals such as mercury, cadmium, lead, and nickel onto a sulfur-functionalized mesoporous carbon, synthesised via the addition of sodium thiosulfate (Na₂S₂O₃) to a carbon precursor¹³⁰. In another study, sulfur-doped carbon particles were achieved through sulfuric acid functionalization of almond shell biochar, and applied to cadmium(II) adsorption¹³¹. In both studies, sulfur-doped chars exhibited significant affinity towards these heavy metals. Although the exact interactions between sulfur functionalities and heavy metals is not fully understood it is generally accepted that heavy metals have an affinity to sulfur containing functionalities¹³⁰. Despite carrageenan-derived

carbons containing high levels of sulfur content, the adsorption of precious metals or heavy metal pollutants on these materials has not been published.

Copper is a valuable heavy metal. It has applications in alloys, construction, electronics, and clean energy ^{132,133}. The demand for copper is increasing with the uptake of clean electronics such as electric cars and solar panels. China is the leading copper producer with around 40% of the global production ¹³⁴. Copper pollution from the production of copper is a severe environmental problem. Copper(II) ions are a major heavy metal pollutant. These ions are formed for the use of copper in electroplating, paints and dyes, metallurgy, and pesticides ¹³⁵. Unfortunately this pollutant ends up in many industrial effluent streams. Copper remediation from wastewater is essential due to the high toxicity of copper(II) to human health and aquatic environments ¹³⁵ and helps towards sustainable development goals 6 (clean water and sanitation) and 14 (conserving oceans, seas, and marine resources). Remediation can be performed using many techniques, examples include precipitation, ion exchange, membrane filtration, electrochemistry, or adsorption. Adsorption is considered to be a low cost and effective method of pollutant removal.

The aim of this section is to explore the possibilities of applying carrageenan-derived sulfur-doped porous carbons for the adsorption and remediation of copper(II) from aqueous solutions. **To the author's knowledge this is the first application of naturally inherent, as opposed to sulfur-doped, sulfur-containing porous carbons for copper(II) remediation.** A noncompetitive adsorption approach will be used to determine the adsorption capacity of copper(II) for the afforded chars in Objective II. Copper(II) adsorption will be determined indirectly using the UV-vis adsorption intensity of the remaining solutions, and adsorption kinetics and isotherms will be produced by varying the contact time and initial concentration of copper(II). The adsorption of copper will also be measured directly by investigating the presence of copper on the used chars. This will be performed by pXRD and SEM-EDS analysis .

1.4.1.3. Commercially cultivated microalgae, ALG01

ALG01 is a novel and proprietary species of algae that has limited literature presence. However, as informed by AlgaeCytes, the proprietary owner, this microalgae resembles *Nannochloropsis sp.*, which is fairly well researched.

Nannochloropsis sp. are spherical microalgae around 2-8 μm in diameter^{136,137} of the eustigmatophyte class (yellow-green algae). They are often cultivated due to their high lipid and PUFA content. In many species a 10-30% lipid content is common. However, limiting the nitrogen and phosphorus availability can result in an increase in lipid content, as well as promote vitamin E enrichment^{136,138}. Benvenuti *et al.* recognised a 5-fold increase (~10 to ~50 %) in TAG content of *Nannochloropsis* over a 120 hour period following nitrogen starvation¹³⁹. The PUFA, EPA (C20:5), is abundant in this microalgae. Zanella and Vianello estimated an average EPA content of 4%, to which they stated "an EPA amount higher than 2% is remarkable"¹³⁶. Other significant fatty acids include palmitic and palmitoleic acid, commonly found in the lipid membrane of cells¹⁴⁰. As a yellow-green algae, the major fat-soluble pigments available in this organism include: chlorophyll a, β -carotene, violaxanthin, vaucherixanthin, canthaxanthin, and astaxanthin^{136,141}. A significant feature of this algal species is the lack of chlorophyll b and c¹⁴¹.

In literature the isolation of lipids is typically achieved via solvent extraction. Folch, and Bligh and Dyer methods are common standard approaches. These methods homogenise biomass with mixtures of chloroform and methanol. The wide range of polarities these solvents possess enables the extraction of both polar and nonpolar lipids from biomass¹⁴². These methods, although effective, use hazardous solvents which conflict with green chemistry principle 5 (see section 1.4.2). Further this method has limited selectivity, and therefore to isolate specific lipid metabolites further purification is required, via the use of additional solvents and processes.

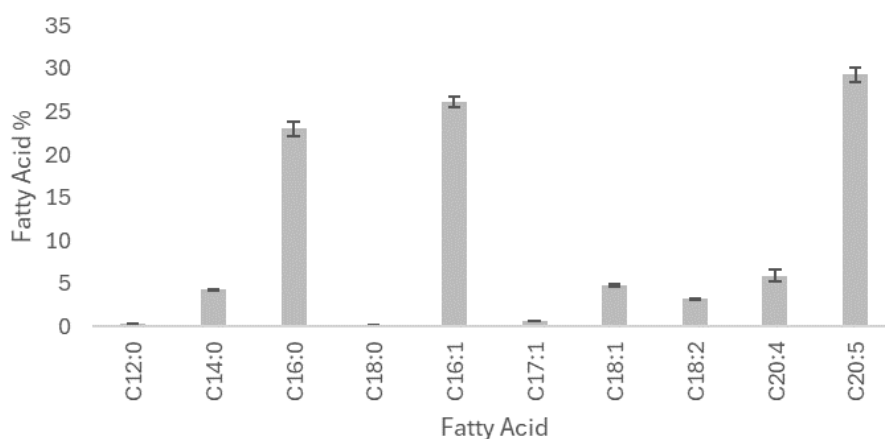


Figure 17: Fatty acid composition of Folch method lipid extracts from *Nannochloropsis gaditana*. Castejón and Marko data reproduced as a bar graph ¹⁴³.

The use of green solvents in the extraction of algal lipids is preferable. Castejón and Marko implement ultrasound assisted extraction with green(er) solvent, ethanol, on *Nannochloropsis gaditana* to afford a lipid extract with omega-3 fatty acid content and yield comparable to a Folch approach ¹⁴³. However, it is important to understand that although greener, ethanol still poses a potential hazard as a volatile and flammable solvent, and the requirement of additional heating to 50 °C and ultrasound processing is comparably more energetically costly than Folch's approach. Other green solvent approaches include: ionic liquids, switchable solvents, microwave assisted extraction, and supercritical fluids ¹⁴⁴.

Nannochloropsis, like many other microalgae, also have significant protein content, approximately 30-40% DW ^{136,137,145}. Contrasting to lipid content, nitrogen starvation affords protein-depleted biomass ^{139,146}. In the same study Benvenuti *et al.* recognised a 5-fold increase in lipid content, an almost equivalent decrease was measured in the estimated protein content (from 44 to 12%) ¹³⁹. Eukaryotic microalgae require nitrogen-rich media to produce proteins, an exception was discovered recently, when a 'nitroplast', a nitrogen fixing organelle, was identified in *Braarudosphaera bigelowii* ¹⁴⁷. The amino acid profile of *Nannochloropsis granulata* exhibited significant EAA content in a study by Tibbetts *et al.* equating approximately 50% of the total protein content. Specifically, valine, leucine,

phenylalanine, and lysine, each accounted for 2-3% (DW) of the biomass ¹⁴⁵. This amino acid profile and protein content is typical of ochrophytes ¹⁴⁸ (Ochrophyta is a subphylum taxonomy class which *Nannochloropsis sp.* are classified).

Proteins, especially small peptides and amino acids, are typically hydrophilic. Although a fraction of proteins are considered water insoluble, such as membrane proteins ¹⁴⁹. The extraction of proteins from biomass can often be achieved via dissolution in water or aqueous acidic/alkaline solutions. Although large proteins can be isolated if extracted in their native form, a large portion of this protein content is bound within organelles of the cell. Water-soluble free peptides and amino acids account for a small fraction of the total protein content ¹⁴⁸ (Free peptides and amino acids, reference soluble metabolites sans the hydrolysis of proteins). Further, in *Nannochloropsis*, non-essential amino acids account for approximately 90% of the free amino acids ¹⁴⁵. These predominantly include proline and glutamic acid, which aren't invaluable, however the trapped essential amino acids are more desirable.

Extraction of lipid and protein contents are restricted due to microalgal cell wall properties. Cells are encased by a phospholipid bilayer embedded with globular proteins, sterols, and glycolipids. At approximately 4 nm thick and bound by hydrophobic interactions, this permeable layer is relatively weak ¹⁵⁰. Hydrophobic solvents, such as hexane or chloroform, penetrate and disrupt the bilayer structure introducing pores and channels for metabolites to be extracted ⁴⁰. Cell walls prevent turgor pressure-based cell lysis in hypotonic solutions, but also offer a protective layer inhibiting organic solvents entering the cell ¹⁵¹. The unyielding nature of microalgal cell walls make them a difficult obstacle to overcome. In *Nannochloropsis*, the cell wall is approximately 100 nm thick ^{39,40}, which will vary depending on the growth phase of the algae ¹⁵². The cell wall in this microalgae is composed of 2 main layers: cellulose-based inner sublayers, and a protective hydrophobic algaenan outer layer ^{39,40,151}.

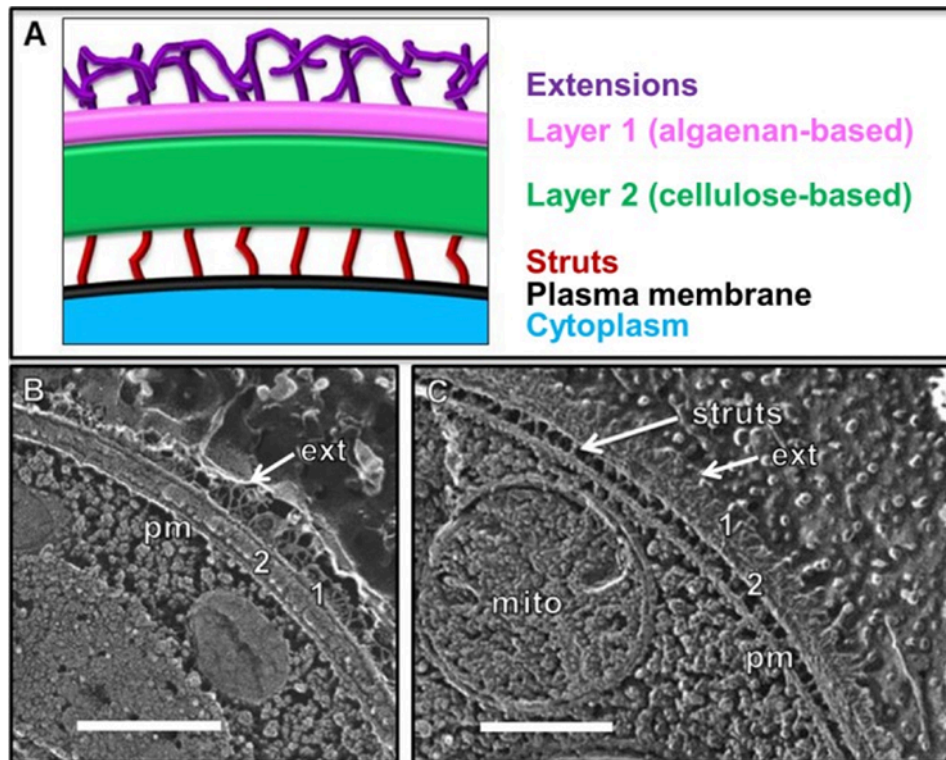


Figure 18: Scholz et al produced diagram of *Nannochloropsis* cell wall indicating algaenan and cellulose-based layers (A) based on quick freeze deep-etch electron microscopy (QFDE EM) images of a cell wall cross-section (B and C)³⁹.

Cellulose is an abundant material. It is a polysaccharide consisting of monomer D-glucose units bound by β -(1,4) glycosidic bonds which form crystalline, linear structures. Within the cell wall, cellulose forms hierarchical strands of microfibrils, fibrils, and cellulose fibres that are bound together by branched, amorphous hemicellulose. In plant cell walls cellulose constitutes a significant fraction, alongside lignin, pectin, and glycoproteins. Algal cell walls, however, lack lignin, and vary greatly in structure depending on the algal species. Many species of algae have very low cellulose contents such as the green algae *Koliella antarctica*. Their cell walls are primarily composed of hemicelluloses. On the other hand, heterokonts, such as *Nannochloropsis gaditana*, have an inner layer of cellulose fibrils that make up around 85% of the total cell wall polysaccharides^{39,151,153,154}. This thick porous mesh of parallel strands is elevated from the plasma membrane by cellulose-based struts^{39,40,151}.

Algaenan is a hydrophobic, insoluble, and non-hydrolysable biopolymer^{40,154,155}. The structure of algaenan is debated, although there is some agreement. It often consists of ~32 carbon hydrocarbon chains cross-linked by ether bridges at mid-chain and terminal positions^{39,154,156}. In some cases, polyester and polyacetal structures have been proposed along with varying degrees of unsaturation^{155,157}. However, many proposed structures are criticised due to the severe lysis conditions used to isolate algaenan, and their potential to chemically alter or contaminate the composition of algaenan³⁹.

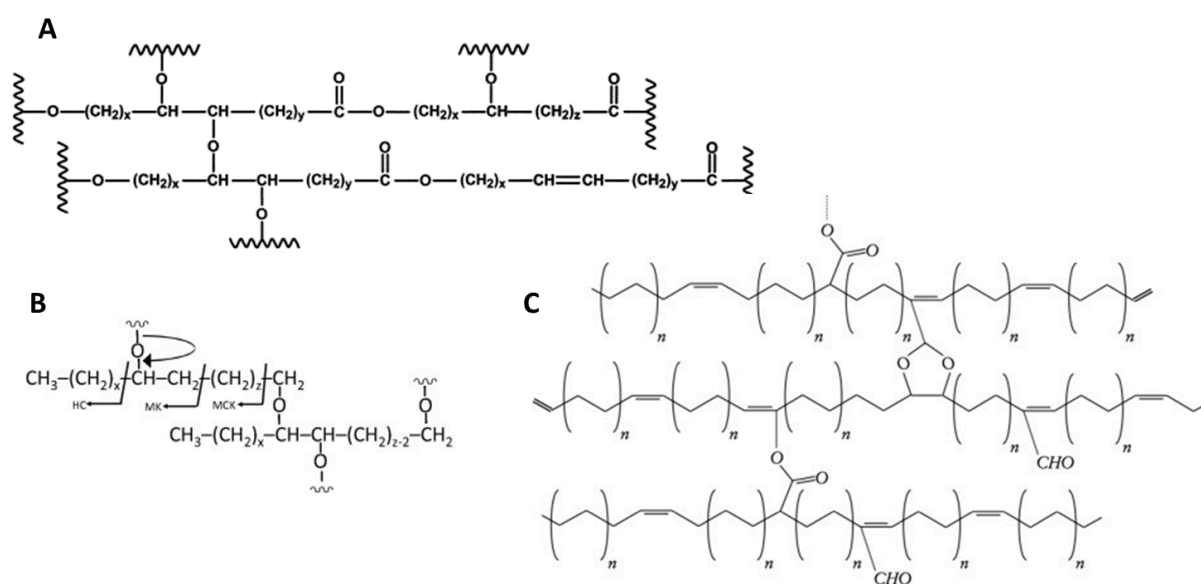


Figure 19: Proposed algaenan structures from algae: *Tetraedon minimum*, *Scendesmus communis*, and *Pediastrum boryanum* (A)¹⁵⁷, *Nannochloropsis* (B)¹⁵⁴, and *Botryococcus braunii* (C)¹⁵⁵.

1.4.1.4. Microalgal valorisation objectives

The aim of this section is the valorisation of commercial microalgae into chemicals and materials in order to develop a potential zero waste biorefinery. Two microalgal biomasses were supplied by Algaecytes: intact spray dried ALG01 and EPA-free spent ALG01, a residue from base-catalysed ethanol extraction of EPA. Both streams were explored to obtain oils, protein and defibrillated celluloses are summarised in Figure 66.

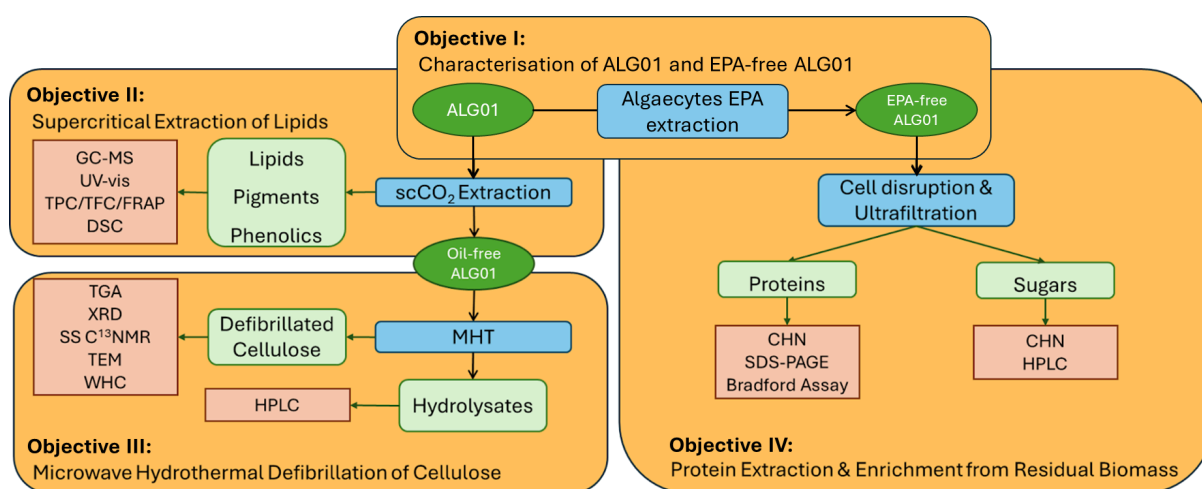


Figure 20: Flow chart depicting the aims of Chapter 4: Valorisation of Commercial Microalgae

Objective I: Characterisation of ALG01 and EPA-free ALG01

ALG01 is an engineered strain of microalgae, despite similarities to *Nannochloropsis sp.* a characterization of this biomass is required. EPA-free ALG01 underwent a specialised transesterification extraction for EPA isolation. Characterisation techniques will be used to determine the composition of EPA-free/spent ALG01 in contrast to the unaltered intact biomass. Elemental analysis (CHN) and Klason analysis, supported by TGA and ATR-IR spectroscopy, will be performed to give a preliminary insight into the structure and composition of these algal biomasses.

Objective II: Supercritical CO₂ extraction of lipids

Supercritical CO₂ is considered a green solvent. It is non-flammable, and has effectively zero-toxicity. Its gaseous state at atmospheric temperature and pressure (ATP) enables simple solvent recovery from the extract and recyclability of the solvent. With current industrial applications, for example the decaffeination of coffee or extraction of hops¹⁵⁸, the technology is well-founded and commercially available, although a substantial investment.

Supercritical fluids are formed when a material is heated and pressured above its critical point. At the critical point a substance will have properties between a liquid and a gas. For CO₂ that point lies at 31.0 °C and 73.8 bar. These are achievable conditions, and although the pressure is substantial, its frequent use has become routine in industry. Supercritical solvents are far less viscous and have a greater diffusivity than liquid solvents, resulting in the solvent permeating and solvating substances within a biomass matrix with greater ease. CO₂ is a linear nonpolar molecule and has limited solubility towards polar solutes, which enables it to be selective towards neutral lipids.

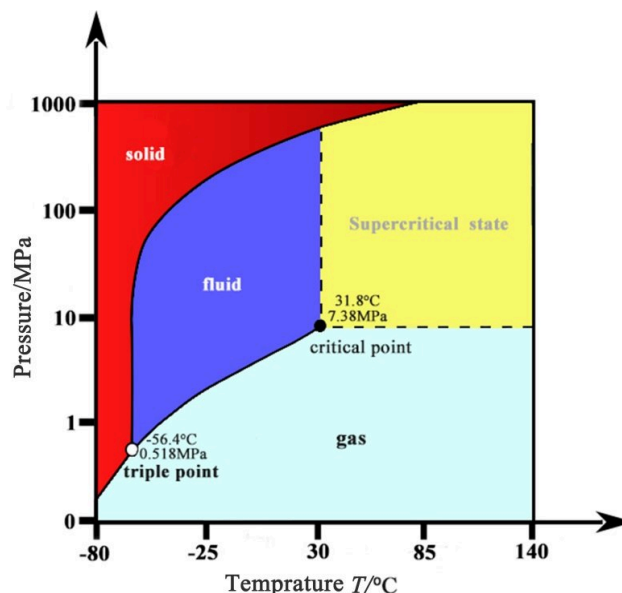


Figure 21: Phase transition diagram of carbon dioxide, indicating the critical point in which the material becomes a supercritical fluid¹⁵⁹.

The polarity of supercritical CO₂ can also be influenced by the addition of co-solvents. Adding small quantities of organic polar solvents enables the solvation of polar molecules. In one example, following the addition of 7.5% ethanol entrainer (300 bar, 60 °C), the extraction yield of pigments: lutein and chlorophyll a from *Chlorella vulgaris*, greatly increased from ~0.5 to ~1.5 mg/g_{biomass}, and 0 to 11 mg/g_{biomass}, respectively ¹⁶⁰. The entrainer effect is an important factor to account when using co-solvents. This effect describes the influence a solute has on the solvating power of the solvent. As the quantity of polar solutes increase, the solvent system itself becomes more effective at dissolving other polar substances, and in turn, less effective at solvating non-polar substances ¹⁵⁸. Although a wider more selective range of solutes can be extracted using co-solvents, it could be argued that the use of organic solvents regardless of quantity still poses similar issues, such as extract contamination and solvent waste.

Supercritical CO₂ extraction is a proven method of extracting lipid, pigment and phenolic materials. Mouahid et al. reviewed a variety of literature using scCO₂ extraction on the microalgae, *Nannochloropsis sp.* Extracts containing fatty acids: palmitic and oleic acids, and EPA were identified, as well as extracts containing carotenoids and α-tocopherol ⁶². They determined the yield of neutral lipids, chlorophyll, and carotenoids are effectively determined by the temperature and pressure of the extraction. Neutral lipid extracts are favoured between 200 and 300 bar, and show rapid increases in yield from 9.5 to 14.5% from 40 to 60 °C, respectively. Carotenoids and chlorophylls, however, are far more pressure dependent, affording low 0.2% yields below 200 bar, but rapidly increased to 1% from 200 to 300 bar ⁶². Further, a study by Molino et al. investigated the effect of temperature and pressure on the yields of β-carotene and neutral lipids from *D.salina*. They operated at temperatures of 50 and 65 °C and pressures 100, 400, and 550 bar and recognised that the β-carotene recovery and purity were highly pressure dependent, and equally the neutral lipid yields followed a similar trend ¹⁵.

As informed by Algaecytes this microalgae is rich in high-value lipid metabolites, such as EPA and β -carotene. To minimise the use of organic solvents, co-solvent-free supercritical CO₂ extraction will be used to isolate the high-value lipid content of spray dried ALG01 (Green Chemistry Principle 5). Further, temperature (35-50 °C) and pressure (200-400 bar) factorial experiments will be applied to investigate the extraction of these metabolites under variable supercritical fluid densities/conditions commonly seen in literature. The extracts will be characterised by NMR, ATR-IR, GC-MS, and UV-vis spectroscopy, to determine the content of the variable extracts.

Oxidation is a process responsible for the degradation of many organic molecules which is detrimental for products in nutrition, cosmetics, and pharmaceuticals. Antioxidant metabolites inhibit oxidation and help prevent the formation of free radicals due to oxidation. Antioxidants are beneficial supplements as they limit the formation of free radicals in the body which are a leading cause of long term illness and ageing ¹⁶¹. The antioxidant activity of these extracts will be determined by TPC, TFC and FRAP assay. Furthermore, the thermal properties of these oils will be determined by DSC to provide insight into the potential application of these oils.

Objective III: Microalgal defibrillated cellulose via microwave hydrothermal treatment

Defibrillated celluloses are traditionally produced from cellulosic rich biomass such as wood pulp. Mechanical and chemical extraction may be used to obtain cellulose fibrils. However, mechanical methods, such as HPH, or grinding, cause damage to the fibres and cannot completely remove lignin, hemicellulose, or pectin ¹⁶². Intensive chemical processing using acid or alkaline retting, digest the labile, amorphous hemicellulose, pectin and lignin, releasing the cellulose fibres. The applications of this material are diverse. Their functional properties; high colloidal stability, high thermal stability, and high mechanical strength, paved the way for their use as films and coatings, barrier materials, packaging, optically transparent materials, aerogels, rheology modifiers, filters, and scaffolds ¹⁶².

There are few studies aimed at isolating defibrillated celluloses from microalgae. One study by Lee et al. isolate cellulose nanofibrils from *Nannochloropsis* residues following lipid and protein extraction. They obtained highly crystalline (91.7% crystallinity) cellulose nanofibrils via a bleaching at 70 °C for 4h followed by delamination using tetramethyl-1-piperidinyloxy (TEMPO)-mediated oxidation. A cellulose fraction of 69% was determined by X-ray diffraction, which is far higher than that of defibrillated cellulose obtained from wood and plants ¹⁶³.

Isolation of cellulose via intensive chemical treatment is clearly successful, however, the hydrolysis of hemicellulose and pectin can also be achieved with far greener and sustainable methods. Microwave hydrothermal treatment (MHT) is the key feature of the hydrothermal microwave assisted selective scissoring (Hy-MASS) concept, which utilises the lysing potential of water at high temperatures to selectively hydrolyse amorphous hemicellulose, pectin and lignin, and yield defibrillated cellulose material ¹⁶⁴. MHT is considered to be a green, and far lower energy and time intensive method than traditional approaches (Green Chemistry Principle 6). MHT is also an acid and bleach-free method of obtaining defibrillated cellulose material from cellulosic biomass, and is therefore more suitable for use in food and medicinal industries than traditional methods . This method has been used to produce crystalline cellulose fibres from a range of biomasses including orange peel ¹⁶⁴, ginger waste ¹⁶⁵, and spent pea biomass ¹⁶⁶.

In this study, MHT will be used to obtain defibrillated cellulose from fresh and scCO₂ spent/deoiled ALG01 biomass. The defibrillated cellulose produced will be characterised by thermogravimetric analysis (TGA), X-ray powder diffraction (XRD), ¹³C cross polarisation magic angle spinning (CPMAS) SSNMR, transmission electron spectroscopy (TEM), and water holding capacity (WHC). 'Waste' hydrolysates will be analysed by HPLC to determine their potential use as either fuel or feed.

Objective IV: Protein extraction and enrichment

Algaecytes obtain EPA-rich extracts from ALG01 for commercial use. Valorisation of the microalgal residue offers this industry a process to drive towards a zero-waste approach. *Nannochloropsis* is known to contain a significant protein content, which can be obtained via simple aqueous extractions. Typically extracted alongside various polysaccharides, protein purification is often required to afford higher value protein extracts. The extraction and purification of proteins is discussed in a review by Liu *et al*¹⁶⁷. They conclude that methods such as chromatography and electrophoresis have the greatest precision regarding protein purification. However, their costs and upscaling difficulties are a limitation¹⁶⁸. Instead, protein enrichment via membrane filtration or precipitation can be used to reach an adequate purity for commercial use¹⁶⁹. Protein precipitation is often achieved through pH manipulation, the addition of organic solvents, or using a salting-out method. Unfortunately each is fraught with disadvantages; causing denaturation or contamination of proteins with organic solvents and salts¹⁶⁷.

Membrane filtration is a considerably green approach that employs a porous membrane and concentration or pressure gradients to divide metabolites based on size¹⁷⁰. Varying the filtration membrane offers selective micro, ultra, or nanofiltration. These methods are often used for desalination of proteins, however, in a few cases ultrafiltration can be used to concentrate proteins. Ursu *et al* achieved a substantial 95% protein purity following filtration via a 300 kDa membrane at pH 12. This success came from the high molecular weight proteins (670 kDa) present in their extracts¹⁷¹. Further, the phycobiliprotein, R-phycoerythrin, was concentrated using a 30 kDa membrane with 100% retention, while removing smaller proteins and polysaccharides¹⁷². However, ultrafiltration may fail when proteins become denatured. Small peptides and amino acids are able to pass through the membrane along with sugar and salt solutes¹⁷⁰.

To overcome the rigid cell walls of microalgal species (Section 1.4.1.2.) cell disruption technologies will be applied. Cell disruption is essentially a method of disrupting the cell

surface to allow for 'easier' dissolution and extraction of metabolites. Categorised into mechanical (physical) and non-mechanical (chemical/enzymatic) techniques, examples of cell disruption methods include: chemical or enzymatic digestion ^{173,174}, ultrasonication ¹⁷⁵, microwave treatments ^{176,177}, homogenisation via high-pressure or speed ¹⁷⁵, and grinding/bead milling ¹⁷⁸. Table 11 summarises some common and novel cell disruption methods and their efficacy.

Carbohydrases and proteases are common enzymes used in cell disruption. This is because algal cell walls are primarily composed of cellulose, hemicelluloses, pectins, and glycoproteins ^{173,179}. They are often mild and effective, although limited by their sensitivity to the extraction conditions and in some cases effectively lyse the desired metabolite ¹⁷⁰. This is an issue amongst chemical disruption methods also; alongside contaminating the extract.

Cell disruption via shear strain includes many different methods. Bead Milling, a common process used for the disruption of microbial ¹⁸⁰ and algal cells ¹⁷⁸, induces shear strain across cells by transferring energy from bead collisions. Ultrasonication, another form of cell shearing, promotes cavitation, the production of microbubbles that upon collapse form waves. These waves induce high energy shear forces on the algal cells ^{175,181}. Homogenisation exists in two forms, high-pressure and high-speed, this method also generates shear forces from high energy impacts and cavitation. However, where one induces these shearing forces using rapid pressure changes (e.g. flow through an impact valve), the other induces the forces near the blades of a high-speed rotor. In comparison, ultrasonication yields a broad cell disruption efficiency of 55% ¹⁸² to 90% ¹⁷⁵, whereas high-pressure and high-speed homogenisation yield 70-100% ¹⁷⁵ and 48% ¹⁸², respectively. Ultrasonication pretreatment also results in an 8-fold increase in lipid extraction yields compared to a 7-fold increase using homogenisation ¹⁷⁵. Beneficially, ultrasonication is also recognised to have a much lower energy consumption than homogenisation techniques ¹⁸¹.

Microwave assisted extraction is a proven green, scalable, more efficient, and faster heating method than conventional heating ¹⁸³. Microwaves induce dielectric heating by molecular rotation of polar materials, typically water. It has a two-fold effect: i) rapid

simultaneous heating of intracellular water molecules exert pressure on the cell, resulting in cell rupture (cell disruption). ii) rapid heating of the surrounding aqueous matrix allows for more rapid dissolution of released cell contents. Using this method the microwave conditions can determine the specific product extracted ¹⁷⁶. It is recognised that this method reduces solvent use and extraction time, while assisting in the recovery of lipids and pigments, such as EPA, DHA, astaxanthin, fucoxanthin, and lutein ^{176,177}. However, there are also many limitations of MAE usage, posing a risk of degrading some of the more heat sensitive products, especially when the cell disruption requires a higher power output ¹⁷⁶. Other issues include its limitation to polar solvents ¹⁷⁶, and the potential of forming free radicals ¹⁸¹. Mechanical methods are often effective but can be inadequate as they can be too severe and lead to the denaturing or destruction of valuable metabolites ¹⁸⁴.

This section will explore green, acid, base, and enzyme-free extraction of proteins from intact, spray dried ALG01 and EPA-spent ALG01 to determine the potential valorisation opportunity of EPA-free ALG01 residues. The following cell disruption technologies will be explored: mechanical grinding, high-speed homogenisation (HSH), ultrasonication, and microwave assisted extraction (MAE), which will be compared against a cell disruption-free extraction using distilled water alone. Enrichment of the protein extracts will be performed by ultrafiltration to afford protein-rich retentates and sugar-rich permeates. Retentates and permeates will be characterised by ATR-IR, elemental analysis (CHN), protein analysis (SDS-PAGE and Bradford assay), and HPLC.

Table 2: A comparison of the cell disruption efficiency and increases in the product yield for a variety of cell disruption methods.

Cell disruption method	Conditions	Cell disruption efficiency / % *	Desired product	Product yield increase /%	
Enzymatic	13.8 mg/g Cellulyve 50LC, 53 °C, pH 4.4, 24h.	-	Lipids	15	174
Bead milling	0.3 mm Y stabilized Zr ₂ O ₃ , 65% (v/v), 6 m/s, 25 °C, 1h.	99	Protein	10	178
Ultrasonication	Vibra-Cell™ ultrasonicator, 40 kHz, 30 min.	97	Lipids	785	175
High-pressure homogenisation	x1 pass through Emulsiflex-C, 862 Bar	68	Lipids	679	175
Microwave-assisted extraction	55 °C, 36 min, 60% KOH (aq) in acetone.	-	Lutein	30	177
Pulsed electric field	x2 cycles of 20 kV/cm treatments	54	Protein	64	185

*by intact cell count

1.4.2. Green Chemistry context

Green chemistry is a concept that attempts to minimise the environmental effects of the chemical industry. Renewable and sustainable manufacturing is vital for preventing further damage to the environment. It is founded on 12 principles, aiming to prevent waste, reduce energy consumption, and limit hazards¹⁸⁶. A full list of the 12 principles are available in appendix 1.1. In this thesis, the key principle addressed is principle 7: the use of renewable feedstocks. Valorising a renewable aquatic biomass feedstock that requires minimal land for its cultivation is an effective approach of reducing land based industries. Land use is a significant global issue and reducing the land requirements will enable routes towards sustainable development goal (SDG) 15: protecting and restoring terrestrial ecosystems. Renewable biomass feedstocks are also effective carbon fixers, using these feedstocks help push towards carbon neutrality/negativity which is an effective approach to reducing/reversing the effects of climate change (SDG 13).

The second principle applied to these works is principle 5: safer solvents and auxiliaries. Four solvents will be used in the synthetic/extraction processes of this thesis. Water, ethanol, acetone, and supercritical CO₂ have been selected according to GSK's green solvent selection guide¹⁸⁷. In almost all cases distilled water will be the primary solvent with no additional additives. Ethanol and acetone will be used in minimal quantities where water is ineffective; and used in a manner where solvent recyclability is possible. The processes used in this work will aim to be as inherently safe as possible (principle 12) and limit the quantity of additional additives. This thesis will also consider all streams of the synthetic/extraction processes where possible. Biomass residues will be considered as potential products in alignment with a zero-waste biorefinery approach. This is a fundamental aspect of sustainable development goal 12: responsible consumption and production of materials. The biorefinery approach for the feedstocks used in this thesis is depicted in figure 22 including the green principles addressed.

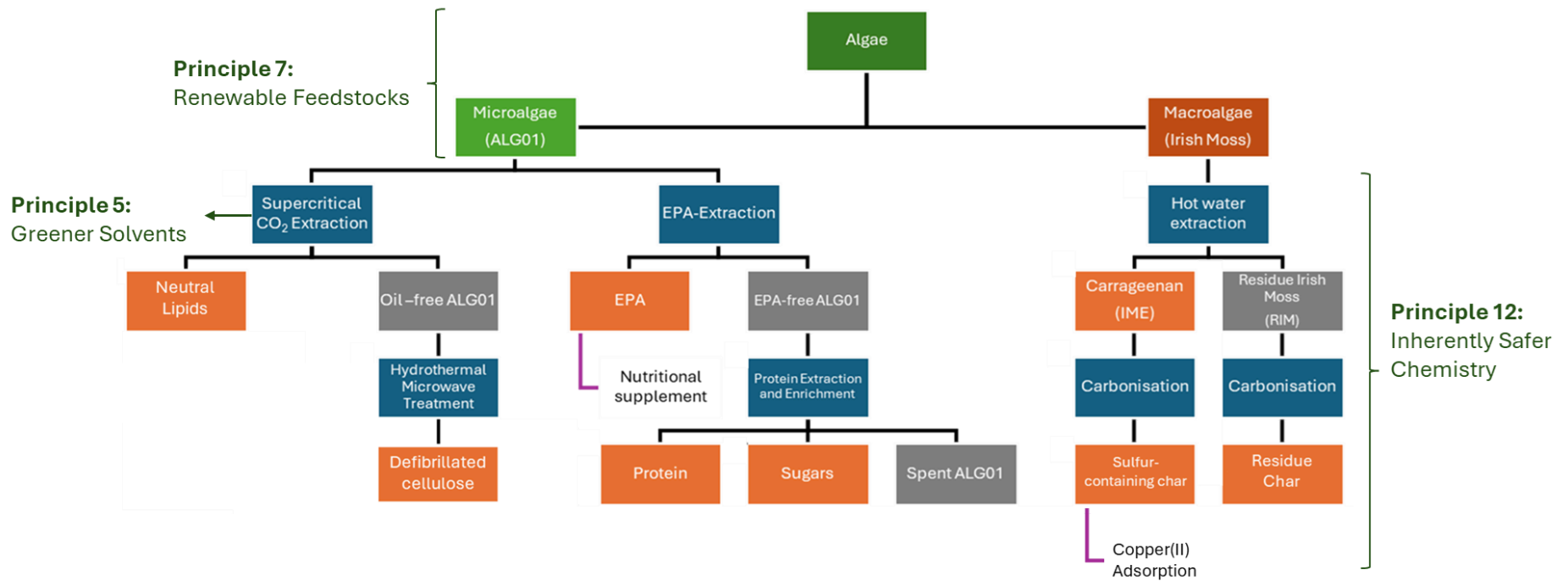


Figure 22: Biorefinery approach for ALG01 microalgae and Irish Moss macroalgae feedstocks highlighting green principles addressed.

Chapter 2: Experimental

2.1 Materials

Irish Moss, *Chondrus crispus*, was obtained from the Cornish Seaweed Company. The dried and flaked Irish Moss was ground by coffee grinder to a granular powder (<50 μm) and labelled IM. This material was then immersed in deionized water (25:1 mL:g) and the contents were stirred and heated conventionally (reflux at 80 °C for 30 minutes). The resulting mixture was then immediately centrifuged using a Thermo Fisher Megafuge 4R (3000 rpm, 30 °C, 30 min) to isolate a supernatant and pellet. Both supernatant and pellet were dried using a Labylo Controlled Freeze Drier for 48h or until dry before being labelled IME and RIM, respectively (IME: $54.6 \pm 3.3\%$, RIM: $38.9 \pm 4.2\%$).

Commercially cultivated (photobioreactors) microalgae (ALG01) were obtained from AlgaeCytes, Kent and spray dried directly after harvesting. Spent EPA-free microalgae was also provided following an ethanol and base extraction of lipids, and subsequent air drying of the residual biomass.

All reagents were used as supplied from either Fischer or Merck without further purification, unless specified otherwise. Deionised water was used throughout.

2.2 Instrumentation and Analysis

2.2.1. IR spectroscopy

Attenuated total reflection infrared spectroscopy was performed using a Perkin Elmer FTIR/FTNIR Spectrum 400 Spectrophotometer. Before sample analysis, the sapphire window was cleaned with ethanol and a background run. For sample analysis a small quantity of sample was placed on the sapphire window and (if solid powder) a pressure was applied to ensure the sample makes sufficient contact with the sapphire window. Spectra were recorded between 650-4000 cm^{-1} (32 scans) at a resolution of 4.00 cm^{-1} .

Where appropriate FT-IR sample discs were prepared by initially drying finely ground potassium bromide in a vacuum oven at 80 °C. Appropriate quantities of finely ground

samples were added to make 0.5 % (w/w) mixtures. These mixtures were again dried via a vacuum oven at 80 °C overnight. 10 mm wide and ~1 mm thick FT-IR discs were formed by compressing 30 mg of diluted sample mixtures under vacuum to ~10 tonnes of pressure using a Specac Manual Hydraulic Press. Samples were kept dry in a dessicator while transferring to the spectrometer to minimise moisture absorption.

FT-IR spectra of the sample discs were taken using a Perkin-Elmer Spectrum Two FT-IR spectrometer. A blank potassium bromide disk was used to produce a spectrum background.⁶

2.2.2. Elemental analysis

2.2.2.1. CHN microanalysis

The samples were analysed using an Exeter Analytical Inc CE440 analyser. Analyses were performed in-house by Dr. Graeme McAllister, Department of Chemistry, University of York, UK. Samples (1.6 mg-1.8 mg) were weighed on a Sartorius SE2 analytical balance and subsequently placed in a high-temperature furnace (975°C) and burnt under oxygen. Two measurements were conducted for each sample and the average is reported in the results and discussion section.

2.2.2.2. Sulfur content

2 mg of sample was weighed on filter paper and then placed into a palladium cage inside an oxygen combustion reaction flask. To the reaction flask 10 mL of the ion chromatography eluent, (9.5 mL) sodium carbonate and sodium bicarbonate, and (0.5 mL) hydrogen peroxide were added. A few drops of dodecanol were added to the filter paper to act as a fuse to start the ignition. The reaction vessel was then flushed with O₂ and the lid placed on. The reaction vessel was then placed in the middle of an oxygen flask combustion unit and combusted. Once combusted the vessel was left to shake for 20 minutes to convert all sulfur to sulfate.

Sulfate analysis was performed using ion chromatography. A standard injection of 1 mL of a 1 in 10 dilution of the stock (Dionex Seven Anion Standard) was carried out on a Thermo scientific Dionex Aquion Ion chromatography system. Pumping an eluent of sodium carbonate and sodium bicarbonate at a flow rate of 1 mL/min through a Dionex IonPac AS22 RFIC 4 x 250 mm Column. This was then followed by 1 mL of the required samples for analysis. All data handling and processing was then carried out by Chromeleon 7 software.

2.2.2.3. ICP-MS

This analysis was performed by Jon Angus at the Biorenewables development centre (BDC), York.

2.2.2.3.1. Sample Digestion

Samples (~0.2 g) were weighed out and placed into digestion vessels. This was followed with 8 mL of trace metal grade concentrated nitric acid and 2 mL of 30% hydrogen peroxide. A sample-free vessel was also prepared in the same way. This vessel was used as the blank to dilute the calibration fluids later.

The digestion vessels were sealed and placed into a microwave. The microwave was programmed to heat the contents of the digestion vessels to 200 °C over a period of 30 minutes and a thermocouple was used to monitor the temperature. Once at temperature, the contents were kept at 200 °C for a period of 15 minutes. After this period, the microwave heating is turned off and the digestion vessels are cooled down. The contents were transferred into 100 mL conical flasks and diluted to up to the mark with distilled water. 10mL of each sample was retained in preparation for the analysis.

2.2.2.3.2. Calibration curve preparation

An environmental stock calibration fluid containing the elements shown in table 3 was used to produce the calibration standards. The calibration fluid contains various metals in either high or low concentration. The environmental standard was diluted into several stock

solutions at concentrations shown in table 4. The diluent was the digestion blank prepared in section 2.2.2.3.1.

Table 3: Elements in the environmental calibration fluid.

Environmental standard	Element
High	Ca, Fe, Mg, K, Na
Low	Ag, Al, As, Au, Ba, Be, Cd, Co, Cr, Cu, Ir, Mn, Mo, Ni, P, Pb, PD, Pt, Sb, Se, Th, Tl, U, V, Zn

Table 4: Calibration concentrations for high and low concentration elements in the environmental standard

Name	Concentration high (ppb)	Concentration low (ppb)
Calibration A	100,000	1000
Calibration B	50,000	500
Calibration C	25,000	250
Calibration D	12,500	125
Calibration E	5000	50

2.2.2.3.2. ICP-MS procedure

An Agilent 7700 series ICP-MS was used to run the calibration solutions and calibration curve was produced (see Figure 23 for high concentration elements). The samples were then analysed and the concentration of each element was determined.

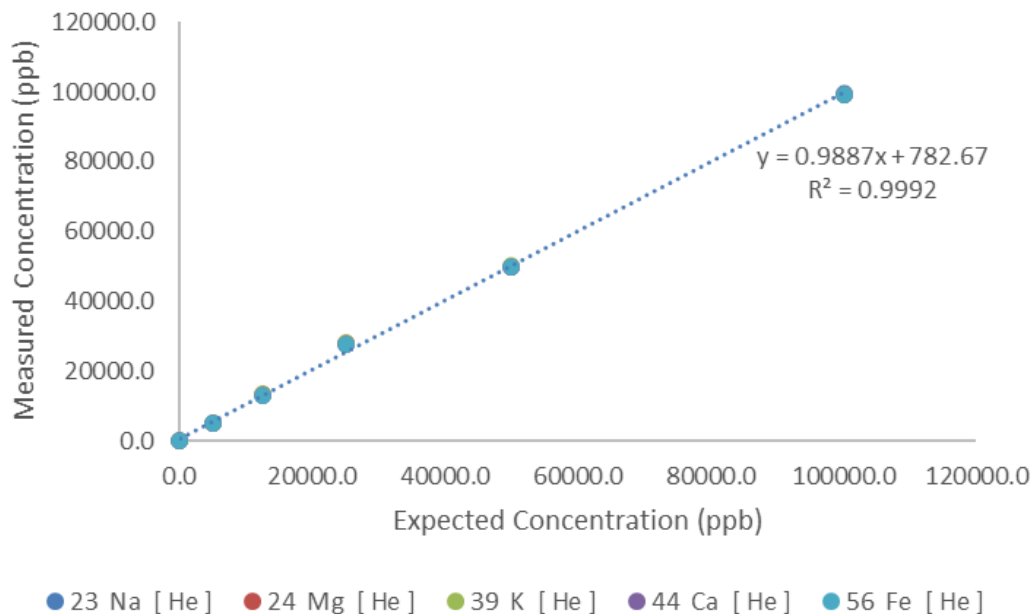


Figure 23: ICP-MS calibration curve of high concentration elements (data points are superimposed).

2.2.3. Differential scanning calorimetry (DSC)

Differential scanning calorimetry was performed on a TA instruments mDSC Q2000. Sample (5-10 mg) was loaded into a Tzero pan and sealed with a corresponding hermetic lid. The sample pan and empty reference pan were heated to 150 °C at a rate of 5 °C/min, cooled to -30 °C at a rate of 5 °C/min, and held isothermally at -30 °C for 30 minutes marking the end of cycle 1. This was repeated 3 times for a total of 3 heat-cool cycles.

2.2.4. Gas chromatography-mass spectrometry (GC-MS)

Gas chromatographic measurements were made with an Agilent Technologies 6890 gas chromatograph, fitted with a Rxi-5HT capillary column (30 m 250 mm x 0.25 mm nominal). Helium was used as the carrier gas at a flow rate of 2.2 mL/min. The initial oven temperature was 30°C and was increased instantly at a rate of 50°C/min to 300°C and held at this temperature for 5 minutes. The injector temperature was 250°C with a 2 µL injection and a split ratio of 10:1.

Mass spectrometric measurements were made with a Agilent 5973 mass spectrometer, with electron ionisation and quadrupole mass analyser. Masses were scanned over 50 m/z to 550 m/z, with a solvent delay of 3 minutes. Total run time of 13.34 minutes. MS data analysed using NIST library version 2.2 (2017).

2.2.5. High-performance liquid chromatography (HPLC)

Standard sugar and common acid analysis was separated using an Agilent Hi-Plex H+ column (300 × 7.7 mm, 8 µm particle size). The operating conditions were an isocratic mobile phase of 0.005 M H₂SO₄ with a flow rate of 0.6 mL/min. An injection volume of 5 µL with a column temperature of 60°C, a refractive index detector at 55°C and a total run time of 55 minutes. Calibrated Standards include: cellobiose, glucose, xylose, fructose, mannitol, rhamnose, arabinose, galacturonic acid, galacturonic acid, levoglucosan, lactic acid, formic acid, acetic acid, and levulinic acid.

2.2.6. High-resolution transmission electron microscopy (HRTEM)

Finely ground test material was suspended in a small quantity of acetone and sonicated before being applied to a lacey carbon film on 200 Mesh Copper grid. A Jeol 2100, 200kV Field Emission Transmission and Scanning Transmission Electron Microscope (TEM/STEM) was then used to determine the morphology of the test material at magnifications ranging from x50k to x500k.

2.2.7. N₂ Adsorption porosimetry

150 mg samples were degassed at 30 mbar and 120 °C for 20 h, before analysis by nitrogen adsorption porosimetry. The nitrogen adsorption-desorption isotherms were recorded at liquid nitrogen temperature (77 K) on a Micromeritics Tristar II porosimeter and analysed using Barrett-Joyner-Halenda (BJH) and Brunauer-Emmett-Teller (BET) methods.

2.2.8. Scanning electron microscopy - energy dispersive spectroscopy (SEM / SEM-EDS)

A Jeol JSM-7800F Schottky field emission scanning electron microscope was used to image the surface topography of the test material. The test material (<5 mg) was suspended on an aluminium mount with carbon tape. An electron beam with acceleration voltage of 5 kV and 15 kV was used at a working distance of 3.0 mm or 10 mm. A secondary electron UED or LED detector was used respectively, and images between x1k and x100k magnification were taken.

Elemental composition was determined via the insertion of Dual Oxford Instruments large area solid state detectors for energy dispersive X-ray spectroscopy (EDS).

2.2.9. Solid-state nuclear magnetic resonance (SSNMR) spectroscopy

Solid State ^{13}C cross polarisation magic angle spinning (CPMAS) spectroscopy was performed on a 400 MHz Bruker Avance III HD spectrometer using a Bruker 4 mm H(F)/X/Y triple-resonance probe and 9.4T Ascend superconducting magnet. Solid State NMR experiments were run with a spin rate of 10,000 +/- 2 Hz, recycle delays of 5 s, a total number of 512 scans and a linearly ramped contacted pulse of 1 ms. Chemical shifts were referenced using adamantane (29.5 ppm) as an external secondary reference and reporting of the chemical shifts was performed with respect to tetramethylsilane (TMS).

2.2.10. Thermogravimetric analysis (TGA)

Samples of test material (50-100 mg) were added to a ceramic thimble before being placed into a Netzch 409 Thermal Gravimetric Analyser. The samples were heated under a 100 mL min⁻¹ flow of nitrogen, from 20 °C to 1000 °C at a rate of 10 K min⁻¹ and held at 1000 °C for 20 min.

2.2.11. Thermogravimetric gas chromatography-mass spectroscopy (TG-GCMS)

Samples (10-15 mg) were analysed by A Netzsch Jupiter STA 449F5 coupled with Agilent 8890 JAS GC system and Agilent 5977B MSD. During a typical measurement the sample is heated up to 1000 °C under helium at a rate of 10°C/min. At specified temperature intervals samples of gaseous decomposition products were transferred to the GC by helium carrier gas in a line at a temperature of 300 °C. The GC system was fitted with an Agilent Technologies HP-5MS (UI) column (30 m 250 mm x 0.25 µm nominal). Helium was used as the carrier gas at a flow rate of 1.0 mL/min. The initial oven temperature was 40°C and was increased instantly at a rate of 10°C/min to 310°C and held at this temperature for 5 minutes. The inlet was set to a split ratio of 10:1. Mass spectrometric measurements were made using an electron ionisation source (230°C) and quadrupole mass analyser (150°C) and solvent delay of 1 minute. MS data analysed using NIST library version 2.2 (2017).

2.2.12. Powder X-ray diffraction (pXRD)

Powder X-ray Diffraction was performed on a Panalytical Aeris Powder XRD. Test material was packed into a 2.5 cm diameter sample holder at a depth of approximately 1 mm. A wide scan from 5° to 100° 2θ was performed at a rate of 0.02° sec⁻¹. Phase identification (probability >40%) was used to identify the signals present within the materials.

2.2.13. X-ray photoelectron spectroscopy (XPS)

This analysis was performed by Dr David Morgan at the University of Cardiff. A Kratos Axis Ultra DLD system was used to collect XPS spectra using a monochromatic Al Ka X-ray source operating at 144 W (12 mA x 12 kV). Data was collected with pass energies of 160 eV for survey spectra, and 20 eV for the high-resolution scans with step sizes of 1 eV and 0.1 eV respectively.

Samples were mounted by pressing firmly into wells of 8 mm diameter of a modified standard Kratos sample bar. The area containing the sample was electrically isolated from the sample bar itself to ensure the samples were floated from the spectrometer.

For high sensitivity, analysis was performed using the Hybrid mode, which utilises a magnetic immersion together with electrostatic transfer lenses to enhance electron detection. Data was collected over a rectangular analysis area of approximately 300 x 700 μm^2 , approximately central to the total illuminated area of 5 x 5 mm^2 . A magnetically confined low energy electron charge compensation system was used to minimise charging of the sample surface, and all spectra were taken with a 90 ° take off angle. A base pressure of ca. 5×10^{-9} Torr was maintained during collection of the spectra.

Data was calibrated to the C(1s) line at 285 eV for samples exhibiting significant sp^3 content and 284.5 eV for samples exhibiting significant sp^2 carbon content as evidenced by peak asymmetry and satellite structure. The data was analysed using CasaXPS v2.3.24¹⁸⁸ after subtraction of a Shirley background and using modified Wagner sensitivity factors as supplied by the manufacturer.

2.2.14. Klason lignin analysis

Klason lignin and sugar analysis was determined from the addition of sulfuric acid (1 mL, 72% w/v) to algal biomass (100.0 mg), stirred and left for 2 hours at 40 °C. This was then quenched with water (28 mL), agitated, and placed in an autoclave at 121 °C for an hour. An aliquot (2 mL) was removed and submitted for HPLC sugar analysis. The remainder was filtered, washed with water, and dried in an oven. The residue was Klason lignin, after recording the weight, the residue was placed in a furnace at 500°C for 6 hours to determine the ash content.

2.2.15. Boehm titration

Boehm titrations were performed according to Shannon¹⁸⁹. For acidic surfaces, three basic solutions (25 ml; 0.05 M NaOH, NaHCO₃ and Na₂CO₃) were prepared. To each, the appropriate test material (0.5 g) was added, purged with nitrogen and agitated for 12 h. The resultant mixture was filtered and the filtrate was separated into five equal aliquots (5 ml each). Each aliquot was acidified with 0.05 M aqueous-HCl (10 ml for NaOH and NaHCO₃, 30 ml for Na₂CO₃), basified with an excess of NaOH (20 ml; 0.05 M) before and back titrated with acid solution HCl (0.05 M aqueous). For basic surfaces the same methodology was used but the material was mixed with 0.05 M HCl solution and treated with 0.05 M NaOH solution, treated with an excess of HCl and back titrated with 0.05 M NaOH solution. Titrations were conducted with a 907 titrando auto titrator with an 804 titrando stirrer set up and using a set endpoint pH (pH 4 and 10 respectively). The first titration would be set to pH 5 with an addition rate of 0.1 ml/min following a second titration with the set endpoint of pH 7.1 with a drift of 0.1 pH and a slow set addition (0.10 µl per min).

2.2.16. PZC analysis by pH drift

The pH of twelve batches of degassed (nitrogen and bubbling) pH solution (20 ml) (pH 1 – 12; achieved by appropriate mixing of potassium chloride solution (0.1 M); hydrochloric acid (0.1 M), and sodium hydroxide (0.1 M)) placed in to glass powder jars were measured using a calibrated pH probe (Jenway model 6505). Once analysed, a portion of the appropriate material (50 mg; IMC250-800WG, IMEC250-800WG, RIMC250-800WG) was added to one powder jar, sealed and stirred for 24 h. Thereafter, stirring was stopped, the mixture was allowed to settle prior to its pH determination.

2.2.17. Zeta potential

Solutions of approximately pH 3, 5, 7, and 9 were achieved by mixing appropriate amounts of potassium chloride solution (0.1 M); hydrochloric acid (0.1 M), and sodium

hydroxide (0.1 M)). Into 1 mL of each solution approximately 5 mg of sample material was immersed before being transferred into a Malvern Panalytical folded capillary cell. Zeta potential values were measured using Smoluchowski method in triplicate by a Malvern Panalytical Zetasizer Nano.

2.2.18. Antioxidant activity

2.2.18.1. Determination of total phenolic content (TPC)

TPC of supercritical extracts was determined using a similar method to Chen *et al.*¹⁹⁰ The gallic acid solution/sample solution 0.5 ml was mixed with 0.5 ml of 1N Folin-Ciocalteu reagent (FCR). After vortexing for 15 s, 9 ml of 2% aqueous Na₂CO₃ solution was added and allowed to stand for 25 min at room temperature. A small aliquot of this mixture was transferred into a clean dry UV-cuvette and its UV-vis spectrum recorded. The absorbance was measured at 730 nm and the TPC ((mg GAE/g dry weight) was determined with respect to a calibration graph of gallic acid standards (0-0.005 mg/ml) against absorbance.

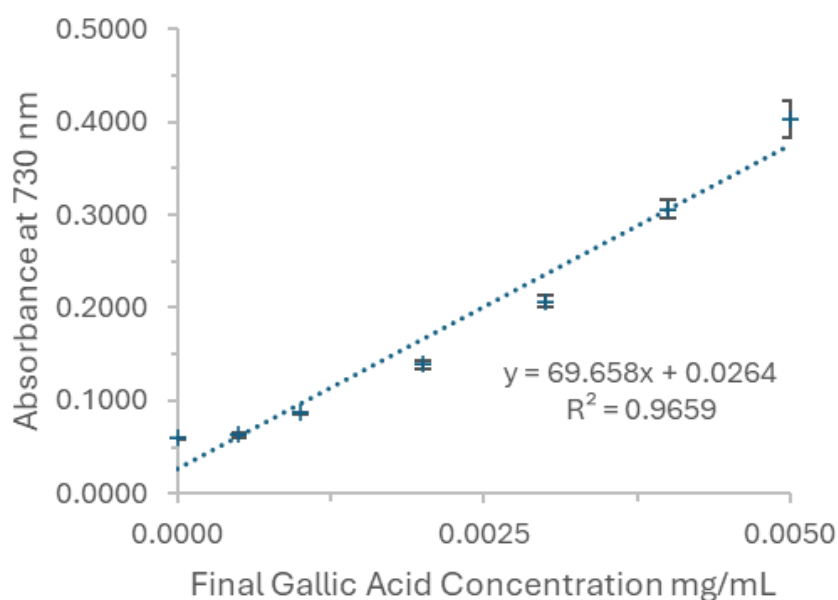


Figure 24: TPC Calibration Curve of Gallic Acid standards (0.000-0.005 mg/mL) determined via UV-vis absorbance at 730 nm.

2.2.18.2. Determination of total flavonoid content (TFC)

TFC was determined using Alara *et al.*'s method ¹⁹¹. 0.5 ml of standard flavonoid solutions/sample solution was mixed with 9 ml of ethanol. Then, 0.5 ml of 2% AlCl₃ (aq) was added and incubated for 1h at room temperature. The contents of flavonoids compounds are measured at 420 nm using ethanol as a reference. A standard flavonoid (quercetin) curve with final concentrations (0-0.010 mg/ml) was plotted and the sample concentrations were then calculated from the standard curve equation and expressed as mg quercetin equivalents per gram of dried weight sample (mg QE/g dry weight).

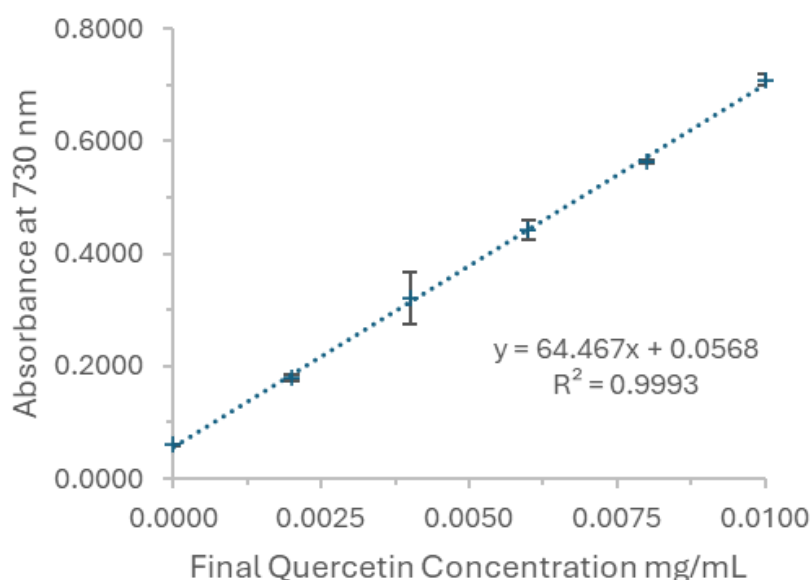


Figure 25: TFC Calibration Curve of Quercetin standards (0.000-0.010 mg/mL) determined via UV-vis absorbance at 730 nm.

2.2.18.3. Ferrous reducing antioxidant power (FRAP) assay

FRAP assay was carried out using a similar method to Olugbami *et al* ¹⁹². Mixtures of 1 ml supercritical extracts (100-1000 ppm), 2.5 ml of phosphate buffer (0.1M, pH 6.6) and 2.5 ml of 1% potassium ferricyanide were incubated at 30°C for 30 min. Then, 2.5 ml of 10% trichloroacetic acid was added to the mixture and centrifuged for 15 min at 3900 rpm. 2.5 ml

of the supernatant was diluted with 2.5 ml of distilled water and shaken with 0.5 ml of freshly prepared 0.1% ferric chloride. The absorbance of mixtures was measured at 700 nm using the Jasso 500 UV-Vis. Ethanol was used as a reference and butylated hydroxytoluene (BHT) and ascorbic acid were used as the standards (10-1000 ppm).

2.2.19. Water holding capacity

Water holding capacity (WHC) was determined by dispersing the appropriate dry material (2 g) and water (38 mL) in a weighted centrifuge tube and strongly agitating for 10 min. The resultant mixture was centrifuged (30 min at 3000 rpm), and the supernatant was carefully decanted from the wet pellet. The wet pellet was weighed and the WHC was calculated from the difference between the wet and dry pellet per gram of sample.

$$WHC (g_{H_2O}/g_{sample}) = (M_{wet} - M_{dry}) \div M_{dry} \quad \text{Equation 2.1}$$

2.2.20. Gel formation

Samples of different concentrations (0.5 % - 3 %, w/v) by mixing an appropriate amount of material with deionised water. The samples were subsequently homogenised at 10000 rpm for 3 min to afford the hydrogels, which were then refrigerated. The inversion test was used to test the success of hydrogel formation. A successful hydrogel has formed if, upon inversion of the vial, the sample maintains position and does not flow.

2.2.21. Ultrafiltration

The supernatant was pumped (450 mL/min) through a microfiltration membrane (Spectrum Labs Hollow Fiber Filter Module, mPES: 0.2 μ m, S.A.: 180 cm³) using the Spectrum Labs KrosFlo TFF System (kR2i). The microfiltration permeate was pumped (350 mL/min) through an ultrafiltration membrane (Spectrum Labs Hollow Fiber Filter Module,

mPES: 10 kD, S.A.: 235 cm³) with a backpressure of 15 psi. The ultrafiltration retentate (30 mL) was then diafiltrated with water (150 mL).

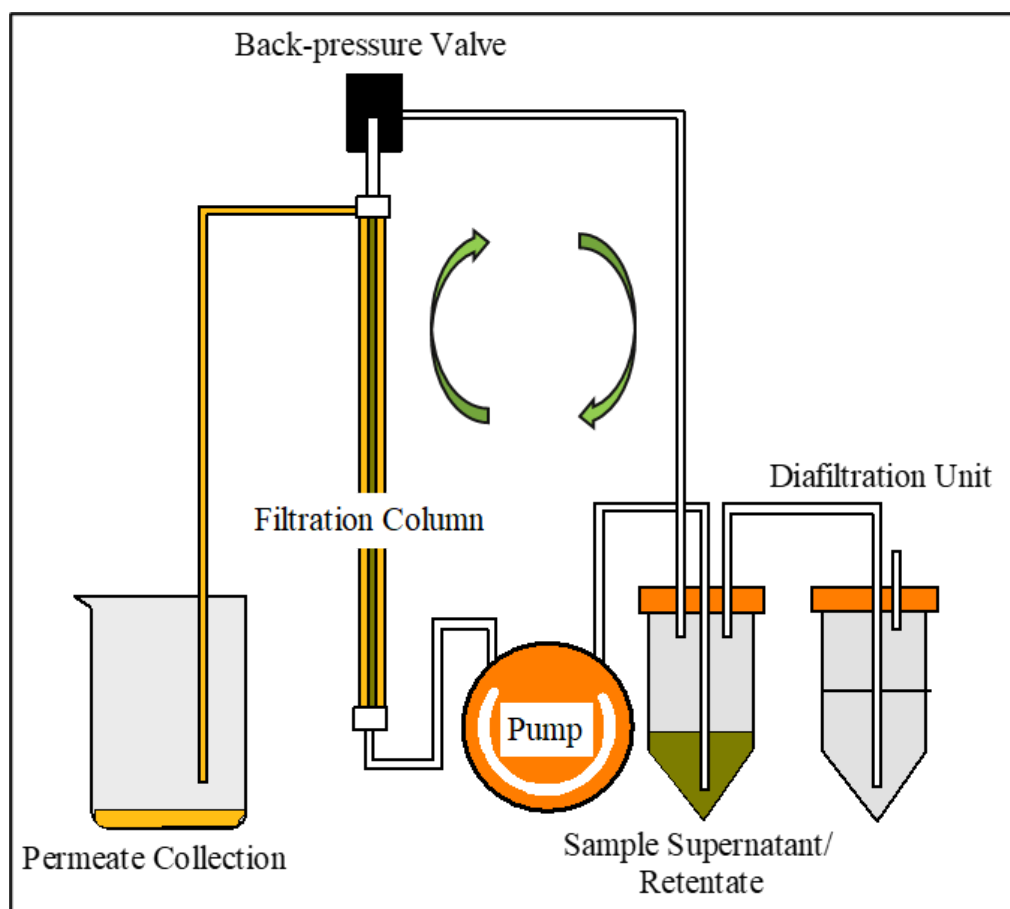


Figure 26: Simplified diagram of a typical micro/ultrafiltration set-up.

2.2.22. Protein analysis

2.2.22.1. Protein precipitation and SDS-PAGE analysis

Retentate/permeate (20.0 mg) was added to an Eppendorf tube and dissolved in water (100 μ L). Acetone (400 μ L, -20 $^{\circ}$ C) was added and the Eppendorf was strongly agitated before being incubated overnight at -80 $^{\circ}$ C. Post incubation the Eppendorf was centrifuged (20590 rpm, 20 min, -10 $^{\circ}$ C) and the supernatant removed via pipette. Further acetone was added (400 μ L, -20 $^{\circ}$ C) and the process repeated (excluding incubation) until the supernatant was colourless. The final pellet was dried in air for 30 minutes to allow for

dissolution for SDS-PAGE analysis. The dried retentate/permeate was dissolved in diluted LDS (500 μL , 1:1 water: LDS sample loading buffer (Invitrogen)), strongly agitated, sonicated for 10 minutes, centrifuged, and heated (70 $^{\circ}\text{C}$) for 20 minutes to denature proteins. 20 μL was loaded into a well of the NuPAGE Bis-Tris Gel (Invitrogen) and electrophoresis by constant voltage (120 V) was performed for approximately 1.5 hours, or until the dye front reached the end of the gel. The gel was stained with Simply-Blue TM Safe Stain (Invitrogen) overnight and de-stained with water for a minimum of 4 hours.

2.2.22.2. Bradford-assay analysis:

Varying dilutions of an albumin standard (BSA) in water (0.05 mL, 2000 – 25 $\mu\text{g mL}^{-1}$) was combined and equilibrated with Coomassie Plus reagent (1.5 mL). A calibration curve was produced using the UV-vis absorbance of these mixtures at 595 nm. This was repeated in triplicate. Permeate/retentate (1.0 mg) was dissolved in water (0.4 mL), to 0.05 mL of this Coomassie Plus Reagent was added (1.5 mL), once equilibrated the UV-vis absorbance was read at 595 nm, also in triplicate.

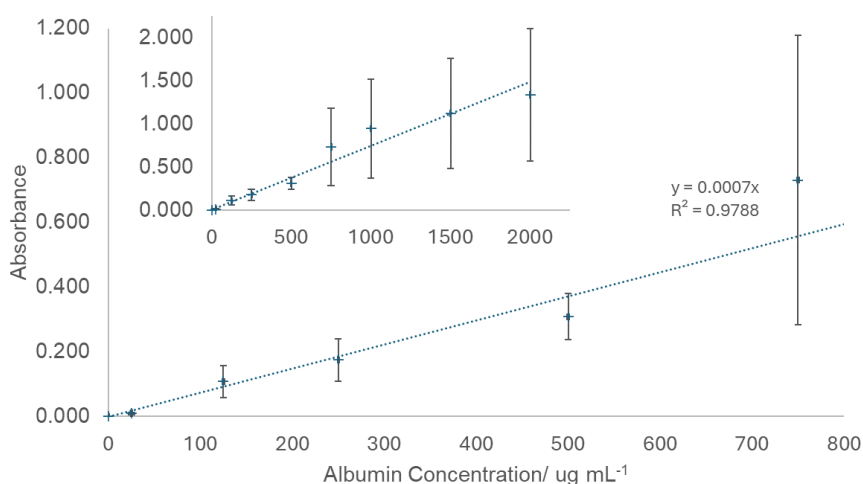


Figure 27: Zoomed region of Calibration curve illustrating the UV-vis absorbance at 595 nm of varying albumin concentrations in Coomassie Plus reagent. Inset is the full curve exhibiting poor repeatability at concentrations higher than 750 $\mu\text{g mL}^{-1}$.

2.3. Methods

2.3.1. Pyrolysis of Irish Moss and Irish Moss components



Figure 28: Barnstead 6000 Muffle Furnace set-up.

Seaweed material (IM, IME, or RIM) (10 g) was loaded into a quartz flask and placed under reduced pressure (~ 30 mbar) and heated within a Barnstead 6000 Muffle Furnace using the following programs: the samples were initially heated to $100\text{ }^{\circ}\text{C}$ at a rate of $5\text{ }^{\circ}\text{C min}^{-1}$, and held at this temperature for 60 min. The samples were then heated to $250\text{ }^{\circ}\text{C}$ at a rate of $0.3\text{ }^{\circ}\text{C min}^{-1}$. Samples labelled C250 were held at this temperature for 30 minutes before being collected (IMC250: 58.7%, IMEC250: 61.3%, RIMC250: 67.0% yield). Further heating to $400\text{ }^{\circ}\text{C}$ at a rate of $0.3\text{ }^{\circ}\text{C min}^{-1}$ proceeded. Samples labelled C400 chars were held at this temperature for 30 minutes before being collected (IMC400: 44.8%, IMEC400: 48.1%, RIMC400: 48.8% yield). The final C800 chars were heated from $400\text{ }^{\circ}\text{C}$ to $800\text{ }^{\circ}\text{C}$ at a rate of $2\text{ }^{\circ}\text{C min}^{-1}$ and held at this temperature for 30 minutes before being collected (IMC800: 29.2%, IMEC800: 31.2%, RIMC800: 29.4% yield). These samples were labelled

with their respective prefix (IM, IME, or RIM) and the pyrolysis temperature (C250, C400, or C800).

After a sample was removed for analysis, the chars were subsequently washed with hot water (100 mL) for 1h, filtered, and rinsed with hot water (2x 50 mL) and acetone (50 mL) before being left to air dry.

2.3.2. Copper(II) adsorption study

The adsorption capacity of IM, IME, and RIM chars (250-800 °C) was determined by suspending varying quantities of test material (10, 50, and 100 mg) in 10 mL of varying concentrations of aqueous copper(II) nitrate solutions (100, 500, 1000, 1500, 2500, 3500 and 5000 mg/L) for 0.5 h, 1.0 h, 1.5 h, 2.0 h, 3.0 h, 4.0 h, 5.0 h, 6.0 h, and 24 h. The UV-vis absorbance spectrum (900-400 nm) and pH of the filtered copper(II) solution was then measured by probe (Jenway model 6505) and the copper(II) adsorption capacity determined via the intensity of λ_{\max} (~810 nm), a calibration curve (figure 23), and equation 1 below.

$$Q_e = \frac{V(c_i - c_e)}{m} \quad \text{Equation (2.2)}$$

Where Q_e is the equilibrium adsorption capacity (mg/g), V is the volume (L), c_i is the initial concentration (mg/L), c_e is the equilibrium concentration (mg/L), and m is the mass of adsorbent (g).

Adsorption studies at pH 1 were performed in a similar manner using aqueous copper(II) nitrate solutions (100-5000 mg/L) derived from 0.1 M nitric acid solutions and copper(II) nitrate. Before use solutions were confirmed to be pH 1 (± 0.1) by pH probe (Jenway model 6505).

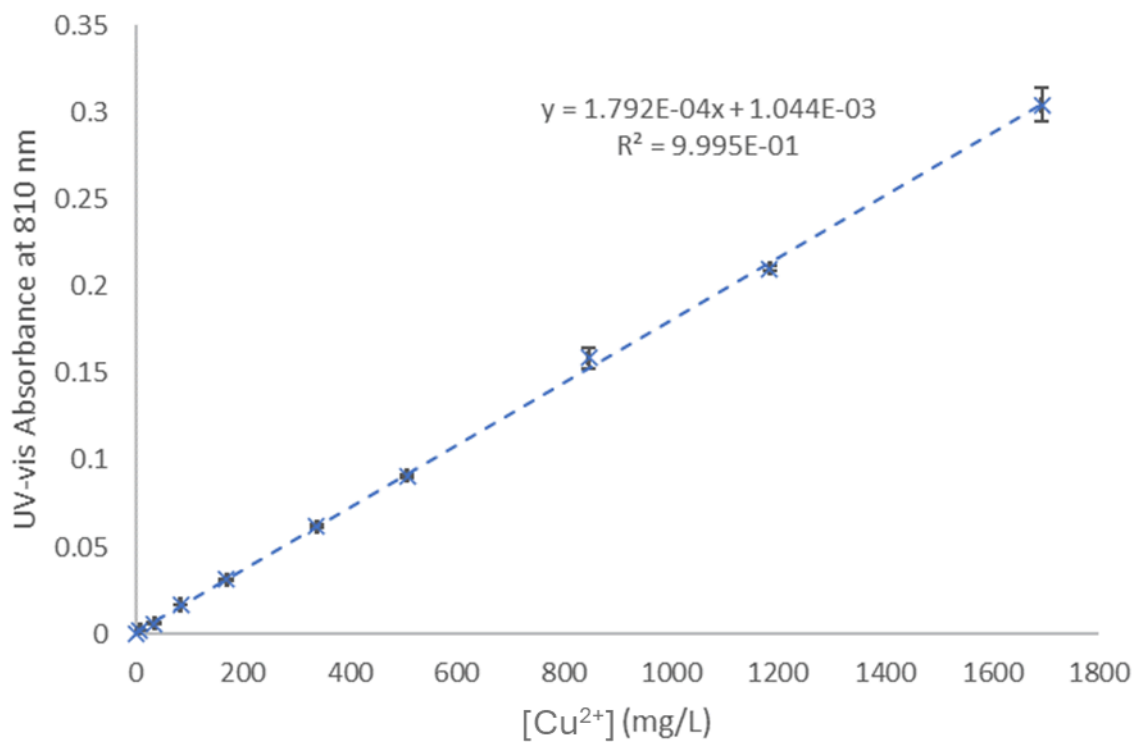


Figure 29: UV-vis Calibration curve indicating the effect of copper(II) concentration on the absorbance intensity at 810 nm.

The residue testing materials from copper(II) adsorption experiments were collected and washed with distilled water and acetone before air-drying. These samples were then analysed by pXRD, XPS and SEM-EDS.

2.3.3. Supercritical CO₂ extraction of microalgal lipids

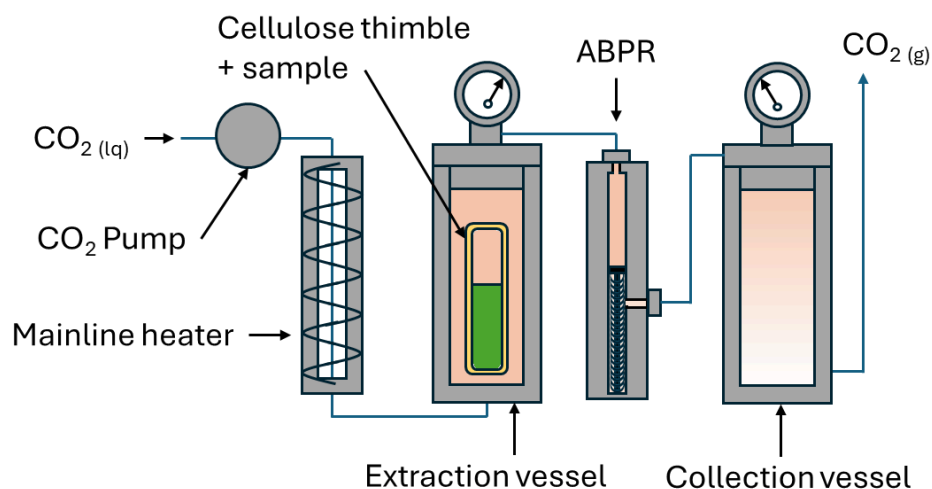


Figure 30: Simplified diagram of a supercritical CO₂ extractor.

Supercritical CO₂ extraction of microalgal lipids was carried out using a supercritical extractor SFE-500 (Thar Technologies). The microalgae, ALG01 (50 g), was loaded into a large cellulose thimble and covered with a layer of filter paper. The thimble was placed into the extractor, sealed, and underwent extraction for 2 h at a fixed CO₂ flow rate of 30 g min⁻¹ but various temperatures (35-50 °C) and pressures (200-400 bar). Upon depressurisation at 0.3 bar s⁻¹, the biomass was removed and the extract collected in acetone, via a 1.5 hour cleaning run with 8% acetone co-solvent (300 bar, 35 °C). The concentrated and dried extracts were analysed using ATR-IR spectroscopy, ¹H and ¹³C NMR spectroscopy, UV-vis spectroscopy, GC-MS, and differential scanning calorimetry (DSC). From now extracts will be labelled by SCXXXYY, where XXX is the pressure in bar and YY is the temperature in °C used to obtain this sample. For example, SC30040, is the supercritical CO₂ extract from microalgae following an extraction at 300 bar and 40 °C. Extractions were completed in triplicate and the average yields are reported.

2.3.4. Microwave hydrothermal treatment and cellulose isolation

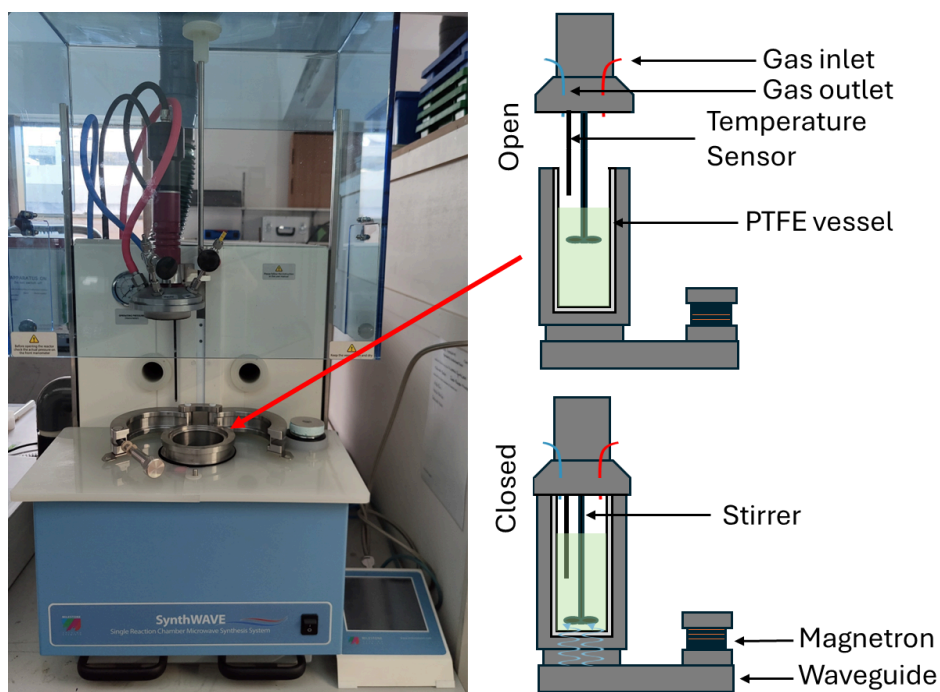


Figure 31: Milestone Synthwave Reactor set-up.

Hydrothermal microwave treatment was carried out on a Milestone Synthwave reactor (1500 W, 2.45 GHz). The spray-dried or scCO₂ deoiled microalgae (10 g) were then mixed with deionized water (350 mL) at a ratio of 1:35 (w/v) in a PTFE vessel (900 mL) and microwaved at different temperatures (160, 180, 200 and 220 °C) for a total time of 30 minutes (50:50 ramp:hold) under 10 bar of nitrogen. The resulting slurry was subsequently centrifuged for 20 minutes on a Thermofisher Megafuge 4R for 20 minutes at 3600 rpm at room temperature. The Supernatant was decanted to separate from the pellet and underwent hydrolysate analysis (section 2.2.5)

The pellet was washed with hot water (300 mL, 15 min, 80 °C) followed by pure hot ethanol (2x 300 mL, 15 min, 65 °C), ethanol (300 mL, 15 min, 20 °C) and pure acetone (300 mL, 15 min, 20 °C) followed by air drying at ambient temperatures for 24 hours in order to obtain the desired defibrillated cellulose.

The supernatant was subject to microfiltration (pore size: 10 µm) on a KrosFlo Research Iii Tangential Flow Filtration System using a mPES MidiKros filter module in order to remove any solid particles and general impurities from the drying process or transport. The resulting fraction was analysed using HPLC in order to evaluate the carbohydrate content.

The defibrillated celluloses were analysed via thermogravimetric analysis (TGA), X-Ray powder diffraction (pXRD), ¹³C cross polarisation magic angle spinning (CPMAS) SSNMR, high resolution transmission electron microscopy (HRTEM), water holding capacity (WHC) and gel formation.

2.3.5. Cell disruption and soluble-protein extraction methodologies

Microalgal biomass (50.0 g) was immersed in distilled water (500 mL), stirred for 5 minutes, and then centrifuged for 20 minutes (3900 rpm, 10 °C). The resulting solution underwent ultrafiltration. The resulting ultrafiltration retentate and permeate were freeze-dried and the solids were weighed and characterised by ATR-IR spectroscopy, elemental analysis (CHN), SDS-PAGE, Bradford-Assay, and HPLC sugar analysis (permeate). This method was repeated for microalgae that had undergone the following cell disruption methods.

2.3.5.1. Mechanical grinding

Microalgal biomass (50.0 g) was ground using a coffee grinder, for 7 second pulses and 3 seconds rest for 5 minutes. The ground biomass was immersed in distilled water (500 mL), stirred, centrifuged, and treated as above.

2.3.5.2. High-speed homogenisation

Microalgal biomass (50.0 g) was stirred into distilled water (500 mL). In 100 mL aliquots the mixture was homogenised for 5 minutes (Ystral laboratory X10 series,

approximate speed: 20,000 rpm). The combined homogeneous mixtures were then centrifuged and treated as above.

2.3.5.3. Ultrasonication

Microalgal biomass (50.0 g) was stirred into distilled water (500 mL). 50 mL aliquots were sonicated (Sonics Vibra-cell VCX 130, 20 kHz, 75% amplitude, 6 mm probe) with 3 second pulses for 20 minutes in an ice bath. The combined aliquots were centrifuged and treated as above.

2.3.5.4. Microwave-assisted extraction

Microalgal biomass (50.0 g) was stirred into distilled water (500 mL) and placed inside the sample vessel of a Milestone synthWAVE apparatus (see section 2.3.4). The vessel was pressurised with nitrogen to 10 bar to avoid solvent boiling and the mixture was stirred and treated with microwave radiation up to 80 °C and held for 5 minutes (ramp rate: 4 °C min⁻¹). Upon depressurising and cooling the resulting mixture was centrifuged and treated as above.

Chapter 3. Biochars from macroalgal biomass

3.1. Characterisation of Irish Moss (IM), Irish Moss extract (IME), and residual biomass (RIM) (Objective I)

3.1.1. Preliminary compositional analysis

The experimentally determined composition of Irish Moss (IM) and its carrageenan extract (IME) and residues (RIM) are summarised in Table 4 and the carbohydrate composition is depicted in Figure 26.

Table 5: Compositional analysis (%) of Irish Moss (IM) and its water-soluble (IMEC) and insoluble (RIM) fractions.

	Composition (%)		
	Irish Moss (IM)	Irish Moss Extract (IME)	Residual Irish Moss (RIM)
Carbohydrate ^a	22.9 ± 3.2	22.3 ± 1.1	23.5 ± 2.4
Protein ^b	7.8 ± 0.1	N.D.	15.0 ± 0.4
Moisture ^c	16.4 ± 0.3	19.3 ± 0.4	6.6 ± 0.7
Residual matter (char) ^c	27.5 ± 0.1	29.1 ± 0.6	30.1 ± 0.7
Ash (estimated) ^d	9.84	10.48	9.79
Acid insoluble content	9.2 ± 4.4	7.3 ± 0.7	13.0 ± 0.9
Acid insoluble ash	<0.1	<0.1	0.5 ± 0.1

^a Derived via Klason acid-digestion and HPLC analysis

^b Estimated from CHN nitrogen content with 3.55 conversion factor

^c Derived via TGA

^d Assuming ICP-MS metal content as metal oxides

3.1.2. Carbohydrate and sugar analysis

In this section the carbohydrate content of each sample was estimated by summing the hydrolysate sugar contents following acid hydrolysis. The Irish Moss biomass (IM) used in this research exhibited a total carbohydrate content of 24.4 % (figure 26). This is significantly lower than literature values expected for this macroalgae. J Olssen *et al* determined a 52.6% carbohydrate content⁸⁶ for *Chondrus crispus*, whilst A. Mathieson and E. Tveter determined a 41-57 % carbohydrate content of which carrageenan contributed 45-87 %¹⁰³. The Irish Moss extract (IME) accounted for 54 % (DW) of the algal biomass and was expected to predominantly contain the polysaccharide carrageenan. This material exhibited a 22.3 % 'carbohydrate content' following acid hydrolysis. This is similar to the 20.7 % value obtained by Meinita *et al*¹⁹³. In their study they implied that acid hydrolysis afforded simpler oligosaccharides not detected by HPLC and that sequential enzymatic hydrolysis was required to afford a higher sugar content in the hydrolysate¹⁹³.

Klason analysis is one of many analytical methods for lignin estimation¹⁹⁴. The principle of this method is to perform an acid digestion of biomass to remove carbohydrate, protein, and lipid content. In plant biomass the remaining acid-insoluble content is typically attributed to lignin. This Klason 'lignin' is typically considered an overestimation^{194,195}. A benefit to this approach is that HPLC sugar analysis may be applied to the subsequent lysates to determine the neutral sugars, uronic acids, and organic acids content which provides an indication of the total carbohydrate content. It is worth noting that this sugar analysis method only attributes common lysate sugars to the carbohydrate content. Those sugars are listed here: cellobiose, glucuronic acid, galacturonic acid, glucose, xylose/fructose/mannose/galactose, mannitol, and arabinose/rhamnose. Organic acids: lactic, formic, acetic, and levulinic acid, and dehydration products: levoglucosan, HMF, and furfural are also included. (Some neutral sugars have overlapping HPLC peaks and are therefore listed together)

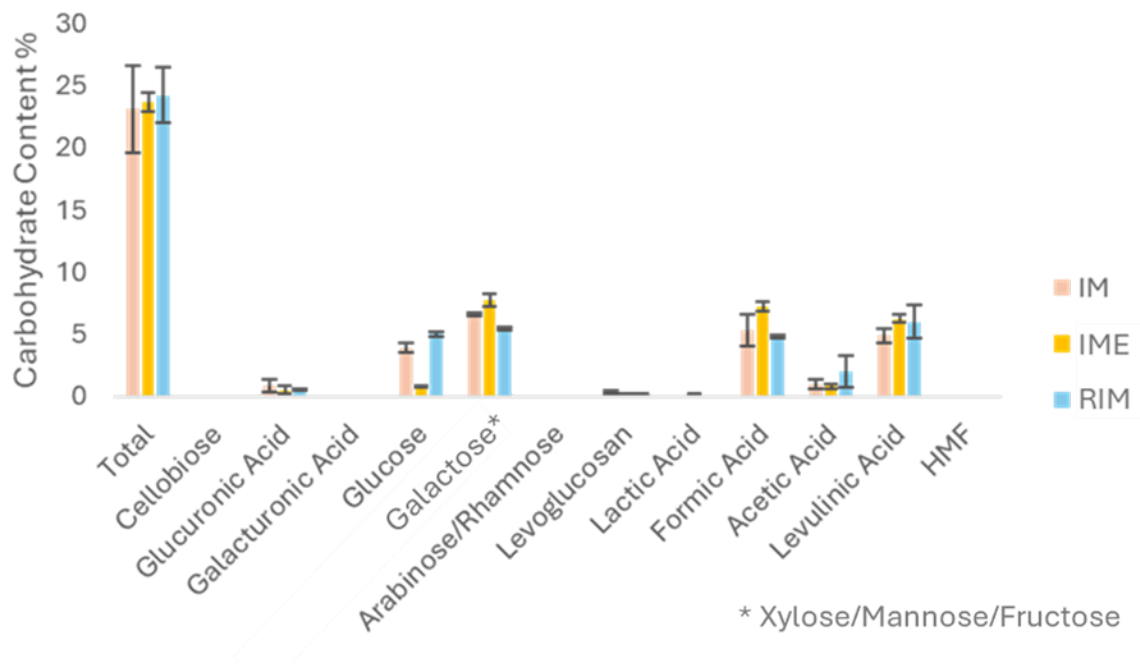


Figure 32: Acid-hydrolysed profile of Irish Moss (IM), carrageenan (IME) and residual Irish Moss (RIM) carbohydrates.

The acid-hydrolysed profile of Irish Moss (IM) indicates predominantly glucose and xylose/fructose/mannose/galactose content accounting for approximately 20 and 30% of the total sugar content, respectively. The acid-hydrolysis of carrageenan in literature results in the desulfation of this polysaccharide leading to neutral sugars of glucose and galactose being identified in HPLC ^{193,196}. The abundance of carrageenan in Irish Moss (IM) and the aqueous extract most likely infers that the unresolved HPLC peak of neutral sugars: xylose, fructose, mannose, and galactose, was predominantly galactose. Organic acids, formic and levulinic acid, were identified, which form following the dehydration and decomposition of sugars which occur during concentrated acid-hydrolysis. This process is discussed in more detail in section 4.1.2. The residual Irish Moss (RIM) exhibited a similar profile to the Irish Moss (IM), whereas the carrageenan extract (IME) indicated a relatively small amount of glucose and an increase in 'galactose' content.

Algae are not known to contain lignin, or at least the true lignin present in plants ¹⁹⁷. The metabolic pathway for lignin production is considered an important step in the evolution of

vascular plants, and only lignin-precursors or lignin-like structures have been recognised in some algal species ^{197–199}.

the 10% or so of ‘lignin’ or acid-insoluble content of Irish Moss, its aqueous extract and residue are most likely due to humins. These are dark-coloured insoluble solids formed from the acid-catalysed polymerisation of glucose and dehydration products ²⁰⁰. The ash content (determined via pyrolysis in air) of the acid-insoluble material is negligible in Irish moss and the carrageenan extract, however, in the residual biomass a small ash content of 0.48 % was recognised, which were expected to be predominantly inorganic salts.

3.1.3. Elemental analysis (CHNS)

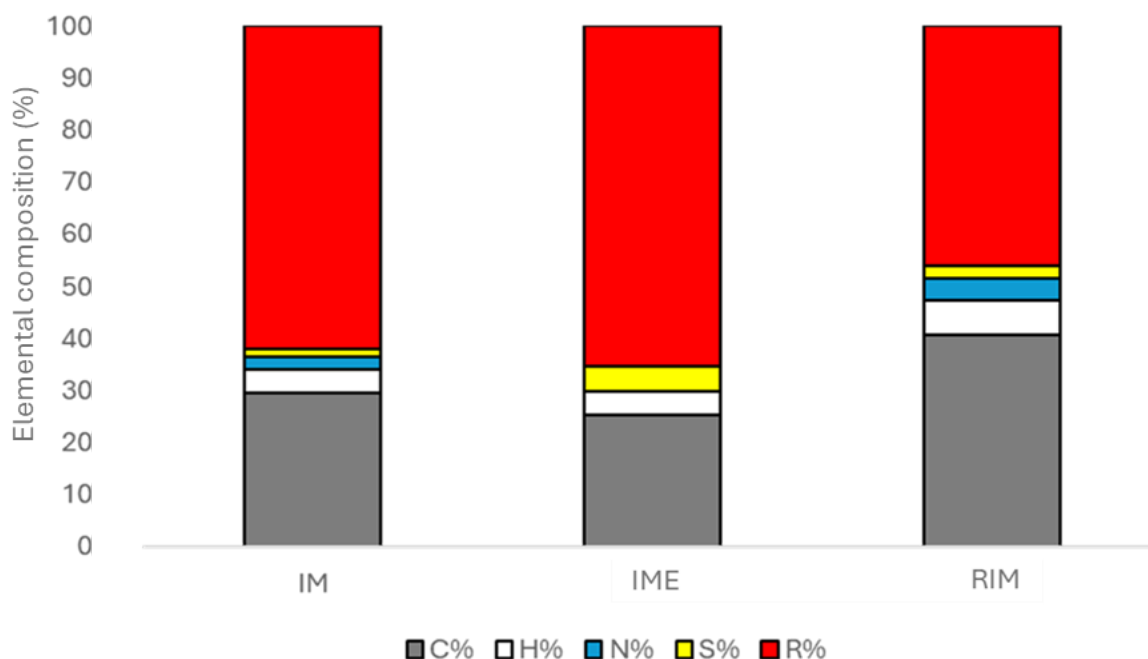


Figure 33: CHNS content of Irish Moss (IM), Irish Moss extract (IME), and residual Irish Moss (RIM).

The elemental analysis (2 s.f) of Irish Moss (IM) revealed a carbon, hydrogen, nitrogen and sulfur content of 29.4 ± 0.25 %, 4.76 ± 0.11 %, 2.19 ± 0.03 %, and 1.56 ± 0.09 %, respectively. For biological material a nitrogen-to-protein conversion factor of 6.25 is

typically used to determine protein content, suggesting that IM contains 13.4 % protein content. Furthermore, this assumes all the nitrogen detected is associated with proteins and overlooks non-protein nitrogen²⁰¹; often resulting in gross overestimations. I. Biancarosa *et al*²⁰² determined the nitrogen-to-protein conversion factors of several seaweed species²⁰² and a 3.55 conversion factor for *Chondrus crispus*. Using 3.55 as a conversion factor yields a protein content of 7.8% in IM. This is slightly lower than literature protein values for this macroalgae (11.2%)²⁰³ which may be attributed to the conversion factor. Often a higher conversion factor of ~4.9 is common for red algae²⁰⁴. The sulfur content of IM is predictably attributed to the sulfated polysaccharide, carrageenan, which has reported 5-13.3% sulfur content²⁰⁵. This is supported by the higher sulfur content of the aqueous extract (IME) at 4.95 %, which is expected to be predominantly carrageenan. This extract also contained negligible nitrogen content, indicating the protein content is mostly insoluble in water and is retained in the residue⁸⁷. This is supported by the higher nitrogen content of the residue, due to the removal of non-nitrogen containing polysaccharides and subsequent concentrating of protein. The removal of this highly oxygen-containing polysaccharide has also resulted in an increase in the carbon content of the residual material.

3.1.4. Mineral analysis

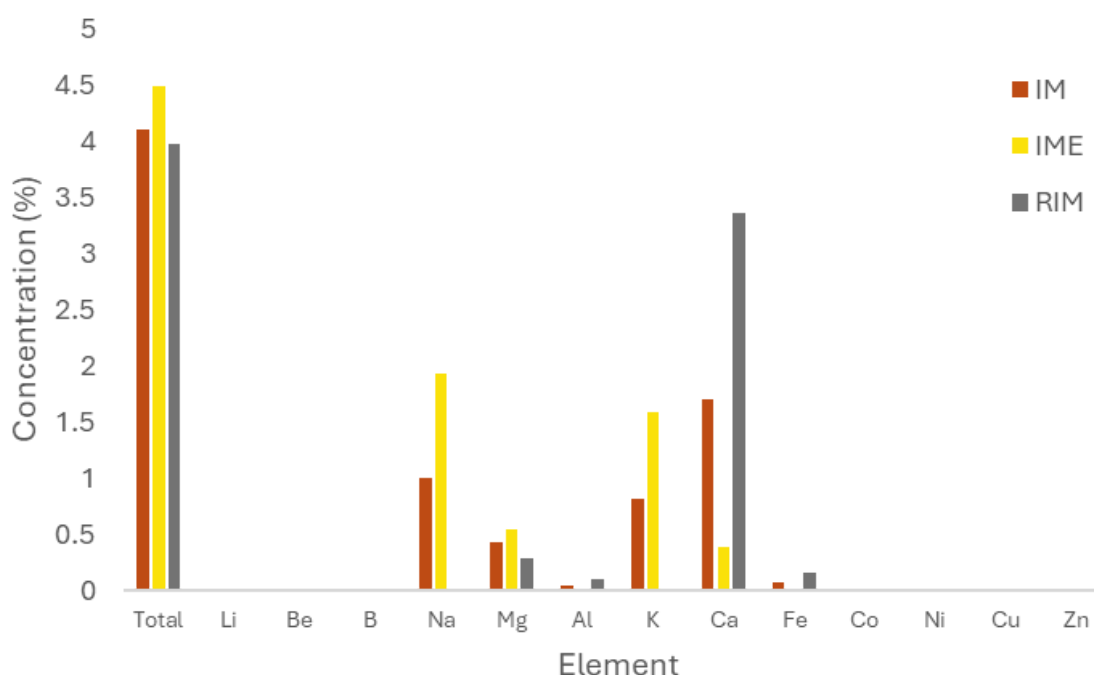


Figure 34: Mineral composition of Irish moss, Irish Moss extract and residual Irish Moss determined by ICP-MS analysis. Full analysis including trace metal quantities is available in appendix 3.1.

Alongside elemental analysis, ICP-MS analysis was performed to determine the mineral or inorganic composition of Irish Moss (IM) and its fractions (IME and RIM). From this data it was concluded that Irish Moss (IM) contained approximately 4.0 % metal content, and the carrageenan extract (IME) and residual biomass (RIM) contained 4.5 % and 3.9 %, respectively. The abundant metals present in these materials were sodium, magnesium, potassium, and calcium. However, the entirety of the sodium and potassium content was extracted in the aqueous extract, and therefore were absent in the residue. Trace minerals: aluminium, iron, zinc, and strontium were also identified, and were noticed to be retained primarily in the residual biomass. Many of these minerals may also be responsible for the residual ash content of this fraction of Irish moss in Klason analysis (section 3.1.2.). The

results here exhibit similarities to ICP-MS analyses of Irish Moss in literature. Todorov *et al* examined the elemental composition of several edible seaweeds including Irish Moss. In this study they recognised significant sodium (5.6%), potassium (1.9%), magnesium (1.3%), and calcium (4.6%) content, and trace amounts of iron (~0.1%)²⁰⁶. Although the quantitative values in this thesis are lower, this is likely attributed to the variability in seaweed biomass due to geographical origin, seawater salinity, harvesting age (carrageenan content), or the harvesting process (if the seaweeds are washed).

3.1.5. Thermogravimetric analysis (TGA)

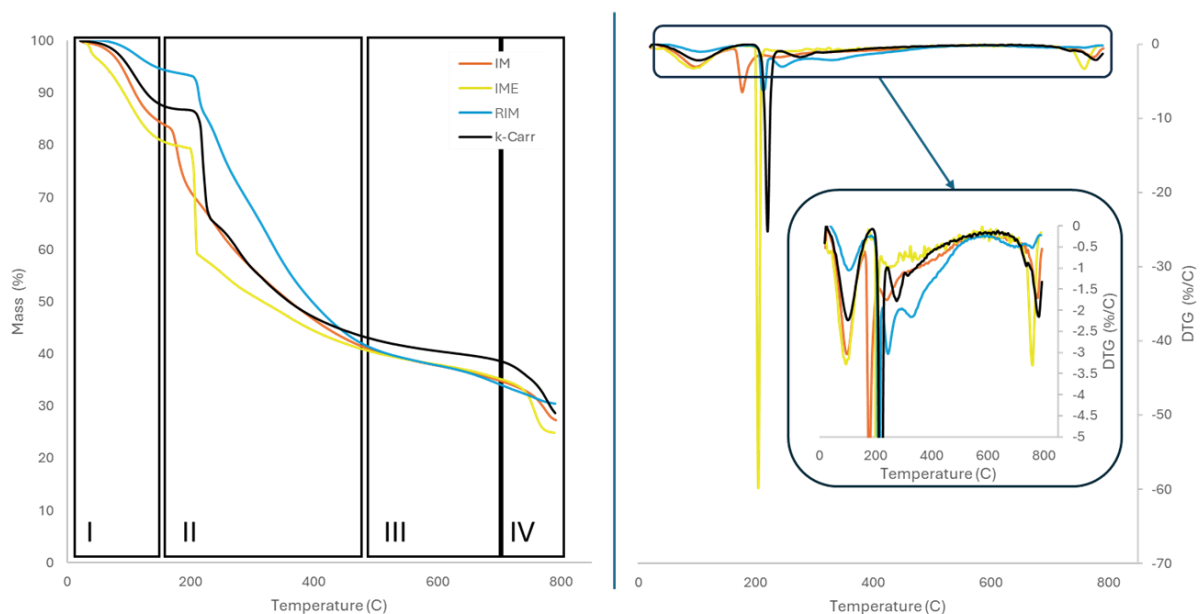


Figure 35: Thermogravimetric analysis of Irish Moss biomass (IM), the aqueous extract (IME) and residues (RIM), and a kappa-carrageenan standard and the respective DTG thermograms.

Thermogravimetric analysis is a method of analysing the loss in mass of a sample as it is heated to a certain temperature. It is an informative method of investigating the pyrolysis of biomass, as the decomposition of metabolites, i.e. proteins, polysaccharides, lipids, occur at relatively consistent temperature ranges.

The thermal decomposition of these macroalgal samples undergo 4 main stages: Stage I, an initial dehydration of the material between 80 and 150 °C. Stage II, a rapid degradation of macromolecular polysaccharides between 180 and 230 °C. Stage III, a slow decomposition to produce a stable carbonised residue between 230 and 750 °C. And finally stage IV, the decomposition of inorganic sulfate salts above 750 °C²⁰⁷⁻²¹⁰.

Both IM and IME had relatively high moisture contents, approximately 15-20%, while RIM was much drier with only 5% moisture content. This could be attributed to the higher polysaccharide content of IM and IME, which undergo dehydration in the early stages of pyrolysis. Carrageenans are also known for their high water retention capacity, so this loss could also be attributed to drying²¹¹.

In Stage II all samples exhibit a similar rapid loss in mass at approximately 210 °C, followed by a smaller loss around 250 °C. This can be attributed to the pyrolysis of carrageenan (figure 29). IME and RIM exhibited their major loss in mass at a similar temperature to pure *kappa*-carrageenan (~210 °C), however this transition was present at a lower temperature (195 °C) in the algal biomass (IM). The decreased purity of the carrageenan in the biomass sample has likely aided the decomposition. The loss in mass at this temperature is an indication of the carrageenan content of the sample. For example RIM expected to contain minimal carrageenan exhibited a smaller loss in mass (6.6 %) at this point compared to IM (13.2 %) and IME (19.8 %) in which carrageenan is expected. The presence of this loss in mass in RIM, may be pertained to the incomplete extraction of carrageenan through hot water extraction. In future studies the application of microwave-assisted extraction should be considered to aid in complete carrageenan extraction (see chapter 5 for preliminary results).

In literature, this mass loss in stage II is dependent on the metal ions present in the carrageenan.. During this stage, C-O-S linkages of the sulfated polysaccharide are broken between 180 and 200 °C resulting in a deposition of metal sulfates¹²⁴. These metal salts have a catalytic effect on the pyrolysis, which varies depending on the metal ion. For example, potassium/calcium carrageenan sees a significant loss in mass between 190-200

°C, whereas in barium carrageenan this decomposition initiates at a cooler temperature (165-200 °C) ^{208,209}. This effect is also visible in other algal polysaccharides, for example Ross *et al* recognised that sodium cations, opposed to calcium cations, catalyse the pyrolysis of alginates, resulting in a reduced pyrolysis temperature and cyclopentenone flue gases as opposed to typical furfural products ²¹². This catalysed pyrolysis explains why the major loss of mass for carrageenan appears at a significantly lower temperature than other polysaccharides such as cellulose (300-350 °C) and hemicellulose (200-350 °C) ²¹³. In stage II, IM and RIM also exhibit another loss in mass between 300 and 500 °C. The rate of this loss in mass (DTG) is much slower than the initial 210 °C decomposition, and is likely due to lipid and protein decomposition assumed to be present in these materials ^{154,214}.

The TGA of all three materials (IM, IME and RIM) also indicated the decomposition of inorganic salts at approximately 760 °C (Stage IV). The decomposition of inorganic sulfate salts, deposited during stage II, likely occurs *via* a carbothermic reduction reaction, resulting in the formation of metal sulfides and CO₂ ²⁰⁷. Due to most of the salts being retained in the aqueous extract, this loss in mass is reduced in RIM. The resulting chars at 800 °C accounted for between 20-30% of the biomass.

3.1.5.1. TG-GCMS

TG-GCMS was performed to further explore decomposition products. GC-MS analysis of sampled flue gases from two temperature ranges was carried out to determine their contents and provide an indication of the pyrolysis mechanism. The two temperatures in which the flue gas was collected were 220-240 °C to look at the volatile compounds lost during the major loss in mass, and 320-350 °C to observe the compounds evolved during the end phase of the major loss in mass/slow decomposition .

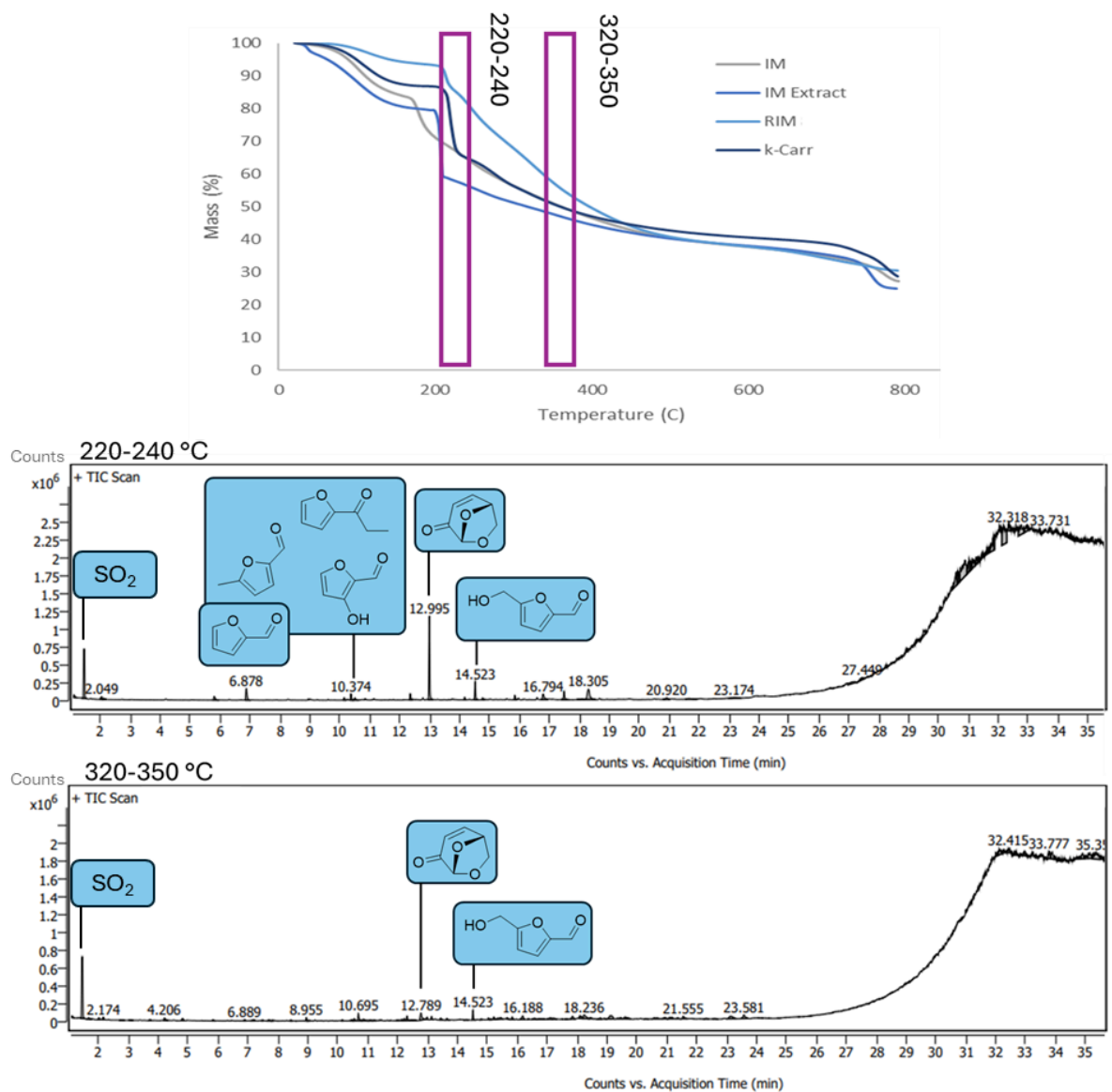


Figure 36: GC-MS spectra of flue gases produced at 220-240 °C and 320-350 °C from the pyrolysis of Irish Moss biomass under inert atmosphere (N_2). Inset are assigned peaks to known polysaccharide decomposition products. The TG plots of IM, IME, and RIM have been included to show the regions by TG-GCMS.

TG-GCMS indicated that the rapid loss in mass observed at ~ 220 °C in the TG spectra was due to the release of levoglucosenone (LGO) and furan-based gases, including furfural, 5-methyl furfural, 2,5-difuraldehyde, and HMF as expected from the pyrolysis of this polysaccharide^{207–210}. Levoglucosenone and furfural are common pyrolysis products of algae and other biomasses²¹⁵. Few studies in literature have described the pyrolysis mechanism

for the decomposition of carrageenan. One of which involves an initial sulfate deposition, followed by lysis of polysaccharides to monosaccharides, ring opening, dehydration, and finally aromatic ring formation. Others suggest a retention of the sulfate group and eventual formation of sulfo-pyruvic acid (figure 31) although this was only seen at temperatures above 800 °C^{209,210}. In a study by Zhang *et al*, flue gas collection at 250 °C observed furan-based compounds, such as furfural, 2-furoyl methyl ester, 5-methyl furfural, and 2-methoxyfuran²⁰⁹. In another study, acid catalysed pyrolysis of iota, lambda, and kappa carrageenan was observed using TG-GCMS analysis. In this study key products included levoglucosenone and furfural, alongside other furan-based compounds and crown ethers. Although LGO was observed without acid catalysis, the yields were significantly higher with the acid catalyst²¹⁶.

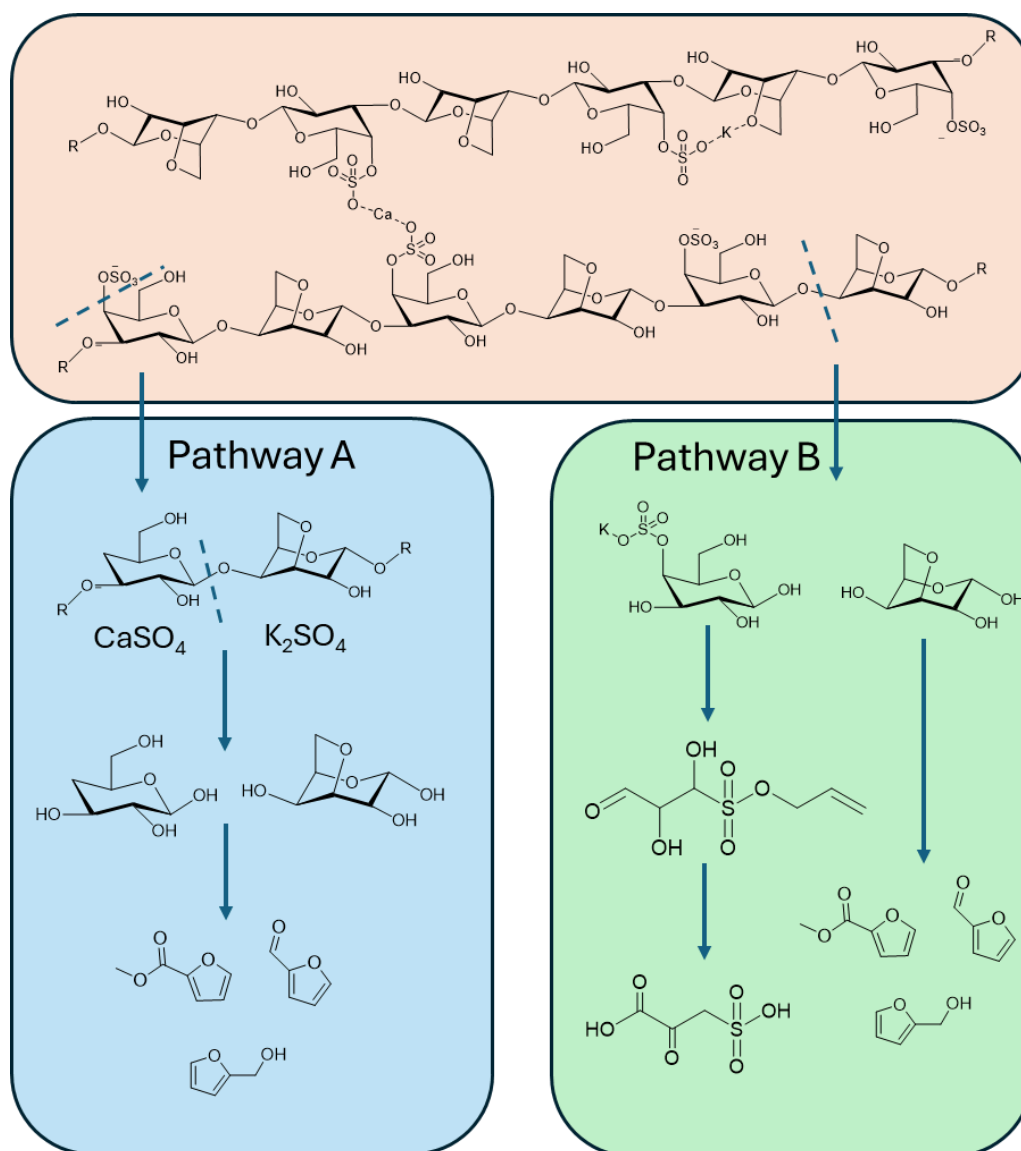


Figure 37: Mechanisms for the pyrolysis of potassium/calcium carrageenan fibres adapted from the proposed Zhang et al mechanism ²⁰⁹.

In this thesis, levoglucosenone was the most abundant pyrolysis flue gas product at this temperature range (220-240 °C) in all three biomasses (IM, IME, RIM). Interestingly, LGO is an important precursor to the green dipolar aprotic solvent, Cyrene™ (dihydrolevoglucosenone) ²¹⁷. The formation of levoglucosenone is typically from the pyrolysis of sawdust. The production of LGO from Irish Moss or carrageenan is an interesting opportunity. The mechanism of LGO formation from cellobiose has been explored in many different studies. A potential mechanism for the formation of LGO from carrageenan is shown in figure 32 ^{2,216,218}.

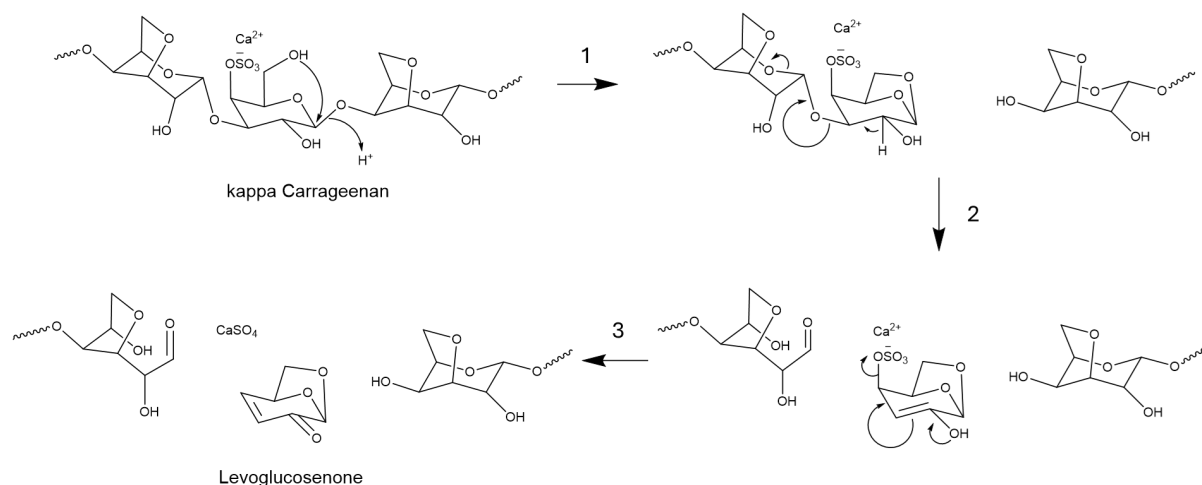
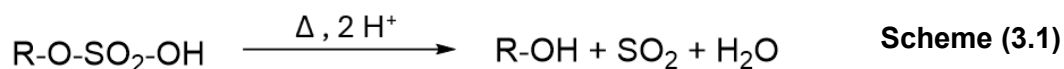


Figure 38: A suggested mechanism for the formation of levoglucosenone from carrageenan.

Depolymerisation by transglycosylation (1) or ring-opening (2)^{2,218}, and deposition of sulphate salts (3)²⁰⁹.

Evidence of sulfur dioxide elimination can be seen at 1.4 min in the GC spectra, this low weight compound with a molecular ion at 64 m/z was observed in all samples and was suspected to be SO₂. This is also supported by literature data showing the evolution of sulfur dioxide from sulfated polysaccharides via a heat elimination reaction (scheme 3.1)²¹⁹. For more confidence in this assignment, however, TG-FTIR would be beneficial as sulfur dioxide would be clearly identified by two adsorption bands at 1450-1300 and 1150 cm⁻¹²²⁰.



At ~350 °C, the yield of furfural and levoglucosenone products decrease and the complexity of the flue gases increase with more unknown smaller peaks being introduced in the GC spectra. This is true for even IM and RIM, which exhibit an additional DTG peak around this temperature, suggesting this loss in mass may be attributed to the evolution of molecular weight compounds not detected in GCMS, for example carbon dioxide. Once again TG-FTIR would be beneficial for the identification of small molecules such as carbon dioxide and water.

3.1.6. Attenuated total reflection infrared spectroscopy (ATR-IR)

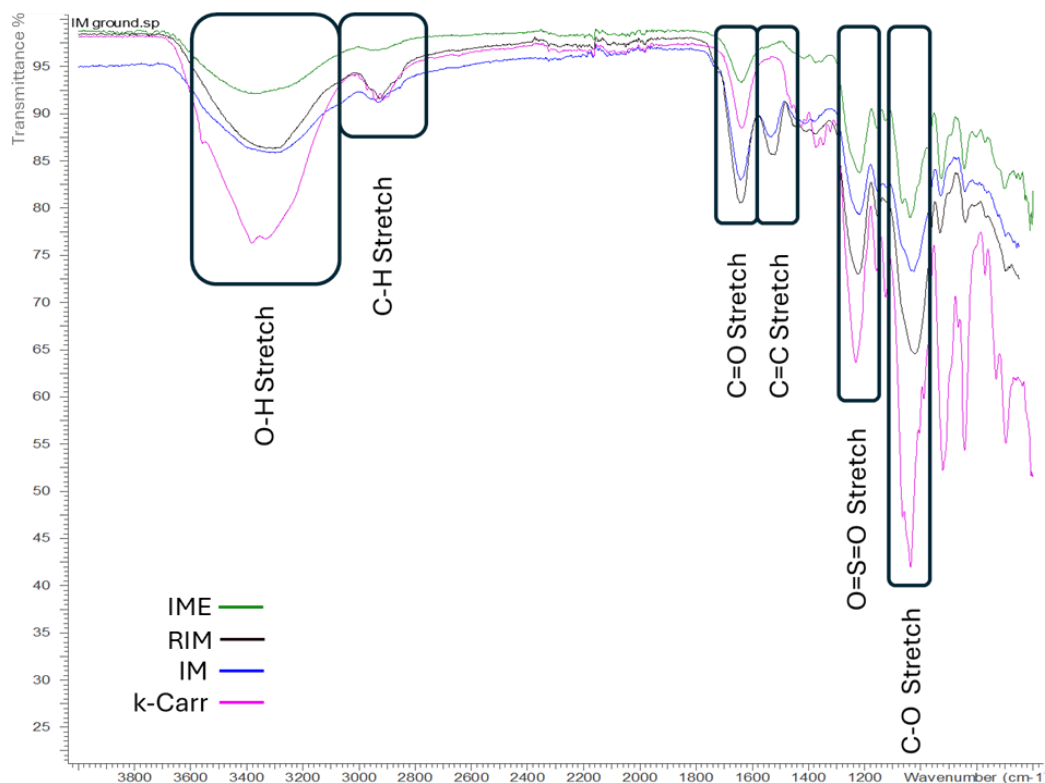


Figure 39: ATR-IR spectra of Irish Moss, Irish Moss extract (IME), residual biomass (RIM), and kappa-carrageenan.

ATR-IR spectroscopy of the macroalgal samples exhibit spectra that are similar to that of κ -carrageenan. Common absorbance bands present in all 4 samples include: O-H stretching at 3303 cm⁻¹, C-H stretching at 2918 cm⁻¹, C=O stretching at 1639 cm⁻¹, C-O stretching at 1030 cm⁻¹, and asymmetric O=S=O stretching around 1230 cm⁻¹. In literature, the band around 1640 cm⁻¹ in κ -carrageenan is due to polymerically bound water, which may also be the case for IME, assuming high carrageenan purity. Furthermore additional bands within the fingerprint region have been attributed to the vibration of functional groups present in κ -carrageenan in literature. Alongside the strong sulfate O=S=O stretching absorbance band, C-O-S stretching at 846 cm⁻¹ is present in these samples²²¹, and a band at 930 cm⁻¹ is attributable to the C-O-C vibration of anhydrogalactose²²². In the Irish Moss biomass (IM) and residue (RIM), an additional band around 1530 cm⁻¹ is observed which may be the

amide I stretching vibration associated with proteins ²²³. Elemental analysis of IM and RIM showed 2.2 and 4.2 % nitrogen content, respectively (section 3.1.3).

3.3.7. Variable temperature ^1H NMR (VT H NMR) of IME

Good resolution in NMR analysis is heavily dependent on the relaxation of nuclei spin states after radio frequency (RF) irradiation. Spatial or temporal fluctuations in the magnetic field caused by molecular motion are key sources of NMR relaxation. Without molecular motion NMR spectral lines exhibit broad chemical shifts. Carrageenan solutions form rigid gels with high viscosity and limited molecular motion or tumbling, which causes line broadening of the proton chemical shifts ²²⁴. Heating the gels enables enough molecular motion to sharpen the chemical shifts and resolve several proton environments, and hence VT NMR has been utilised to analyse carrageenan in these extracts. Tojo *et al* utilise this NMR method to quantify carrageenan blends as the anomeric proton appears at significantly different chemical shifts depending on carrageenan type. Note: the anomeric proton is the proton of the (hemi)acetal functional group in ring-closed sugars. This stereocenter leads to the formation of two anomers α or β .

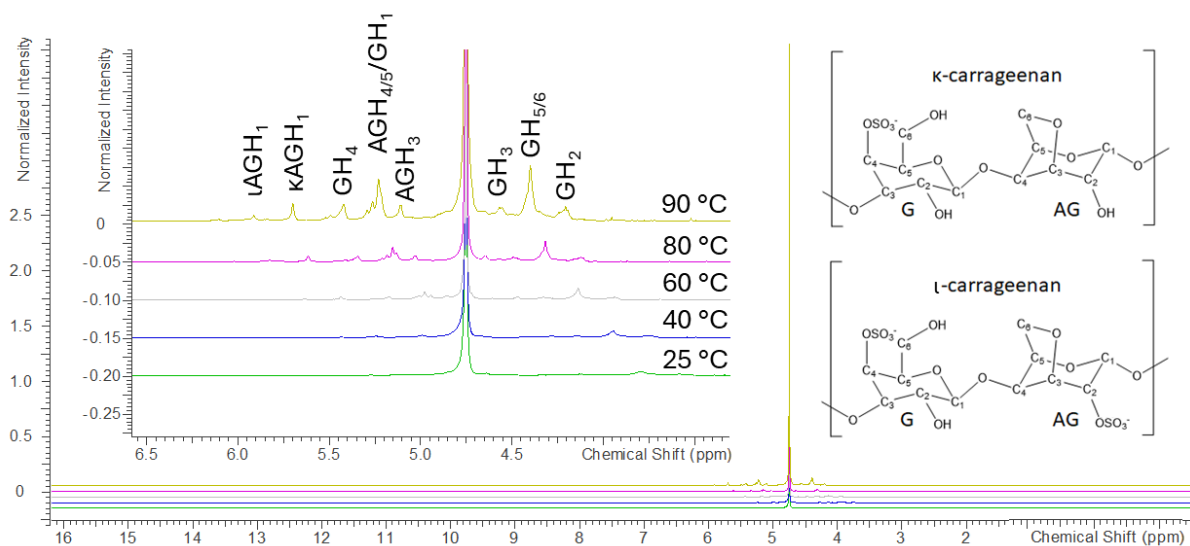


Figure 40: Overlaid VT (20 to 90 °C) 500 MHz ^1H NMR spectroscopy of conventionally extracted IME in D_2O . Assigned as κ -carrageenan (structure inset), specifically noting anomeric anhydrogalactose protons between 5.75 and 6.00 ppm of both iota and kappa carrageenan.

In IME, the chemical shifts of protons at 25-40 °C are broad and unresolved as expected. Above 60 °C, the spectra clearly improve as the molecules are allowed to tumble. At 80-90 °C, the resolution is at its highest. Although the resolution is significantly improved, the signals produced from carrageenan have low intensity. This is due to the limited quantity of sample that could be dissolved before the viscosity of the solution afforded a gel that was impossible to transfer into an NMR tube, even at 80 °C.

The increases in NMR operating temperature have also caused a downfield shift in the signals. The same was recognised in Tojo *et al*'s study. Assuming a consistent shift to all signals, they can be assigned to the pyranose monomers in carrageenan. There are two different pyranose environments in κ -carrageenan: the sulfated β -galactose monomer and the α -anhydrogalactose monomer. As displayed in figure 34, galactose protons on carbons: C₅, and C₆ are visible at all temperatures studied. At 80 °C, signals between 5.0 and 6.0 ppm become resolved and can be assigned to various galactose and anhydrogalactose environments.

Key signals in this spectrum are those between 5.5 and 6.0 ppm. These are the anomeric protons of α -anhydrogalactose (C₁). In the study by Tojo *et al*, the anomeric proton appears at 5.73, 5.97, and 6.09 ppm at 80 °C, for κ -carrageenan, ι -carrageenan, and λ -carrageenan, respectively²²⁵. In the extracts from Irish Moss at 80 °C, two anomeric proton signals were observed, a major signal at 5.63 ppm and a minor signal at 5.82 ppm. This suggests that κ -carrageenan is the major component extracted with a small quantity of additional ι -carrageenan. Carrageenans of Irish Moss in literature are often κ - ι hybrids⁹⁵, typically 64-81 % kappa carrageenan²²⁶. Integration of the two anomeric proton peaks indicates an approximate ratio of 2.2:1 kappa:iota (or 69 % kappa carrageenan). A detailed assignment is included in chapter 5.

3.3.8. Gel formation of IME

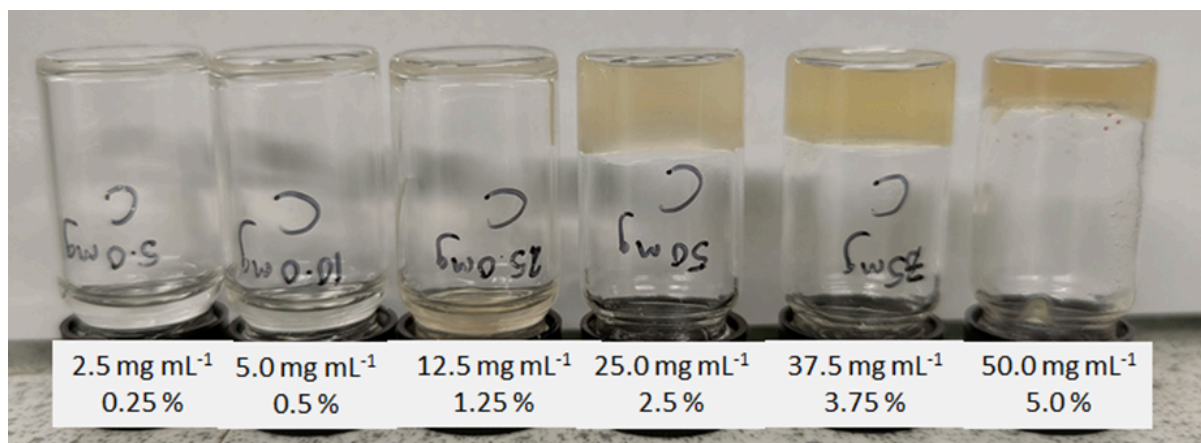


Figure 41: Varying concentrations of IME in water, depicting the gelling properties of carrageenan as the gels resist gravity.

As mentioned in section 1.4.1.1.1 kappa and iota carrageenans are well known for their gelling properties. They have also been recognised to show varying gelling properties based on the cations present ²²⁷. In a study by Robal *et al*, kappa, iota, and lambda carrageenan, and furcellaran (a specific hybrid form of carrageenan extracted from *Furcellaria lumbricalis*), exhibited increased rheology or gelling properties with select cation combinations. For example, κ-carrageenan (1.5% gel) containing K⁺ and Ca²⁺ underwent a 20-fold increase in gel shear strength, compared to that of monocationic K⁺ forms ²²².

In this thesis, hybrid κ/ι-carrageenans containing a mixture of K⁺, Na⁺, Mg²⁺, and Ca²⁺ (section 3.1.4) have qualitatively exhibited hard gels at a concentration of 25 mg mL⁻¹ or 2.5 % and weak gels; one that would flow slowly and upon inversion slide with gravity, from 12.5 mg mL⁻¹ or 1.25%. The strength of carrageenan gels is also strongly influenced by the presence of short polysaccharides ²²⁸. Their presence has not been confirmed experimentally due to the viscosity of carrageenan gels causing difficulties in the HPLC analysis of sugar or oligosaccharide content.

3.2. Production and characterisation of Irish Moss chars

(Objective II)

IM, IME and RIM were carbonised at 250, 400 and 800 °C and the resulting washed ‘chars’ (Figure 36) were analysed using a variety of techniques in order to determine the elemental composition, chemical structure, porosity, and surface topography of these materials.

3.2.1. Char appearance and composition

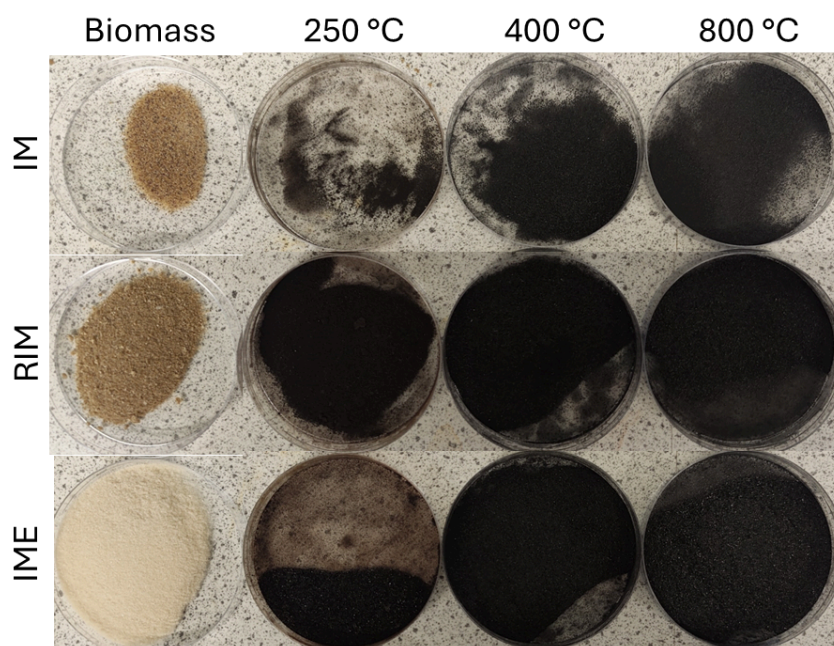


Figure 42: Appearance of IM, IME, and RIM biomass materials and resulting chars following pyrolysis at 250, 400, and 800 °C.

IM, IME and RIM materials produced black powders of varying intensity following pyrolysis. After a 250 °C pyrolysis, the chars exhibit the brown hue of brown carbon, a material produced from the incomplete carbonisation of organic matter ²²⁹. At higher pyrolysis temperatures the chars exhibit more intense darker blacks, indicating the presence

of graphitic black carbon. In terms of the powder's texture, IMCs and RIMCs were granular, however, IMECs appeared almost glittery due to reflective, flat, plate-like particles.

3.2.1.1. Thermogravimetric analysis (TGA)

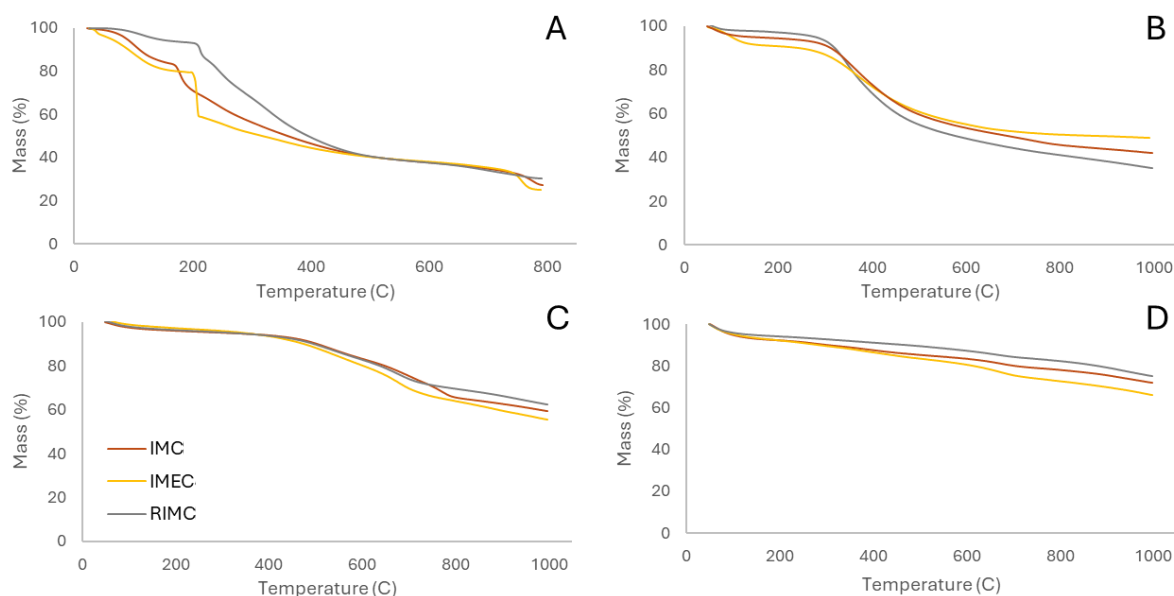


Figure 43: TGA thermograms of Irish Moss biomass: IM, IME, and RIM (plot A), and their carbons: C250s (B), C400s (C), and C800s (D).

In contrast to the biomass materials (Figure 37 A) and as expected the chars (Figure 37 B-D) exhibit a greater stability at higher pyrolysis temperatures. The differences in the TG plots between the three starting materials becomes less significant with pyrolysis temperature. After 250 °C the materials behave in a similar way under temperature. These C250 chars showed very little loss in mass up to 300 °C. The C400 chars were stable up to 475 °C, and the C800 chars maintained a fairly slow decomposition up to 1000 °C. This suggests an increased level of carbonisation from C250s to C400s to C800s.

C400 and C800 materials of IM and IME exhibited a loss in mass due to inorganic salt decomposition between 700 and 800 °C, which is due to a carbothermic reduction of sulfate salts as described in section 3.1.5. This loss of mass was significantly reduced in RIM. The C250 carbons also showed minimal loss in mass at this point, which may be due

to the removal of salts during the washing of the chars post pyrolysis. C400 chars appear to have retained trapped salts as composites within the chars so that they could not be solubilised, whereas the salts were 'free' after pyrolysis at 250 °C. A minor loss in mass was witnessed in the C800 chars at this temperature compared to C400s as a large portion of the salts have already undergone decomposition during pyrolysis.

3.2.1.2. Elemental analysis (CHNS)

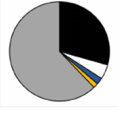

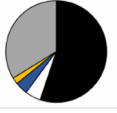


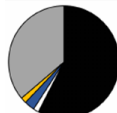







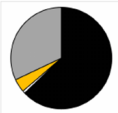
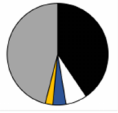



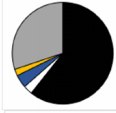
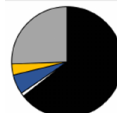


Material	Pyrolysis Temperature						
	0 °C	250 °C	250 °C Washed	400 °C	400 °C Washed	800 °C	800 °C Washed
IM	 HHV: 9.91 MJ kg ⁻¹		 HHV: 21.9 MJ kg ⁻¹		 HHV: 20.8 MJ kg ⁻¹		 HHV: 21.7 MJ kg ⁻¹
IME	 HHV: 8.02 MJ kg ⁻¹		 HHV: 20.0 MJ kg ⁻¹		 HHV: 19.3 MJ kg ⁻¹		 HHV: 20.4 MJ kg ⁻¹
RIM	 HHV: 17.9 MJ kg ⁻¹		 HHV: 21.3 MJ kg ⁻¹		 HHV: 22.0 MJ kg ⁻¹		 HHV: 20.2 MJ kg ⁻¹
							

Figure 44: CHNS content charts for IM, IME, and RIM at various pyrolysis temperatures before and after washing with hot water and acetone, and HHV values determined by the Channiwala formula²³⁰ (Numerical data available in appendix 3.2).

In concert with the TGA data (Figure 37), the elemental analysis of the chars suggests an increase in carbonisation following increasing pyrolysis temperatures. The carbon content of the biomass material starts at 25-40% but as the material thermally decomposes the content increases to 53-55%, then to 57-60%, and finally to 61-63% for C250, C400, and C800 chars, respectively. Interestingly, IMEC800s (char produced from IME at 800 °C) carbon content is substantially lower than literature values for other carbonised polysaccharides which after an 800 °C pyrolysis exhibit a 75-90% carbon content²³¹. As expected the hydrogen content of the chars decreases with carbonisation temperature as do the sulfur and nitrogen content after an initial increase from biomass to C250 char. However, even at 800 °C the chars show heteroatom presence. IMC chars contain sulfur and nitrogen at almost equivalent quantities, maximising at around 3.0% in washed IMC400. Whereas, IMEC contains sulfur sans nitrogen, maximising at 7.5% in washed IMEC250. RIMC, like IMCs, also contain sulfur and nitrogen, with the nitrogen content maximising at 5.8% in washed RIMC250. In literature this quantity of heteroatomic doping is not exceptionally high, however, it can still have major effects on their electrochemical, sorption, or catalytic properties^{110,113–115}.

The theoretical higher heating values (HHV) were determined using Channiwala's formula²³⁰ (equation 3.2).

$$HHV (MJ/kg) = 0.3491C + 1.1783H + 0.1005S - 0.1034O - 0.0151N - 0.0211A \quad \text{Equation (3.1)}$$

Where C, H, S, O, N, and A indicate the carbon, hydrogen, sulfur, oxygen, nitrogen and ash content, respectively. In these works, oxygen content was assumed to be equivalent to the Rest% fraction minus the ash content, which was estimated by ICP-MS of the chars (see appendix 3.3). These chars have comparable HHV to common solid fuels, such as low rank coal²³⁰, however the significant sulfur content of these chars would make them poor for fuel applications. Macroalgae also typically make for poor biofuel applications as their high ash content (specifically alkali) causes slagging, fouling and corrosion in the combustion process

²³².

3.2.1.3. CPMAS solid-state nuclear magnetic resonance (SSNMR) spectroscopy

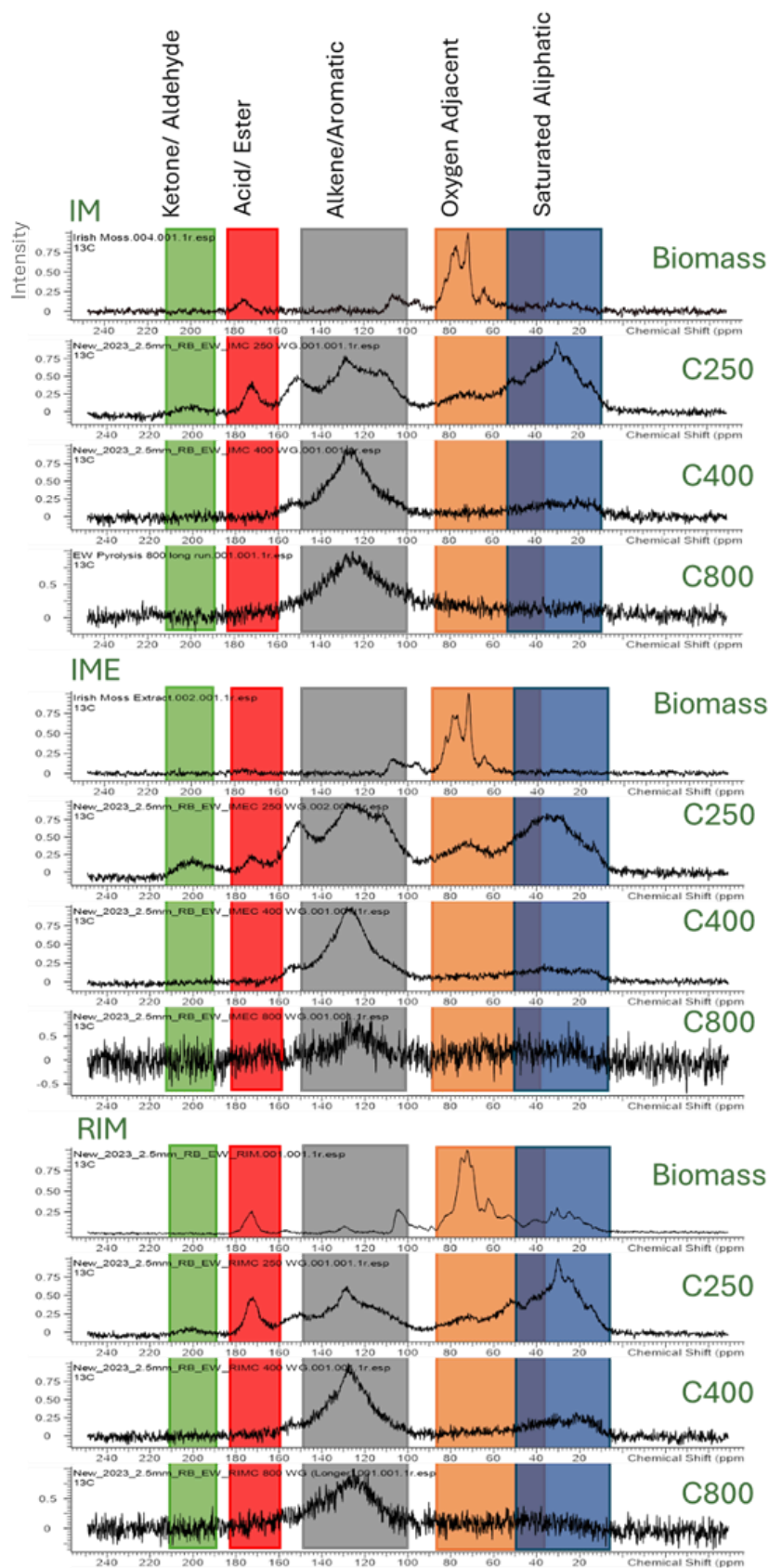


Figure 45: ^{13}C SSNMR spectra of Irish Moss biochars (IM, IME, RIM)

Cross polarisation magic angle spinning (CPMAS) solid-state NMR analysis is useful to overcome the chemical shift anisotropy and dipolar coupling in solid samples that broaden NMR peaks. SSNMR analysis of Irish Moss biochars (Figure 39) further indicate hierarchical carbonisation of the biomass materials. IM, IME, and RIM starting materials display a range of sharp NMR peaks indicating carbon environments including oxygen adjacent and carbonyl between 50-100 ppm and 150-200 ppm, respectively. RIM materials also indicated aliphatic (10-50 ppm) and alkene (120-140 ppm) carbon environments, attributable to lipid content in the residues.

C250-800 biochars exhibited much broader NMR peaks. In C250 chars, the conversion of pyranose structures towards that of phenolic or furfural derivatives is evident via the loss of oxygen adjacent carbon environments and the formation of aliphatic and alkene/aromatic environments. Further, carbonyl carbon environments implies these chars have retained significant oxygen functionality. Acid/ester carbonyl peaks around 170 ppm had significantly higher intensities in IMC250 and RIMC250. However, these chars (specifically RIM) also exhibited simpler alkene/aromatic environments, with a peak at 130 ppm, compared to IMEC250, which had an intense additional shoulder around 115 ppm.

The C400 chars display further carbonisation as the aliphatic material is converted into primarily alkene/aromatic carbon (130 ppm). In the IM and IME biochars a minor peak at 150 ppm indicates oxygenated aromatic groups, such as the presence of phenolics²³³; this peak is strong in IMC250 and IMEC250 chars also. In these C400 chars there is also a minor implication of remaining aliphatic carbon between 10-40 ppm. C800 biochars also only indicate aromatic and alkene environments with a broad peak at 100-150 ppm, suggesting a highly graphitised material with little to no C¹³ NMR active functionality visible.

3.2.1.4. FT-IR spectroscopy

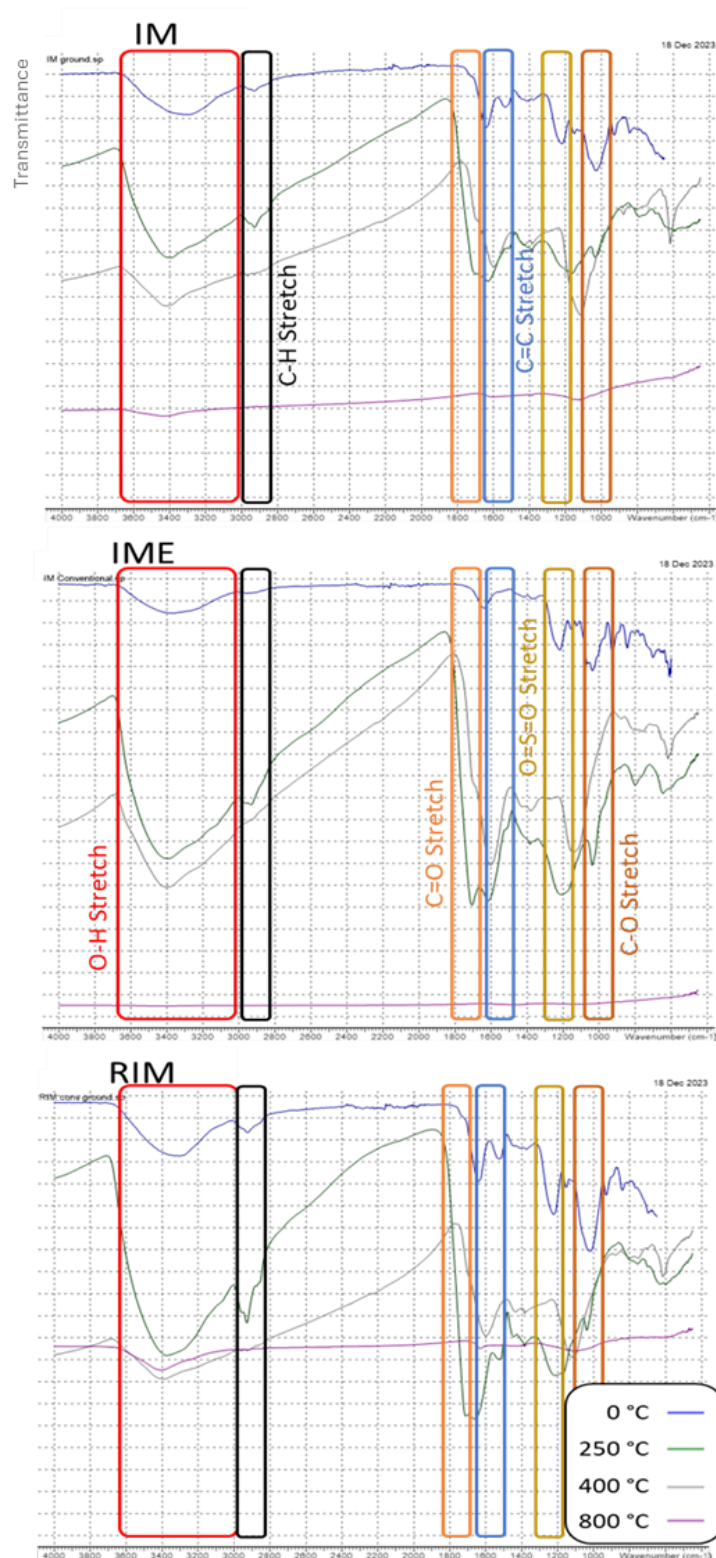


Figure 46: FT-IR spectra of Irish Moss biochars (IMC, IMEC, RIMC) from carbonisation temperatures 250, 400, and 800 °C, alongside ATR-IR spectra of native non-carbonised biomasses, indicated by 0 °C.

Similar to the CPMAS SSNMR results (section 3.2.1.3), the FT-IR analysis also indicated the presence of carbonyls in the C250 biochar materials. Strong stretching vibrations at 1708 cm^{-1} (C=O stretch) and at approximately 1620 cm^{-1} (C=C stretch) may be attributed to phenolic and furfural groups forming from the thermal decomposition of polysaccharides. A loss of carbonyl stretching appears after further heating to $400\text{ }^{\circ}\text{C}$, whilst C=C stretching is retained, which is also in support of the CPMAS SSNMR results and can be attributed to graphitisation of the material. Broad O-H stretching between 3000 and 3600 cm^{-1} is present in the C250 chars, which becomes more tapered towards a point in the C400 chars which could imply less hydrogen bonding or free O-H such as in phenols or carboxylic acid functionalities (note: tapering may also be an artifact of sample presentation in KBr pellets). The sulfate O=S=O stretch of carrageenan present in the starting materials appears to be retained in the C250 chars, but like the carbonyl stretch is diminished following further pyrolysis to $400\text{ }^{\circ}\text{C}$. In its place around 1100 cm^{-1} C-O stretching of phenols/ethers remains. The C800 chars displayed little IR activity similar to literature graphitic materials ²³⁴. However, IMC800 and RIMC800 exhibited weak O-H, C-O, and C=C stretching vibrations potentially indicating some retained phenolic presence.

3.2.1.5. Powder X-ray diffraction (pXRD)

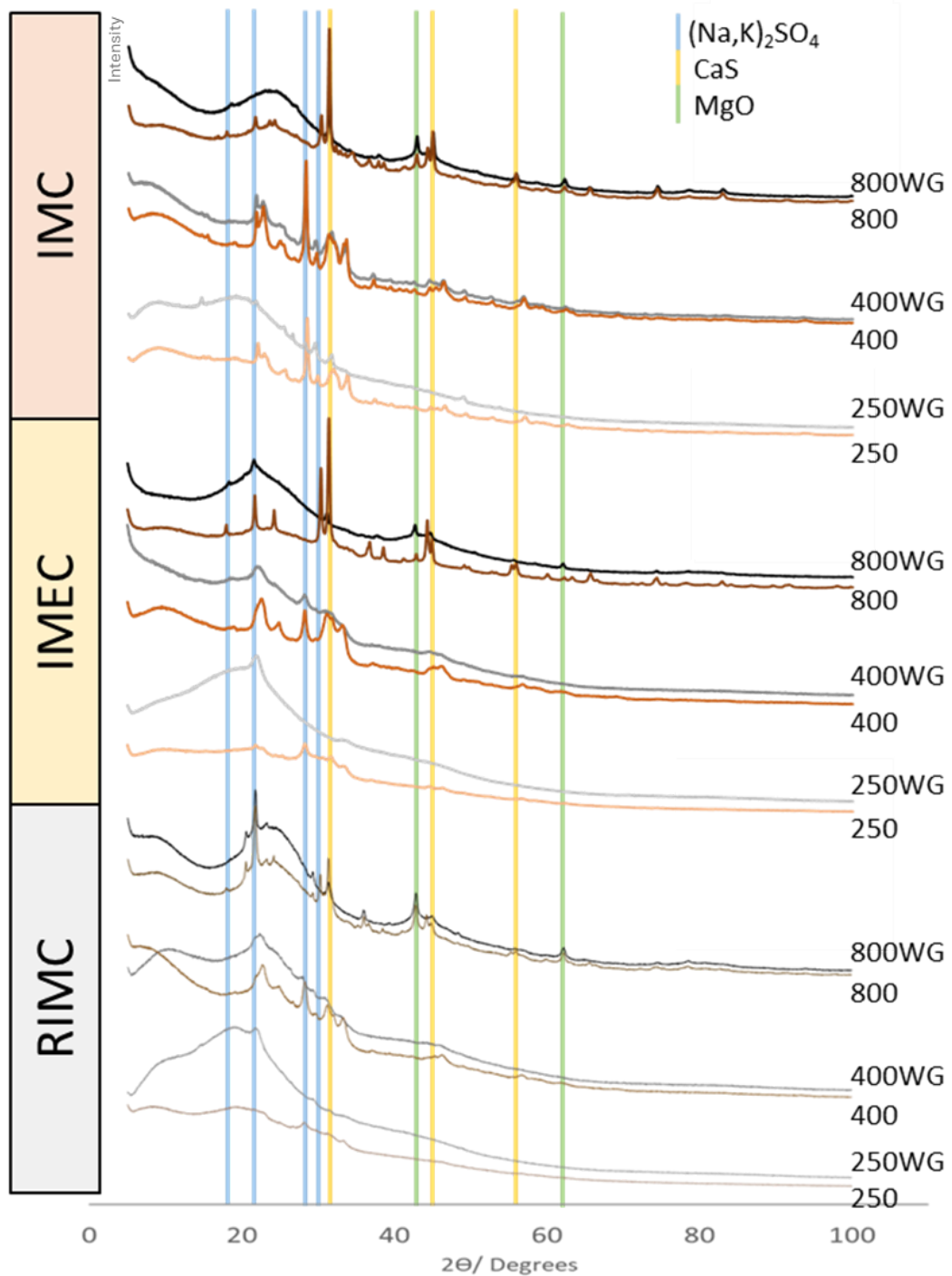
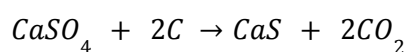


Figure 47: pXRD diffractogram of IM, IME, and RIM materials carbonised at 250 °C , 400 °C, and 800 °C, phase identification of $(\text{Na,K})_2\text{SO}_4$, CaS and MgO salts have also been included.

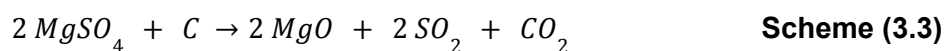
Powder X-ray diffraction (pXRD) utilises X-ray radiation to determine the inorganic composition or crystalline structure of materials. A sample interacts with X-rays due to the similarity in atomic distance and X-ray wavelength; resulting in diffraction. Using Bragg's Law ($\sin\theta=n\lambda/2d$), for a specific distance between crystal lattice planes, a series of angles will result in constructive interference of the X-ray waves and a measurable increase in intensity. Assuming anisotropic crystal arrangement in a powder, patterns of intensities at certain angles of diffraction indicate the presence of certain crystal structures.

pXRD supported and emphasised the presence of salts being formed and deposited during the pyrolysis of Irish Moss materials by the presence of sharp reflexes in their diffractograms; especially in the unwashed chars. In the C250 chars, pXRD indicated the presence of sodium/potassium sulfate salts, by their characteristic (101), (102), and (110) signals at 21.7°, 30.0°, and 31.4°, respectively (Figure 41). This was more prominent in IMC250 than IMEC250 and RIMC250. As the temperature increased, the C400 chars exhibited a greater range of sulfate salts, including those of magnesium and calcium. The reflexes in the low temperature char diffractograms are broad and sharpen in the C400 and C800 chars, a potential explanation for this is the gradual increase in crystal size as a greater quantity of salts are deposited/formed²³⁵. In the IMC800 and IMEC800 chars the presence of sulfate salts are somewhat depleted and in their place calcium sulfide is the dominant salt. This is evident due to the presence of (200), (220), and (222) reflexes at 31.4°, 44.9°, and 55.8°, respectively. As mentioned previously this is due to carbothermic reduction of calcium sulfate²⁰⁷. pXRD also suggests magnesium oxide presence in the C800 materials, especially in RIMC800. This is likely also due to the thermal decomposition of magnesium sulfate salts. The mechanism of the formation of these salts can be explained in literature. Calcium sulfate undergoes decomposition in the presence of carbon at 800 °C to produce calcium sulfide and carbon dioxide²³⁶:



Scheme (3.2)

Magnesium sulfate, however, undergoes a different mechanism in the presence of carbon resulting in the formation of magnesium oxide at temperatures above 600 °C^{237,238}:



Magnesium hydroxide was also identified in these chars following the hydration of MgO after aqueous washing. Hydrated silica was also recognised in some chars, however, it is likely due to contamination as silicon is not commonly abundant in this biomass. One could suggest this is due to sand. As a coastal species, sand is a likely contaminant of this biomass. ICP analysis of IM and IME materials confirm sodium, potassium, magnesium, and calcium presence, at 1-2%, 0.75-1.5%, 0.4-0.6%, and 0.4-1.7% (DW), respectively. Supporting hypotheses from thermal data, washed C250 chars exhibit very little salt presence, whereas the C400 and C800 retain a portion of the sulfate salt content after washing, likely due to trapping of these soluble salts as composites. The retained salt content also explains the difference in the low carbon content of these chars in comparison to chars produced from starch.

The diffractograms may be used to indicate the degrees of carbonisation in these materials. A broad diffraction at 18.0-20.0° in C250 chars disappears/shifts to a higher angle in the C400 chars suggesting a deterioration of order and crystallinity in the material. In C800 chars this broad reflex appears at 20.0-23.0° and a second diffraction around 42.0-45.0° develops, which indicates the presence of amorphous graphitic carbon material²³⁹. In literature graphite these appear at 26.5° and 42.4° and account for the (002) and (100) reflexes²⁴⁰. The location of the (002) broad diffraction also signifies the intermolecular distance between the graphitic sheets^{240,241}, suggesting a broader polyarene interlayer distance in these chars (0.39-0.44 nm) compared to graphite (0.34 nm). This could indicate heteroatom (sulfur) presence within the graphitic sheets or intercalated salts between them. This is discussed further in section 3.2.2.4.

3.2.2. Surface topography and elemental analysis

3.2.2.1. Scanning electron microscopy (SEM) and energy dispersive X-ray spectroscopy (EDS)

Scanning electron microscopy (SEM) is an imaging technique that uses an electron beam to determine the topography of surfaces within a nanometer scale. A scanning beam of electrons fired at a sample causes the emission of different electrons. Important detected electrons in this technique are backscattered (BSE) and secondary electrons (SE). Secondary electrons are caused by inelastic scattering and result in the emission of low energy electrons. These electrons provide topographic information. The variable distance from the detector (i.e. a raised or depressed surface) results in varying intensity of secondary electrons, and hence the topography can be distinguished. Elastic scattering due to electrostatic repulsion between nuclei in a sample causes the emission of backscattered electrons. These electrons distinguish different surface compositions as heavier nuclei cause greater intensities of backscattered electrons. Electron dispersive X-ray spectroscopy (EDS) also provides elemental composition, but can distinguish specific elements. The principle of EDS uses the characteristic X-ray emission as a result of electrons from high energy states falling into vacant lower energy states formed when secondary electrons are emitted from inner electron orbitals. The measured X-ray spectrum indicates the presence of electronic structures of specific elements and therefore by combining SEM and EDS, elemental maps can be produced. The spatial resolution of elements using this technique is limited to micrometre scale because of the penetration of the electron beam into a sample's surface.

SEM images of the IME biochars (Figures 43, 46, & 50) reveal the shape and surface topography of the char and biomass particles. The effect of pyrolysis on the materials is visually similar. Despite there being variation in the shape and general topography, the different biomass surfaces at the microscopic level are smooth and amorphous. Following a pyrolysis at 250 °C, each biomass deposits salts, which have been recognised to contain

metals: potassium, sodium, magnesium, and calcium using EDS analysis. This is in support of pXRD and ICP-MS results (section 3.2.1.5 & appendix 3.2.) Two main types of deposit appear: round clusters, and spindles, the crystal types of these solids remain difficult to determine via SEM imaging. As the pyrolysis temperature increases the size of the deposits also increases, ranging from tens of nanometres in the 250 °C chars, to hundreds in the 400 °C chars, to a few micrometres in the 800 °C chars. Most of these deposits are water-soluble and are washed off, however, in the 800 °C chars a few salt deposits remain. This visually confirms the suspicions deduced from pXRD analysis.

Post-washing the textures of the surfaces of each char become clear. Increasing degrees of pyrolysis afford increasing degrees of surface decomposition. At 250 °C the surface looks dried and cracked, heating further (400 °C) introduces micropores on the surface, and finally at 800 °C the surface is visibly crumbling as more pores are introduced. An example of the change in surface porosity is shown below (figure 42). The following sections discuss IMCs, IMECs, and RIMCs separately.

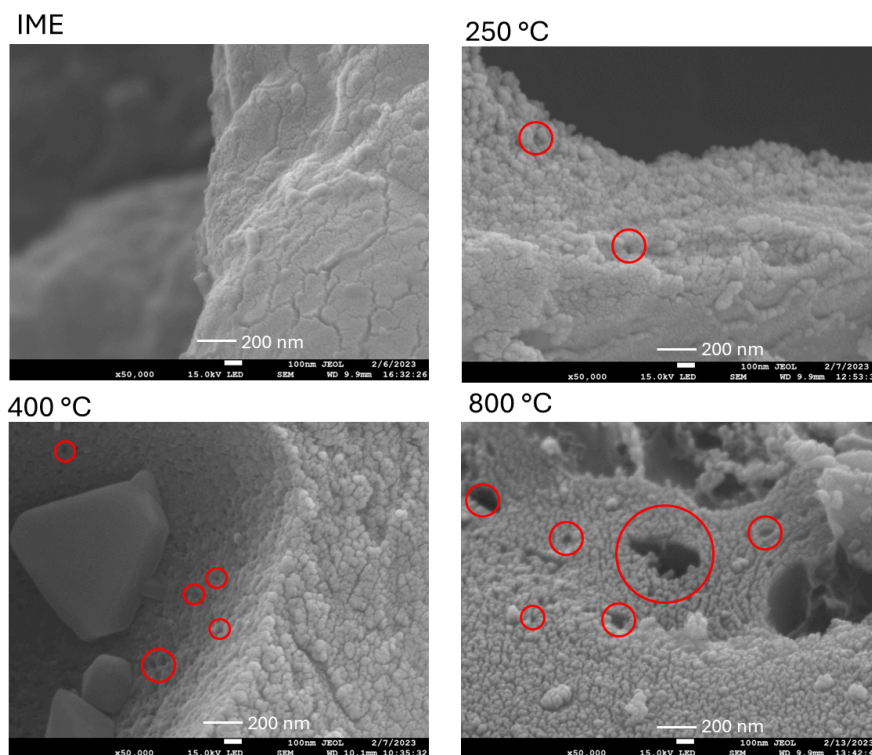


Figure 48: SEM images of IME and IMEC (250-800) at a magnification of x50,000. Indicating the change in surface porosity with temperature (red circles).

3.2.2.1.1. Irish Moss chars (IMC)

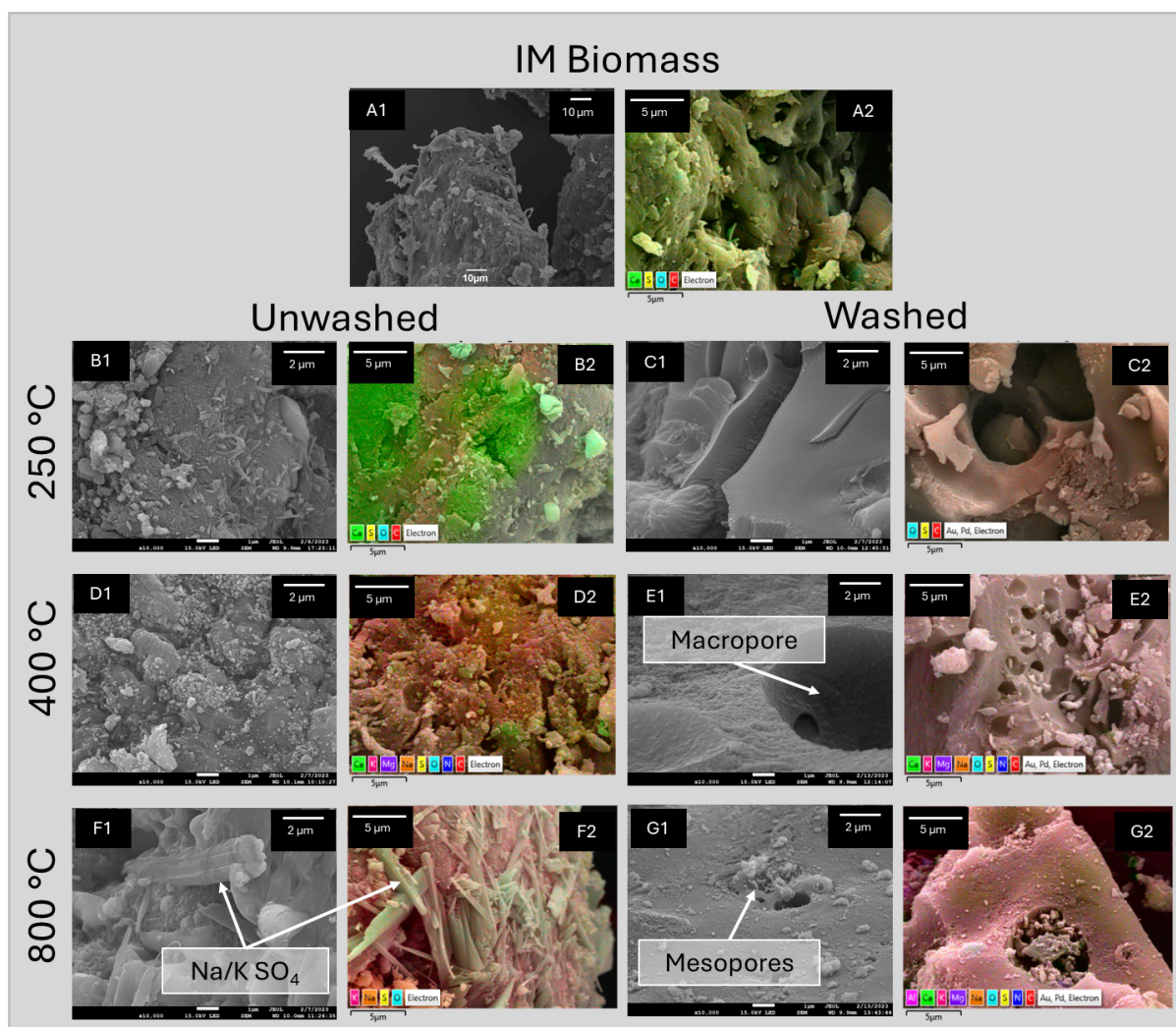


Figure 49: SEM/SEM-EDS images of IM and IMCs (250, 400, 800 °C) at magnifications of x10k (SEM) and x5k (SEM-EDS).

The macrostructure of IM is composed of fragments of blades and stipes. Figure 43 A1 shows a cross-sectional view of one of these fragments and reveals the dried hull of algal cells. The material is mostly smooth with granules of amorphous material clustered on the surface. After pyrolysis, the granules are coated with salt crystals. In figure 44 EDS elemental mapping clearly shows areas rich in sodium, sulfur, and oxygen. Combined with pXRD analysis it can be said with high certainty that these salts are predominantly sodium sulfates. Other metals, such as calcium are also found amongst sulfur rich areas. The metal

content accounts for ~6%, ~13%, and ~26% (%Wt) of the surface in unwashed IMC250, 400, and 800, respectively. Indicating the increasing deposition of salts with temperature. In the biomass materials inorganic metals, calcium and potassium, appear to be dispersed homogeneously across the surface, however, after pyrolysis these metals appear clustered in these salt composites. In the washed IMCs the salt content drops significantly (<1.0%Wt) and typically only calcium and magnesium are present (maximum 3.0%Wt in IMC800).

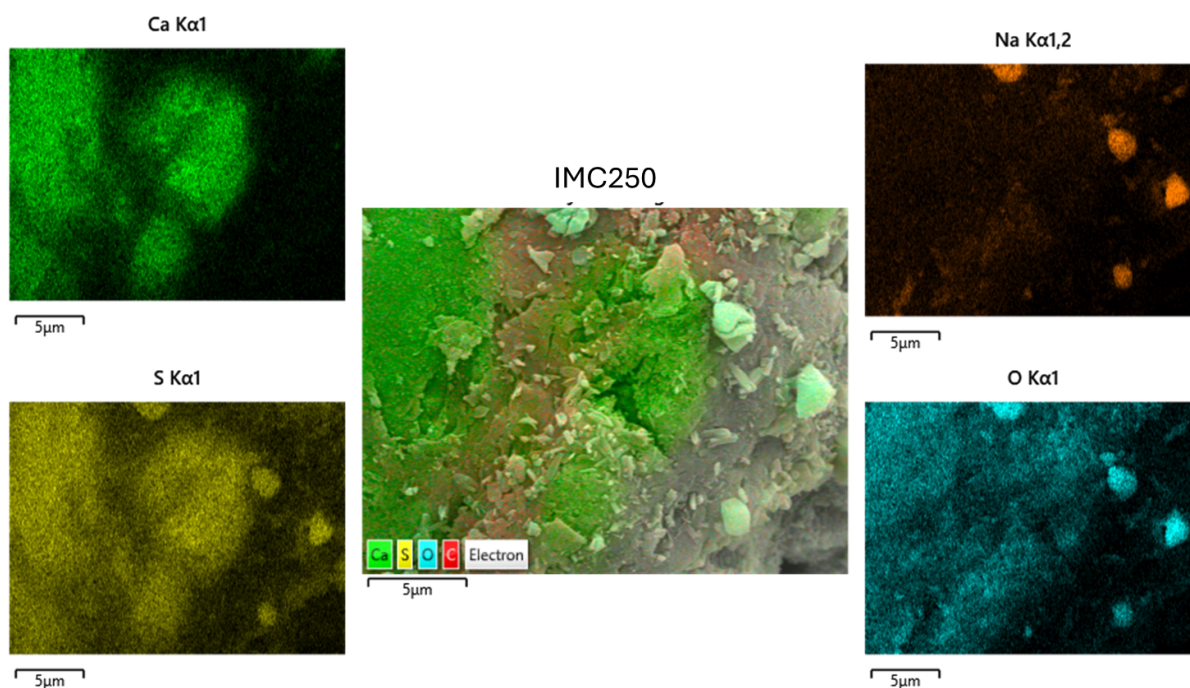


Figure 50: SEM-EDS elemental mapping of an area of unwashed IMC250 at a magnification of x5k. Individual calcium, sodium, sulfur, and oxygen element maps are included for clarification of the metal sulfates present.

The surface elemental composition of the chars is somewhat consistent with CHNS microanalysis, however, it is worth noting SEM-EDS only provides surface (~1 μm) elemental analysis for a selected region rather than the overall average content. The sulfur content at the surface of the washed chars ranged between 4-6 %wt, which is similar to the initial sulfur content of the seaweed biomass. The sulfur content appears to increase generally with pyrolysis temperature, although the content varies within the same sample

across different particles so it is hard to distinguish any real trends. Similarly the oxygen content appears to decrease with temperature, which does align with the trends shown across other analytical techniques (CHNS/SSNMR/FT-IR).

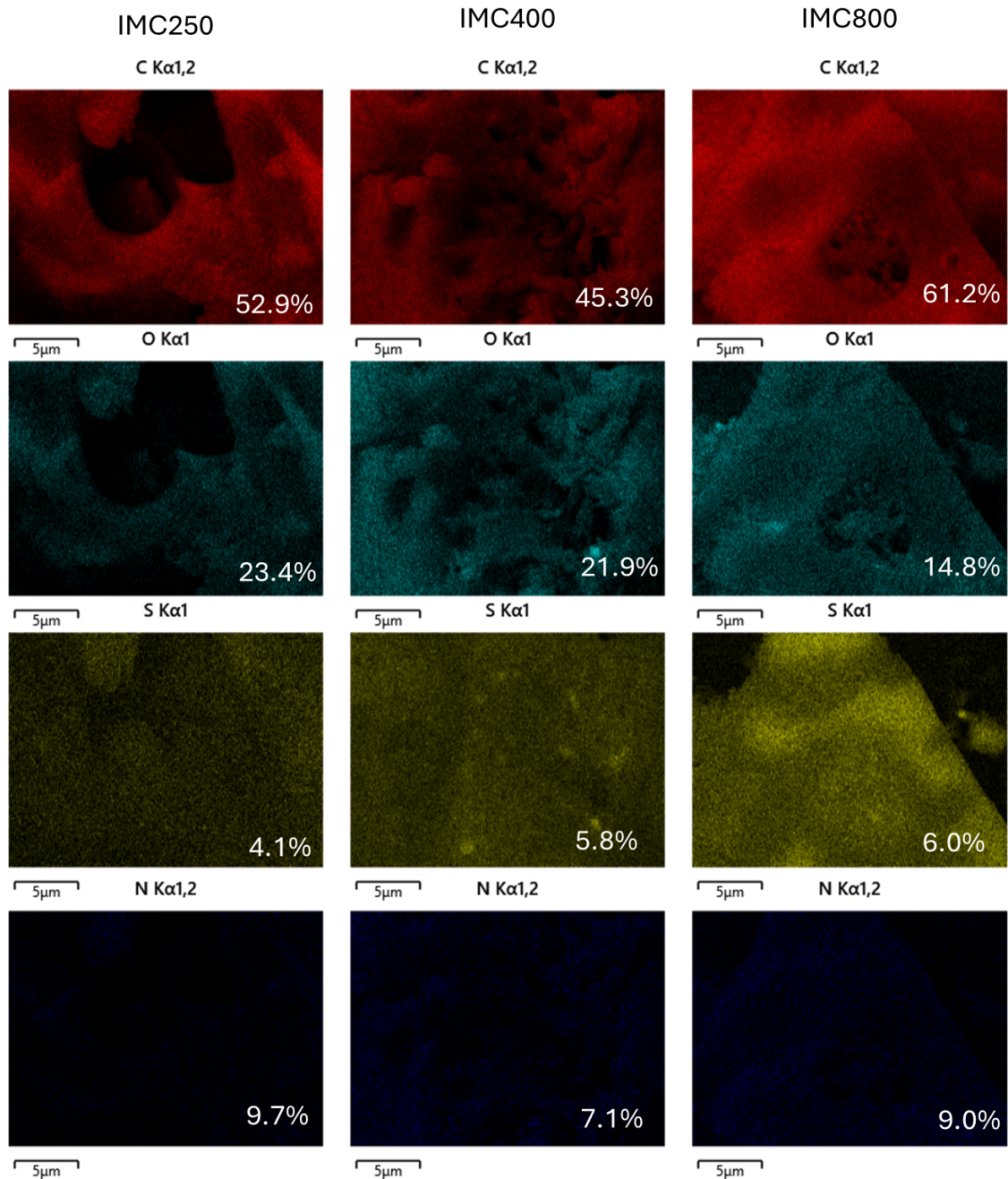


Figure 51: SEM-EDS element maps of carbon, oxygen, sulfur, and nitrogen for IMC250-800.

Inset are the %Wt values for each element.

Besides the general porosity changes caused by pyrolysis temperature discussed earlier, the porosity of the IMC surfaces seems to be mostly composed of circular macropores a few micrometres wide. These macropores seem to be a product of the formation and then removal of salt composites. Many of the macropore structures also appear as deep tunnels running into the material. Other macroporosity includes cracks between conglomerates of particles. Smaller oval mesopores are also present on the surface. These appear to be produced during the decomposition of the material's surface and are around 15-20 nm in diameter. The porosity is further discussed in section 3.2.2.2 (N₂ adsorption porosimetry).

3.2.2.1.2. Irish Moss extract chars (IMEC)

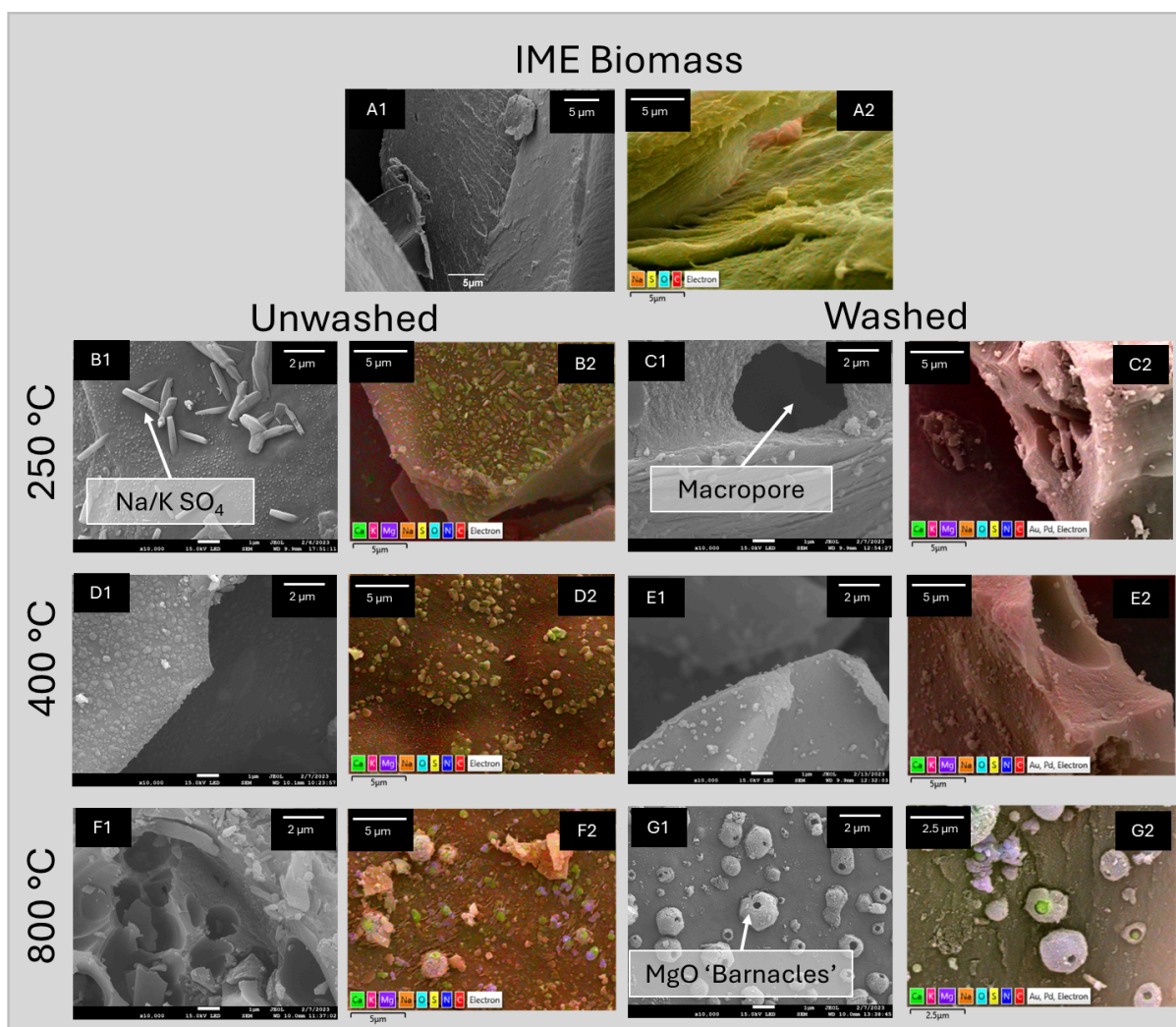


Figure 52: SEM/SEM-EDS images of IME and IMECs (250, 400, 800 °C) at magnifications of x10k (SEM) and x5k (SEM-EDS).

IME also has a smooth surface but with sheared sharp cross-sectional edges that exhibit a flaky, layered texture. The particles appear as plates that vary in size from 10 µm to a few 100 µm and when the plates are broken the internal structure appears macroporous.

As stated previously this material also deposits a large quantity of salts during pyrolysis. In contrast to the seaweed, IM, its extract, IME, affords chars with a far lower salt coverage as metals (Na, K, Ca, and Mg) account for no more than ~15 %wt at each temperature interval. Also the substantial deposition occurs at a lower temperature than in

IM. In the 250 °C chars potassium and sodium account for ~11 % of the surface by EDS, which only gradually rises by a few percent between 400 °C (~13 %) and 800 °C (~14 %). This is explained by the deposition of metal salts in carrageenan at temperatures exceeding 180-200 °C ¹²⁴ as discussed in section 3.1.5.

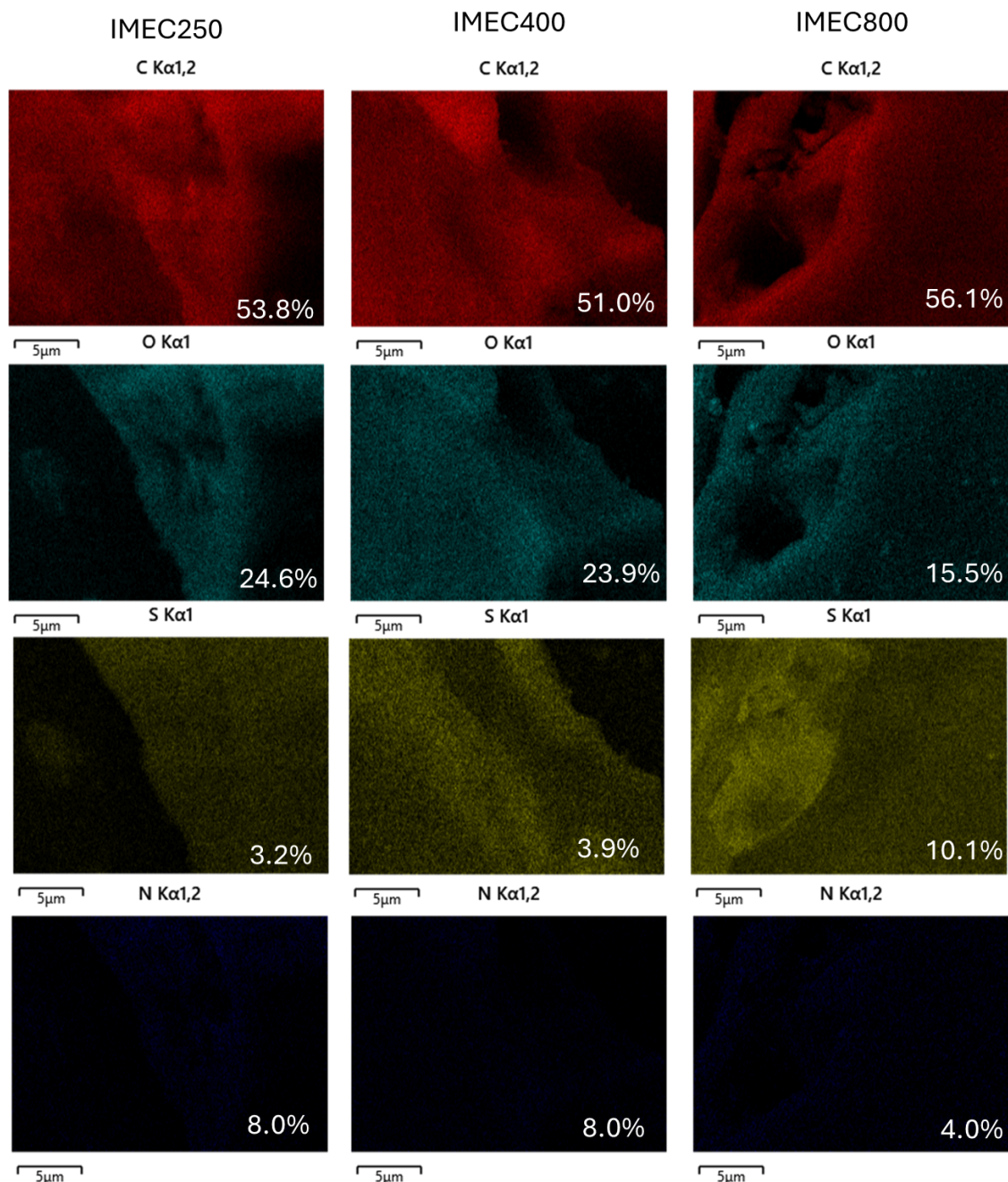


Figure 53: SEM-EDS element maps of carbon, oxygen, sulfur, and nitrogen for IMEC250-800. Inset are the %wt values for each element.

Washing chars IMEC250 and IMEC400 afford materials of little to no salt content, which in turn substantially decreases the sulfur content from ~10 % in extract to 3-4 %wt at the surface suggesting that sulfur in these chars is primarily inorganic sulfates. This decrease is very visible between images A2, and C2 and E2 in figure 46 by the reduction in yellow hue. In washed IMEC800, however, the sulfur content is retained around 10 %. Unexpectedly, a nitrogen content is measurable on the surface of these chars, unlike elemental analysis by CHN (section 3.2.1.2).

Interestingly, above 800 °C and due to the decomposition of salts at this temperature, the surface topography of IMEC800 differs from that of the other chars in this family. In both the washed and unwashed chars, although far more prevalent in the washed chars, spherical deposits appear across the surface. These deposits are composed of magnesium, calcium, oxygen, and sulfur. After washing, barnacle-like structures are preserved and under closer inspection via SEM-EDS, these barnacles are composed of a calcium sulfide core and magnesium oxide shell, which is supported by the pXRD results. Curiously, each barnacle, although varying in size (~0.5-3 µm) also fashions a single hole of almost uniform size (~200 nm) to its neighbouring barnacles.

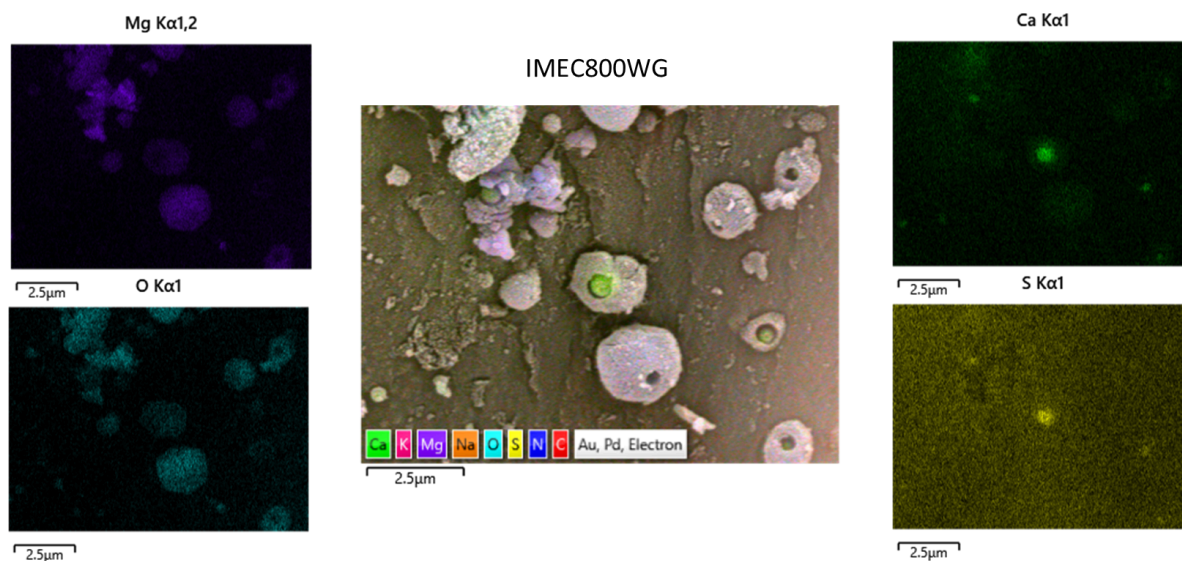


Figure 54: SEM-EDS image of washed IMEC800 at x10k magnification. Elemental maps of magnesium, calcium, oxygen, and sulfur have been included to show the elemental composition of magnesium oxide 'barnacles'.

The presence of these salts is explained in section 3.2.1.5, however, the formation of these structures is not entirely understood. M. Scheidema studied the reductive formation of magnesium oxide from magnesium sulfate in the presence of various metal sulfate impurities²³⁸. Magnesium sulfate and iron sulfate in a carbon monoxide reducing environment formed similar structures to this thesis, but with an iron sulfide core instead. M. Scheidema suggested that the iron sulfate aids in the reduction of magnesium sulfate and hence this structure appears. Under the conditions of this study, one could suggest the calcium sulfate acts similarly to that of iron sulfate. However, when M. Scheidema performed the same experiment with calcium sulfate impurities this was not seen, instead a conglomerate of calcium, magnesium, oxygen, and sulfur was formed, which may be due to the reductive difference between carbon and carbon monoxide, or the complexity of carrageenan and the conditions of M. Scheidema's study²³⁸.

Regarding the porosity of the carrageenan chars, it would seem the external plates underwent little decomposition and rather the walls of porous internal structure began to degrade and thin. At 800 °C the internal structures become very fragile and allow the outer

plates to be free as the internal structure crumbles (Figure 49). The residual structure at this temperature is almost sponge-like. A macroporous structure containing small circular mesopores around 5-15 nm.

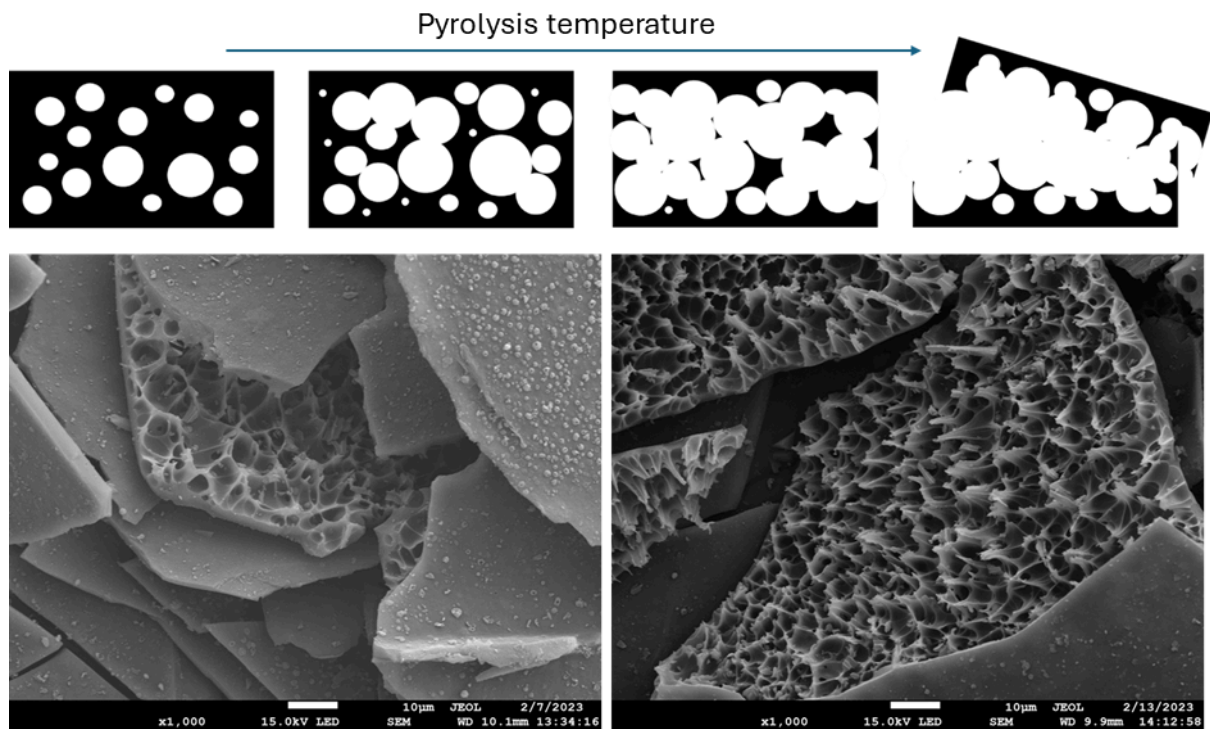


Figure 55: A simple diagram showing the formation of IME porous structures, and SEM images of IMEC800WG at x1000 magnification exhibiting the porous internal structure and smooth flat external structure.

3.2.2.1.3. Residual Irish Moss chars (RIMC)

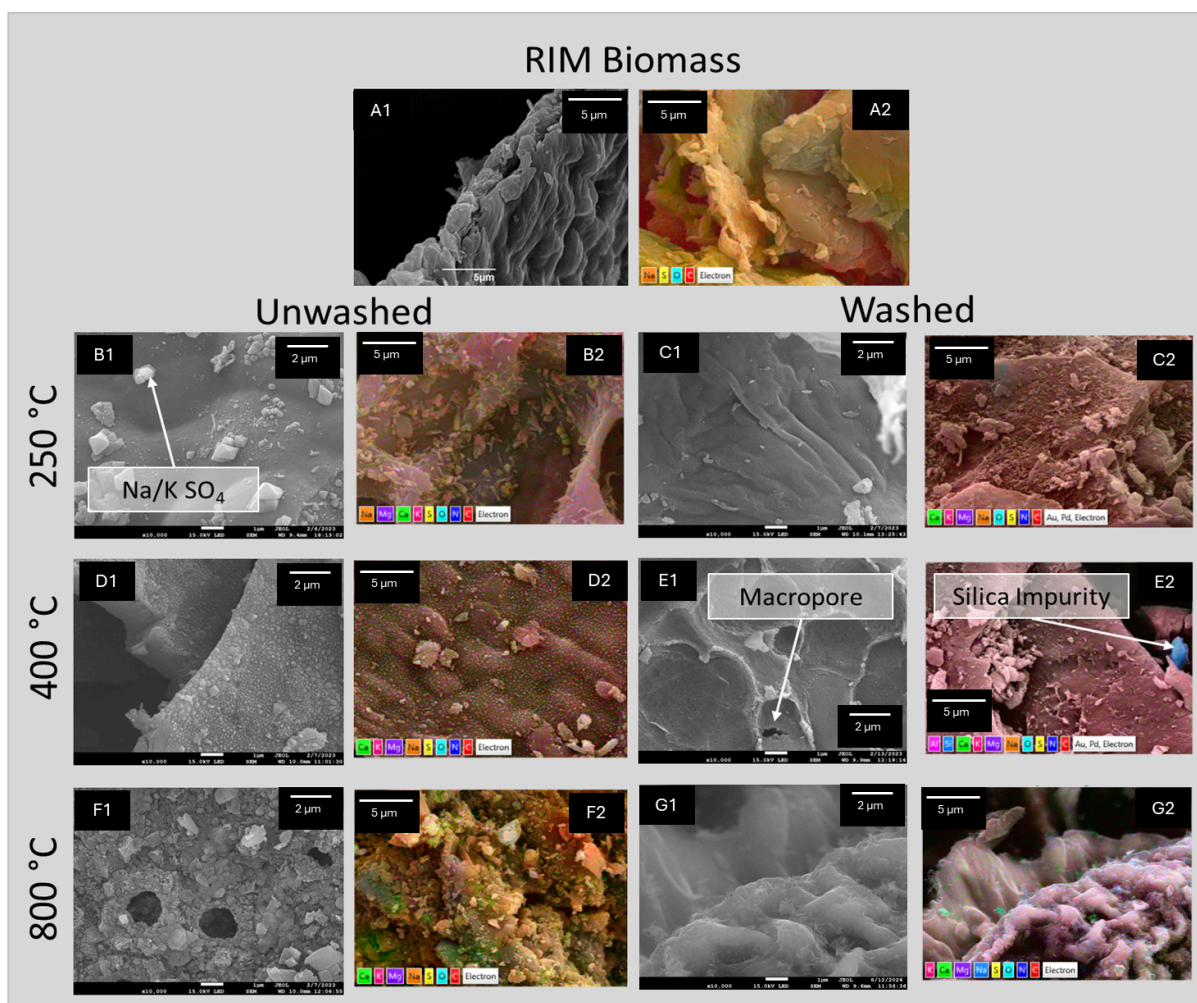


Figure 56: SEM/SEM-EDS images of RIM and RIMCs (250, 400, 800 °C) at magnifications of x10k (SEM) and x5k (SEM-EDS).

RIM particles appear as smooth amorphous granules. The defined structure of what was once IM has been lost during the hot extraction process. After pyrolysis and similar to IM biomass, the RIM particles become coated in salt deposits and their surface becomes dried, cracked and porous. The deposited salts are predominantly potassium and sodium at ~8 %wt in C250 and C400, and ~20 %wt in C800, although calcium and magnesium are also present at ~2 % in C250 and C400, and ~4 % in C800.

These chars contained substantially more nitrogen (maximum 14 % in RIMC250) than the IM or IME materials. Elemental analysis by CHNS gave quantitatively different

values to SEM-EDS, however, it also recognised significant nitrogen content in RIM chars. These materials also had a quantity of silica impurities present throughout the material (which can be seen in E2 of figure 50), however, these are likely fragments of sand particles present on the seaweed's surface as discussed earlier in section 3.2.1.5. The position of heteroatomic elements oxygen, sulfur and nitrogen are dispersed relatively evenly across the surface with the exception of a few concentrated regions of sulfur and oxygen which are likely due to metal sulfate salts in RIMC400 (figure 51). Most of the porosity of this material appears to have formed from folds or cracks in the surface, or from the clustering of RIMC particles. Due to the nature of these pores most are macropores a few microns in size. Areas of these RIMC particles had spherical/oblong mounds extruding from the surface which had increased nitrogen content and reduced sulphur content.

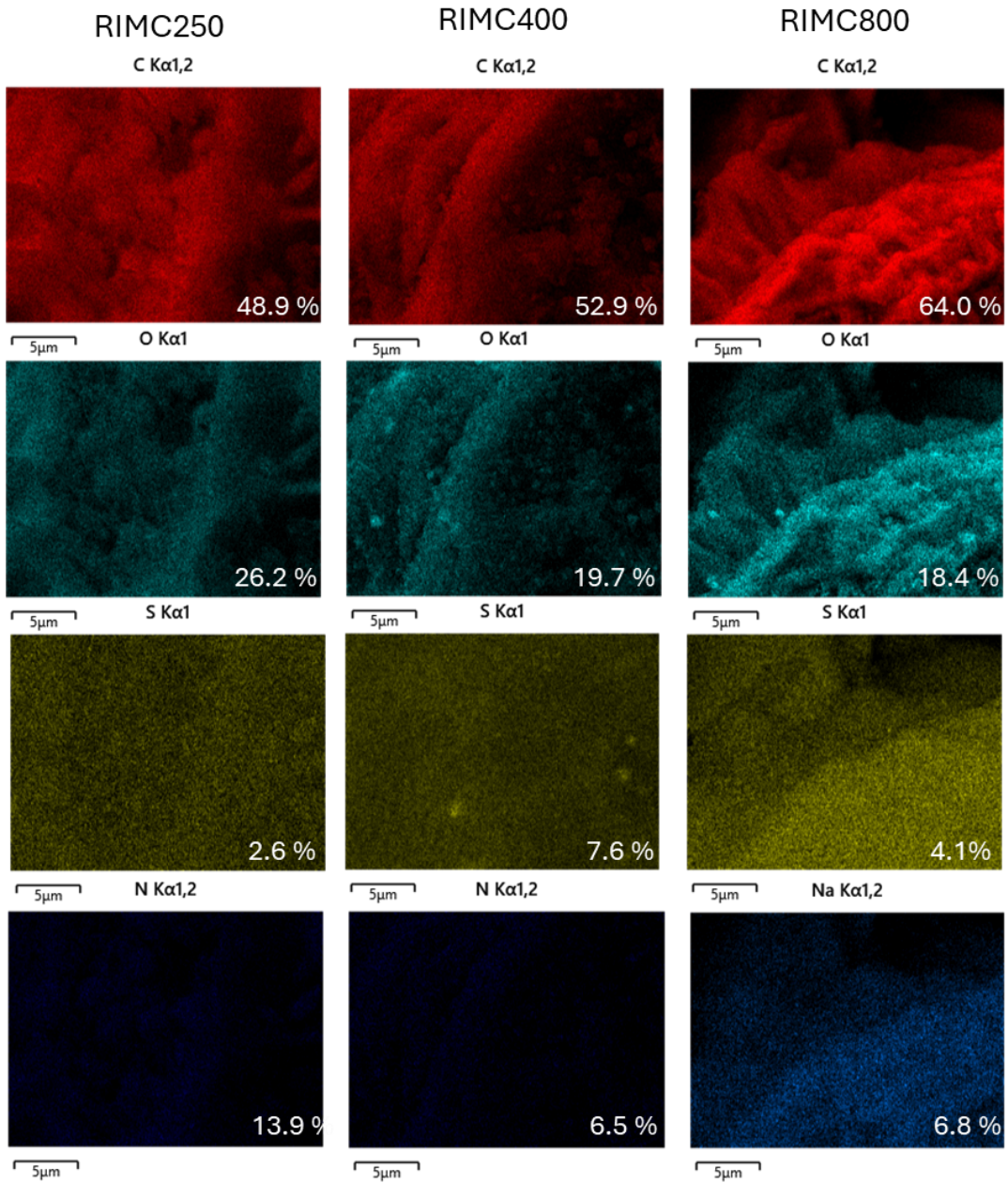


Figure 57: SEM-EDS element maps of carbon, oxygen, sulfur, and nitrogen for RIMC250-800. Inset are the %Wt values for each element.

3.2.2.2. Porosity

Porosimetry is often measured using gas adsorption, particularly that of nitrogen. This porosimetry method measures the physisorption of nitrogen gas onto an adsorbent at approximately $-196\text{ }^{\circ}\text{C}$ or 77 K and implements a model isotherm to calculate the materials surface area, pore volume and pore diameter. Common models include: linear (Henry's), Langmuir, Freundlich, and Brunauer-Emmett-Teller (BET) isotherm models ^{189,242}. In a system at a particular temperature, the number of sites on the surface occupied by adsorbate molecules will depend on the pressure (in the case of a gas) or concentration of the adsorbate. At low pressures or concentrations all isotherms obey Henry's law and are linear. At higher pressures the Langmuir isotherm has been successfully applied to a number of different systems, however it is restricted to monolayer coverage ²⁴³. BET is the common model implemented for nitrogen adsorption due to its effectiveness for physisorption and multilayer coverage ²⁴⁴.

Adsorption isotherms exhibited by surfaces can be attributed to one of six types classified by Brunauer, Denning, Denning and Teller (BDDT) (see figure 52). Type I closely resembles a Langmuir isotherm plateauing at monolayer coverage; it may also be characteristic of 'micropore filling'. Type II is characteristic of non-porous or macroporous solids exhibiting multilayer adsorption. Type III indicates weak interactions between adsorbent and adsorbate and therefore adsorption occurs due to high relative pressure. Type IV is characteristic of mesoporous solids. The hysteresis upon desorption indicates pore condensation within narrow pores. Type V is rare and type VI indicates a multilayering system where each step corresponds to first, second and third layers ^{105,245}.

The hysteresis in type IV or V isotherms may also define the type of mesopore shape present. Figure 52 also includes observed hysteresis shapes for common pore structures. H1 indicates uniform cylindrical mesopores, whereas the delayed desorption in H2 implies ink-bottle-like mesopores with a narrow opening. H3 and H4 are characteristic of slit-like

pores. The narrower opening in H4 mesopores also presents a more perturbed desorption but of low volume ¹⁰⁵.

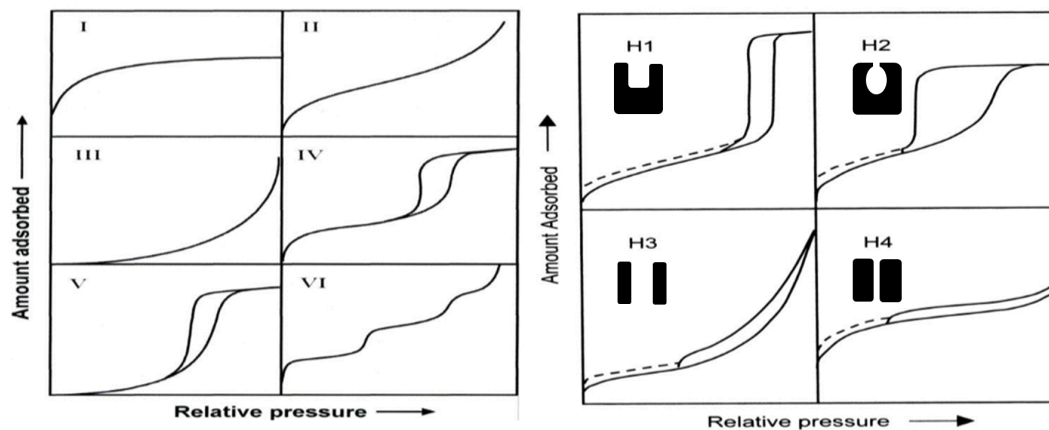


Figure 58: The IUPAC classification of adsorption isotherm types (I-VI) (left) and the hysteresis shapes for different pore types (H1-4) (right) ¹⁰⁵.

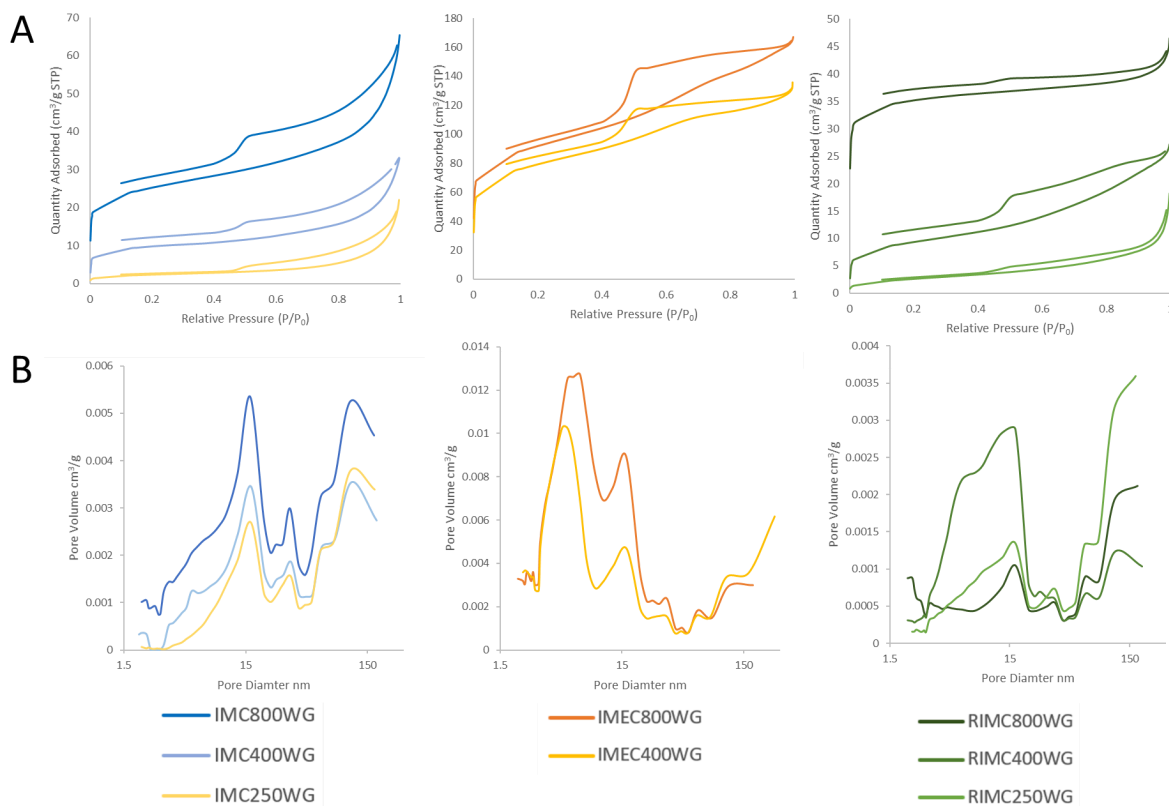


Figure 59: N_2 adsorption porosimetry isotherms (A) and pore size distributions (B) for carbonised IM, IME, and RIM at temperatures of 250, 400, and 800 °C.

N₂ adsorption porosimetry data supports the microscopy data in most cases. IM, IME and RIM exhibit mesoporous hysteresis curves in the isotherms of their chars, and the pore distribution curves of these materials indicate a volume of pores around 15 nm in IMC400 and IMC800, and groups of pores around 5 and 15 nm in IMEC400 and IMEC800. These chars exhibit limited microporosity.

The volume of mesopores appear to also increase with carbonisation temperature in both IMC and IMEC chars. Similarly they also increase in RIMC chars, with a broad range of mesopores between 4 and 15 nm in RIMC400, however, they appear to have collapsed in the RIMC800WG materials which appears to result in a small increase in microporosity and hence the difference in micropore:mesopore ratio. All three materials carbonised at 400 °C and 800 °C exhibit incomplete hysteresis curves indicating some pore blocking. Some of the C250 chars are likely considered non-porous due to their low surface area and pore volume. It is important to note, however, that these materials have undergone no activation or doping with catalytic acids, and hence their surface area is likely to be lower than those that have. This is evident in comparison to Starbon materials ¹⁰⁴, activated carbons or comparable red seaweed biochars. These IM chars exhibited a fraction of the surface area or pore volume of Norit (a commercially available activated carbon), red seaweed chars, or carrageenan chars (table 5). These samples exhibit very high surface areas and pore volumes but are synthesised using activation (AC-κ) or acid etching (SWBC and SCA-700) ^{128,246}. Despite a lack of activating agent the C800 Irish Moss chars exhibit increased porosity, which could be attributed to the etching of the surface as the sulfate salts undergo carbothermic reduction around 750 °C. Remaining inorganics, however, have likely filled pores reducing surface area and porosity.

Table 6: Surface Characteristics of IMC, IMEC, RIMC washed Chars from temperatures of 250 °C, 400 °C, and 800 °C, and literature values comparable red seaweed chars.

Material	BET Surface Area (m ² g ⁻¹)	BJH Adsorption Pore Volume (cm ³ g ⁻¹)	BJH Average Pore Width (nm)
IMC	800WG	80	8.4
	400WG	31	12
	250WG	8.2	20.2
IMEC	800WG	290	5.3
	400WG	253	4.8
	250WG	N/A	N/A
RIMC	800WG	104	5.6
	400WG	31	7.1
	250WG	9.5	11.1
Norit	612	0.49	7.8
Red Seaweed Biochar (SWBC)	926	0.57	2.45 ²⁴⁷
Iota-carrageenan char (SCA-700)	1669	-	1.0-2.3 ²⁴⁶
kappa-carrageenan char (AC-κ)	2346	1.34	2.3 ¹²⁸

The isotherm types of Irish Moss chars are typical type IV mesoporous, exhibiting two key inflection points in their hysteresis. There are significant differences in the hysteresis between IMC, IMEC, and RIMC biochars. IMCs exhibit only a minor delay in desorption due to pore condensation at high relative pressure (P/P_0), before reaching a plateau around 0.6 P/P_0 and rapid desorption around 0.5 P/P_0 . This H3 hysteresis shape could indicate slit-like pores, however, there were only minor instances of that seen in SEM. The hysteresis in the isotherm of IMEC materials reach their desorption plateau at high relative pressure and maintain the absorbed nitrogen until 0.5 P/P_0 . This behaviour implies H2 mesopore

structures or ink-bottle pores. There also appears to be a small step within the hysteresis region around $0.7 P/P_0$ which could indicate the formation of an additional layer within the mesopore region (type VI). Unlike IME carbons, carrageenan carbons in literature (AC-κ and SCA-700) are predominantly microporous, although this may be a result of activation/acid etching^{128,246}. RIMC materials displayed fluctuating hysteresis shapes. In RIMC400 the hysteresis was similar to that of IMEC chars, whereas in RIMC250 and RIMC800 the isotherm hysteresis indicated slit shaped pores. Folds and channel-like cracks were commonly seen across the surface in SEM analysis which supports this.

To note, IMEC250 N₂ adsorption porosimetry data has not been included due to the variability of the data. On one instrument (Micromeritics Tristar II porosimeter) the material showed an unusual linear adsorption isotherm, whereas when tested on another instrument (Micromeritics ASAP 2020) the material behaved as non-porous (see appendix 3.3 for isotherm plots). At this point it is not clear as to why the material has behaved this way. One could suggest that the low temperature char may have been susceptible to a thermal restructuring during the heated degassing process.

3.2.2.3. X-ray photoelectron spectroscopy (XPS)

XPS analysis of these seaweed-derived chars describes the elemental composition of the materials at the surface (approximately 1 μm) and their electronic state. This analytical technique works on the principle of the photoelectric effect. Photoionization using X-ray radiation results in the emission of electrons with specific kinetic energies. From these electrons the the binding energy of each electron can be calculated using the photoelectric equation:

$$E_k = h\nu - E_b - \phi \quad \text{Equation (3.2)}$$

Where E_k is the kinetic energy, $h\nu$ is the incident photon energy, E_b is the binding energy, and ϕ is the work function of the material. The measured binding energies indicate the specific elements and electronic states of said elements present in the material.

This analysis identified a range of elements at the surface of these chars many of which were to be expected (Table 6). Once again silicon was observed in some samples, which has been attributed to sand impurities as mentioned previously. A clear observation from this analysis is the increase in metals, sodium, calcium, and magnesium on the surface after pyrolysis at 800 $^{\circ}\text{C}$. Magnesium is a very abundant element at the surface in C800 chars, especially RIMC800, and is found in almost equivalent quantities to nitrogen and sulfur. The binding energies of the magnesium 2s electrons at 90 eV and 2p at 51 eV ²⁴⁸, suggest a mixture of magnesium sulfate and oxide, as previously determined in XRD analysis. Appropriate deconvoluted spectral lines in the oxygen 1s (531.5 and 532.7 eV) and sulfur 2p (168.0 eV) are also present and support this ²⁴⁹.

Table 7: Elemental Composition of the surface of washed IMC, IMEC, and RIMC chars from pyrolysis at 250 °C and 800 °C.

Material	XPS Elemental Surface Composition %						
	C 1s	O 1s	N 1s	S 2p	Na 1s	Ca 2s	Mg 2s
IM	62.4	28.7	4.6	1.9	0.8	0.6	0.5
IMC250	73.6	20.5	3.9	1.2	0.1	0.1	0.3
IMC400	73.4	16.5	4.5	1.8	1.2	0.6	1.1
IMC800	78.1	13.8	2.6	2.5	0.2	0.4	2.0
IME	50.1	40.4	1.3	4.2	2.5	0.2	0.6
IMEC250	74.2	22.1	1.8	1.0	0.2	0.1	0.2
IMEC400	68.5	22.3	2.3	1.3	0.4	0.4	4.0
IMEC800	73.5	19.8	1.3	1.3	0.4	0.5	3.1
RIM	65.8	27.8	2.0	2.5	0.7	0.4	0.5
RIMC250	77.8	17.2	3.9	0.7	0.0	0.0	0.1
RIMC400	71.2	17.5	6.3	1.3	0.5	0.8	1.9
RIMC800	66.8	22.1	4.9	0.8	0.6	0.7	3.7

The elemental composition is somewhat similar to CHNS elemental analysis, however, higher carbon contents and lower heteroatom (oxygen, sulfur, and nitrogen) contents were measured. In IMC and IMEC materials there is a reduction in O:C ratio from the biomass to C800 chars suggesting a loss of oxygen functionality at the surface (figure 54). This ratio significantly decreases from 0 to 250 °C and plateaus from 250 to 800 °C. The exception is RIM biochars which appear to gradually increase after the initial drop in O:C ratio, potentially due to the very large presence of magnesium sulfate and oxide on the surface in the C800 char. Carbon 1s deconvoluted spectral lines support the loss in oxygen functionality as C-O, C=O and O-C=O spectral lines at 286, 287, and 289 eV, respectively, are reduced and replaced with graphitic carbon binding energies at 284 eV (Figure 55).

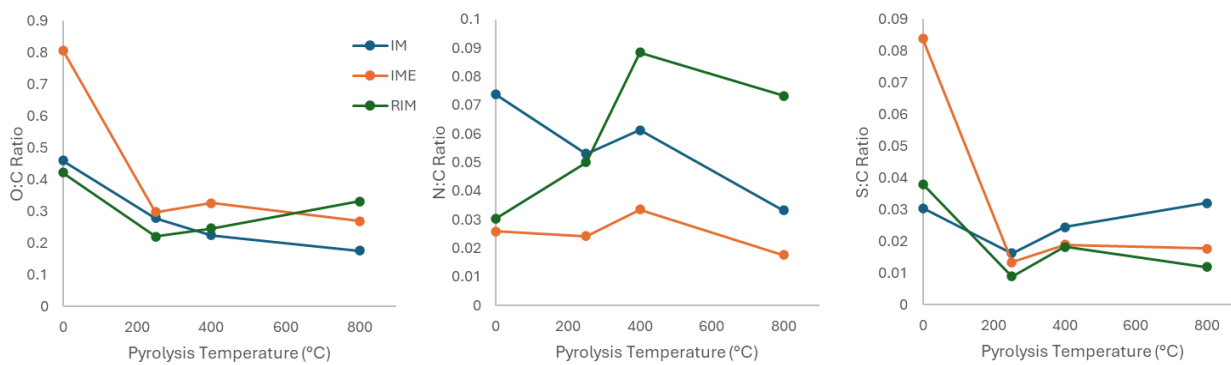


Figure 60: O:C, N:C, and S:C ratios at the surface of IMC, IMEC, and RIMC biochars quantified by XPS analysis.

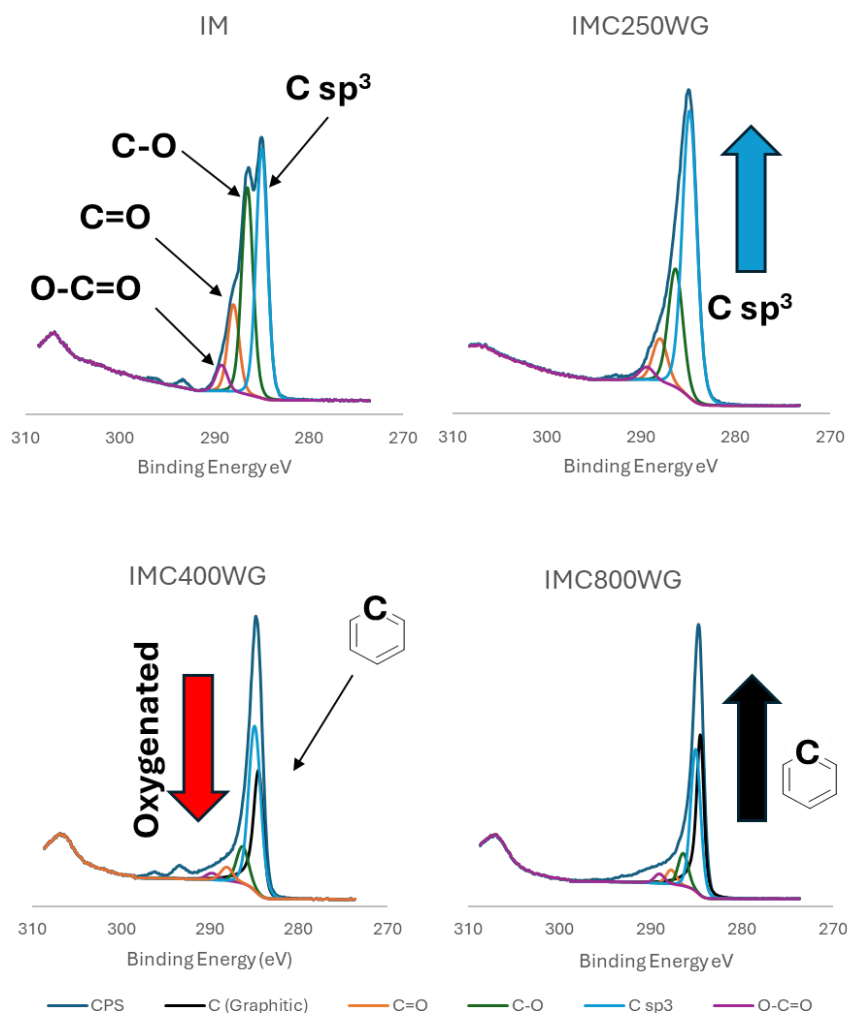


Figure 61: XPS spectra of IM and IMC(250-800) showing the carbon binding energy region C1s (280-300 eV) and identification of the deconvoluted spectral lines.

XPS suggests nitrogen is present on the surface of all three materials, in contrast to CHN analysis. These extract chars, however, exhibit a far smaller quantity of nitrogen in contrast with the other two biomasses. Apparently the nitrogen content in these IMEC samples is below the detection limit for CHN analysis (0.15%) which may indicate a concentration of nitrogen at the surface. Comparing materials from 0 °C to 800 °C the N:C ratio is variable across all three biochars. In RIM the N:C ratio increases before dropping above 400 °C, whereas in IM and IME the N:C ratio tends to decline with pyrolysis temperature. Deconvolution of the XPS data shows primarily a nitrogen spectral line at 400 eV in the C250 chars, which could be assigned to a range of nitrogen compounds including amines (C-NR₂), amides (N-C=O), and carbamates (N-(C=O)-O) to name a few ²⁵⁰. In the C800 chars, the deconvoluted spectra become more complex with binding energies ranging 398 and 406 eV, suggesting a far greater number of nitrogen environments have been produced during pyrolysis. RIM and RIMC250-800 N 1s XPS plots are available in appendix 3.4.

Sulfur is found in lower concentrations than expected in contrast to CHNS determinations, and decreases with carbonisation temperature likely due to the deposition and removal of sulfate salts. Similar to the oxygen content the S:C ratio on the surface decreases across the chars, however, the chemical complexity of the sulfur increases (Figure 56). Unlike nitrogen, the spectral lines of sulfur compounds are more resolved and can be identified. As mentioned previously a binding energy around 168-169 eV was assigned to a metal sulfate of magnesium, this area between 167 eV and 170 eV is typical of sulfur 2p_{3/2} spectral lines of oxidised sulfur in sulfates and sulfonic acid groups ^{120,251}. These are dominant in C250 chars, and are more complex in IMC250. Another sulfur environment binding energy is recognised in the C250 chars between 163 eV and 165 eV, and could be assigned to organic sulfur (C-S), or elemental sulfur (S₈). In C250 chars, this is likely caused by retained sulfur (sulfo-pyruvic acid) seen in literature and its gradual incorporation into the carbon material. One may also suggest that this organic sulfur in the low temperature chars could be associated with sulfur-rich proteins/amino acids such as cysteine, however without

an amino acid profile or protein contents of these biomasses this is just speculation. However, this band is present in IM and RIM biomass and more intense in IM and RIM C250s which would correlate to the insoluble protein content often found in Irish Moss⁸⁷.

In C800 chars, the region between 163 eV and 165 eV becomes more complex which could be due to deposition of elemental sulfur¹¹⁰ or the inclusion of sulfur into organic structures such as thiols or thiophenes. In the C800 chars a third sulfur environment is visible in some chars between 161 eV and 163 eV, this is assigned to highly reduced sulfur in metal sulfides. As can be seen in the XPS spectra these account for a small quantity of the sulfur content at the surface, as a large portion of the calcium sulfide deposits as previously mentioned in XRD analysis are removed during washings. Further due to these washings, the presence of metal sulfates in C250 and C800 chars is not expected, and hence in the C800 materials it is likely the oxidised sulfur in these materials is due to sulfones or sulfonic acid groups.

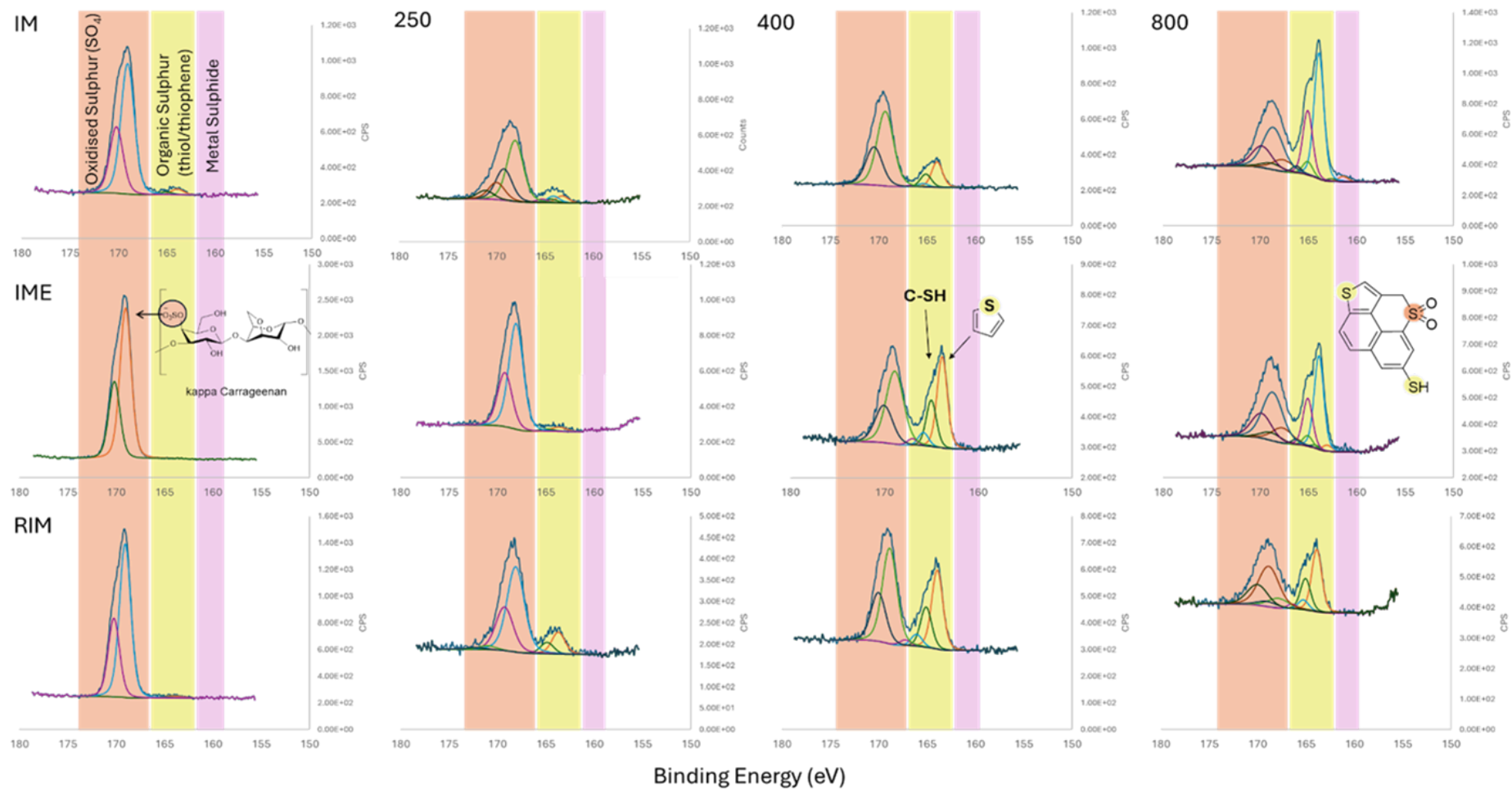


Figure 62: XPS spectra of IM, IME, and RIM biomass and chars from pyrolysis temperatures of 250 °C to 800 °C showing the sulfur binding energy region (280-300 eV) and identification of the deconvoluted spectral regions.

3.2.2.4. High-resolution transmission electron spectroscopy (HRTEM)

The internal structures of the chars have been determined using TEM imaging. From these images, it is recognised that the internal porosity of these chars increases with temperature, and tend to align well with the N₂ adsorption porosimetry results. IM chars after 250 °C pyrolysis exhibit little contrast in their images suggesting the granules are solid nodules, which occasionally contain pores around 20-50 nm in diameter. After 400 or 800 °C pyrolysis, however, these chars show a much greater degree of porosity. The images of these materials have regions of high and low contrast almost storm-cloud-esque, indicating small mesopores between 10-20 nm in size (figure 57).

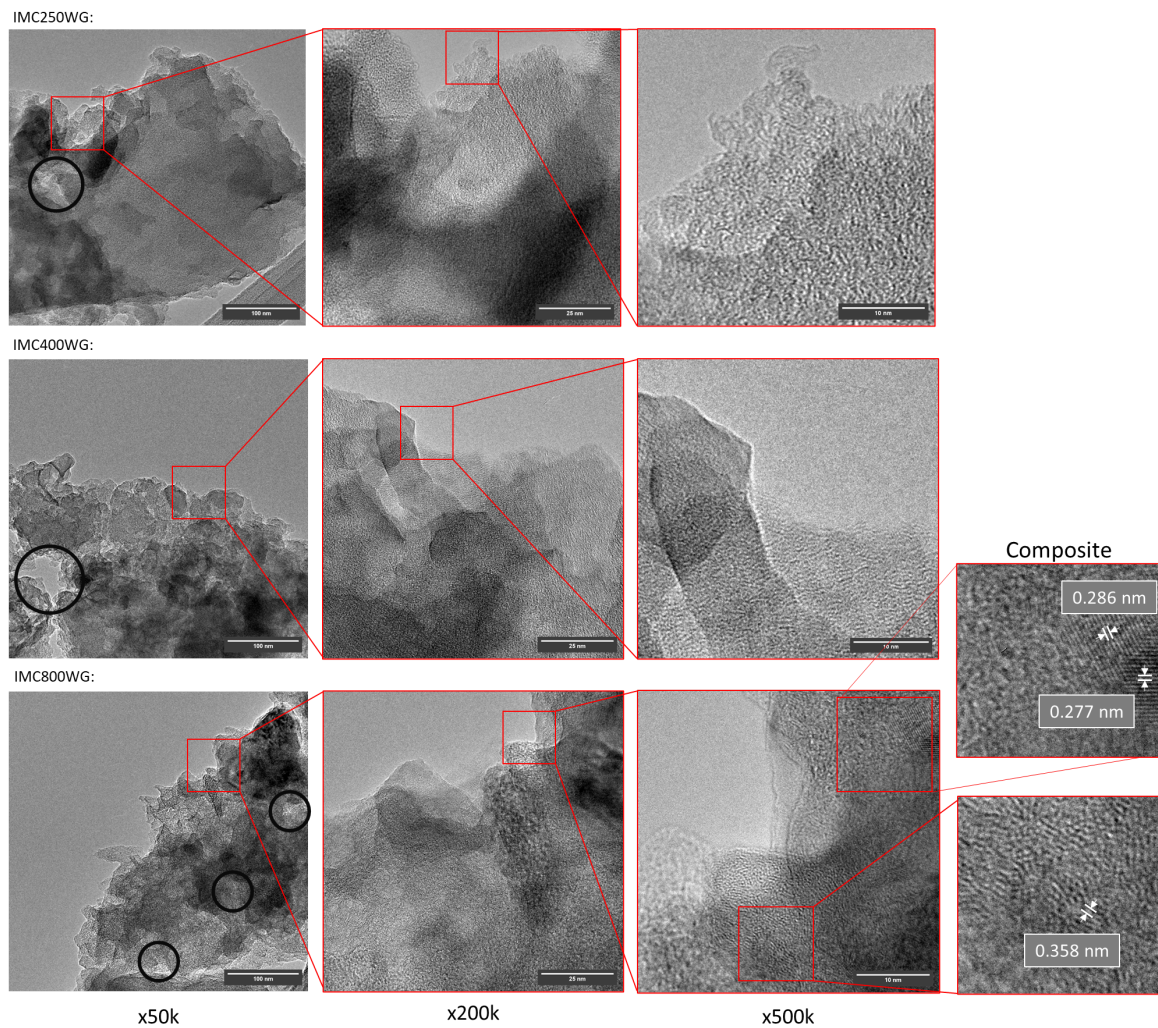


Figure 63: HRTEM images of washed IMC250, IMC400, and IMC800 chars at magnifications of x50k, x200k, and x500k. Circled areas indicate regions of porosity.

A similar trend is visible in the extract chars (IMECs), however, the 250 °C chars are initially far more porous, containing far more macropores (50-100 nm) and mesopores (10-30 nm) and appear sponge-like. At 800 °C, the particles of this char are not homogeneous and their pore sizes vary, in some mesopores of 20-50 nm are most common, in others mesopores of 5-10 nm make up the internal structure (pictured in figure 58). RIMCs are recognisably the least porous, with RIMC250 to RIMC800 all exhibiting what appears to be solid particles, the only porosity present appears to be changes in the surface texture (figure 59).

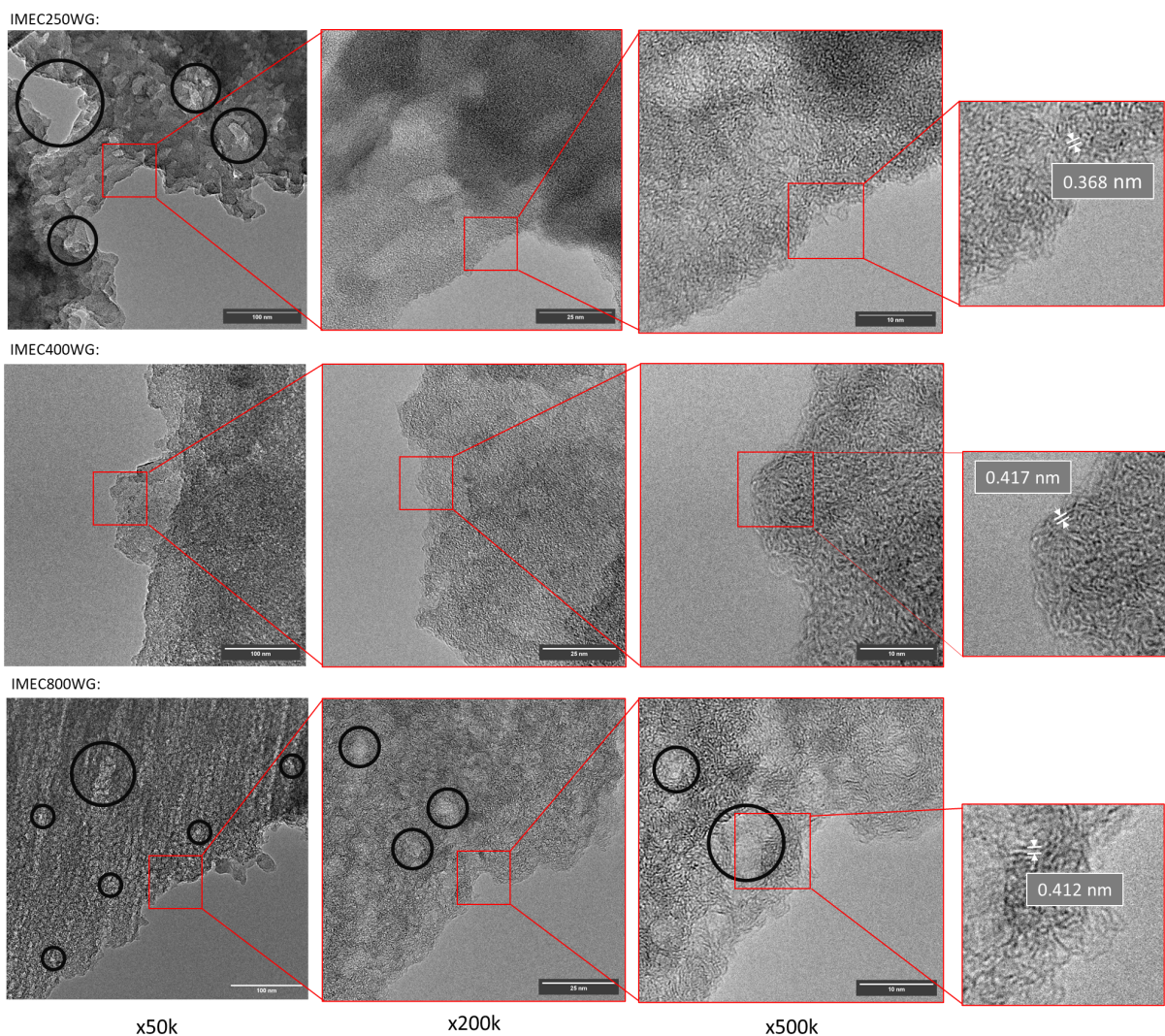


Figure 64: HRTEM images of washed IMEC250, IMEC400, and IMEC800 chars at magnifications of x50k, x200k, and x500k. Circled areas indicate regions of porosity.

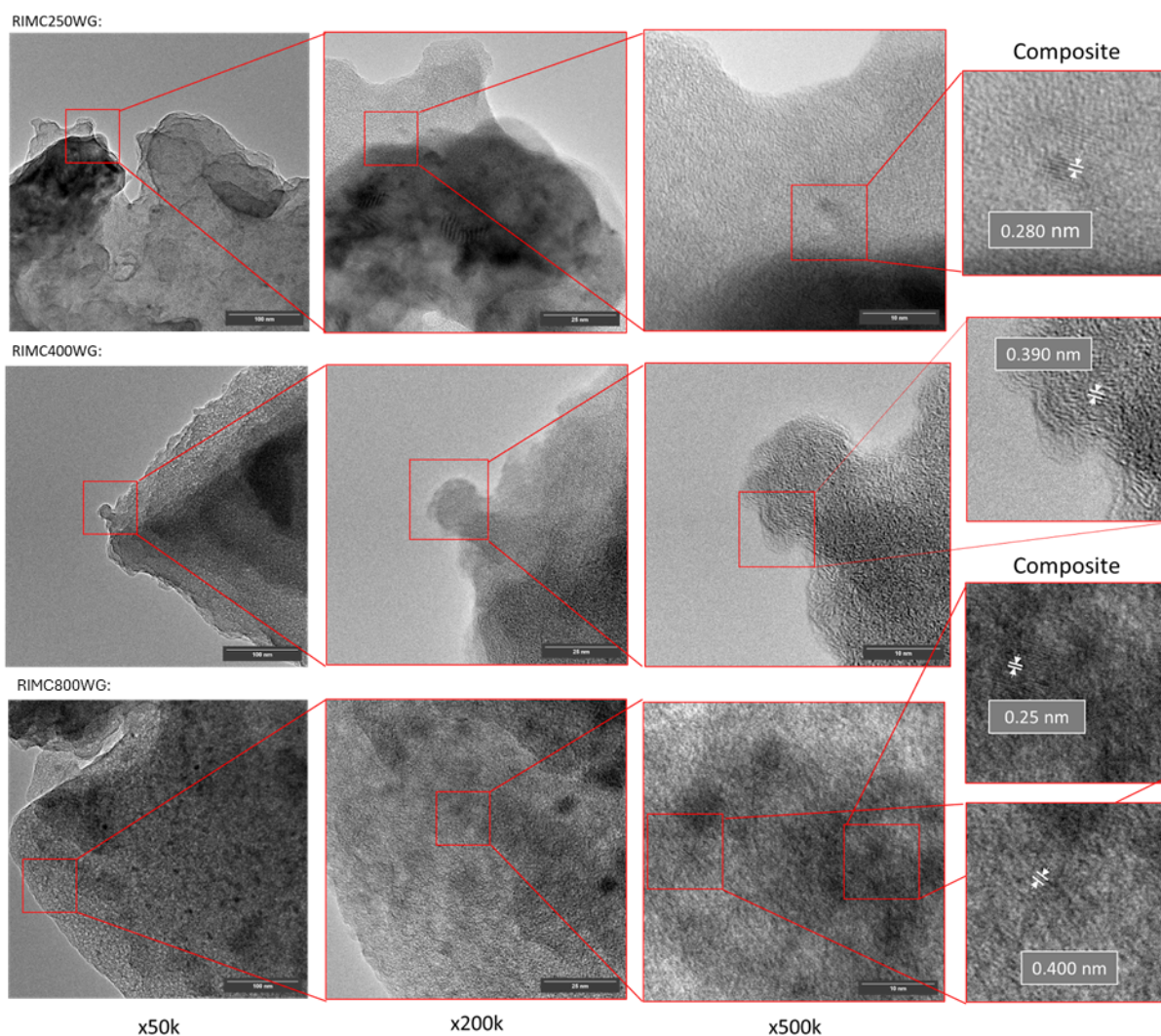


Figure 65: HRTEM images of washed RIMC250, RIMC400, and RIMC800 chars at magnifications of x50k, x200k, and x500k. Circled areas indicate regions of porosity.

In all 3 biomasses, their washed chars contained crystalline composites. In IMC800 two sizes of composites were imaged. Large (>100 nm) composites were imaged using HRTEM and interplanar distances of approximately 0.28 nm were measured. Unfortunately, this could not be assigned as both calcium sulfide and magnesium hydroxide exhibit a 0.284 (200) and 0.272 (100) nm interplanar distance, respectively. Due to the abundance of magnesium in comparison to calcium, one could assume that these composites are the latter. Smaller (5-10 nm) composites are also present in this sample and in RIMC800. These

composites were assigned as magnesium oxide using the interplanar distances of 0.20 (200) and 0.25 (111) nm measured.

Most IMEC800 particles contained very few composites. Rarely round 100 nm composites were identified with interplanar spacing of approximately 0.27 and 0.24 nm, which were assigned to the (100) and (101) planes of magnesium hydroxide. Since each of the chars underwent prolonged grinding to produce small enough particles for TEM, this could be a remnant of a hydrated magnesium oxide barnacle (figure 60).

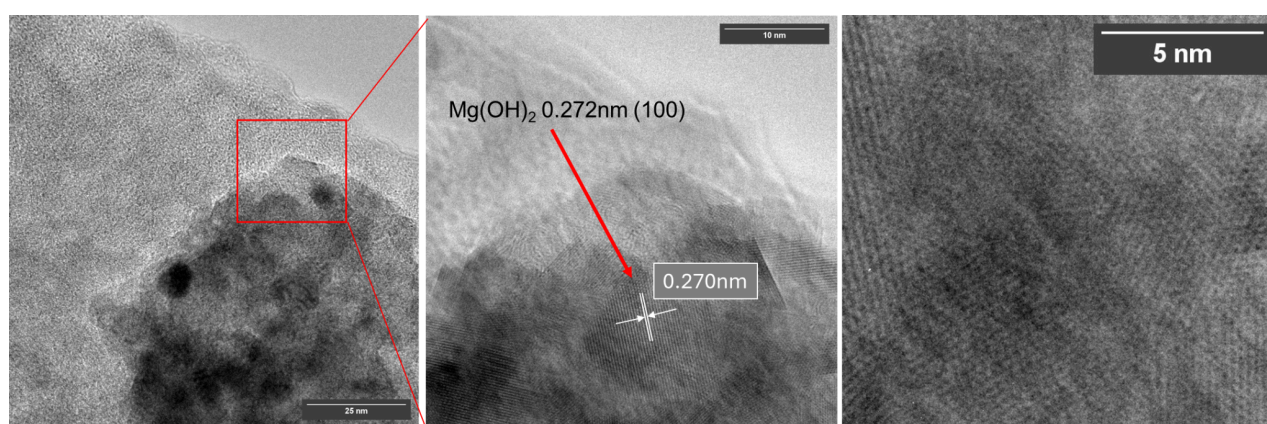


Figure 66: Magnesium hydroxide composite observed in IMEC800 using HRTEM imaging at magnifications of x200k (left) and x500k (middle). A zoomed in region of the middle image has been included to show the lattice structure (right).

HRTEM also enabled the microstructures of these chars to be imaged. In low temperature (250 °C) chars, the material is amorphous and disordered. At 400 °C and 800 °C, graphitic microcrystals begin to appear. The graphite planes appear curved and their interplanar distances measured to be 0.36, 0.39 and 0.41 nm in IMC800 (2.5%S), RIMC800 (2.6%S), and IMEC800(4.2%S) respectively. The substitution of sulfur (and nitrogen in the case of IM and RIM) into the graphite sheets appears to have effectively enlarged the interlayer distance compared to that of pure graphite (~0.34 nm)²⁴⁰. The presence of sulfur (IMEC ~0.41-0.42 nm) also has a much greater effect than that of nitrogen (RIM ~0.39-0.40 nm), consistent with literature²⁴¹.

3.2.2.5. Boehm titration, PZC analysis, and zeta potential

The surface of materials often shows acidity or basicity depending on the functional groups present on the materials surface. pH Drift analysis determines the pH in which the surface exhibits a neutral charge, or point-of-zero charge (PZC). A low pH_{pzc} indicates an acidic surface and high pH_{pzc} indicates a basic surface. Boehm Titration then allows the types of surface acidity to be classified depending on their ability to neutralise certain bases. This method typically determines carboxylic acid, lactonic, or hydroxyl group quantities, however, it is important to note that various other heteroatomic functionalities are acidic/basic and may interfere with quantification.

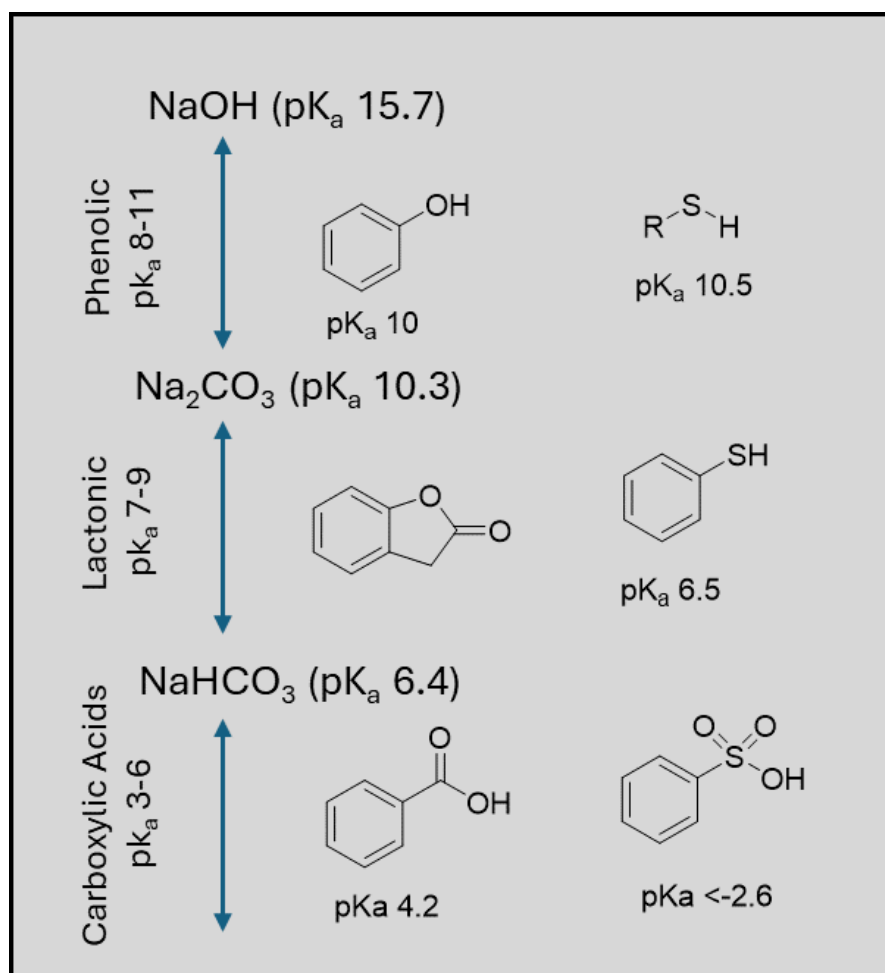


Figure 61: pK_a values of Boehm titration bases and common acidic sites present on chars

²⁵². Included are common acidic sulfur functional groups.

pH Drift analysis of the washed C800 chars indicate a highly basic surface, this is to be expected from the 'fully' carbonised C800 materials as the surface chemistry becomes more graphitic. The pH_{pzc} of these IM-based chars, however, are more basic than activated carbon or Starbon materials, these materials tend to have pH_{pzc} values around 8.0-9.0, whereas our chars range from 10.5 to 10.8 to 11.1, for IMEC800, IMC800, and RIMC800, respectively. This increase in basicity may be due to the presence of basic sulfide/oxide salts embedded on the surface.

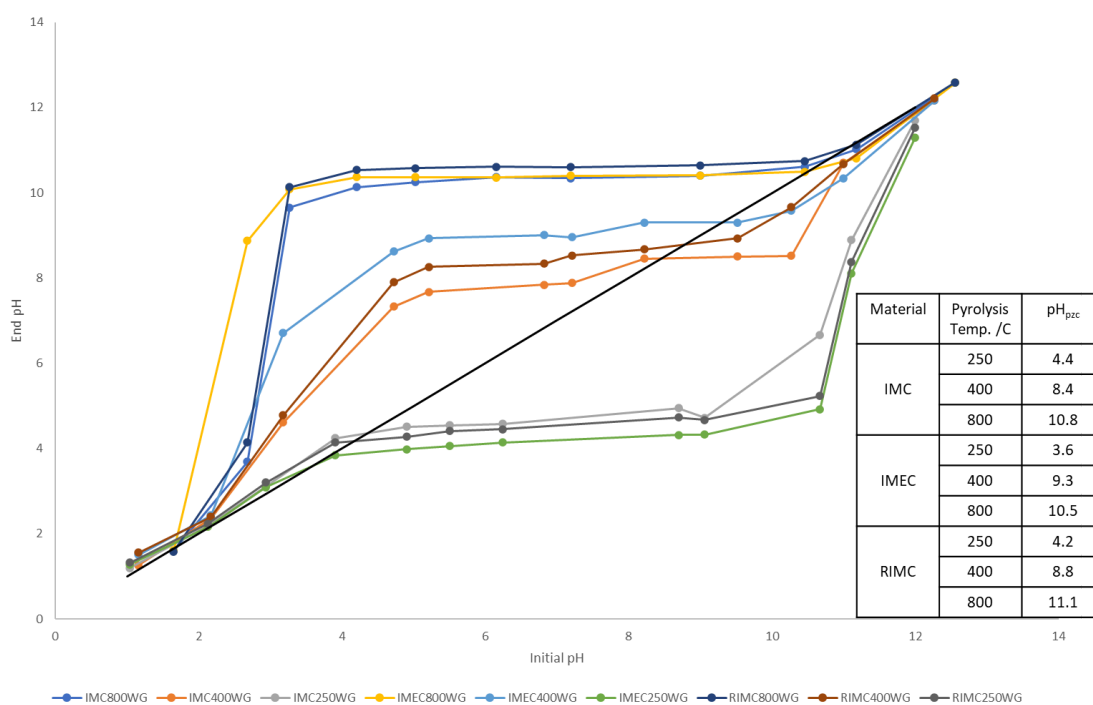
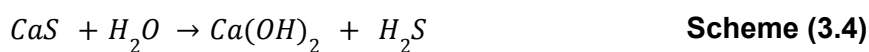


Figure 68: pH Drift analysis for the determination of pH_{pzc} values of washed IMC250-800, IMEC250-800, and RIMC250-800 chars.

Boehm titration supports pH_{pzc} determination. Basic C800 chars were recognised to have little total acidity (<0.2 mmol/g) and greater total basicity (0.30-0.45 mmol/g), due to graphitisation of the polysaccharides, loss of surface functionality, and the deposition of basic salt composites on the surface. Whereas, the acidic C250 chars have the reverse; high total acidity (0.4-0.5 mmol/g) and low total basicity (<0.1 mmol/g). The loss of highly oxygenated and acidic carboxylic groups from C250s to C800s likely due to decarboxylation at high temperature, is also in agreement with XPS results. Reviewing the structure of carrageenan, acidity at 250 °C is to be expected as some original functionality is likely to be retained, suggesting the presence of acidic sulfate groups.

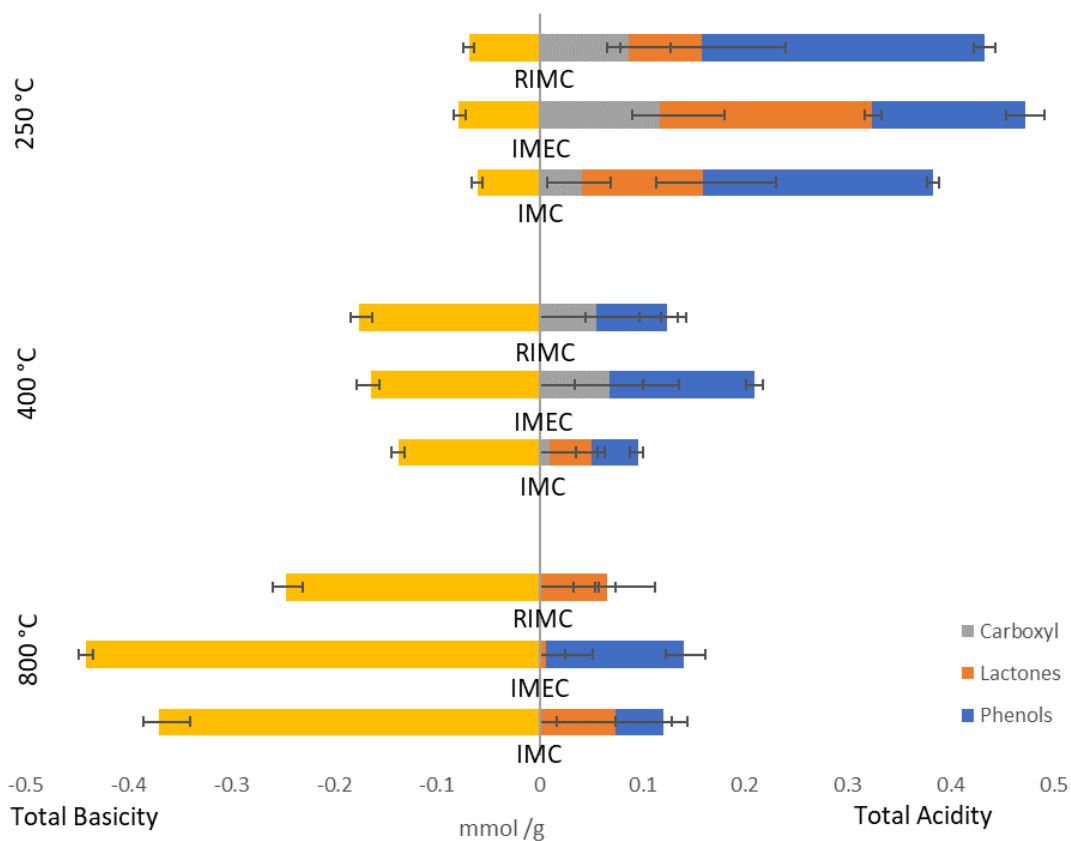


Figure 69: Total Acidity (and acidic breakdown) and Basicity determined via Boehm Titration of washed Irish Moss Chars, IMC, IMEC, and RIMC, carbonised at 250, 400, and 800 °C.

Zeta Potential is a parameter that measures the size of a bound solvent layer at a particle-solvent interface. A charged particle's surface in a solvent system has a Stern layer of solvent counter-ions that are adsorbed to the surface, beyond that layer there are more diffuse counter-ions. The solvent layer that travels with the charged particle is known as the slipping plane and is measured when calculating the zeta potential. Measurement of this parameter is often achieved using electrophoretic light scattering (ELS). This technique measures the variation in scattered light caused by the Doppler effect of particles in motion. By applying an electric field to a solution, the charged particles move according to their charge and their electrophoretic velocity (v_e) can be determined. The zeta potential (ζ) can then be calculated using the Smoluchowski equation:

$$\zeta = \frac{v_e \eta}{\epsilon_r \epsilon_0 E} \quad \text{Equation (3.3)}$$

Where η is the viscosity, ϵ_r is the relative permittivity (dielectric constant) of the solution, ϵ_0 is the electric permittivity of a vacuum, and E is the applied electric field.

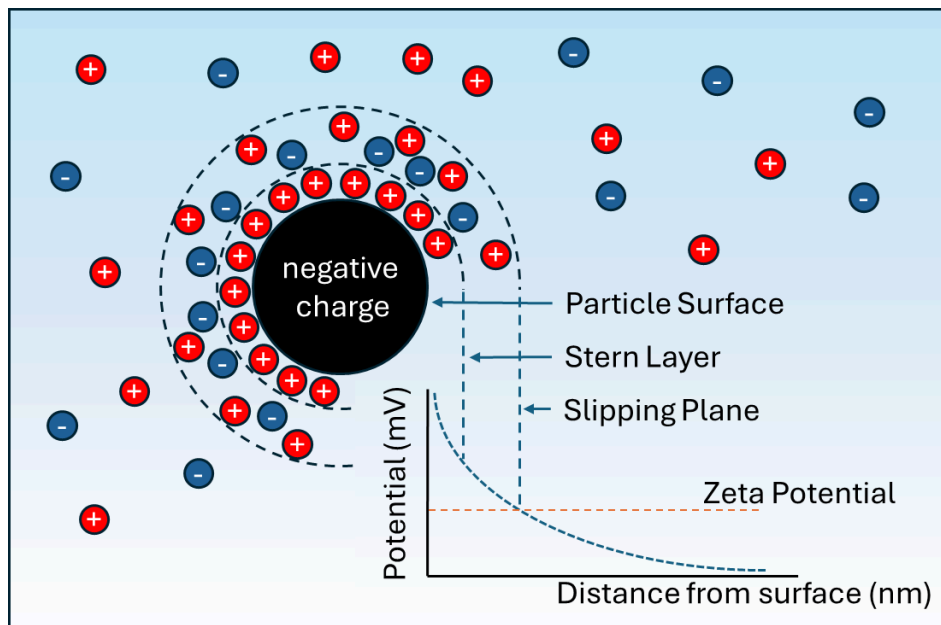


Figure 70: An illustration of zeta potential showing a charged particle and the layers of solvent counter ions at the particle-solvent interface, adapted from Yakasai et al. ²⁵³

Zeta potential measurements of Irish Moss derived chars were performed to determine the surface charge. All materials exhibited a negative charge between pH 3 and 9, and under more acidic conditions the surfaces trended towards having a closer to neutral charge. The C250 chars experienced the greatest change in zeta potential ($\Delta\zeta$) attributed to the presence of oxygen or sulfur functionality on the surface that undergo deprotonation in more basic solutions and afford an anionic surface (i.e. carboxylic acids pK_a 3-6). The C400 and C800 materials experience a smaller $\Delta\zeta$ due to fewer functionalities that deprotonate within this pH range (i.e. phenolics pK_a 8-11). These materials, specifically those of IM and IME, had a more consistent negative zeta potential around -15 mV to -25 mV. RIMC400 and RIMC800, however, showed a similar $\Delta\zeta$ to its C250 counterpart. These results can be explained by the Boehm titration acidic functionality. RIMC materials retain a fraction of carboxylic or lactonic-like groups on the surface even in C800 chars. In IMC800 a greater quantity of the acidic sites are associated with phenolic-like groups, and in IMEC800 almost all of the acidic sites are phenolic-like.

Nogueira *et al* explored the zeta potential of kappa, iota, and lambda-carrageenan hydrochars and activated carbons. In this study they recognised the oxygen containing groups present in the hydrochars afforded more negative values of ζ in basic solutions, whereas the activated carbons, which were more carbonised and had fewer oxygen functional groups on the surface, appeared less charged¹²⁸. They also commented that very negative zeta potential values (<-30 mV) indicate high colloidal stability which would prevent flocculation. This is discussed further in section 3.3.1.1.

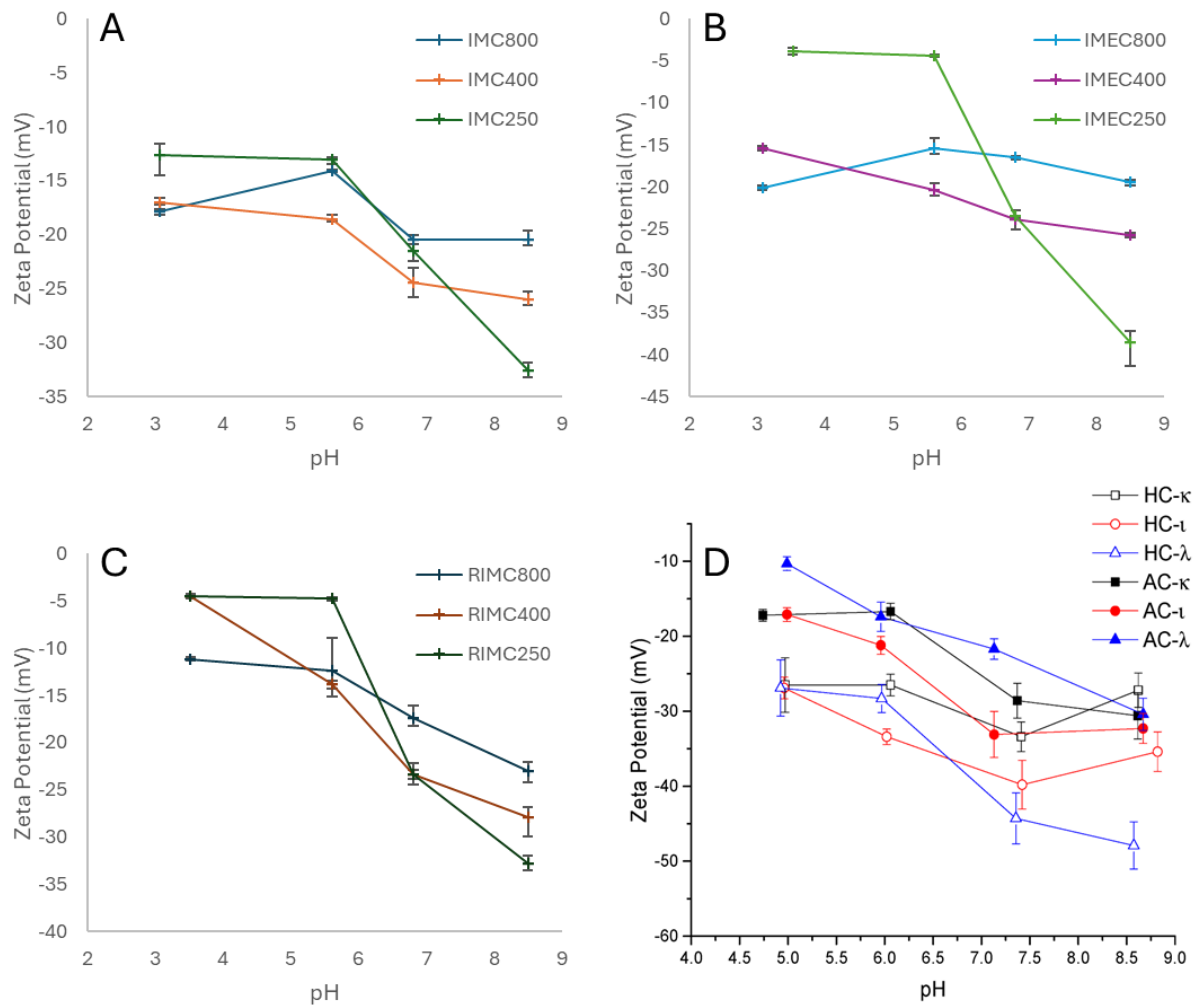


Figure 71: The effect of pH on Zeta potential measurements of IMC (A), IMEC (B), and RIMC (C) materials suspended in aqueous KCl electrolyte solution. For comparison literature zeta potential values of carrageenan-derived hydrochars and activated carbons have been included (D) ¹²⁸.

3.3. Copper (II) adsorption kinetics and mechanism

(Objective III)

3.3.1. Indirect copper(II) adsorption measurement (UV-vis)

Noncompetitive adsorption of copper(II) was achieved by immersing the Irish Moss-derived chars in varying concentrations of aqueous copper(II) nitrate solutions. After a specified length of time had passed the solution was filtered and its UV-vis absorption spectrum measured. Copper(II) forms a distorted octahedral $[\text{Cu}(\text{H}_2\text{O})_6]^{2+}$ species in acidic aqueous solutions that have a λ_{max} at 810 nm²⁵⁴. Figure 66 shows the UV-vis spectra of this species formed from varying concentrations of aqueous copper(II) nitrate (see section 2.3.2 for calibration curve). The effect of adsorbent dosage, initial copper(II) concentration, and adsorption contact time were explored to determine the adsorption capacity, kinetics, and isotherms for each char (IMC250-800, IMEC250-800, and RIMC250-800).

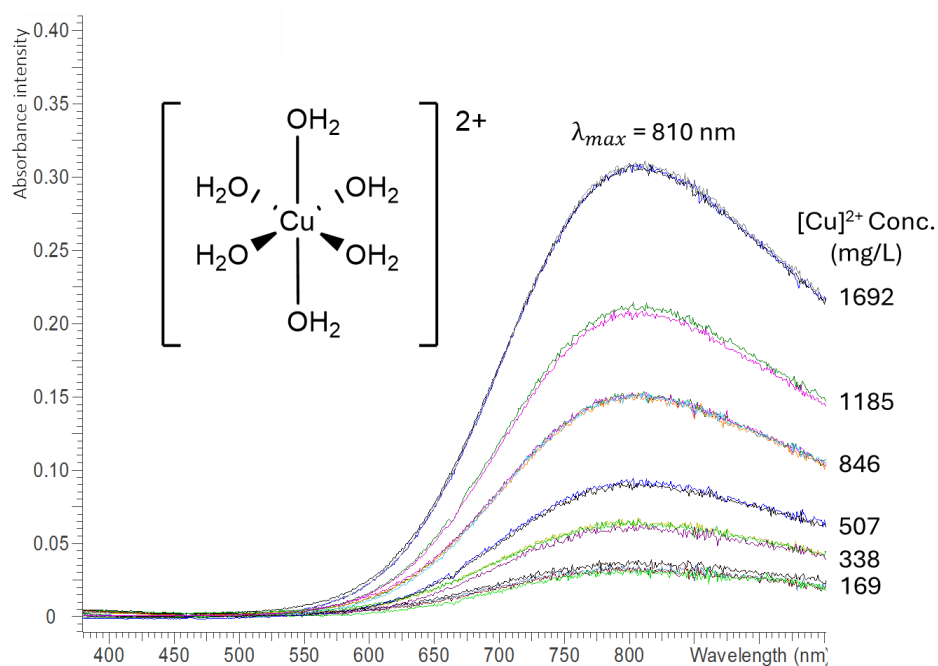


Figure 72: UV-vis spectra of aqueous copper(II) nitrate solutions at varying concentrations (500-5000 mg/L $\text{Cu}(\text{NO}_3)_2$).

3.3.1.1. Effect of char dosage

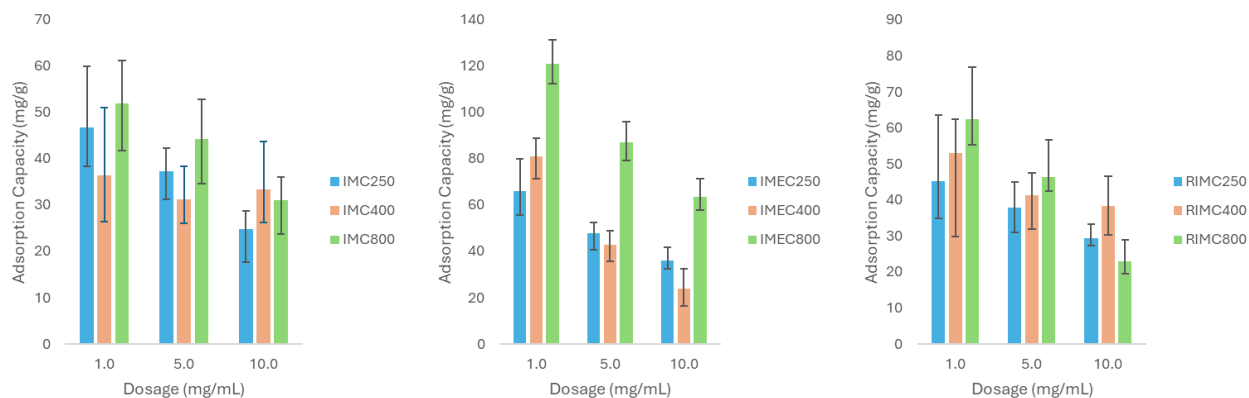


Figure 73: Copper(II) adsorption capacity of IMC, IMEC, and RIMC (250-800) materials, determined indirectly by UV-vis analysis of copper(II) nitrate solution (5000 mg/L, 10 mL, pH 4.5) after 24h dosed with 10, 50, or 100 mg of char material.

Preliminary adsorption experiments of copper(II) onto Irish Moss-derived chars exhibited adsorption capacities ranging from 20 to 120 mg/g. A dosage of 1.0 mg/mL tended to show the maximum adsorption capacity of the char materials under these conditions. Although at this dosage the margin of error was typically larger and significantly overlapped with the adsorption capacities derived from a 5.0 mg/mL dosage. At this stage the chars derived from carrageenan (IMECs) exhibit the highest adsorption capacities, specifically that of IMEC800 (121 ± 11 mg/g, 1.0 mg/mL dosage). The effect of pyrolysis temperature on IM and RIM chars' adsorption capacity is yet to show any significant trends.

A trend recognised from these experiments was the decrease in adsorption capacity with increasing material dosage. As the quantity of copper(II) available was in an excess it is unlikely that an increase in dosage resulted in a lower adsorption capacity due to competition (i.e. copper being shared over a larger quantity of material). Instead it is more likely that at higher dosages flocculation of the char particles becomes an issue. The initial pH of the copper(II) nitrate solutions was approximately 4.0-4.5. At this pH, these chars

exhibit zeta potential values of approximately -5 to -20 mV (section 3.2.2.5) indicating limited stability or instability of these chars in solution ²⁵⁵. After a 24 h period in the water-shaker bath obvious sedimentation of the char material had occurred. This is likely to have a greater effect at higher doses of material due to a lower surface area of char being available for the adsorption of copper(II). From this point onwards a dosage of 5.0 mg/mL has been used.

3.3.1.2. Effect of initial copper(II) concentration

Measuring the adsorption capacity of an adsorbent against the initial concentration of the adsorbate produces an adsorption isotherm. The type of adsorption can then be determined by applying appropriate adsorption models. In this section two adsorption isotherm models were applied, Langmuir and Freundlich. As mentioned in section 3.2.2.2, the Langmuir isotherm model assumes monolayer formation on a homogeneous surface and indicates a saturated coverage ²⁴². The Langmuir equation is written below:

$$q_c = \frac{q_m K_L C}{1 + K_L C} \quad \text{Equation (3.4)}$$

Where q_c is the measured adsorption capacity at concentration, C , q_m is the maximum adsorption capacity, and K_L is the Langmuir constant.

The Freundlich isotherm, on the other hand, is applicable to multilayer adsorption on heterogeneous surfaces ²⁵⁶. The Freundlich equation is written below:

$$q_c = K_F C^{1/n} \quad \text{Equation (3.5)}$$

Where, once again, q_c is the measured adsorption capacity at concentration, C , K_F is the Freundlich coefficient, and n is the Freundlich constant.

The surface topography and chemistry will have a significant effect on the adsorption isotherm. The surface chemistry is variable under different acidities and basicities (section 3.2.2.5). Linear regression has been used to determine Freundlich and Langmuir isotherm constants for the adsorption of copper(II) at pH 4.0-4.5 and pH 1.0. They are summarised in

table 7 (pH 4.0-4.5) and table 8 (pH 1.0). Linearised plots of the two models are listed in appendix 3.5.

3.3.1.2.1. pH 4.0-4.5

Table 8: Isotherm model constants determined for the adsorption of copper(II) to IMC, IMEC, and RIMC chars (C250-800) at a pH of 4.0-4.5.

Material	Langmuir Isotherm			Freundlich Isotherm		
	K_L (L/mg)	q_m (mg/g)	R^2	K_F (L/mg)	$\frac{1}{n}$	R^2
IMC250	0.00172	35.0	0.867	0.973	0.447	0.893
IMC400	0.00970	20.6	0.969	0.707	0.475	0.755
IMC800	0.0128	27.0	0.941	2.48	0.352	0.932
IMEC250	0.0125	38.6	0.876	2.85	0.391	0.872
IMEC400	0.0148	35.1	0.927	4.72	0.292	0.800
IMEC800	0.00298	87.0	0.523	6.93	0.346	0.894
RIMC250	0.000920	56.8	0.989	0.214	0.703	0.991
RIMC400	0.000195	156.3	0.999	0.0333	0.957	0.983
RIMC800	0.00175	45.2	0.985	0.649	0.549	0.971

Excluding IMEC800, all chars exhibited an R^2 between 0.867 and 0.999 for the Langmuir model. The chars also showed R^2 values between 0.755 and 0.991 for the Freundlich model. In many cases the R^2 values of the two applied models were very close indicating both models showed a good fit with the experimental data. In some cases the char material showed an adsorption isotherm with closer similarity to a specific model. IMEC800 best fits a Freundlich model, indicating the adsorption of copper(II) of this surface has multilayer character and heterogeneous adsorption sites. IMC400 and IMEC400, however, best fit a Langmuir model which indicates the adsorption of copper(II) to these surfaces has monolayer character and the surfaces have uniform adsorption sites. IMC250, IMC800, and IMEC250 showed R^2 values that were too close to distinguish a better fit. χ^2 errors, and sum

square errors (ERRSQ) have been calculated alongside linear regression R^2 values in an attempt to determine the better fit (appendix 3.6 & 3.7). In most cases there is agreement between the two errors and R^2 values regarding best fit. Considering this additional error analysis, IMC250, IMC800 and IMEC250 indicate a better fit to a Freundlich isotherm model. RIMC materials also showed R^2 values that were too close to distinguish a better fit, however, error analysis did not improve the ability to distinguish between the models. This is clearly visible in the RIMC plots of the isotherm models alongside the measured adsorption capacities shown in figure 68.

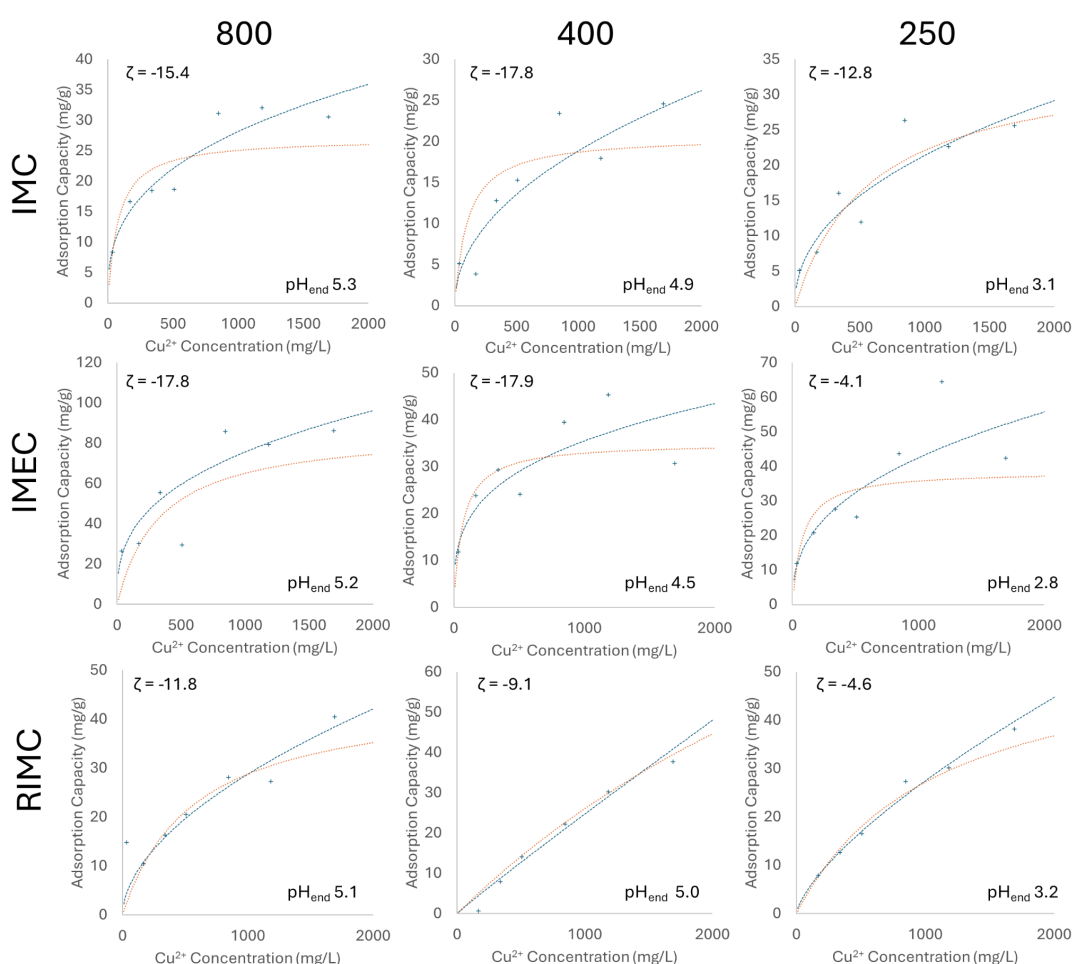


Figure 74: Copper(II) adsorption isotherm plots at pH 4.0-4.5 of IMC, IMEC, and RIMC (250-800). Freundlich (blue line) and Langmuir (orange line) isotherm models have been plotted for each material. Inset are zeta potential (ζ) values for each char at pH 4.5 and the end pH after 24h.

Langmuir calculated q_m values showed some similarities to the experimental data in most cases. The value calculated for RIMC400, however, was significantly higher than the value experimentally determined at the highest copper(II) concentration used. This material exhibited some linearity in its experimental data indicating surface saturation had not been achieved within this concentration range. Adsorption capacities of these chars exhibited no obvious trend with carbonisation temperature or zeta potential. With the exception of RIMC400, C400 materials appeared to exhibit the poorest adsorption capacities, compared to their C250 and C800 counterparts. This may be attributed to the reduced surface functionality compared to C250 materials, but without the higher surface area and pore volume achieved at higher carbonisation temperatures (i.e. at 800 °C).

Copper speciation varies with the pH of the solution. As stated earlier, in acidic solutions the free cupric ion (Cu^{2+}) forms the metal hydroxo complex as shown in figure 66. With increasing pH the removal of a proton forms the hydrated CuOH^+ complex and further deprotonation affords the precipitation of copper hydroxide^{257,258}. Figure 69 shows the effect of pH on the absorbance intensity of aqueous copper(II) at 810 nm. A significant decrease in absorbance around pH 5 is observed indicating the conversion of $[\text{Cu}(\text{H}_2\text{O})_6]^{2+}$. In these adsorption experiments the surface acidity and basicity of the char materials resulted in a shift in the pH of the copper solution. The C250 materials caused a decrease in pH to approximately pH 3 due to the acidity of the surface of these chars. This likely had little effect on the copper speciation and the difference in absorbance is therefore a result of copper(II) adsorption (see figure 69). The C400 and C800 materials, however, have basified the solution to pH 5 (excluding IMEC400) (figure 68), which would have potentially resulted in a change in copper(II) speciation. Figure 69 also shows the effect of IMEC800 on copper speciation. The plot of pH against UV absorbance intensity for this adsorption experiment follows the copper (II) speciation curve, implying that the measured adsorption capacity is, at least partially, a result of basification. Adsorption under more acidic conditions should

minimise the effect of basification, however, it will likely protonate anionic adsorption sites on the chars also. Copper(II) basification is also evident in SEM-EDS and XRD analysis covered in sections 3.3.2.1 and 3.3.2.2, respectively.

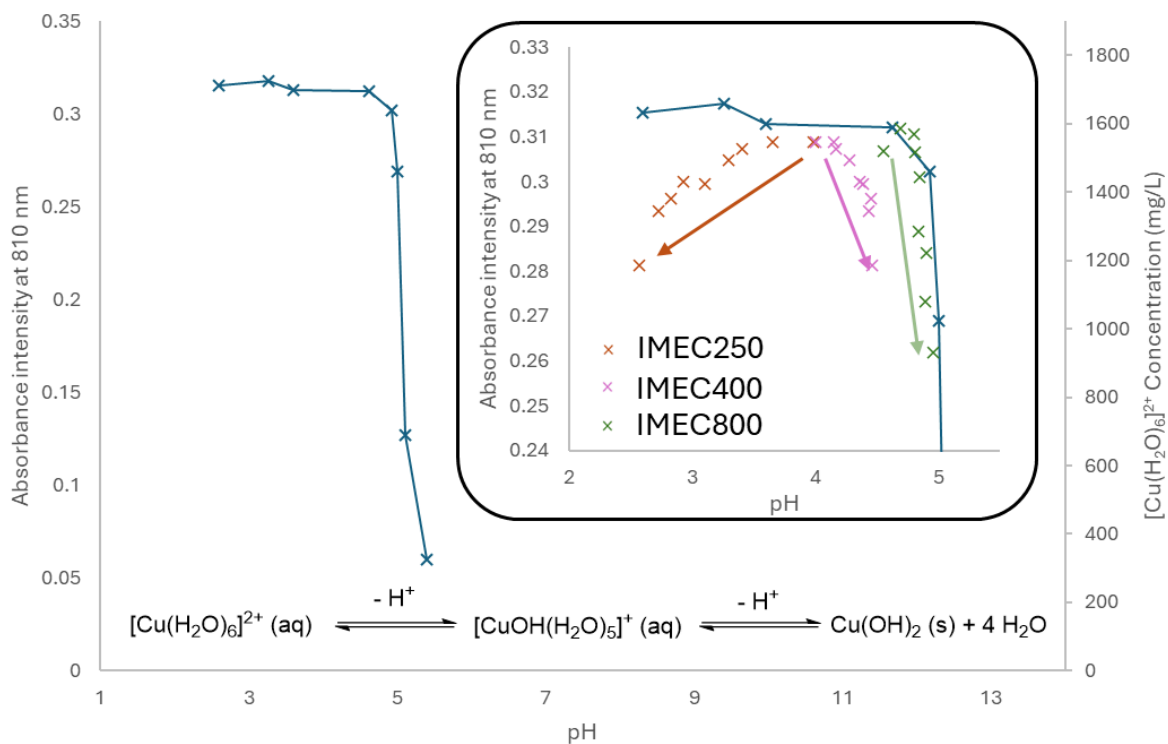


Figure 75: The effect of pH on the adsorption intensity at 810 nm of the $[\text{Cu}(\text{H}_2\text{O})_6]^{2+}$ complex and expected transitions as the solution becomes alkaline^{257,258}. Inset is the change in the pH of the copper(II) solution plotted against the corresponding UV absorbance at 810 nm for IMEC adsorption experiments. Arrows indicate the first pH measurement ($t = 0.5 \text{ h}$) and last ($t = 24 \text{ h}$) of the adsorption experiments.

3.3.1.2.2. pH 1.0

Table 9: Isotherm model constants determined for the adsorption of copper(II) to IMC, IMEC, and RIMC chars (C250-800) at a pH of 1.0.

Material	Langmuir Isotherm			Freundlich Isotherm		
	K_L (L/mg)	q_m (mg/g)	R^2	K_F (L/mg)	$\frac{1}{n}$	R^2
IMC250	0.000370	58.5	0.922	0.178	0.647	0.844
IMC400	0.00231	29.3	0.825	0.707	0.475	0.755
IMC800	0.000740	30.7	0.829	0.249	0.569	0.611
IMEC250	0.00081	100.0	0.930	0.188	0.790	0.936
IMEC400	0.000440	91.7	0.480	0.0300	1.01	0.873
IMEC800	0.00103	62.1	0.533	0.466	0.614	0.671
RIMC250	0.0000786	263.2	0.980	0.0208	0.991	0.976
RIMC400	0.000100	196.1	0.987	0.0305	0.918	0.988
RIMC800	0.00042	48.1	0.879	0.0205	0.970	0.911

The adsorption isotherms for these chars under strongly acidic conditions (pH 1) differ from those under mild acidic conditions (pH 4). In these experiments the isotherm plots exhibit a poorer fit with both the Langmuir and Freundlich models compared to the previous section (3.3.1.2.1). All IMC materials showed a best fit with the Langmuir model ($R^2 = 0.825-0.922$). Whereas all IMEC materials exhibited better fitting to the Freundlich model ($R^2 = 0.671-0.936$) and RIMC materials once again showed a good fit to both models. These results indicate that certain materials, specifically IMC250 and IMEC400, exhibit different surface characteristics under these more acidic conditions. In IMC250, this may be attributed to a transition from copper adsorption occurring at carboxylate adsorption sites (monolayer) to adsorption within pore structures (multilayer), as the carboxylate sites become protonated under these acidic conditions. Whereas, in IMEC400 and the other C400 and C800 materials, the effect of basification is removed and the remaining adsorption can be

attributed to surface characteristics. The end pH values further imply a lack of basification occurring, which for each adsorption experiment was less than pH 2 (figure 70).

Langmuir calculated q_m values were often overestimated compared to the experimental data (figure 70). In some cases, such as RIMC materials and IMEC400, the isotherms once again exhibited linearity and cannot be extrapolated to determine the maximum adsorption capacity. However, in IMC250 and IMEC250 the experimental data appears to plateau around 20 and 53 mg/g, but the Langmuir's calculated values suggest a maximum of 58.5 and 100.0 mg/g, respectively. Despite having a good R^2 fit, this could suggest a different model would be better suited to these adsorption experiments. The measured experimental adsorption capacities for IMCs and RIMCs have decreased between pH 4 to pH 1, but for IMECs the adsorption capacities have increased (excluding IMEC800, where adsorption via basification has been prevented).

In regards to the trends across materials, it is evident that a higher carbonisation temperature results in poorer copper(II) adsorption under strongly acidic conditions. Likely as a result of anionic adsorption sites in these materials becoming protonated, but also due to the ceased basification. For all three materials: IM, IME, and RIM, the highest adsorption capacities were achieved by the C250 materials, which decreased sequentially for the C400 and C800 materials. This may be attributed to the functional sites on the chars surface, specifically those that are strongly acidic, and remain deprotonated at pH 1. For these materials this is likely sulfate functionality ($pK_a < -2.6$), which is likely to decrease with carbonisation temperature (section 3.2.2.3). That also implies that the surface chemistry has a greater impact on the adsorption of copper(II) over material porosity, which is known to increase with carbonisation temperature (section 3.2.2.2).

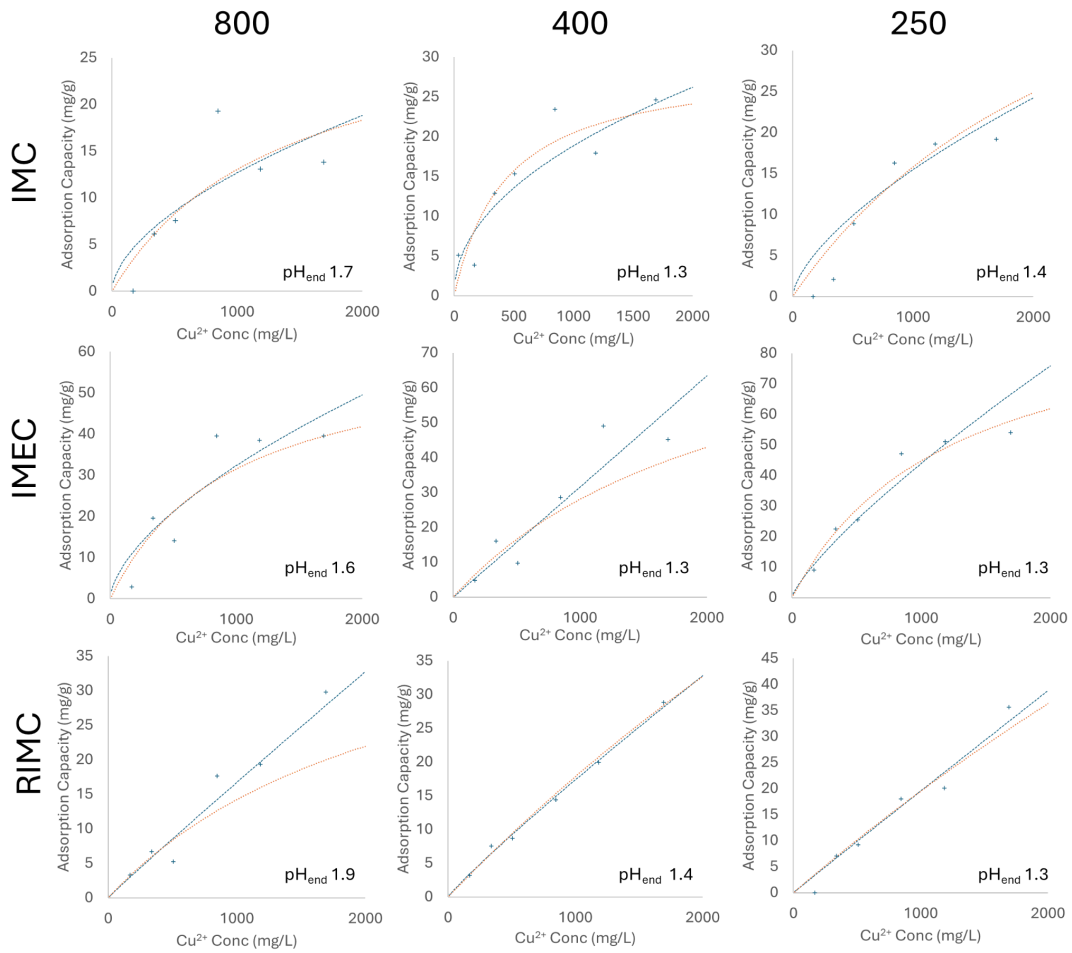


Figure 76: Copper(II) adsorption isotherm plots at pH 1.0 of IMC, IMEC, and RIMC (250-800). Freundlich (blue line) and Langmuir (orange line) isotherm models have been plotted for each material. Inset is the end pH after 24h.

3.3.1.3. Effect of adsorption contact time

An adsorption kinetic study was performed by measuring the adsorbed copper(II) at intervals of time. Applying a kinetic order model enables the metal adsorption mechanism and rate controlling steps to be estimated. The most widely used kinetic models are the pseudo-first order and pseudo-second order models.

Pseudo-first order:
$$\frac{dq_t}{dt} = k_1(q_e - q_t) \quad \text{Equation (3.6)}$$

Pseudo-second order:
$$\frac{dq_t}{dt} = k_2(q_e - q_t)^2 \quad \text{Equation (3.7)}$$

Where q_t is the adsorption capacity at time, t , q_e is the adsorption capacity at equilibrium (in the pseudo-first order model equilibrium was assumed to be met after 24 h), and k_1 and k_2 are the rate constants for the pseudo-first and second order models, respectively. The pseudo-first order model typically describes physisorption adsorption processes, whereas the pseudo-second order model better describes chemisorption. The determination of kinetic parameters for the two models are summarised in table 9 for the adsorption of copper(II) at pH 4.0-4.5 and table 10 for the adsorption of copper(II) at pH 1.0. Linearised plots of the two models are available in appendix 3.8.

3.3.1.3.1. pH 4.0-4.5

Table 10: Kinetic parameters for pseudo-first and second order models determined for the adsorption of copper(II) to IMC, IMEC, and RIMC chars (C250-800) at a pH of 4.0-4.5.

Material	q_e (mg/g) ($q_t, t = 24h$)	Pseudo-first order		Pseudo-second order		
		K_1 (min^{-1})	R^2	q_e (mg/g)	K_2 ($\text{g mg}^{-1} \text{min}^{-1}$)	R^2
IMC250	25.69	0.0045	0.953	26.39	0.00097	0.998
IMC400	24.64	0.0051	0.472	20.53	0.0049	0.857
IMC800	30.61	0.0070	0.756	40.82	0.00029	0.893
IMEC250	43.27	0.0019	0.460	44.24	0.00030	0.993
IMEC400	30.72	0.0047	0.975	32.26	0.00065	0.952
IMEC800	86.24	0.0033	0.936	95.24	0.000084	0.992
RIMC250	38.23	0.0070	0.5461	38.46	0.00092	0.981
RIMC400	37.70	0.00070	0.406	15.02	0.00012	0.709
RIMC800	40.48	0.0058	0.589	44.05	0.00039	0.956

In almost all cases every material exhibited a better fit towards a pseudo-second order model ($R^2 = 0.709-0.998$). The only exception was IMEC400 which had a good fit to both models ($R^2 > 0.95$). This implies that the adsorption of copper(II) onto the Irish Moss-derived chars is undergone by a chemisorption-like mechanism. The calculated q_e values were often also close to the experimental values. In literature, the adsorption of transition metal ions onto bio-derived chars typically exhibits pseudo-second order rate kinetics^{131,259,260}. In one particular study by Zhao *et al*, a sulphur-doped graphene sponge exhibited rapid adsorption of copper(II) ($k_2 = 0.0544 \text{ g mg}^{-1} \text{ min}^{-1}$) which was described well by a pseudo-second order model ($R^2 = 0.999$)²⁶⁰. Of the materials tested here IMCs exhibited the fastest adsorption kinetics ($k_2 = 0.00029-0.0049 \text{ g mg}^{-1} \text{ min}^{-1}$), followed by RIMCs ($k_2 = 0.00012-0.00092 \text{ g mg}^{-1} \text{ min}^{-1}$), and IMECs were significantly slower ($k_2 = 0.000084-0.00065 \text{ g mg}^{-1} \text{ min}^{-1}$). Compared to literature, such as the study by Zhao *et al*

above, the inherent sulphur-containing materials derived from Irish Moss showed far slower adsorption kinetics than that of the sulphur-doped material in Zhao *et al's* study.

Although the carbonisation temperature showed little correlation with the pseudo-second order rate constant under these conditions. The plotted data shown in figure 71 could indicate otherwise. The copper(II) uptake by the C800 materials appears significantly slower than the uptake of copper by the C400 and C250 materials. In the C800 adsorption kinetic plots the linear portion of adsorption is measurable within the first 2 hours of contact time. In comparison the C400 and C250 materials have achieved approximately 50% of their maximum uptake potential within the first 30 minutes (excluding RIMC400). This difference could be attributed to the wetting of the char materials, as the aromatic surface of the C800 chars is likely to be more hydrophobic than the oxygen functionalized surface of the C250 materials. However, it is more likely a characteristic of the mechanism of basification as this slower rate is subdued in the more acidic pH 1 solutions (see the following section 3.3.1.3.2.).

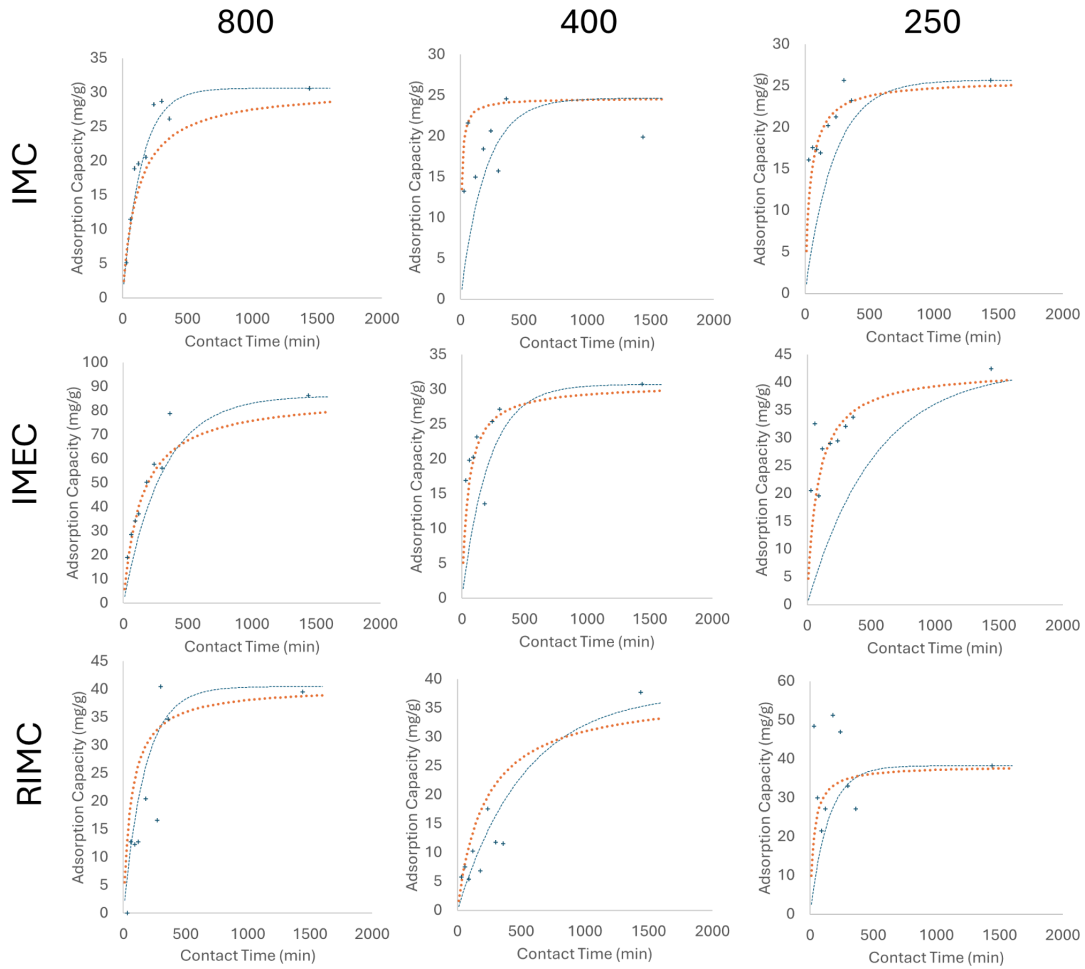


Figure 77: Copper(II) adsorption kinetics at pH 4.0-4.5 of IMC, IMEC, and RIMC (250-800).

Pseudo-first order (blue line) and pseudo-second order (orange line) kinetic models have been plotted for each material.

3.3.1.3.2. pH 1.0

Table 11: Kinetic parameters for pseudo-first and second order models determined for the adsorption of copper(II) to IMC, IMEC, and RIMC chars (C250-800) at a pH of 1.0.

Material	q_e (mg/g) ($q_t, t = 24h$)	Pseudo-first order		Pseudo-second order		
		K_1 (min^{-1})	R^2	q_e (mg/g)	K_2 (g mg^{-1} min^{-1})	R^2
IMC250	19.22	0.00068	0.617	20.04	0.00045	0.948
IMC400	20.01	0.00081	0.502	21.05	0.00040	0.954
IMC800	13.87	0.0027	0.201	14.41	0.00065	0.932
IMEC250	54.09	0.004	0.503	54.95	0.00069	0.999
IMEC400	45.19	0.0054	0.724	45.87	0.00086	0.999
IMEC800	39.52	0.020	0.747	37.88	0.0032	0.999
RIMC250	35.60	0.018	0.449	34.48	0.0029	0.998
RIMC400	28.83	0.0008	0.109	27.25	0.00091	0.917
RIMC800	29.76	0.0063	0.527	29.85	0.00289	0.998

Under strongly acidic conditions these materials still show a good fit to a pseudo-second order rate model ($R^2 = 0.917-0.999$), and once again the calculated q_e values are close to the experimental value. As a result of the more acidic conditions the mechanism of adsorption has likely changed and in many cases this has affected the adsorption kinetics. IMCs now exhibit slower adsorption kinetics and IMECs and RIMCs exhibit much faster kinetics. A slower rate of adsorption can be easily explained by the less negative zeta potential value which would result in a reduced/slower interaction between the chars and the metal copper(II) ions, but also by an increase in the competition between Cu^{2+} and H^+ at anionic sites on the char under these more acidic conditions. An increase in rate, at least for the C800 materials, could be explained by the removal of a slow but abundant adsorption mechanism (i.e. basification), so that a faster but less abundant adsorption mechanism is visible. Hence, a smaller adsorption capacity (q_e) and an increased rate

constant (K_2) are measured. The rapid chemisorption of copper(II) onto C800 materials under the strongly acidic conditions is likely as a result of an interaction between copper(II) and organic sulphur sites present on these materials. The vacant 4s orbital of copper(II) and other transition metals interact strongly with electron donating elements such as sulfur or sulfur containing groups such as thiols and thiophenes and form stable Cu-S-R structures²⁶¹. These structures are likely the adsorbed form of copper on the surface of the thiol rich chars (C800s).

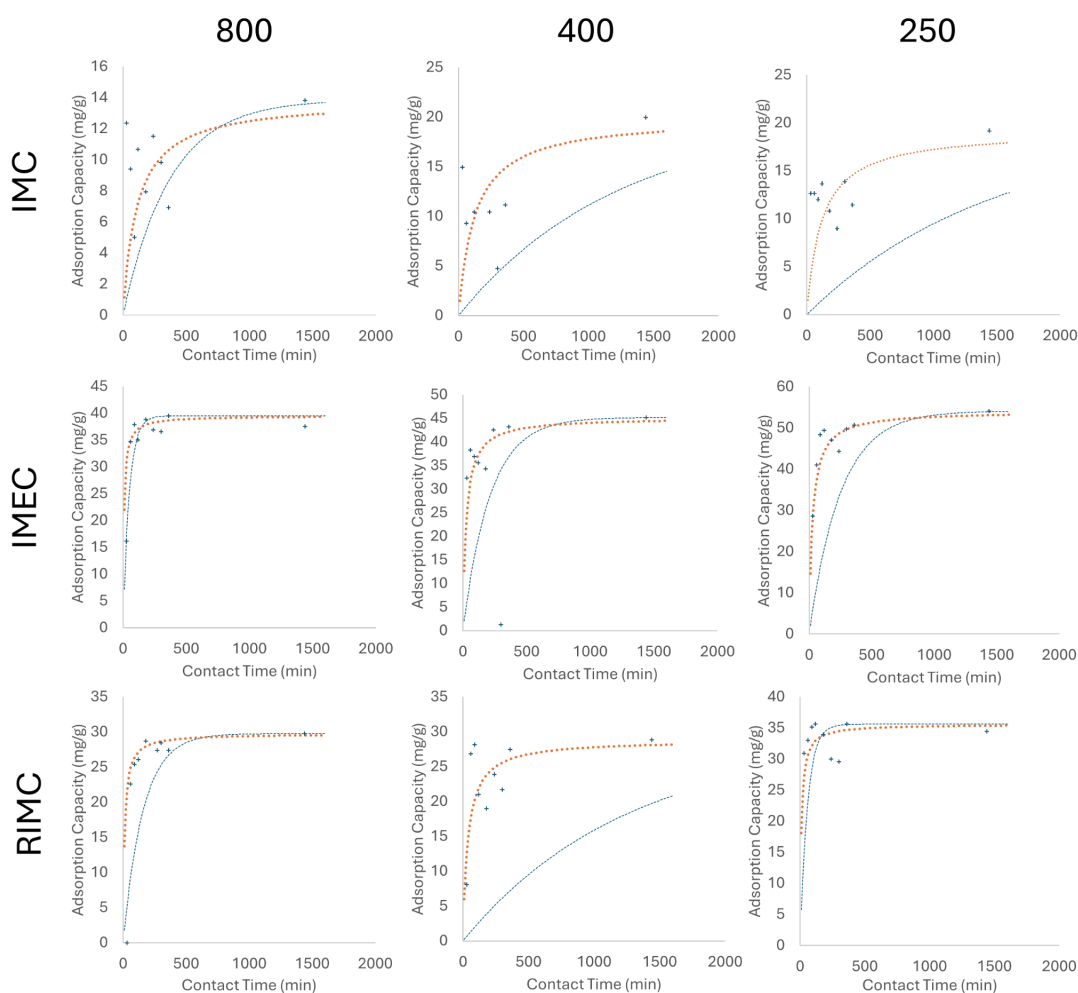


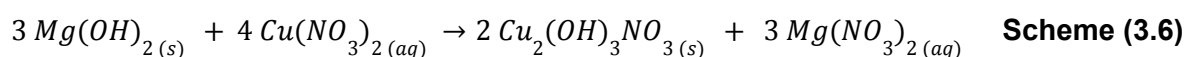
Figure 78: Copper(II) adsorption kinetics at pH 1.0 of IMC, IMEC, and RIMC (250-800).

Pseudo-first order (blue line) and pseudo-second order (orange line) kinetic models have been plotted for each material.

3.3.2. Direct copper(II) adsorption measurement

3.3.2.1. SEM-EDS

SEM-EDS analysis of the char materials post-copper(II) adsorption indicates the presence of copper on the surface of these chars and the success of copper(II) adsorption. C800 and C400 materials (excluding IMEC400) showed the formation of concentrated copper-containing structures on the surface following adsorption at pH 4. These structures were only present on materials that caused the basification of the copper solution above pH 5, and when the same materials underwent copper adsorption at pH 1 the structures no longer appeared. This is an indication that they are a direct result of basification and the precipitation of copper. These structures were rich in copper and oxygen and are likely the copper hydroxy salts recognised in the following section (3.3.2.2). The C250 materials following adsorption at both pH 1 and 4 showed a dispersion of copper across the surface which appears to favour areas where oxygen is present. This supports the hypothesis of these materials adsorbing copper via oxygen-containing functionalities such as carboxylates and sulfates. C400 and C800 materials following pH 1 adsorption display an even copper dispersion without a clear indication of an affinity towards sulfur or oxygen. Images of IMEC are visible in figure 73. IMC and RIMC images are available in the appendix 3.11 and 3.12. A feature of IMEC800 copper(II) adsorption was the interaction of the material's magnesium oxide 'barnacles' with the copper(II) solution. Post-adsorption the barnacle structures were enriched with copper and indicated that the basic magnesium oxide barnacles (magnesium hydroxide in aqueous solutions) acted as a site for adsorption. The formation of the copper salts are likely as a result of the following reaction recognised in a study by Aguirre *et al*²⁶² and are supported by the presence of copper hydroxy nitrate in the pXRD analysis of IMEC800.



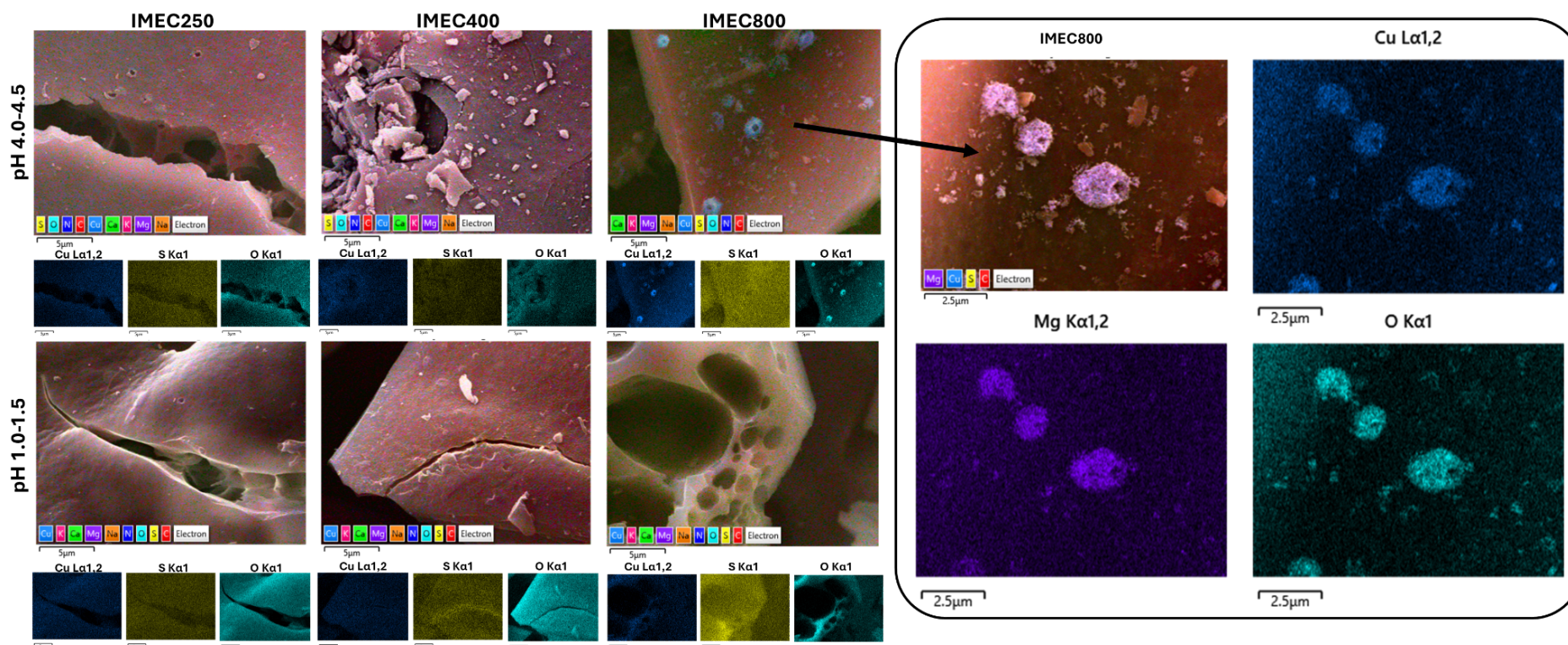


Figure 79: SEM-EDS images of IMEC materials (C250-800) following the aqueous adsorption of copper(II) from a copper nitrate solution (5000 mg/L) at pH 4 and 1 after 24h. Overlaid element maps and individual element maps of copper, sulfur and oxygen have been included. Inset are element maps of IMEC800 'barnacles' post copper(II) adsorption.

3.3.2.2. pXRD

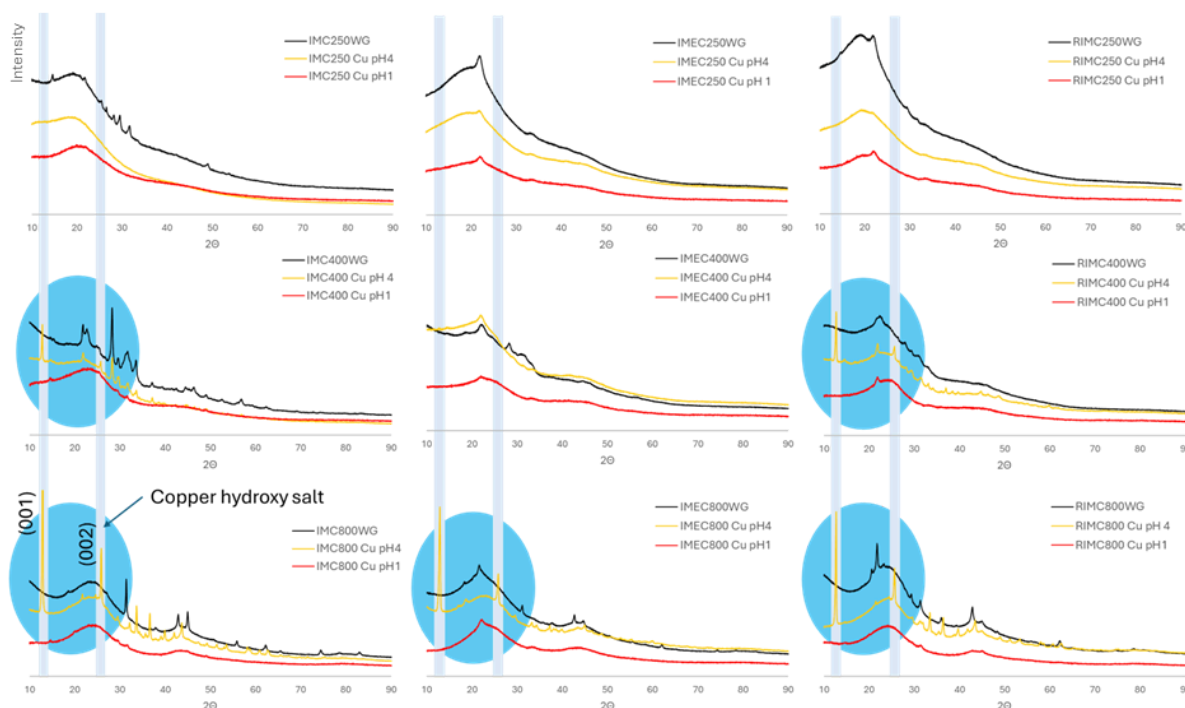


Figure 80: pXRD diffractograms of IMC, IMEC, and RIMC materials (C250-C800) before and after copper(II) adsorption at pH 4 and pH 1. (001) and (002) phases of copper(II) hydroxy salts are highlighted.

pXRD analysis of the copper-containing Irish Moss-derived materials identified the copper composites present in some of the material's SEM-EDS maps. They were identified as copper hydroxy nitrate salts ($\text{Cu}_2(\text{OH})_3\text{X}$, where X represents a variable anion in this case NO_3). The formation of these hydroxy salts are often achieved via the treatment of copper(II) nitrate with sodium hydroxide. The pH, temperature and reagent concentration are controlled to avoid copper hydroxide or copper oxide formation^{262,263}. Characteristic (001) and (002) phases of the layered structure of copper hydroxy salts were recognised in IMC400, IMC800, RIMC400, RIMC800, and IMEC800. The presence of weaker bases such as MgO or metal sulphates on these chars appears to have allowed the formation and deposition of

these salts on the surface of the material. In the case of IMC400, which is rich in sulfate anions due to retained sulphate salts, copper hydroxy sulfate was identified. Similar to C250 materials in both adsorption experiments at pH 4 and 1, the C400 and C800 materials exhibited no crystallinity due to copper following copper(II) adsorption at pH 1. In almost all cases no indication of crystallinity was recognised in these materials besides the broad phases of graphitic carbon, suggesting the increased acidity resulted in the dissolution of any remaining/trapped salt content.

3.4. Section summary

This chapter has explored the extraction, pyrolysis, and application of Irish Moss carrageenan. In these works it was recognised that the strain of Irish Moss used in this study was rich in carrageenan, accounting for up to half of the biomass' dry weight. Simple hot water extraction was sufficient to produce this extract (IME). IME exhibited no sign of protein content according to elemental analysis and the sharp loss in mass during thermogravimetric analysis, similar to that of the industry standard, indicated high carrageenan purity. Kappa and iota carrageenan were the recognised forms of carrageenan in a 2:1 ratio, respectively, which explained the ability of these extract's gelling properties and rich sulfur content. The residual Irish Moss material displayed similar characteristics to the starting Irish Moss biomass, but lacked a significant portion of carbohydrate content causing an increased nitrogen content and reduced oxygen and moisture content.

Pyrolysis of the Irish Moss-extracted carrageenan and residual fractions under variable temperatures afforded 9 different carbons. Much like the pyrolysis of other biomass materials in literature, such as pectin, starch or alginic acid ^{115,244}, a hierarchical degree of carbonisation was recognised in all three families of carbons (IMCs, IMECs, and RIMCs). At 250 °C, the materials exhibited poorer thermal stability, but higher levels of oxygen functionality such as carboxyls, carbonyls, and alcohols, which gave the materials an acidic surface. At 400 °C the materials lost much of this functionality but exhibited an increased thermal stability and porosity. Finally at 800 °C the materials were almost entirely graphitised, showing limited (phenolic) oxygen functionality on its now basic surface, and had very high thermal stability, and increased porosity.

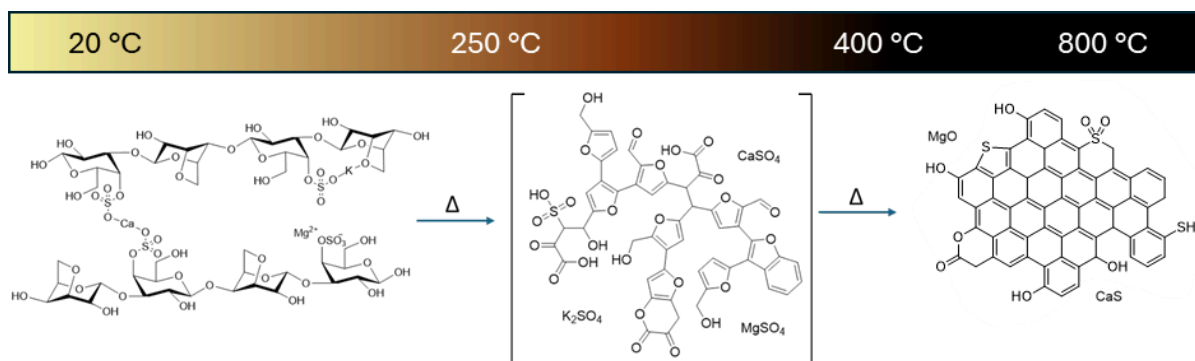


Figure 81: Chemical structure of carrageenan (left) and the proposed structures for carrageenan-derived low temperature chars (250-400 °C, centre) and high temperature chars (800 °C, right).

Sulfur-containing porous carbons were successfully produced in these works. All three chars in the carrageenan family (IMECs) exhibited sulfur content (3.9-7.6 %). This content began as sulfate functionalities in carrageenan, which were partially retained following pyrolysis at 250 °C and 400 °C. A significant portion of the sulfur content was deposited as metal salts during pyrolysis and removed during the washing process. Above 400 °C some of the sulfur content was incorporated into the chars as organic sulfur, which was evidently present in the graphitic structure by a widening of the interplanar distance in IMEC800. Without the addition of any activating agent these chars exhibited high mesoporosity with pores around 5 nm. Washed IMEC800 showed the highest surface area and pore volume at 290 m²/g and 0.18 cm³/g, respectively. One may also suggest that this porosity is aided by the deposition of sulfate salts, either by acting as a pseudo-activating agent or by leaving pores following the removal of these soluble salts.

Retained salts in the C400 and C800 materials attributed towards the basic surface of all 9 of these materials. These salts aided in the copper(II) adsorption at pH 4 via the basification of the solution and providing a surface for precipitation. IMEC800 exhibited the highest experimental copper(II) adsorption capacity (86 mg/g) at this pH which was described well by a Freundlich adsorption isotherm and followed a pseudo-second order adsorption kinetics. The formation of copper hydroxy nitrate salts at magnesium oxide sites

on IMEC800 supported this multilayer chemisorption mechanism. At pH 1 the basic sites on the chars were effectively neutralised preventing basification of the copper solution. Under these conditions IMEC250 exhibited the highest experimental adsorption capacity (54 mg/g). The adsorption was described well by a Langmuir adsorption isotherm and followed a pseudo-second order kinetic model suggesting an adsorption mechanism of a uniform chemisorption at sulfate sites across the surface.

IMC and RIMC materials exhibited both sulfur and nitrogen content, and appeared to have similar surface chemistry to the IMEC materials despite the additional nitrogen content. These materials exhibited poorer copper adsorption to IMEC materials. The key difference between these materials was the porosimetry/surface topography characteristics suggesting the increased surface area of IMEC materials was a significant factor for the increased copper(II) adsorption capacity of these materials. RIMC materials showed potential for copper(II) adsorption. Langmuir adsorption isotherm models predicted high adsorption capacities at pH 1, despite experimental values being far lower. Future work could entail the measurement of copper adsorption at higher initial concentrations to compare against the extrapolated Langmuir model predictions. However, one could debate the need for a material of this kind that only has high adsorption at high concentrations of copper(II).

These works have successfully demonstrated a simple hot water extraction of Irish Moss carrageenans, the conversion of freeze-dried carrageenan aerogels to sulfur-containing porous carbons without dopants or activating agents, and the first application of these materials to copper(II) adsorption.

Chapter 4. Valorisation of commercial microalgae

4.1. Characterisation of spray dried and EPA-free ALG01 biomass (Objective 1)

4.1.1. Preliminary compositional analysis

The preliminary composition of ALG01 and spent ALG01 is summarised in table 12:

Table 12: Summarised ALG01 composition.

	Composition (%)	
	ALG01	EPA-free ALG01
Carbohydrate^a	25.3 ± 4.0	29.3 ± 0.9
Protein^b	34.7	36.2
Moisture^c	5.1 ± 1.3	4.2 ± 0.2
Residual matter (Char)^c	24.3 ± 3.3	25.7 ± 4.3
Acid-insoluble content	28.1 ± 3.2	15.3 ± 3.9
Acid-insoluble Ash	<0.1	<0.1

^a Derived via Klason acid-digestion and HPLC analysis

^b Estimated from CHN nitrogen content using 5.1 as a conversion factor

^c Derived via TGA

4.1.2. Carbohydrate and sugar analysis

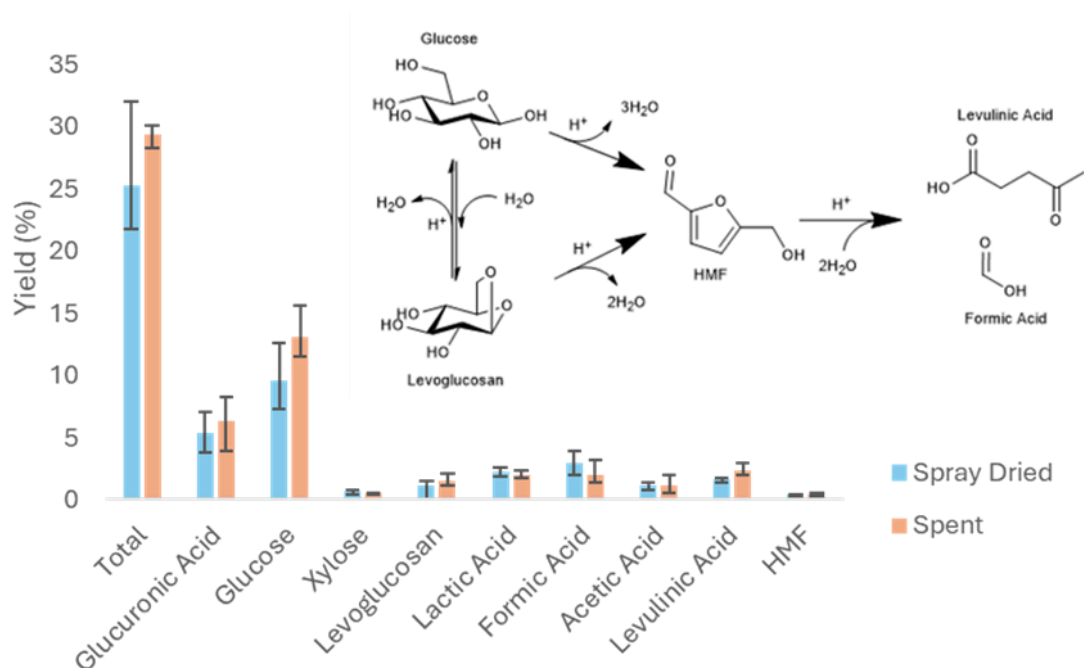


Figure 82: Acid-hydrolysed carbohydrate content of ALG01 and EPA-free spent ALG01 derived via Klason analysis. Component sugars and decomposition products are depicted and decomposition mechanism inset ²⁶⁴.

The carbohydrate content of ALG01 and EPA-free ALG01 was estimated by Klason analysis (Figure 78). An average carbohydrate content of 25.3 % was determined for this algae and 29.3 % for its spent counterpart. This increase in carbohydrate content may be attributed to lipid removal during EPA extraction. The carbohydrate content is mostly retained in the biomass during this process. One should note the carbohydrate content of ALG01 is incredibly variable, especially between different batches supplied by AlgaeCytes. As discussed in section 1.3 the metabolite content is very sensitive to minor changes in the cultivation conditions.

In both biomasses the types of monosaccharides present were predominantly glucose and glucuronic acid, contributing 35-50 and 20-25 % of the total carbohydrate

content, respectively. Glucose is the monomer constituent of structural and storage polysaccharides such as cellulose and laminarin, respectively ^{39,265}. Glucuronic acid is a common component of hemicellulose ²⁶⁶, but is also present in many storage or exo polysaccharides ²⁶⁷. Another component of hemicellulose, xylose, was also identified, contributing approximately 2 %. The remaining content was organic acids: formic, acetic, lactic, and levulinic acids, levoglucosan, and hydroxymethylfurfural (HMF). Levoglucosan and HMF form from the dehydration of sugars like glucose, and further decomposition affords these organic acids (figure 78) ²⁶⁴. The carbohydrate profile is similar between ALG01 and EPA-free ALG01, any base-catalysed hydrolysis of polysaccharides during EPA extraction is hidden following the harsh acid-catalysed hydrolysis during this analytical technique. In comparison to literature, microalgae such as *Nannochloropsis sp.* is suggested to have around 20% carbohydrate content, 60% of which accounted for by glucose and hemicellulose sugars, mannose/mannitol ⁷². This aligns well with ALG01, however, in this algae mannose/mannitol does not appear to be present in the hemicellulose content.

Klason Analysis estimated an average 'lignin content' of 28.1 and 15.3 % for ALG01 and EPA-free ALG01, respectively. Microalgae in literature often have no lignin so a fraction of this content could be pertained to algaenan or humins ^{200,268}. The cause of the difference between intact and spent algae "lignin content" is unclear. It could be associated with an acid-insoluble lipid content present in ALG01 that has been extracted during EPA extraction, although there is little literature to support this. It is unlikely that the base-catalysed process has any effect on algaenan content as this material is considered highly resistant to both acid and base hydrolysis ^{40,154,155}. Pyrolysis of the insoluble fraction afforded negligible ash content in both biomasses, indicating very little inorganic content accumulates within the insoluble material.

4.1.3. Elemental analysis (CHN)

CHN determination (2 s.f) of ALG01 revealed a carbon, hydrogen, and nitrogen content of $47 \pm 1.7 \%$, $6.6 \pm 0.20 \%$, $6.8 \pm 0.23 \%$, respectively. In comparison, EPA-free ALG01 exhibited a minor reduction in carbon (40 %) and hydrogen (5.5 %) content and an increase in nitrogen content (7.1 %).

As stated previously in section 3.1.3 a nitrogen-to-protein conversion factor of 6.25 is often a gross overestimation. Templeton and Laurens deduced nitrogen-to-protein factors for several microalgal species. Nitrogen contents of 2.6-6.8 % was determined for *Nannochloropsis* sp., and across the *Nannochloropsis* sources tested they suggested an average conversion factor was 5.1²⁶⁹. For ALG01, this is equivalent to an estimated protein content of 34.7 %, which is comparative to literature data⁷². Assuming no nitrogen content is extracted in the EPA extract, an estimated protein content of 36.2 % could be given to EPA-free ALG01. However, this may be an underestimation if non-protein nitrogen is removed during the EPA extraction process.

4.1.4. Thermogravimetric analysis (TGA)

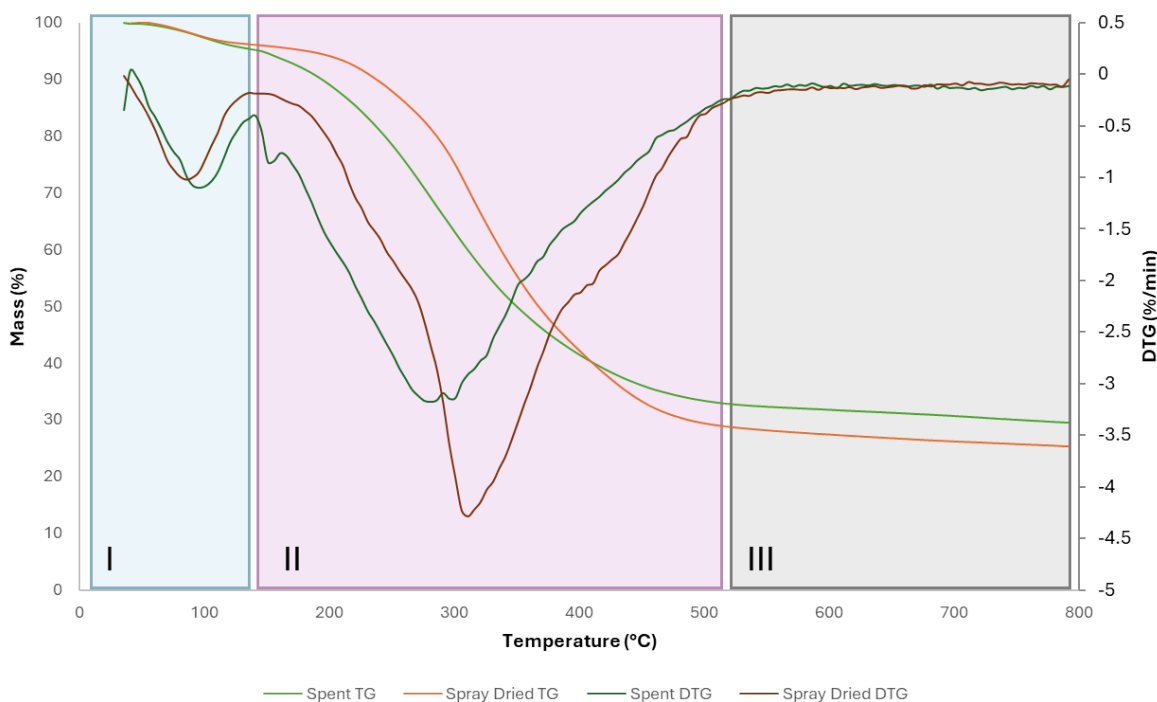


Figure 83: TGA of the dried and spent microalgae ALG01, presenting the mass lost (TG/%) as the biomass is heated from 20 °C to 800 °C at 10 K min⁻¹ under a Nitrogen atmosphere (100 mL min⁻¹ flow rate). The rate of mass loss (DTG/% min⁻¹) has been included. The 3 decomposition stages are highlighted.

Intact and spent ALG01 biomass underwent 3 main decomposition stages during TGA analysis: dehydration (stage I), devolatilization (stage II), and finally the slow decomposition of the carbonaceous char content (stage III) (figure 79). In ALG01, stage I occurs between 40 and 120 °C and has a maximum rate of mass loss (or DTG peak) around 90 °C. A shift in maxima occurs in the spent biomass towards 100 °C. This stage accounts for the moisture content and is equivalent to approximately 5 % in both biomasses.

Stage II, between 150 and 500 °C, accounts for a mass loss of approximately 60 and 70 % for the spent and intact biomasses, respectively. The difference here is once again associated with lipid removal. This stage in ALG01 has a DTG peak around 310 °C, with points of inflection at ~260 and 410 °C. From literature, carbohydrate decomposition takes

place between 150-400 °C, protein between 250-350 °C, and lipid between 310-450 °C^{154,214}. This suggests the change in the rate of mass loss at 260, 310, and 410 °C may be a result of overlapped carbohydrate, protein, and lipid decomposition, respectively. In literature, the macromolecule, algaenan, typically undergoes decomposition between 460-560 °C¹⁵⁴, and is therefore likely to undergo slow decomposition in stage III.

In EPA-free ALG01, the maximum rate of mass loss of stage II occurs at a lower temperature (285 °C). This is likely associated with the base-hydrolysis of carbohydrate and protein content during EPA extraction reducing the thermal stability of these metabolites. Furthermore, the shoulder at 410 °C is significantly reduced indicating the absence of lipid content within this biomass⁴⁵. Alternatively, any remaining fatty acid content will likely have been esterified during Algaecytes EPA extraction. The volatile fatty acid ethyl esters will likely boil before their TAG or free fatty acid counterparts, and may be lost in the bulk mass loss²⁷⁰. An unidentified additional DTG peak appears in this sample around 150 °C, likely due to liberated volatiles following base hydrolysis. The final stage above 540 °C accounts for the remaining 25.7 and 24.3 % for the spent and intact biomass, respectively, and signifies the fixed carbon or char content.

4.1.5. Attenuated total reflection infrared spectroscopy (ATR-IR)

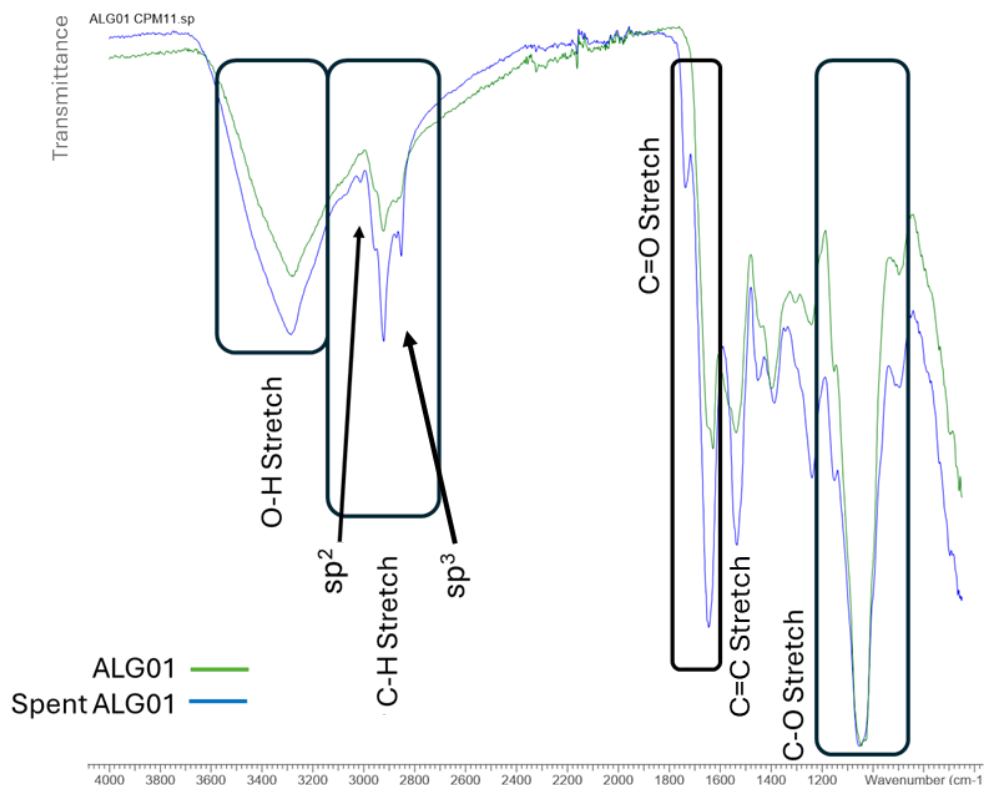


Figure 84: ATR-IR Spectroscopy of spray dried and spent ALG01.

ATR-IR spectroscopy of dry ALG01 and EPA-free ALG01 (figure 80) exhibit absorption bands at 3280 cm^{-1} associated with hydroxyl O-H or N-H stretching. Alongside C-H and C-O stretching at 2895 and 1064 cm^{-1} , respectively, these three absorption bands are characteristic of glucans. Further, hydrogen bonding between hydroxyl groups is indicated with a broad O-H absorption band. This intermolecular interaction is significant in many structural polysaccharides, such as cellulose and hemicellulose.

Unsaturated organic compounds are recognised by their characteristic C=C stretching and sp^2 hybridised C-H stretching present in this spectra at 1646 cm^{-1} and 3013 cm^{-1} , respectively. Neighbored with carbonyl stretching at 1738 cm^{-1} , these absorption bands could be associated with PUFA content. These absorption bands are significantly reduced in EPA-free ALG01, especially the carbonyl stretch which is absent, further evidencing lipid absence in this biomass.

4.2. Supercritical CO₂ extraction of lipids (Objective II)

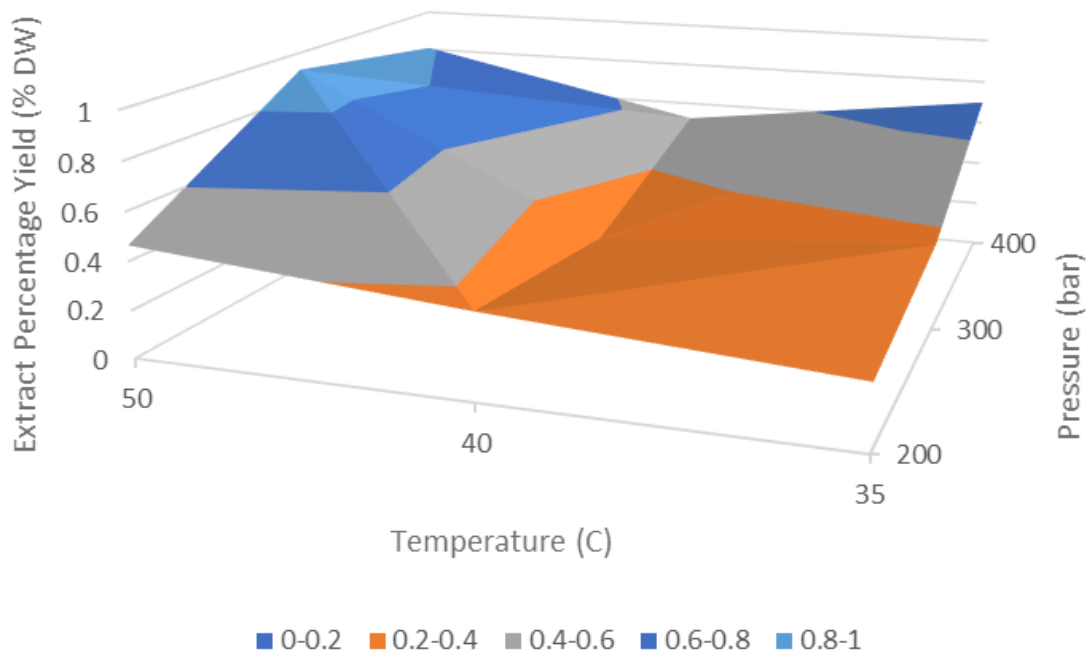


Figure 85: Variation in supercritical CO₂ extract yield from the microalgae, ALG01, at various temperature and pressure extraction conditions.

An increase in yield was observed at the highest extraction temperature (50 °C), however, increasing extraction temperature did not consistently increase extraction yield. In the high-pressure extractions (400 bar) the temperature appeared to have minimal effect on the yield. There was, however, significant overlap in the extractive yields across the varying extraction conditions. Only the low-pressure extracts had consistent data, showing low yields of around 0.3-0.6% DW. The low yields of this extraction method compared with literature, suggests a significant portion of the lipid content in ALG01 is polar and has poor affinity towards this non-polar solvent. This is evident in comparison to solvent extractions. Ethanol and heptane extractions yielded approximately 25% and 6%, respectively (see appendix 4.1). The poorer supercritical CO₂ yields may also be attributed to the resistant nature of algal cell walls preventing efficient extraction of lipid material ²⁷¹.

The nitrogen content is negligible across all extracts (<0.5% nitrogen). As expected, this supercritical fluid has little affinity towards proteins, and hence they are absent in these extracts. The extracts exhibited similar carbon and hydrogen contents at around 70 and 10%, respectively. H/C ratio ranges between 1.7 and 2.1. Comparatively, *n*-Octane has a ratio of 2.25, suggesting these oils have potential applications as fuels. However, the extract yields are significantly low and it is expected that the composition of these oils have higher value in nutrition, cosmetics, or pharmaceuticals.

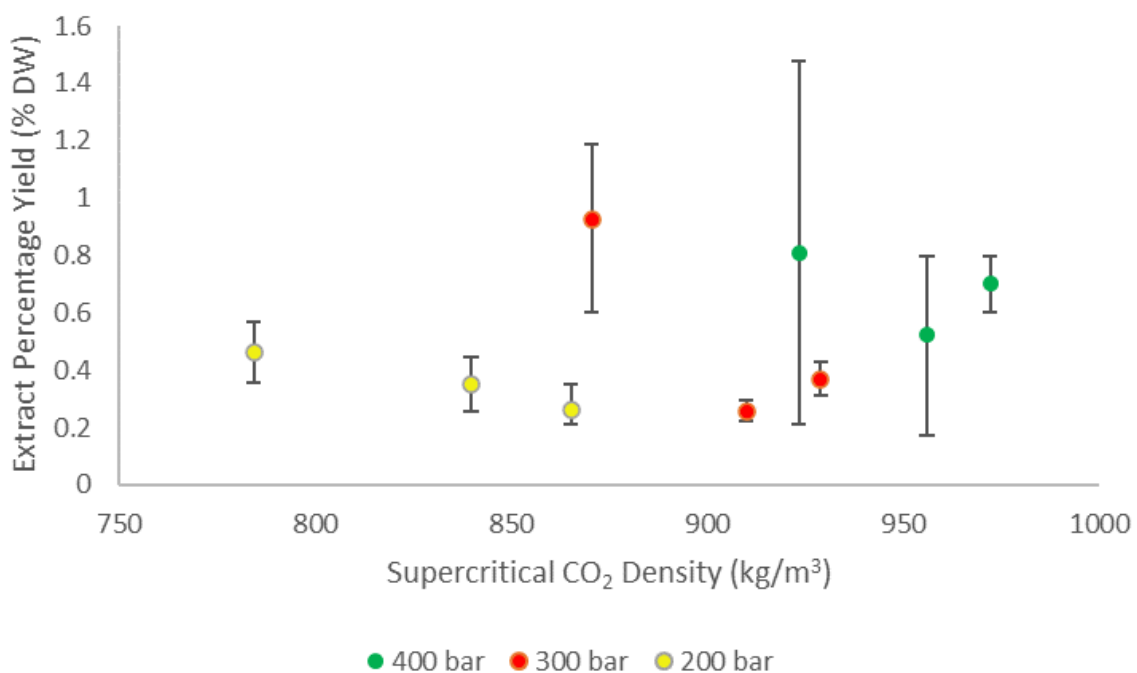


Figure 86: The effect of supercritical CO₂ density on the extractive yield from a 2h extraction from the microalgae, ALG01.

4.2.1. UV-vis spectroscopy

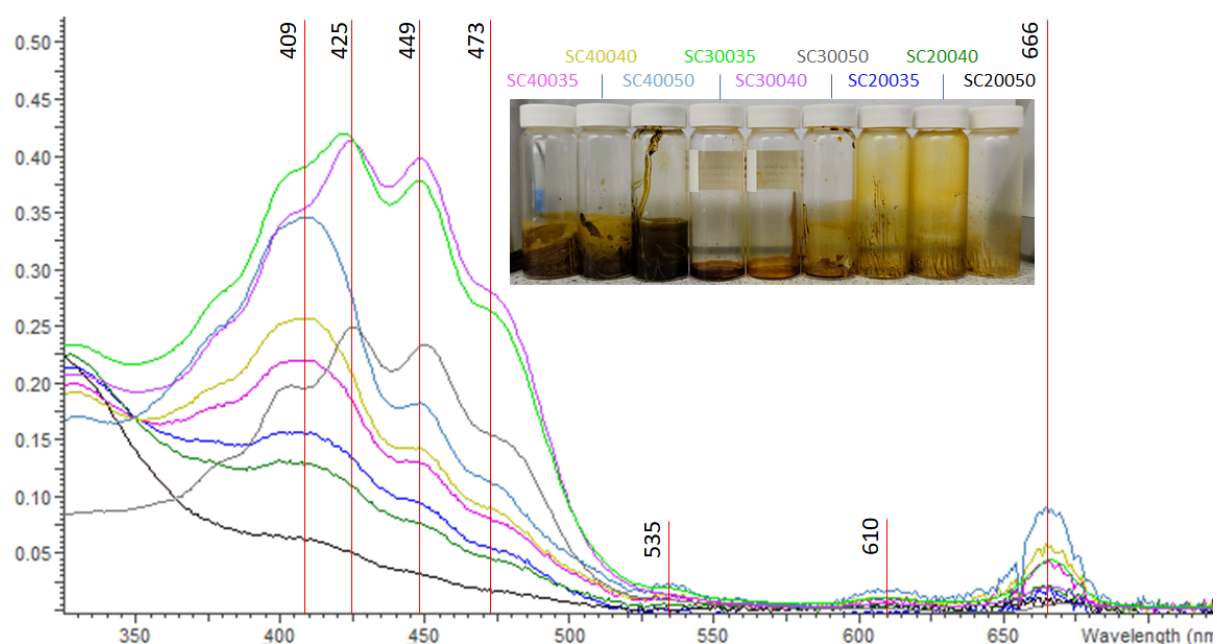


Figure 87: UV-vis absorption spectra of the supercritical extracts (200–400 bar and 35–50 °C) from ALG01 after a 2-hour extraction (focused specifically on the region 325–725 nm). The extracts are dissolved in ethanol at a concentration of 0.1 mg mL⁻¹. Intense characteristic Chlorophyll and Carotenoid absorption bands are visible in 400 bar and 300 bar extracts, respectively.

The appearance across the range of extraction conditions indicated a change in extract pigment composition. From 200 to 300 to 400 bar, the colour of the extracts turned from yellow/brown to red/brown to green/brown, respectively. The red/brown hue of the extracts deepened from 50 to 35 °C (figure 83). The consistency of the oils also varied. High pressure extracts (400 bar) exhibited solid waxy oils, whereas those of lower pressure were thinner viscous liquids.

UV-vis spectra suggest carotenoid and chlorophyll-like content in some of the extracts. The UV-vis spectra of chlorophyll a in literature is recognised by characteristic Soret (430 nm) and Q_y (610 and 661 nm) bands (in ethanol). Carotenoids are similarly identifiable by a 'triplet' of absorption bands (I, II, III) between 400 and 500 nm. The intensity

and wavelength in which the bands appear vary depending on the specific carotenoid ²⁷². Violaxanthin (419, 440, 470 nm), vaucheriaxanthin (420, 442, 470 nm), canthaxanthin (474 nm), astaxanthin (478 nm), and β,β -carotene (425, 450, 477 nm) have been identified in *Nannochloropsis* ^{141,273}, and each could be attributed to the 425, 449, and 473 nm absorption bands present in some of these extracts.

Figure 83 collectively displays UV-vis spectra of the supercritical extracts. SC400 extracts exhibited absorbances at 409 and 666 nm, indicating chlorophyll-derivative presence. In these samples the Soret absorption band has undergone a hypsochromic (blue) shift (-21 nm) and the Q_y band a small bathochromic (red) shift (+5 nm). This transition could suggest the conversion of chlorophyll to pheophytin, by loss of its magnesium centre, a process caused by acidification, heat, or light exposure ^{274,275}. Borello *et al* explored the evolution of chlorophyll a into pheophytin a by UV-vis in the presence of acetic acid (pH 4), and recognised a complete conversion after 166 min ²⁷⁴. Supercritical CO₂ is inherently acidic in the presence of water due to the formation of carbonic acid (pK_{a1} 6.4, pK_{a2} 10.3) ²⁷⁶. Considering the moisture content of the biomass, the extraction process may be responsible for chlorophyll degradation.

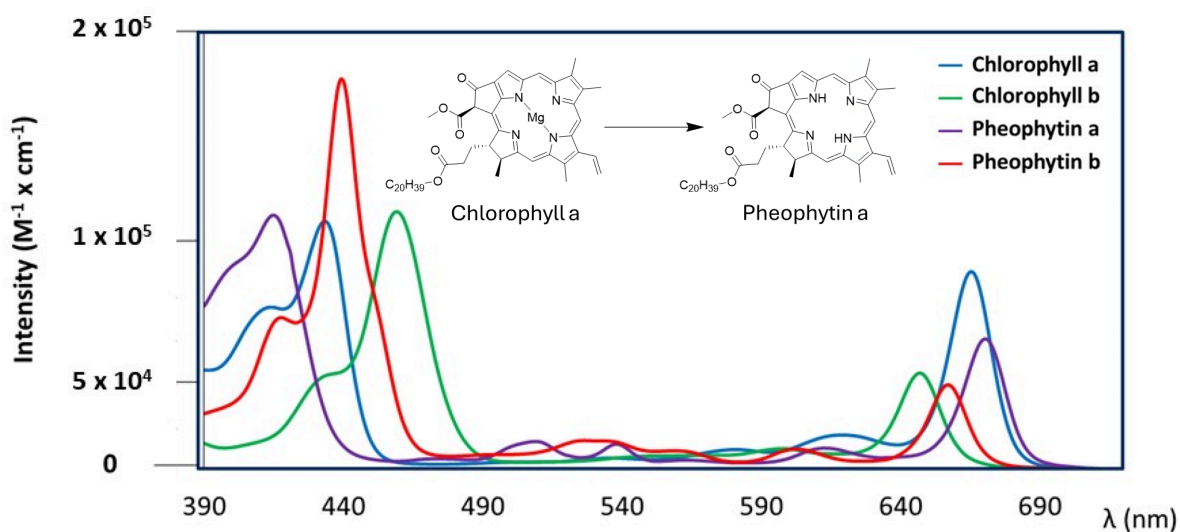


Figure 88: Literature UV-vis spectra of chlorophyll a/b and their respective pheophytin ²⁷⁴

The SC300 extracts also exhibited the absorption bands of chlorophylls, however, these were a minor component of the overall UV absorption of these extracts. The highest intensity absorbances of the SC300 extracts were at 425 and 449 nm, characteristic of the carotenoid materials mentioned earlier ²⁷². The SC30040 and SC30035 extracts had the greatest intensity of these carotenoid bands, whereas those of the SC30050 and SC400 extracts were less intense. In fact, the 425 nm band is absent or hidden in the SC400 extracts. Further, many of the bands exhibit shifts in the absorbance wavelength: SC30050 exhibits a blue shift and red shift of the 409 and 449 nm bands, respectively. Additionally, SC30035 exhibits a blue shift of the 425 nm band. This could indicate variation in the carotenoid profile, or simply the presence of compounds interfering with the π to π^* transition responsible for these absorption bands.

The UV-vis spectra of the SC200 extracts, however, suggested little chlorophyll or carotenoids, with their major absorption band between 250 and 350 nm in the near-ultraviolet region, likely due to saturated fatty acids ²⁷⁷.

These results suggest that the supercritical extraction conditions are selective of the pigments extracted from the microalgae. The increased pressure of the SC400 extraction conditions appear to favour chlorophyll/pheophytin solubilisation and extraction. Whereas, the 300 bar extraction conditions favour carotenoid extraction instead. Increased extraction temperature, however, has a negative effect on extraction of carotenoids, but a positive effect on the extraction of chlorophylls/pheophytins.

4.2.2. Gas chromatography-mass spectrometry (GC-MS)

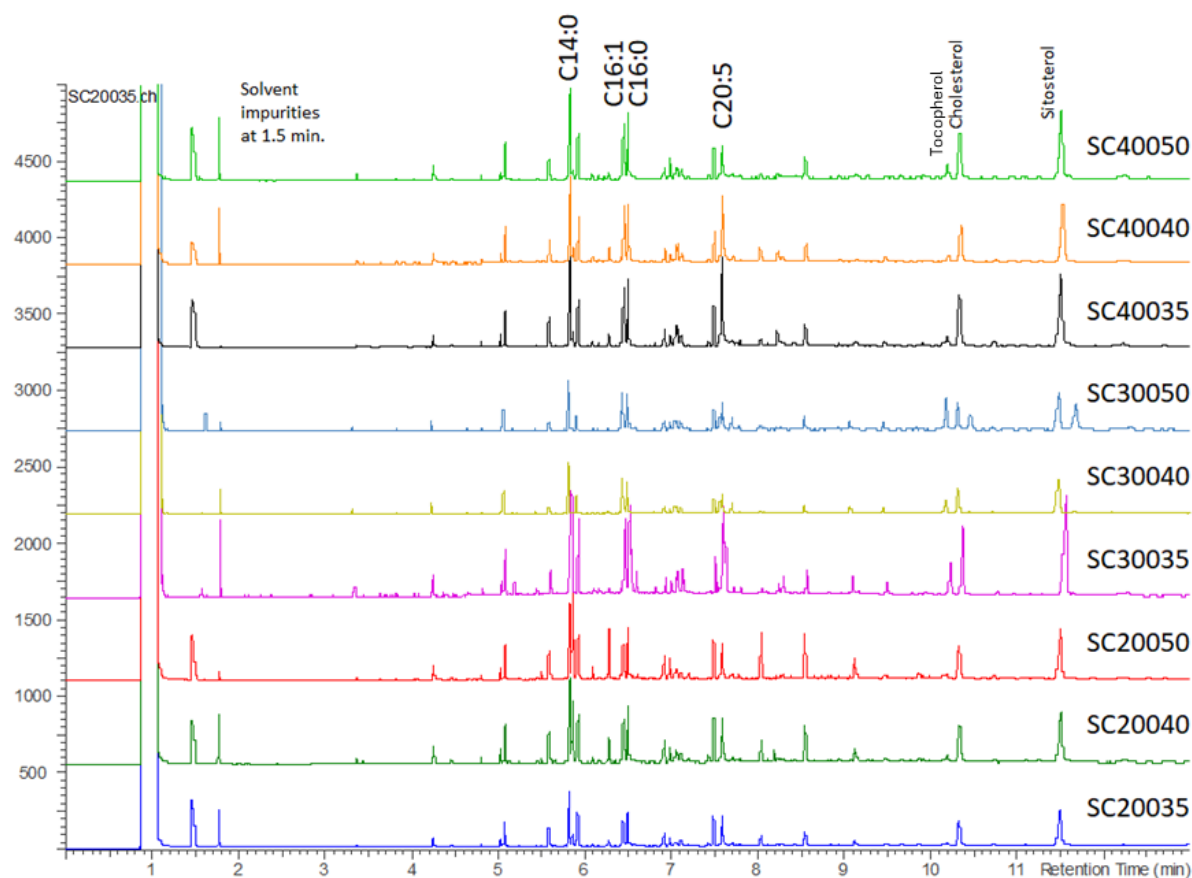


Figure 89: GC spectra of supercritical extracts SC(200-400)(35-50). Compounds with a high probability (>50%) MS match with NIST library data have been labelled. Major FFA and sterol components were identifiable by GC-MS. Sample concentrations vary between 10-25 mg mL⁻¹.

In the supercritical extracts, 4 major FFAs were identified with good certainty by GC-MS: myristic (C14:0), palmitoleic (C16:1), palmitic (C16:0), and EPA (C20:5). This aligns well with the *Nannochloropsis* lipid profile seen in literature¹⁴³. EI mass spectra of myristic and palmitic saturated fatty acids exhibited a series of oxygen-containing (m/z 45 [COOH]⁺, 59 [CH₂COOH]⁺, etc.) and alkyl fragments (29 [C₂H₅]⁺, 43 [C₃H₇]⁺, 57 [C₄H₉]⁺, etc.), as well as characteristic McLafferty rearrangement m/z 60 peak (figure 86)¹⁵⁸. The molecular ion and retention time were key distinguishing characteristics between these fatty acids.

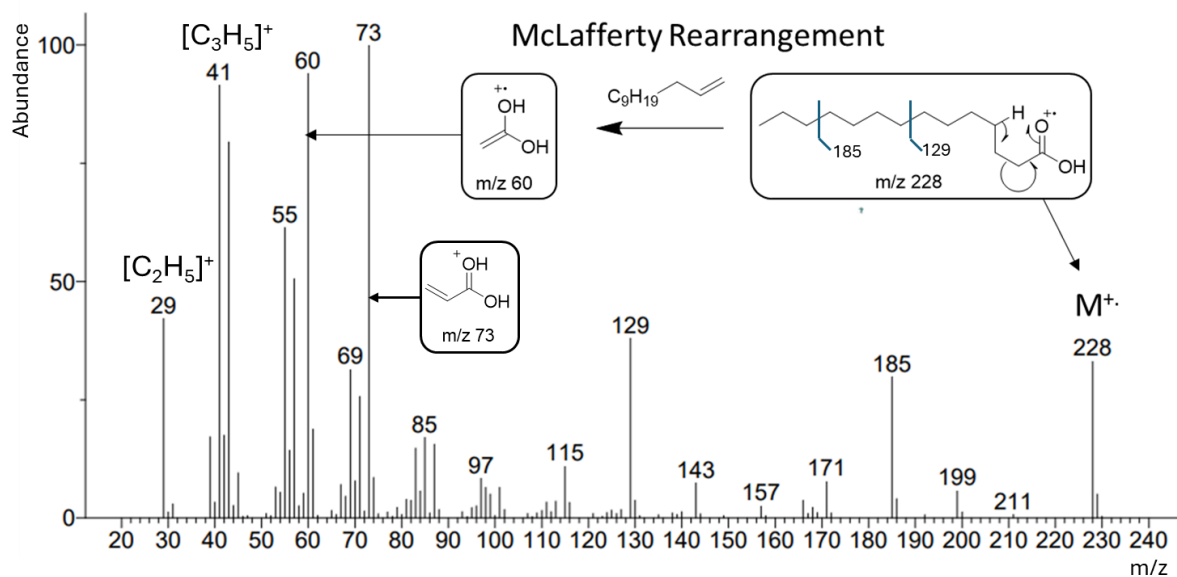


Figure 90: Mass Spectrum of myristic acid (C₁₄:0) from ALG01 extract (85.2% similarity with library fragmentation fingerprint).

Highly unsaturated fatty acids tend to have a molecular ion peak with low intensity due to instability and fragmentation. In some cases [M-18]⁺ ions from the loss of water are common fragments which can help identify these molecules. However, underivatized fatty acids of this kind have few distinguishable features to locate double bond positions. Detection of EPA or DHA is particularly difficult by mass spectra, therefore the retention times of commercially available standards were used to identify these fatty acids (EPA: 7.58 min, DHA: 7.95 min); although no extract exhibited DHA presence.

All extracts exhibited myristic acid as their primary fatty acid component. Its GC peak was often shouldered by an unidentified compound eluting around 5.95 min. The ratio of these free fatty acids shifted with the variation in the extraction conditions. EPA exhibited a large variation across supercritical extraction conditions. At higher supercritical fluid densities SC40035, SC40040, and SC30035 (~972, 956, 929 kg m⁻³, respectively) the myristic acid to EPA ratio is around or just under 1:1. Below 925 kg m⁻³ the ratio is >2:1 (Myristic:EPA). This suggests high CO₂ density favours an EPA richer extract. Palmitic and palmitoleic acids were extracted in a fairly consistent ratio with myristic acid, similarly the compound at 5.1 minutes

was also extracted in a consistent manner. Three unidentified compounds, eluting at 7.5, 8.0 and 8.5 minutes were significant in the 200 bar extracts. They appeared to favour low density scCO₂ conditions gradually increasing in intensity from 35 to 50 °C.

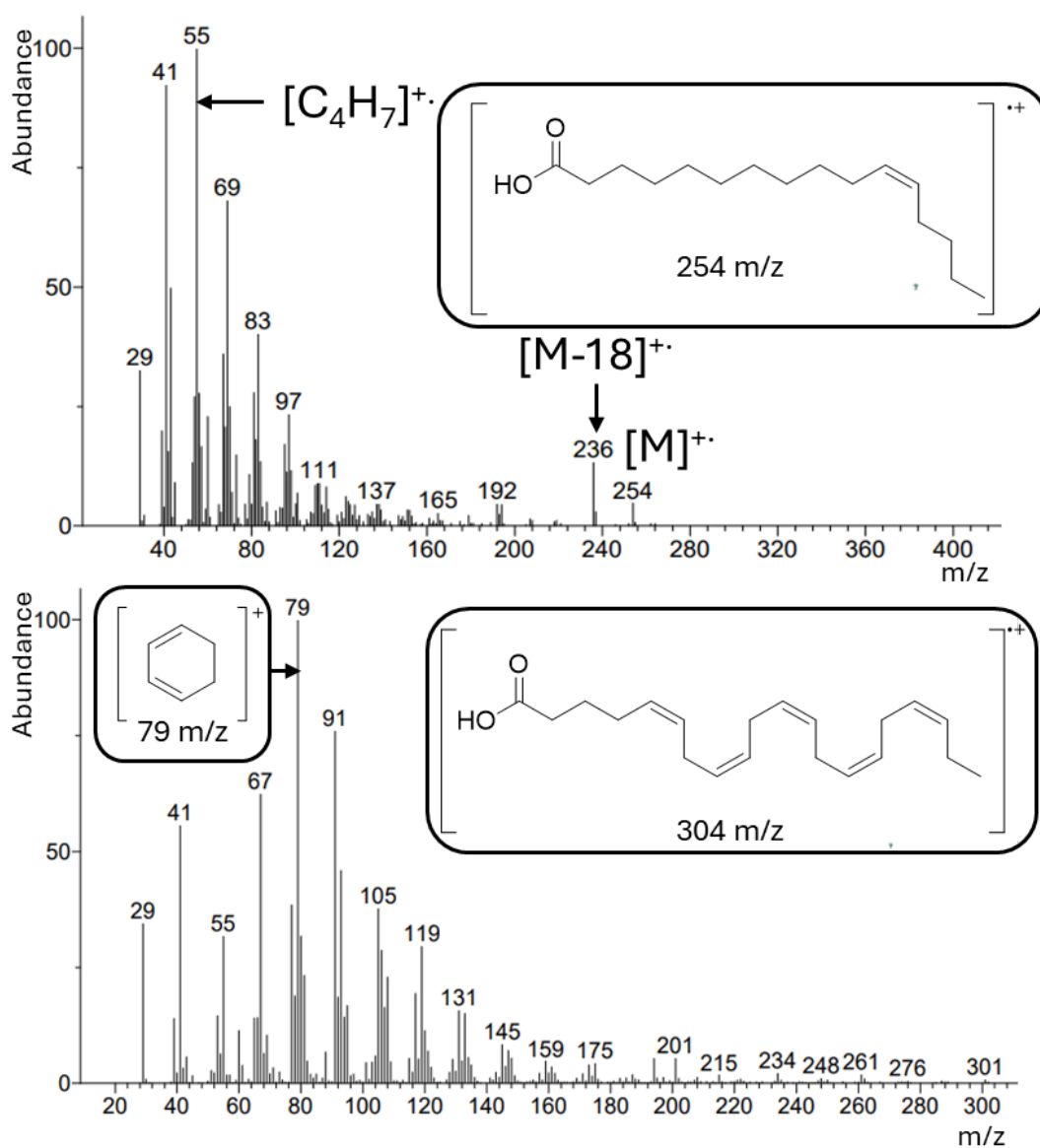


Figure 91: Mass Spectrum of palmitoleic acid (C16:1, top) and EPA (C20:5, bottom) from ALG01 extract (49.7% and 35.8% similarity with library fragmentation fingerprint).

Other metabolites detected via GC-MS include phytosterols: cholesterol (10.4 min) and γ -sitosterol (11.5 min), and in very small quantities, terpenes: neophytadiene (6.1 min) and phytol (7.0 min). These lipids are commonly found in *Nannochloropsis* and other

microalgae ^{271,278}. In the SC300 extracts, additional compounds eluted after 10 minutes accompanying the identified sterols. A compound eluting at 10.2 minutes is present in almost all extracts, and in SC30050 it is a considerably major component. The corresponding MS spectra suggests that this compound is α -tocopherol, characteristic 430 m/z molecular ion and 165 m/z fragments, is supported in literature ²⁷⁹. Proton NMR of SC30050 also exhibited significant aromatic proton environments which further indicates phenolic presence (figure 94).

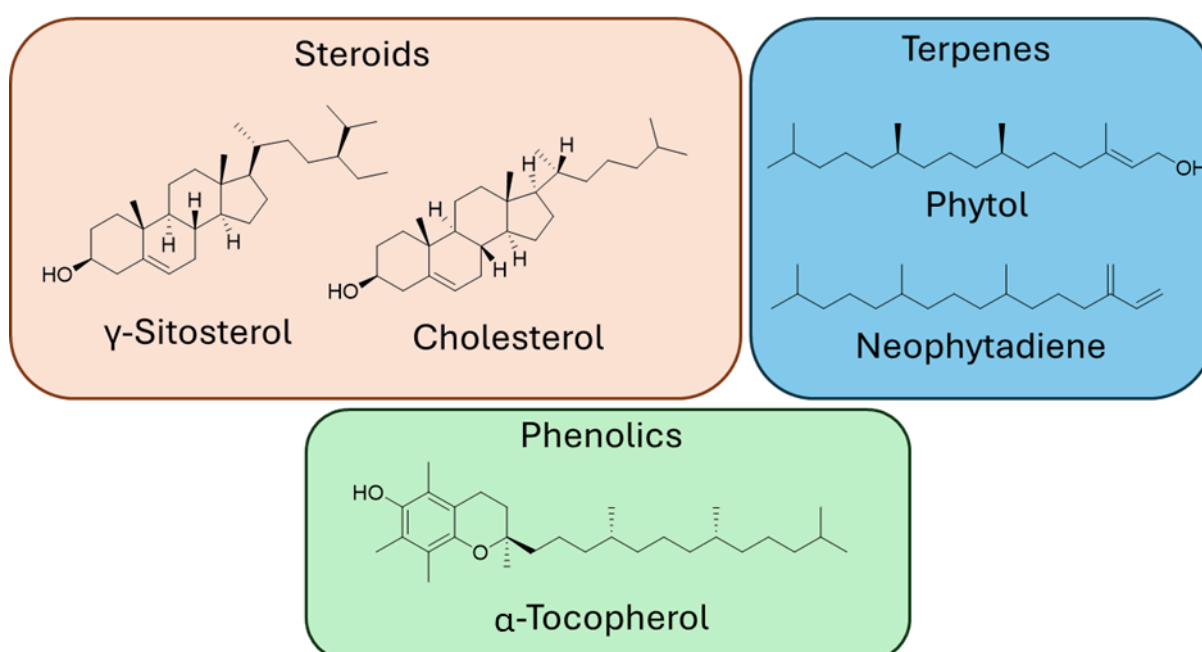


Figure 92: Chemical structure of identified steroids, terpenes and phenolics in supercritical CO₂ extracts.

These microalgal extracts are a complex mixture of lipids. In contrast to typical sharp peaks of typical proton NMR these spectra often contain broad bands of compiled proton environments. NMR spectroscopy of these extractives utilising ¹H, ¹³C, HSQC, and HMBC provided supporting evidence of lipid material. Vinylic carbon and hydrogen environments are characteristic of PUFA content, as well as carotenoids and chlorophyll. Alcohol and oxygen-adjacent protons present between 3.5 and 4.5 ppm, could be associated with fatty

alcohols. Further, prominent alkyl environments suggest long chain hydrocarbons, associated with most lipids.

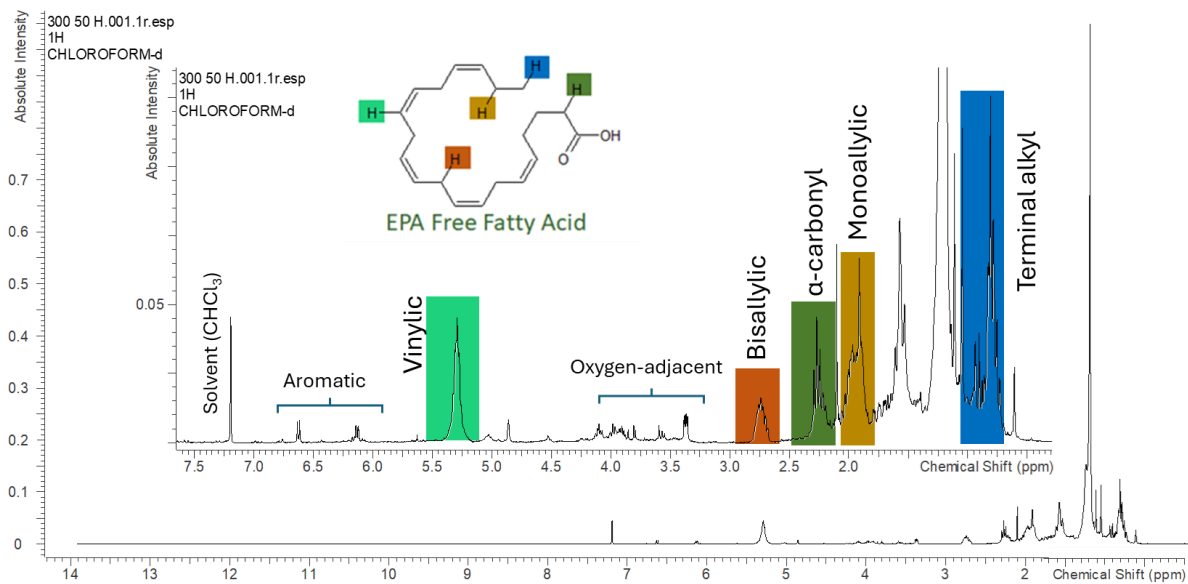


Figure 93: 300 MHz ^1H NMR spectra of a supercritical CO_2 extract from ALG01 in Chloroform-d. Major signals have been labelled using HSQC and HMBC spectra. Highlighted are hydrogen environments and the corresponding proton in the fatty acid, EPA, these environments are also common in many other PUFAs.

4.2.3. ATR-IR spectroscopy

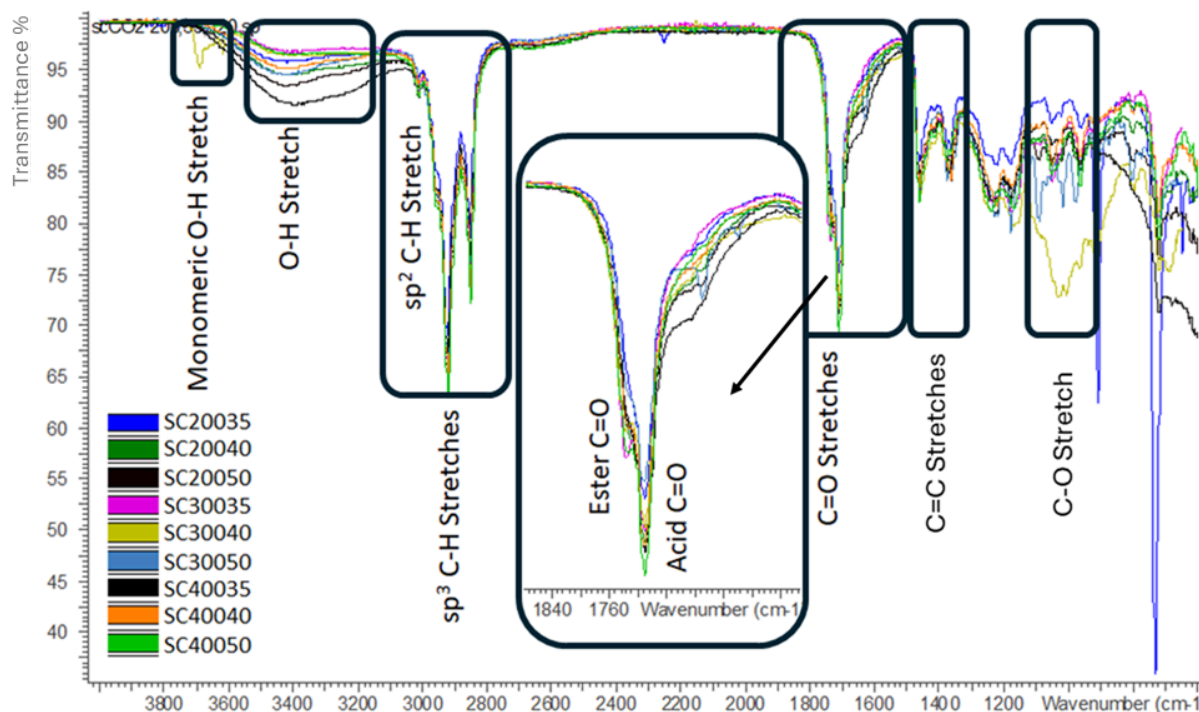


Figure 94: FT-IR spectra of the dried supercritical extracts (200-400 bar and 35-50 °C) from ALG01 after a 2-hour extraction. Inset shows zoomed carbonyl region.

Evidence of fatty acid presence was supported by ATR-IR spectroscopy. Carbonyl C=O stretching of acid and ester functional groups was prevalent in all extracts, coupled with C-H stretching around 2900 cm^{-1} . Sp^2 hybridised C-H stretching and C=C stretching supports the presence of unsaturated alkene environments of PUFAs. Further, an absorption band appears in some extracts that shoulders the carbonyl stretching around 1680-1700 cm^{-1} . This could potentially be assigned to a conjugated carbonyl. Broad O-H stretching was evident in most extracts, however, only one extract, SC30040, exhibited monomeric (free) O-H stretching. This may be attributed to phenolics or xanthophylls, present in these extracts. In this same extract C-O stretching was also prominent.

4.2.4. Antioxidant activity: TPC, TFC, and FRAP assay

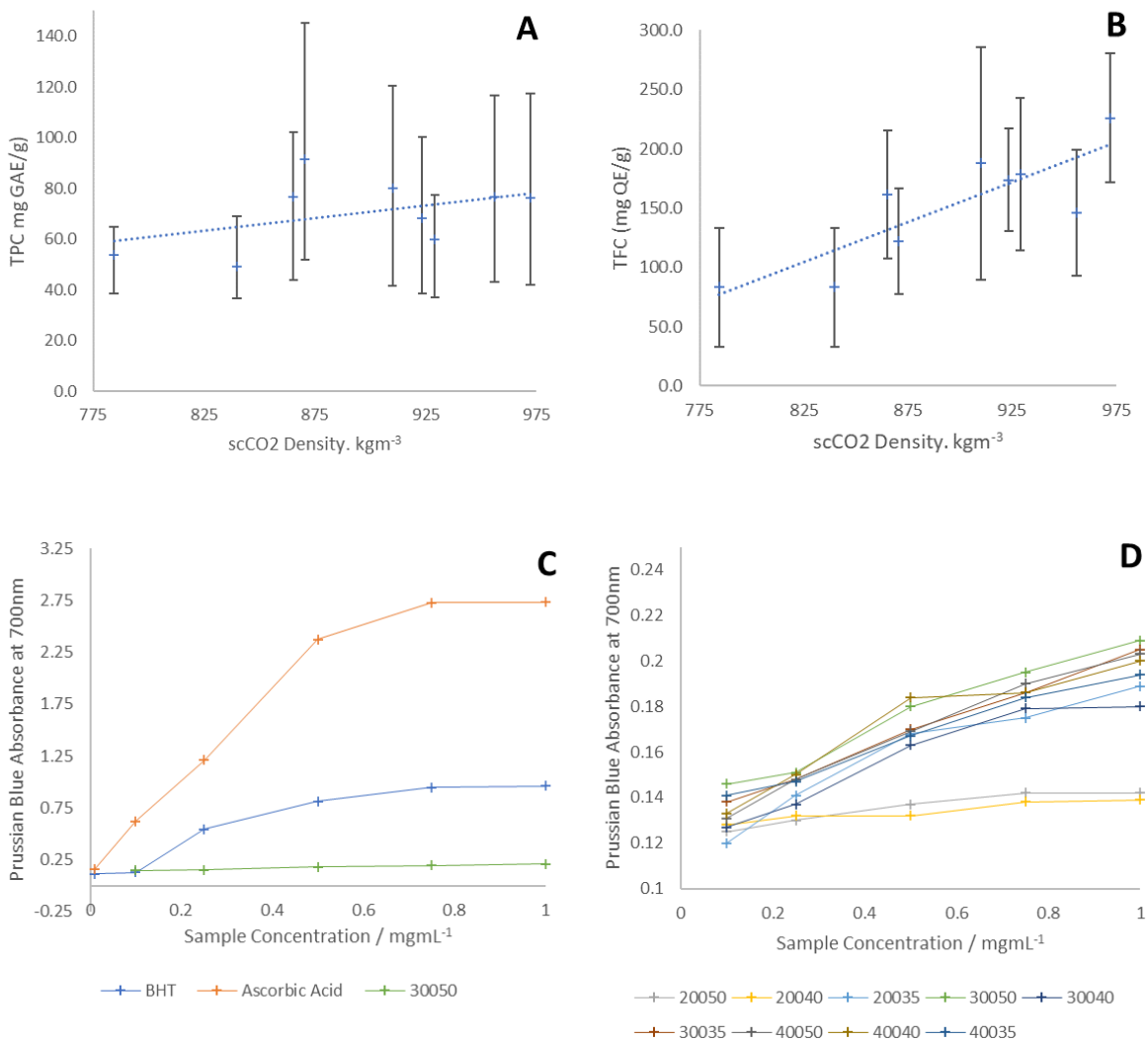


Figure 95: Antioxidant activity of supercritical CO₂ extracts from ALG01 using varying extraction conditions. Figures A and B show the effect of supercritical CO₂ density on the TPC and TFC of the supercritical extracts, respectively. Figure C and D show the ferrous reducing power of the supercritical CO₂ extractives in comparison with known strong antioxidants, BHT and Ascorbic Acid.

Total phenolic content (TPC) and total flavonoid content (TFC) are useful for determining antioxidant properties of biomass extracts as these phytochemicals are common antioxidants found in plant materials. TPC is determined using the Folin-Ciocalteu (F-C)

method. In alkaline solutions the F-C reagent (FCR) is reduced by phenolic compounds, which is recognisable by the formation of a blue complex (765 nm). Compared to a known phenolic standard, often gallic acid, the TPC is expressed in gallic acid equivalents²⁸⁰. TFC is deduced via aluminium chloride colorimetric assay. The absorbance of the flavonoid-aluminium chloride complex formed during this experiment is variable dependent on the flavonoid. Quercetin is a common flavonoid standard for TFC determination and its complex exhibits a maximum absorbance around 420 nm^{280,281}.

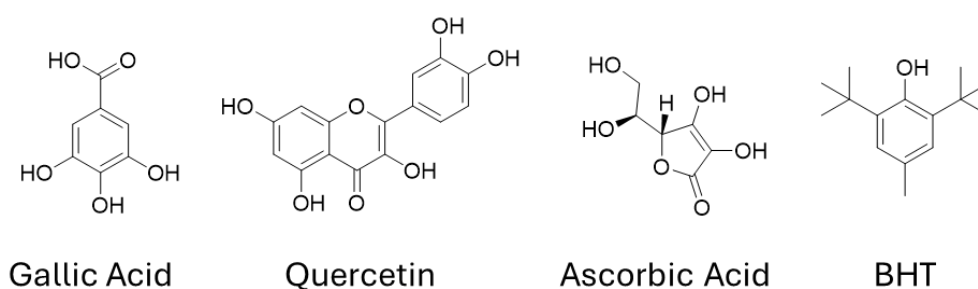


Figure 96: Chemical structure of TPC, TFC and FRAP standards, gallic acid, quercetin, ascorbic acid, and BHT.

TPC and TFC of the supercritical CO₂ extractives will be expressed in gallic acid (GAE) and quercetin (QE) equivalents, respectively. These extractives contained between 40 and 140 mg GAE/g with the maximum achieved using 300 bar and 35 °C supercritical extraction conditions. No clear trend between extraction conditions and TPC of the extractives was observed due to large overlaps in the TPC repeat tests. TFC tests, however, indicated a gradual increase in the presence of quercetin equivalent compounds in the extractives with supercritical CO₂ density of the extraction, despite similar overlaps in the repeat tests. A maximum TFC content was observed in the 300 bar, 40 °C supercritical CO₂ extract (285 mg QE/g). Supporting these tests, proton NMR spectroscopy of these extractives revealed weak aromatic signals between 6.0 and 7.7 ppm (figure 94). Phenolic

and Flavonoid compounds have been recognised in many algal species and their presence in lipid extracts is not unfamiliar in literature ²⁸².

Ferric reducing antioxidant power or FRAP assay is one of many methods of determining the antioxidant activity of a compound. Potassium ferricyanide, the ferric reagent used in this assay, undergoes reduction to form Prussian blue which is quantified by spectrophotometry (see figure 93) ²⁸³. The quantity of iron(III) chloride must be limited to avoid the precipitation of Prussian blue. For comparison FRAP assay was performed on known antioxidants, ascorbic acid (vitamin C) and butylated hydroxytoluene (BHT).

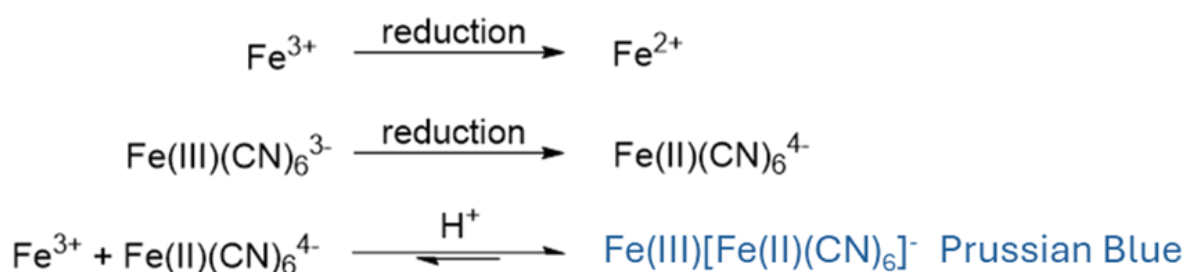


Figure 93: Reaction scheme for the formation of Prussian Blue from ferricyanide and iron(III)

283

The supercritical CO₂ extracted lipids exhibited antioxidant activity via FRAP assay, specifically those extracted under 300 bar and 50 °C conditions. At 1 mg/mL this extract revealed equivalent antioxidant power to BHT at 0.1 mg/mL. However, the extracts produced via supercritical extraction conditions of low pressure and high temperature; otherwise recognised as low density supercritical fluids, resulted in poorer antioxidant power. The high antioxidant activity could be explained by the suggested presence of phenolics and flavonoids in these extracts, but also due to the presence of unsaturated fatty acids (C16:1 and C20:5) and carotenoids, which too have antioxidant properties.

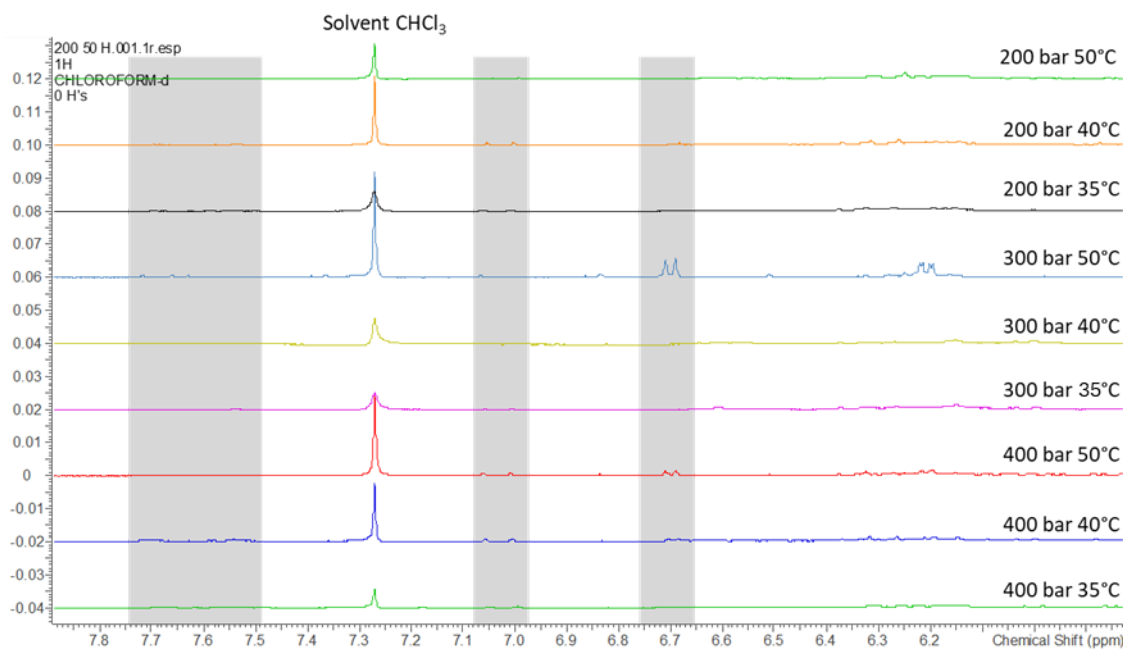


Figure 98: Cropped 300MHz 1H NMR spectrograms of various supercritical CO₂ extracts in chloroform-d. Highlighted are weak aromatic proton signals at 6.70, 7.00-7.05, and 7.50-7.70 ppm.

4.2.5. Differential scanning calorimetry (DSC)

The extracts tended to become more solid and waxy from higher pressure and lower temperature extractions or as the density of the supercritical fluid increased. DSC analysis of the extracts revealed that the extracts were composed of a complex mixture of materials. Melts and crystallizations were typically broad across all samples.

First heat-cool cycles (Figure 95) showed the presence of thermally labile material in SC30050 and SC40040, as an irreproducible exothermic transition was observed between 80-110 °C in both samples. The presence of chlorophyll suggested by UV-vis spectroscopy could explain the presence of this transition in SC40040. Literature decomposition of chlorophylls is around 117-130 °C²⁸⁴, however, in the presence of a complex mixture the melt/decomposition is likely to have been reduced to lower temperatures.

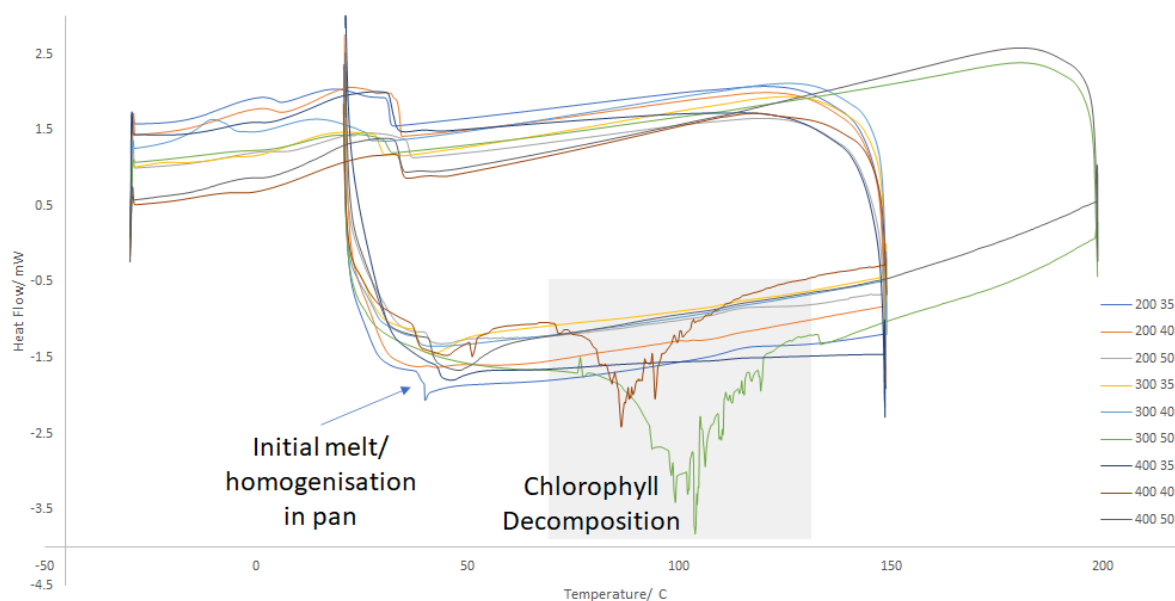


Figure 99: DSC spectra showing the 1st heat-cool cycle of supercritical extracts SC(200-400)(35-50). An irreproducible exothermic transition at 80-100 °C in SC30050 and SC40040, suggest the thermally labile presence of chlorophylls.

Second and third heat-cool cycles (Figure 96) showed 2 main melts and corresponding crystallisations in all extracts. Generally as the extracts are heated from -30 °C the extracts begin to melt. The first melt peak (m^1) appears between 0 and 10 °C, which could be attributed to the unsaturated fatty acids. In literature, palmitoleic and linoleic acid melt just below 0 °C²⁸⁵. EPA melts at -53 to -54 °C, therefore it is unlikely this study's experimental range will exhibit a transition associated with this lipid. The second melt (m^2) occurs between 20 and 40 °C. Despite aligning closer in literature with lauric acid (m_p 44 °C)²⁸⁵, this transition m^2 is likely due to abundant fatty acid, myristic acid melting which will have been shifted from around 54 °C to lower temperatures due to its low purity²⁸⁶. The sample continues to melt slowly until around 110 °C, no further noticeable transitions occur up to 150 °C (or 200 °C in SC40050 and SC30050 extracts). Upon cooling a rapid first crystallisation (r^2) occurs around 35 °C (between 29 and 37 °C across all samples) corresponding to the

second melt and a following second slower crystallisation transition (r^1) occurs between 0 and 10 °C corresponding to the first melt.

The peak of these transitions shift depending on the extract. The lower pressure extracts tend to show first melts at higher temperatures than those of the high pressure extracts. The lower pressure, 200 bar extracts are assumed to contain 'solely' fatty acid material, this higher purity could explain this transition. The ratio of the first melt in comparison to the second melt also varied across the extracts with the first melt being more prevalent in the SC20035, SC20040, SC300 35, and SC30040 extracts. These extracts are not necessarily enriched in unsaturated fatty acids that have been associated with this melt, however, unidentified compounds in these extracts could be responsible also. The second melt also varied across the extracts, however, a trend was not recognised. In the high pressure extracts (SC400) an additional melt (m^3) and recrystallisation (r^3) was observed around 45 °C.

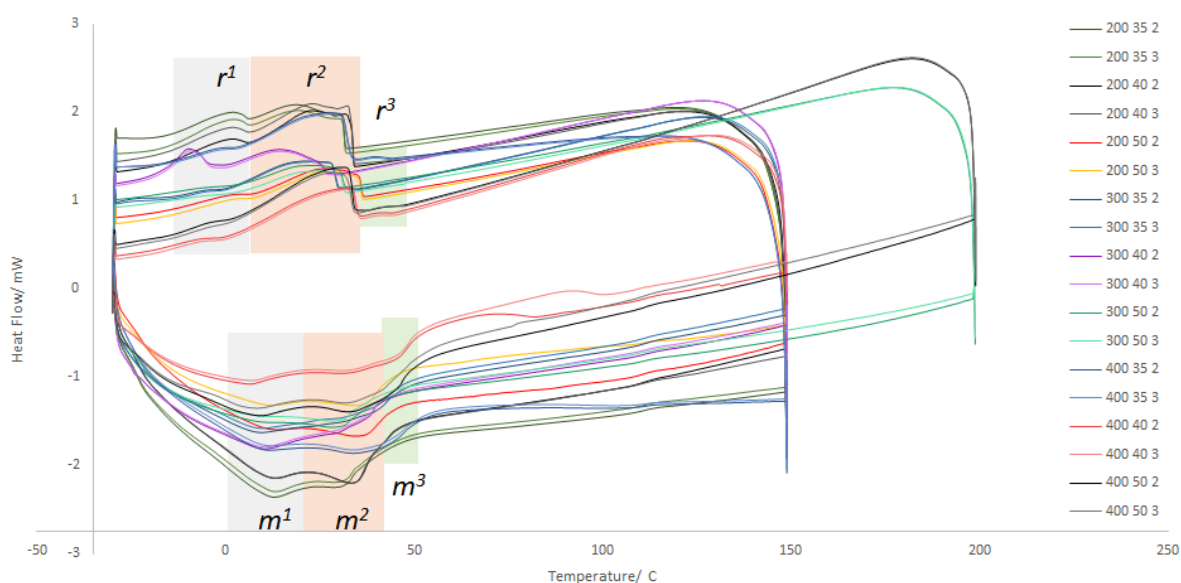


Figure 100: DSC spectra showing the 2nd and 3rd heat-cool cycles of supercritical extracts SC(200-400)(35-50). Labelled are the main two melts and corresponding recrystallisations of the extracts at 0-10 °C and 20-40 °C. Also labelled is the third melt and recrystallisation present in the SC400 extracts.

4.3. Microwave hydrothermal defibrillation of microalgal cellulose (Objective III)

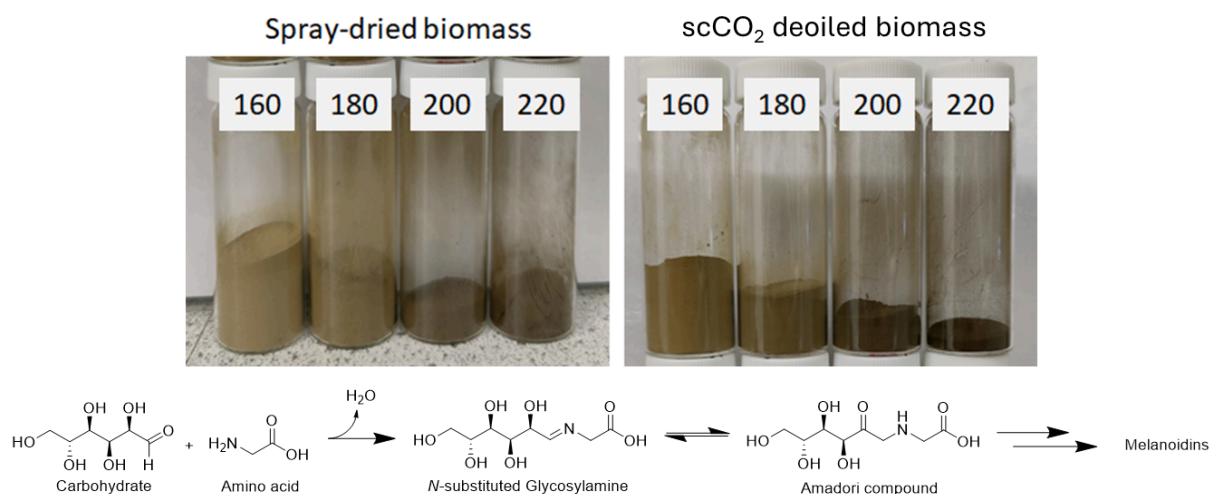


Figure 101: Defibrillated cellulose obtained via microwave treatment at the temperatures of 160, 180, 200 and 220 °C for a total of 30 minutes (50:50 ramp:hold). Brown colour potentially described by the Maillard reaction inset.

Defibrillated celluloses from both spray dried microalgal biomass as well as scCO₂ deoiled biomass has been successfully generated during microwave processing at various different temperatures (160-220 °C). As shown in figure 97, an increased brown coloration can be observed with increasing temperature which is a result of the Maillard reaction or development of humins (section 3.1.2). The Maillard reaction involves the interaction of carbohydrates and proteins at high temperatures, which in this case are achieved during the microwave treatment, to form brown polymers known as melanoidins²⁸⁷⁻²⁸⁹.

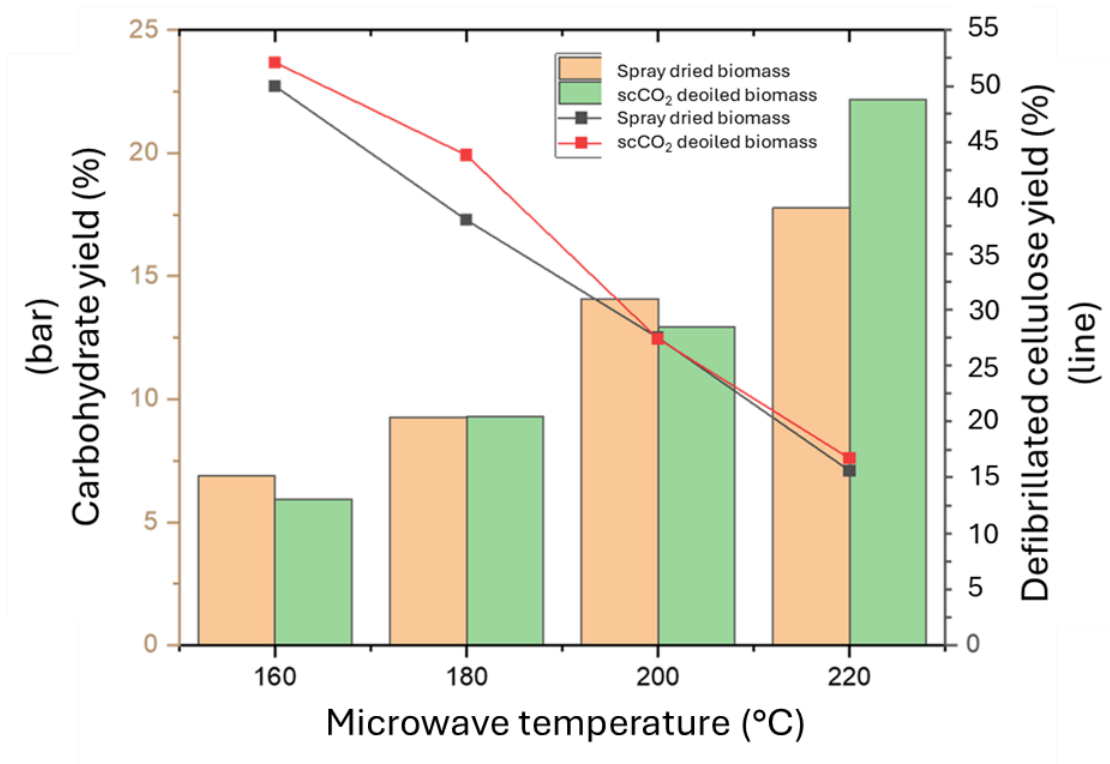


Figure 102: Defibrillated cellulose yield (line chart) and carbohydrate yields (bar chart) of spray dried and supercritical treated microalgal biomass at different microwave temperatures.

Figure 98 depicts the trends in defibrillated cellulose yields and hydrolysate carbohydrate yields. The former decreases by approximately 10 % per every 20 K increase from 51 % down to 15 % reflecting the effect of microwave-induced degradation and removal of microalgal cell components such as lipids, pigments, hemicellulose and proteins^{290–292}. Both spray dried as well as the deoiled biomass afford similar yields within a margin of 5 % of each other suggesting a limited effect of the supercritical process on the cellulose material within microalgal biomass. Analogous with the degradation and defibrillation of cellulose, the carbohydrate hydrolysate yield similarly increases linearly from 6 % to a maximum of 22 %^{164–166}. Characterisation of the hydrolysate is covered in more detail in section 4.3.6.

4.3.1. Thermogravimetric analysis

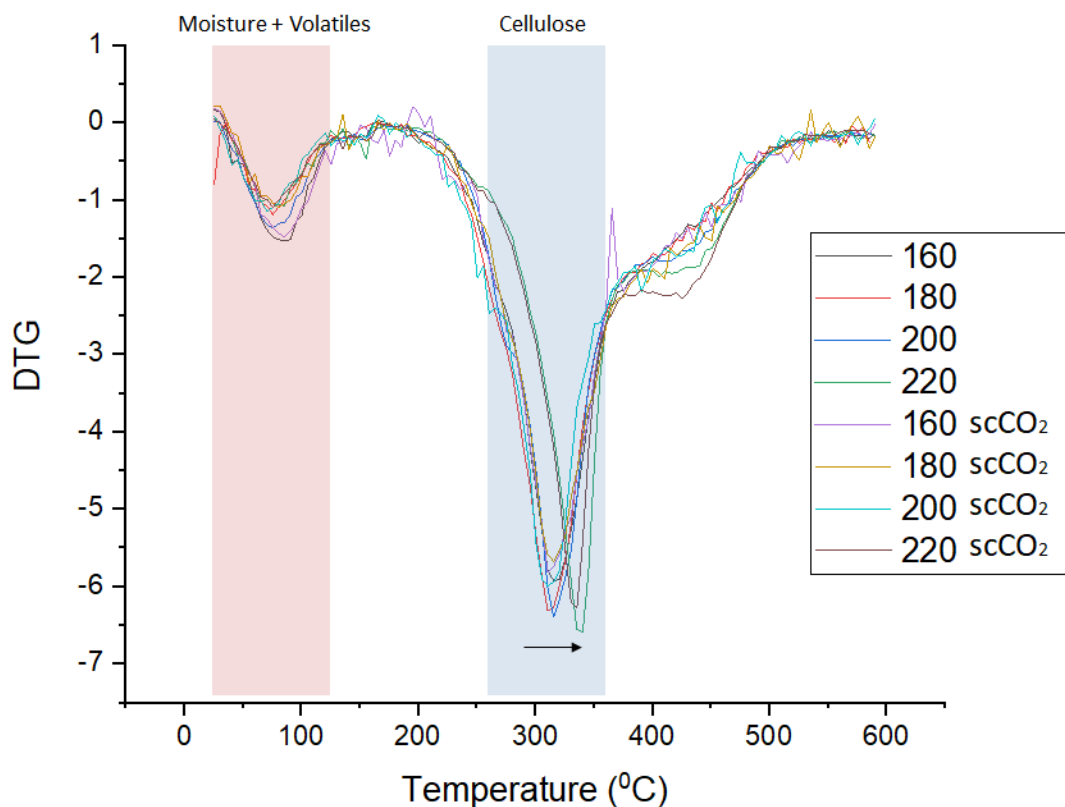


Figure 103: DTG thermograms of spray-dried biomass and scCO₂ deoiled biomass produced defibrillated celluloses. Spectra produced from TGA from 20-800 °C under a 100 mL min⁻¹ N₂ atmosphere.

Thermogravimetric analysis of defibrillated celluloses derived from both biomasses are shown in figure 99, plotting the first derivative (difference thermogravimetry, DTG). From the DTG traces more information about the nature of the hierarchical MHT-derived defibrillated celluloses can be extracted.

Similar to the decomposition of the initial biomasses, these materials undergo two stages of decomposition between 0 and 500 °C. The first stage (50-125 °C) involves the loss of volatiles and moisture accounting for 4-8 % of mass. The second stage (280-390 °C)

involves cellulose decomposition accounting for 55-65 % of mass. For the first 3 temperatures (160, 180, and 200 °C) the DTG spectrum is comparable with the spray dried and deoiled biomasses. However, there is a noticeable shift in the second stage for the highest microwave temperature run (220 °C). The peak maximum for cellulose decomposition shifted approximately 30 °C higher in temperature (see arrow in figure 99). This indicates microwave heat treatment results in a shift towards a more stable crystalline structure of cellulose. Only at the highest temperatures does this behaviour occur; it is therefore likely that microalgal cellulose requires very high temperatures for this structural change to take place.

4.3.2. X-ray diffraction

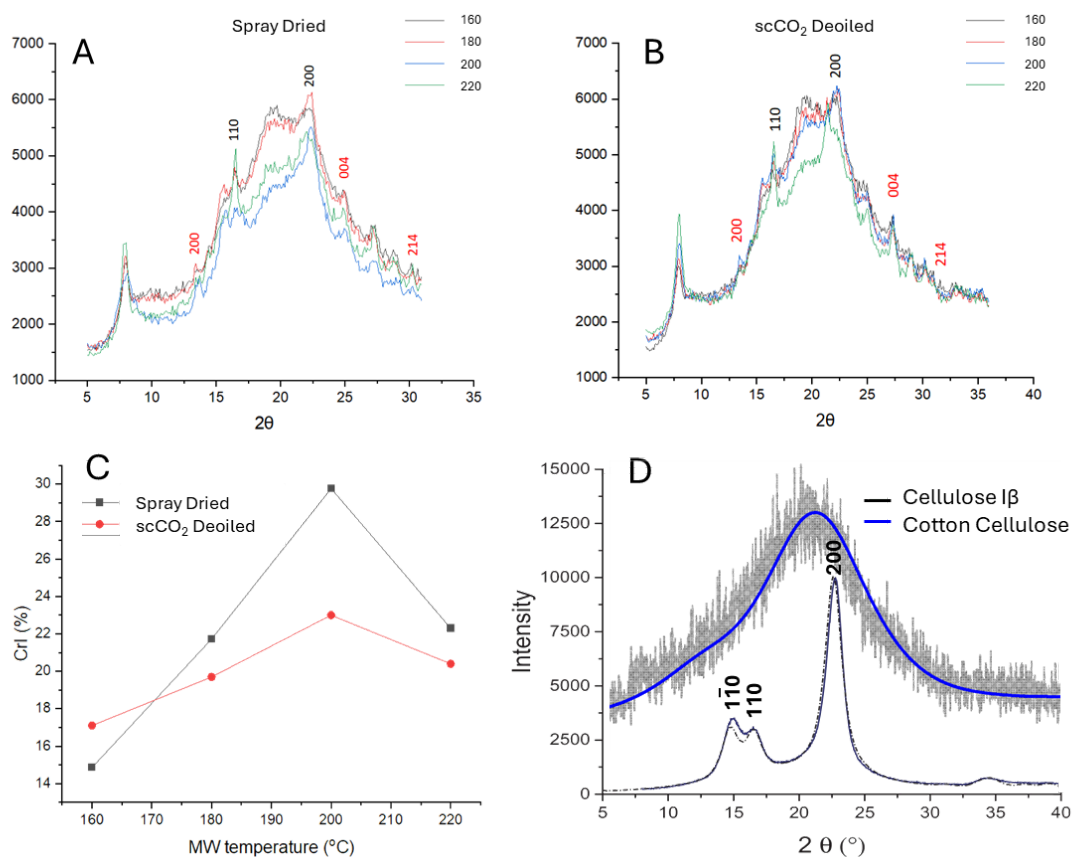


Figure 104: X-Ray diffractograms of defibrillated celluloses derived from (A) Spray Dried biomass and (B) $scCO_2$ deoiled biomass. Black numbers indicate crystalline cellulose I planes, red numbers indicate CaC_2O_4 planes. (C) Crystallinity index (Crl) of defibrillated celluloses against microwave temperatures calculated via Segal's method²⁹³. (D) Literature x-ray diffractograms of crystalline cellulose I and predominantly amorphous cotton cellulose.

The XRD patterns of defibrillated celluloses derived from both biomasses are shown in figure 100. The diffraction patterns arising from crystalline cellulose are marked in black numbers arising at $2\theta = 16.5^\circ$ and 22.5° ^{293–295}. With the higher microwave temperatures the intensity of the peak at $2\theta = 16.5^\circ$ increases indicating a higher crystallinity which is confirmed by the crystallinity index derived from the XRD patterns. The crystallinity index was determined via Segal's method, which is the ratio of the intensity of crystalline cellulose

(22.5°) to amorphous cellulose (18.0°). Interestingly, the traces of the 200 °C and 220 °C defibrillated celluloses (only 220 °C from the deoiled biomass) follow a slightly different pattern than the lower temperatures. In these samples the 18-20° peak is diminished, indicating a perceivable shift in cellulosic structure towards a more crystalline structure which is in line with DTG findings portrayed in figure 99.

Additional sharp peaks at $2\theta = 15.1^\circ$, 24.4° , and 30° might indicate the presence of insoluble calcium salts, most notably calcium oxalate (CaC_2O_4) which can be present in microalgal cell structures, especially the vacuole and the cell wall ^{166,296,297}. There does not seem to be any noticeable change in intensity for these calcium salt peaks, suggesting they are a constant component of microalgal MFC regardless of the temperature of the microwave treatment.

The crystallinity index (Crl) reveals a steady increase in the crystallinity peaking at 200 °C for both methods (29.8 % for spray dried and 23.0 % for the scCO₂ deoiled defibrillated celluloses) followed by a subsequent drop for the highest temperature of the microwave processing to levels similar to the ones seen at 180 °C ^{293,298,299}. Large differences can also be recognised between the defibrillated celluloses of the two biomasses. Spray dried biomass yields a higher cellulose crystallinity from 180 °C onwards. The difference in Crl at the same temperatures reaches its largest value at the peak position at 200 °C with $\Delta = 6.8\%$. Crystallinity values increase with temperature due to the gradual removal of amorphous impurities from the biomass such as starch and hemicellulose which will be hydrolysed and released from the cellulose matrix. Compared to previous studies on pea, orange and ginger waste, which unlike microalgae also contain lignin, the values seem to be comparable with similar Crl as well as developments showing a peak at 200 °C ^{164–166}. The final drop of Crl at the 220 °C can be explained by temperature-induced cellulose decomposition ^{300,301}. The slight discrepancy in overall Crl between the two methods indicates scCO₂ pre-treatment to have a preventive effect with regards to crystallinity formations within the cellulose structure while still following the same general trend as the standard method.

4.3.3. Solid state ^{13}C cross polarisation magic angle spinning NMR

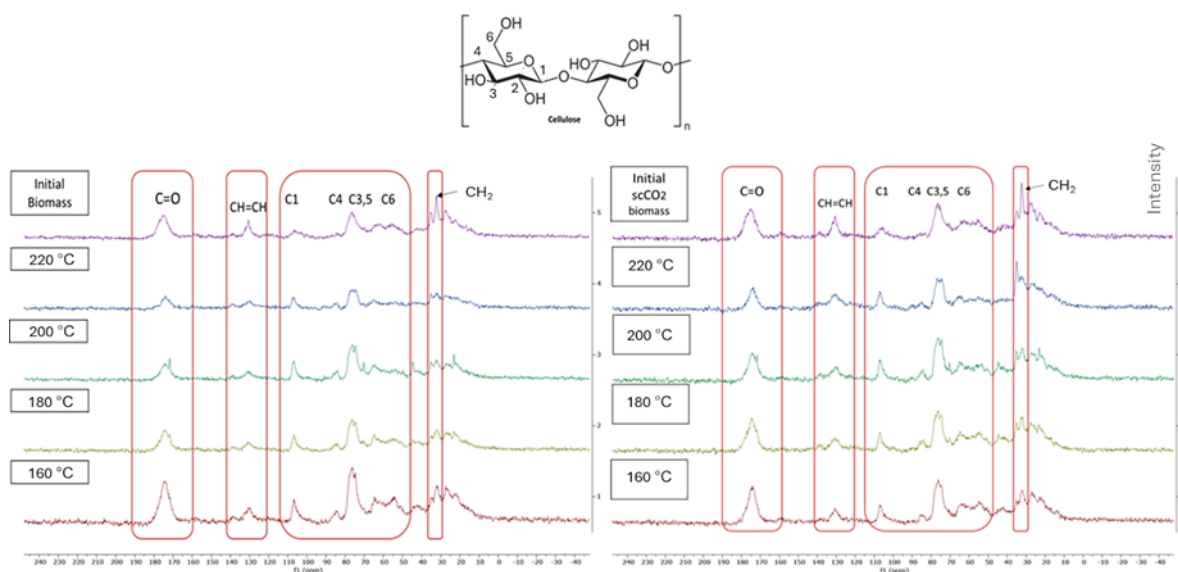


Figure 105: Solid state ^{13}C CPMAS NMR spectra of defibrillated celluloses derived from spray dried and scCO_2 deoiled biomasses using microwave hydrothermal treatment (160-220 °C)

Figure 101 shows the ^{13}C SSNMR spectra of the defibrillated celluloses. A signal at 175 ppm present in all defibrillated celluloses corresponds to the carbon environment of carbonyl and carboxylic acid groups, typically found in hemicellulose, more specifically regarding this biomass it could be attributed to glucuronic acid in hemicellulose (section 4.1.2). As the hydrothermal temperature increases this signal in the spray dried samples appears to reduce in intensity suggesting hemicellulose hydrolysis. Whereas in the deoiled samples this signal's intensity is retained, which further suggests the scCO_2 pretreatment has a preventative effect. A chemical 'hardening' of hemicellulose content may also be evident in the preliminary characterisation of scCO_2 oil-free ALG01 biomass (appendix 4.2 & 4.3). Klason analysis of this biomass exhibited an increased acid-insoluble 'lignin' content and reduced hydrolysate sugar/organic acid content compared to the spray-dried ALG01 biomass, suggesting the supercritical CO_2 treatment has induced a resistance to carbohydrate hydrolysis.

The signal at around 130 ppm indicates the presence of C=C carbon. In the spray dried biomass this could correspond to the unsaturation found in the polyunsaturated fatty acids (PUFAs) which contribute a significant fraction of this microalgae³⁰². However, the presence of this signal in the deoiled biomass suggests it could also be attributed to algaenan³⁰³. Another signal appears at 32 ppm which can also be attributed to alkyl carbon environments present in lipids and algaenan. As microwave temperature increases the intensity of these signals in the spray dried materials decrease suggesting lipid degradation at higher temperatures. Once again the deoiled biomass exhibits a resistance to degradation, likely due to the non-hydrolysable nature of algaenan.

Cellulose carbon signals are present in the region between 120 ppm – 60 ppm and are assigned in figure 101³⁰². These signals are broad, which is likely caused by retained amorphous polysaccharides, in contrast to sharper signals typically found in crystalline cellulose³⁰⁴.

4.3.4. Transmission electron microscopy

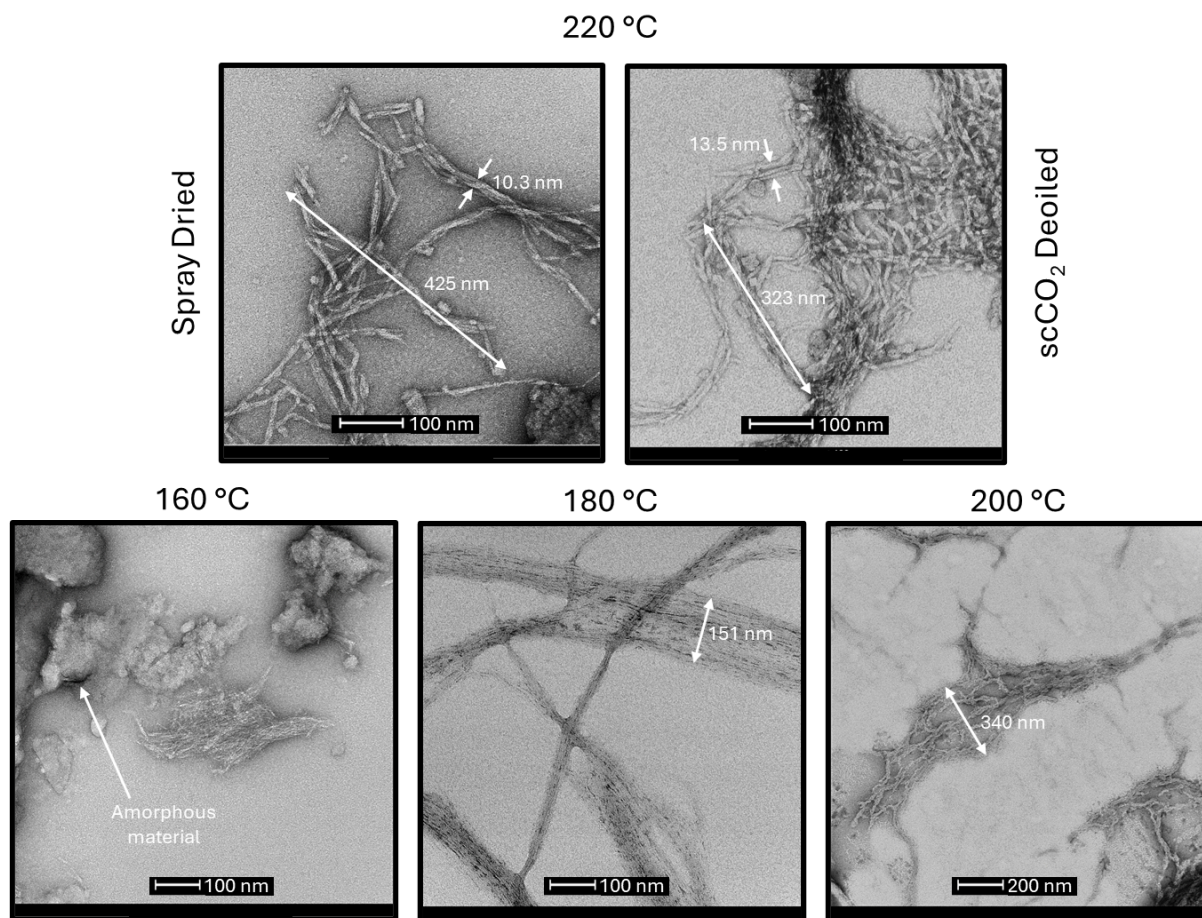


Figure 106: TEM images of defibrillated celluloses derived from spray dried biomass (160-200 °C). Defibrillated celluloses of both biomasses are shown at 220 °C to contrast the defibrillation resistance of the scCO₂ deoiled biomass.

TEM imaging of the afforded defibrillated celluloses displays the effect of hierarchical hydrothermal temperatures. In the 160 °C materials, the structure appears mostly amorphous, showing globular structures of what is likely hemicellulose. Any visible cellulose is still found clustered together in fibres. In the 180 °C materials, large quantities of the amorphous hemicellulose have been removed to reveal the cellulose fibres around 20-200 nm wide. The finer microfibrils appear to be highly ordered and remain bound together in parallel. Further heating to 200 °C and these cellulose fibres begin to bulge to +300 nm. Amorphous materials binding the cellulose microfibrils have undergone hydrolysis enabling the individual fibrils to spread, however free fibrils cannot yet be seen. In the final heating

stage, the individual fibrils are free, disordered and have cleaved into smaller individual units, concurrent with literature ^{164–166}. These fibrils are now around 10-20 nm wide and around a hundred to a few hundred nanometers long. This is true for the spray dried biomass, however, the deoiled biomass continues to appear resistant to hydrolysis.

Contrasting the two defibrillated celluloses from 220 °C hydrothermal treatments, the fibrils from the deoiled biomass still appear to be bound together in clusters, potentially by retained hemicellulose suggested in SSNMR analysis (section 4.3.3). Although some regions appear to have fragmented into smaller units and are no longer clearly ordered.

4.3.5. Water-holding capacity and gel formation

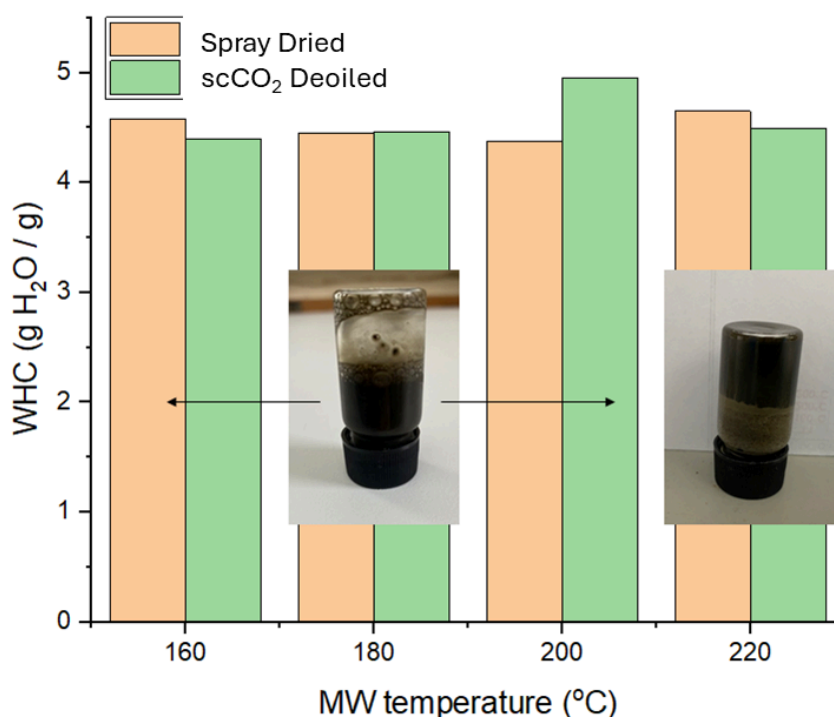


Figure 107: Water holding capacities (WHC) of defibrillated celluloses derived from both spray dried and scCO₂ deoiled biomass. Inset is the visual gelling properties of the high temperature MHT treatments at a concentration of 3.0% in water. (Biomass WHC and error analysis available in appendix 4.4)

The water holding capacities (WHC) of the different defibrillated cellulose samples are summarised in Figure 103. WHC values fluctuate around 4.5 g H₂O/g without any noticeable trend between the microwave temperatures or initial biomass. These values are lower than literature lignocellulosic or pectinaceous biomass derived defibrillated celluloses suggesting that the material generated from microalgal biomass is not able to hold as much moisture as the compared defibrillated celluloses^{164–166}. This may be due to retained hydrophobic algaenan present in the microalgal celluloses preventing water retention.

Hydrogel formation tested at various concentrations of defibrillated cellulose in deionized water (0.5 %, 0.75 %, 1.0 %, 1.5 %, 2.0 % and 3.0 %) has shown that hydrogel formation is possible. However, only the materials produced from microwave temperatures above 200 °C formed a gel; and only at the highest concentration (see inset Figure 103). These gels are also unstable, maintaining inversion for only 5 seconds before breaking and sliding to the bottom of the vial. Gel formation is also temporary, after a few hours the gel properties subside and the sample needs to be re-homogenised to reform the gel.

These defibrillated celluloses have the ability to hold water and form hydrogels which presents a potential application for these materials in sectors such as food, pharmaceutical and cosmetics, as coatings, films and barrier materials .

4.3.6. Hydrothermal microwave hydrolysate sugar content

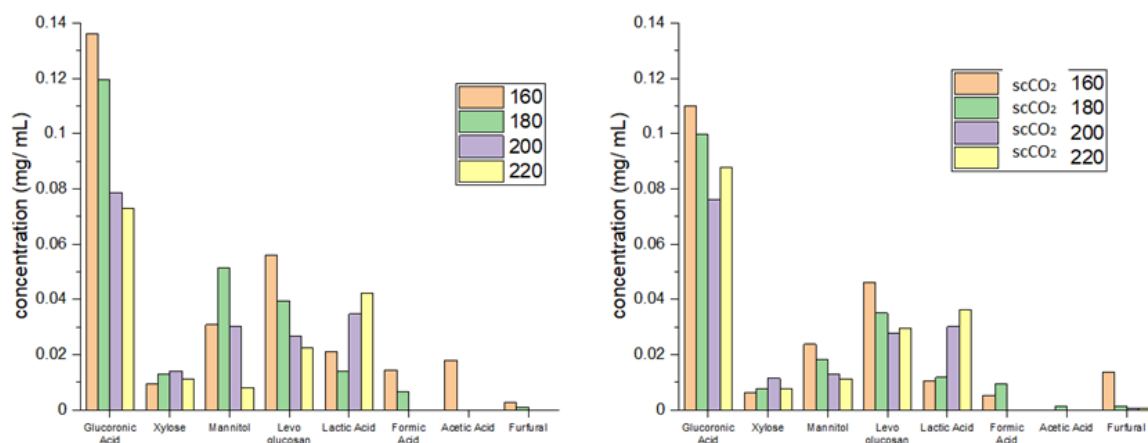


Figure 108: Hydrolysate carbohydrate content obtained from HPLC for spray dried biomass (left) and scCO₂ deoiled biomass hydrolysates (right).

Figure 104 shows the HPLC-determined sugars obtained via microwave hydrolysis of algal biomass. Most concentrated in the sugar-rich hydrolysate is glucuronic acid, which is, as stated earlier, an integral building block of the algal cell wall hemicellulose, along xylose and mannitol which both appear in the hydrolysate but at lower concentrations^{305–307}. Unlike acid-hydrolysed ALG01 carbohydrate content (section 4.1.2), mannitol is present, which aligns with literature⁷². Increasing yields of total hydrolysates are afforded with greater microwave operating temperatures. Amorphous polysaccharides hydrolysed below 200 °C contribute primarily glucuronic acid to the hydrolysate, however, above 200 °C there is a decrease in concentration. This may be attributed to hydrothermal decomposition of glucuronic acid to lactic acid³⁰⁸. In contrast to glucuronic acid and mannitol which decrease in concentration with temperature, xylose concentration remains fairly constant. No significant quantity of glucose has been identified in these hydrolysates, this is likely because microwave hydrothermal treatment at these temperatures is unable to hydrolyse crystalline cellulose^{164–166}.

Comparing the hydrolysates of ALG01 to the deoiled biomass, the deoiled biomass exhibits a perturbed release of glucuronic acid and mannitol, further indicating the treatment with a supercritical fluid has caused a hardening of hemicellulose content.

The concentration of lactic acid (Figure 104) continues increasing with increasing microwave temperature, indicating that the depolymerization of carbohydrates into small organic acids is a significantly favoured process under increasing temperatures. Lactic acid also appears to be the main breakdown product for microwave treatment of this biomass at these temperatures.

4.4. Extraction of proteins from EPA-free spent ALG01

(Objective IV)

This section explores acid, base, and enzyme-free cell disruption methods in tandem with ultrafiltration to afford protein rich extracts. These approaches have been applied to both ALG01 and EPA-free spent ALG01 to determine the validity of sequential EPA extraction and protein extraction for application in a zero-waste biorefinery.

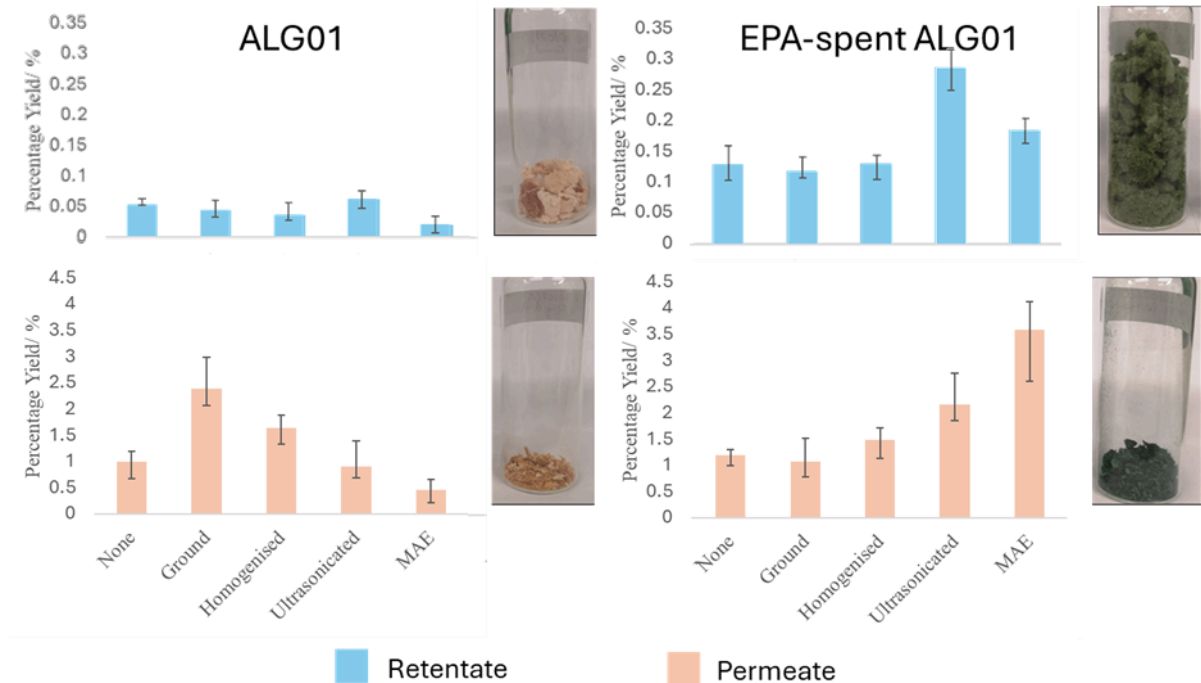


Figure 109: Yields of ultrafiltration obtained retentate and permeate extracted from spray dried and EPA-spent ALG01. Inset are images of the typical appearance of freeze-dried retentate and permeate samples.

Aqueous extraction was performed on spray dried and EPA-spent samples. Following ultrafiltration a retentate was obtained, in most extracts this accounted for around 10 % of the total water soluble content. Assuming ultrafiltration is successful, the majority of the

water-soluble content are small molecules <10 kDa in size, such as sugars, amino acids, and salts.

An increase in retentate and permeate yield was observed in extracts from EPA-free ALG01. The EPA extraction process has been recognised to have a destabilising effect on residual ALG01 biomass (section 4.1), which has increased its free water-soluble content. The green colour of EPA-spent ALG01 extracts, plausibly suggests chlorophyll presence. Suggesting the EPA extraction process has liberated pigmentation which is not attainable through dissolution in water alone. Unlike similar studies performed by Ribeiro *et al* and Safi *et al*, the pigmentation is evident in both retentate and permeate. Literature suggests that in aqueous extracts chlorophyll is contained within small lipid droplets, which would suggest in this work some of these droplets are small enough to pass through the ultrafiltration membrane^{170,309}. A potential cause for the extraction of chlorophyll in spent ALG01 protein extracts may be due to the saponification of fatty acids during the base extraction of EPA; resulting in micelles of captured chlorophyll (figure 106). Chlorophyll presence in protein extracts is undesirable for certain applications where a green colourant is not desired¹⁷⁰, however, the pigmentation can be removed using acetone precipitation, which affords a dark green solution and precipitates a pale grey/pink protein precipitate. Despite the simplicity of chlorophyll removal, avoiding the use of organic solvents, like acetone, is preferable.

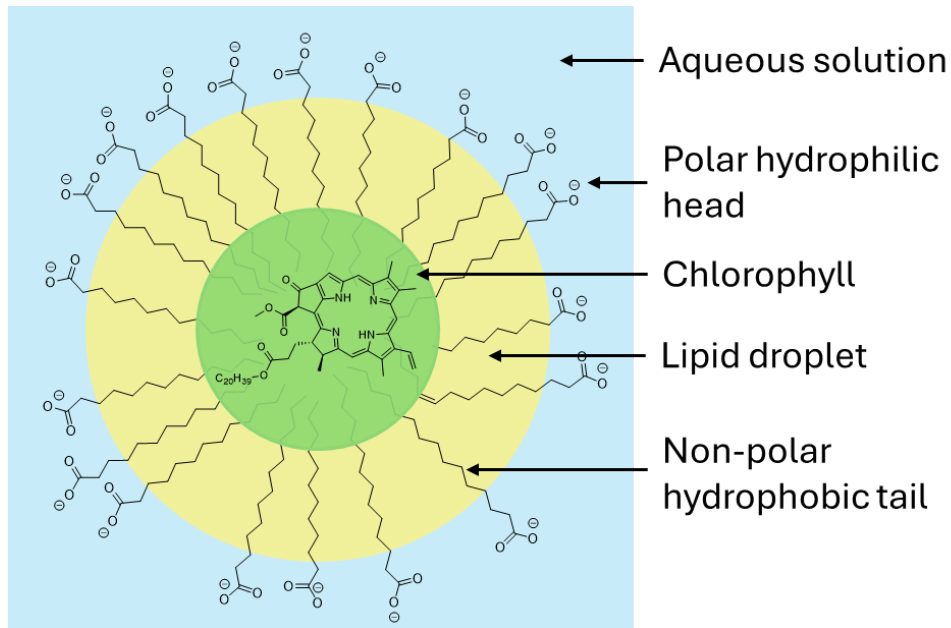


Figure 110: Simplified diagram of a micelle formed from saponified fatty acids containing chlorophyll within a lipid droplet.

In both the spray dried and spent ALG01, the appearance of the retentates are fibrous and ‘fluffy’, whereas the permeates are crystalline. Following cell disruption treatments, the appearance of the retentates and permeates changed very little. The cell disruption methods used in this study also caused little change to the retentate yields afforded from spray dried ALG01. In some cases the retentate yield decreased, for example using microwave assisted extraction (MAE). The permeate yield following mechanical grinding or homogenisation of this biomass increased significantly. These results suggest mechanical grinding and homogenisation assist in the release of water soluble content; but specifically metabolites less than 10 kDa in size. Ultrasonication and MAE appear to have no positive effect on the extraction of water soluble content from spray dried ALG01.

Spent ALG01 was more susceptible to ultrasonication and MAE cell disruption. These methods exhibited approximately a 2 and 1.5 times increase in the retentate yield and a 2 and 4 times increase in the permeate yield, respectively. Mechanical grinding and homogenisation, on the other hand, had very little effect. It is interesting that these cell disruption methods, mechanical grinding and homogenisation, were effective at disrupting

spray dried ALG01 but not spent ALG01 and vice versa for ultrasonication and MAE. It would seem that some of these physical cell disruption methods are ineffective on ALG01's small microalgal cells without chemical treatment (i.e. base hydrolysis during EPA extraction). In the future, microscopy would be a useful technique to see if any cell disruption is visible, and potentially explain this phenomenon.

4.4.1. Elemental analysis (CHN)

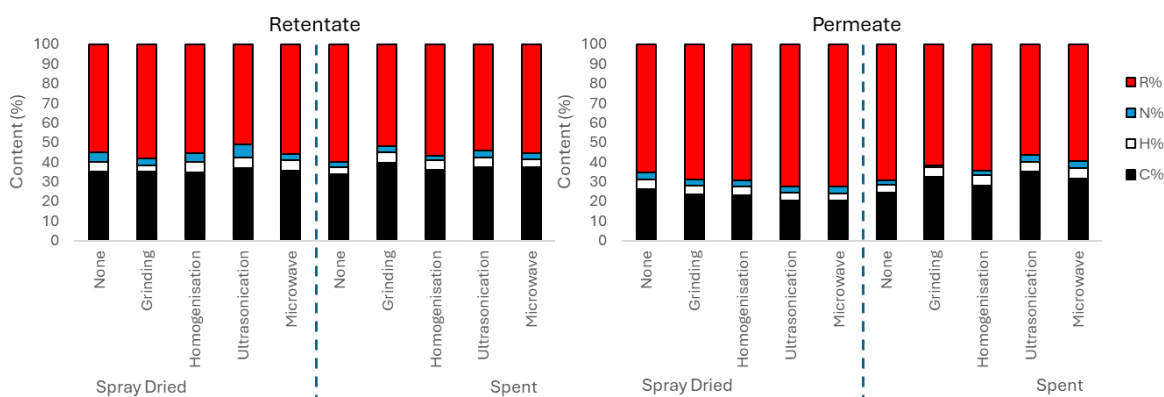


Figure 111: CHN microanalysis contents for spray dried and EPA spent ALG01 retentate and permeate samples following aqueous extraction and ultrafiltration, and variable cell disruption methods.

Although EPA-spent ALG01 exhibited higher retentate yields, CHN determination revealed a nitrogen content of 2.69% compared to a 4.69% content for the retentate of the spray dried sample. In fact, the retentates and permeates of EPA-spent ALG01 almost always had lower nitrogen contents than those of ALG01, regardless of cell disruption method. Furthermore, for both algal biomasses, retentate nitrogen content was typically higher than that of the permeate, indicating protein enrichment in the retentate. A few minor exceptions include: a) the water soluble content obtained from ALG01 via grinding and that obtained from EPA-spent ALG01 via ultrasonication, which both exhibited equivalent nitrogen content in both retentate and permeate. b) the water soluble content obtained from both EPA-spent and spray dried ALG01 via microwave assisted extraction, which both exhibited a greater nitrogen content in the permeate. The nitrogen content ranged from 2-5% across all samples, which is equivalent to a protein content of 13-31% assuming all nitrogen is associated with protein (6.25 conversion factor). Permeate samples typically had a higher residual content than retentate samples. Assuming the residual content is predominantly oxygen, one could associate this with polysaccharide presence also high in oxygen content.

4.4.2. Protein visualisation

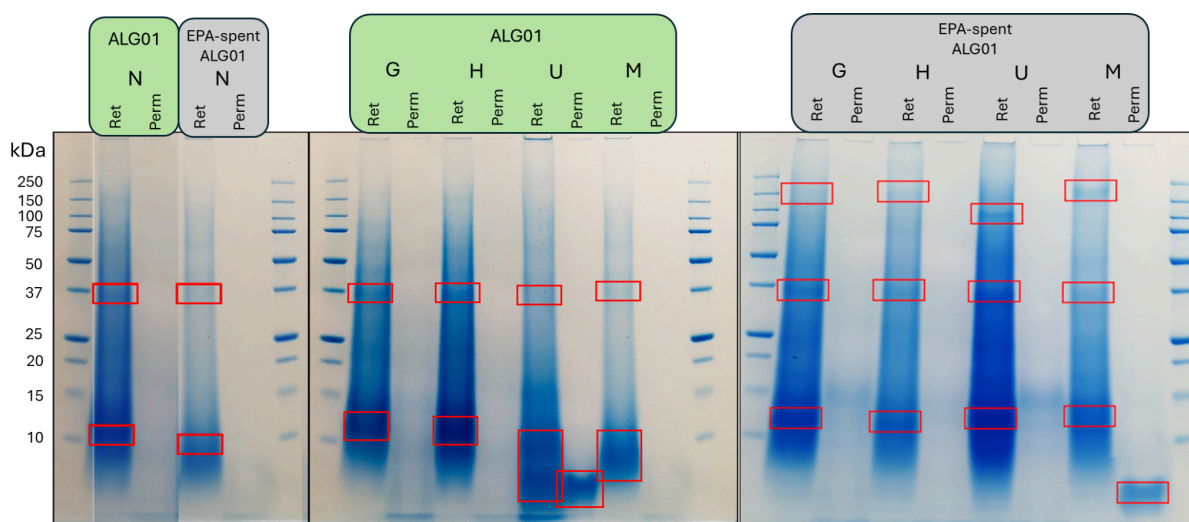


Figure 112: SDS-PAGE gel presenting the distribution of protein sizes, stained in blue, within ultrafiltration obtained retentate and permeate samples, extracted from ALG01 and EPA-spent ALG01 samples following different cell disruption methods: None (N), Grinding (G), Homogenisation (H), Ultrasonication (U), and Microwave assisted extraction (M).

SDS-PAGE was used to determine the molecular weight distribution of the protein content in ALG01 and EPA-spent ALG01 retentates and permeates. This electrophoresis technique resolves unfolded, charged, SDS-bound proteins based on their ability to pass through a polyacrylamide gel, which is typically determined by protein length/size³¹⁰. All samples exhibited heavy smearing, even after several dilutions and acetone precipitation to remove impurities, which could indicate degradation of the protein content. This degradation has produced a mixture of protein fragments that are not clearly resolved and resulted in a significant quantity of low molecular weight proteins around and below 10 kDa. Cell disruption does not seem to be the immediate cause of proteolysis as smearing is evident even without cell disruption. It is likely that spray drying, which involves a process of pressurised spraying from a 180 °C nozzle, and the EPA extraction process have degraded a significant portion of protein content.

Despite the above problem, a faint protein band at 37 kDa in size was recognisable in all retentate samples. In EPA-spent ALG01 retentates, following cell disruption, bands between 100-150 kDa appear. These were not present in the ALG01 retentates or EPA-spent retentate without cell disruption, suggesting a combination of base-catalysed weakening of the cell wall (EPA extraction) and these cell disruption methods enabled the liberation of larger proteins trapped within the cell.

In most of the permeate samples little to no protein was identified by SDS-PAGE. Ultrasound extracted ALG01 and microwave extracted EPA-spent ALG01 permeates, exhibit a strong band below 10 kDa. Due to their low weight and size these proteins have been able to pass through the ultrafiltration membrane. In some cases ultrafiltration fails with proteins of approximately 15 kDa in size appearing in the permeate. Why the technique fails in these samples is not clear.

4.4.3. Protein content via Bradford Assay

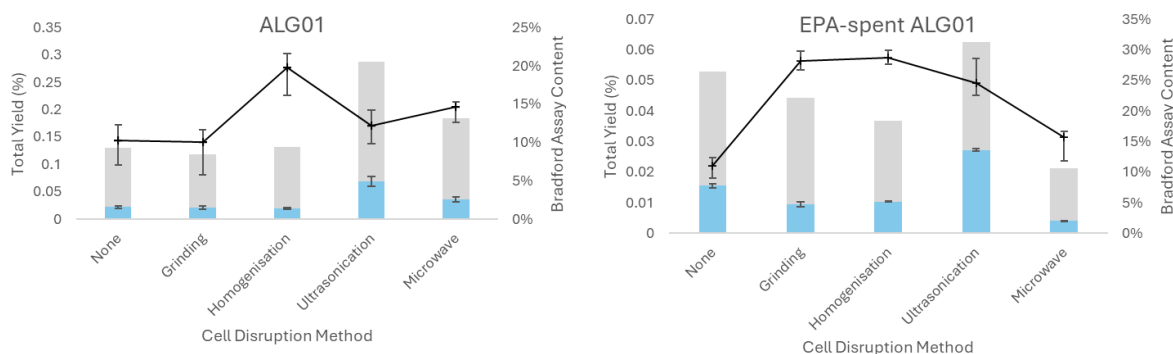


Figure 113: ALG01 and EPA-spent ALG01 retentate yields and protein contents determined by CHN nitrogen-to-protein conversion (bar) and Bradford assay (line).

Bradford assay is a technique that utilises Coomassie Blue G250 dye to quantify protein content. In the acidic assay reagent solution this dye takes on a protonated cationic form, which is red in colour (470 nm). The dye undergoes a colour change when bound to proteins and becomes a brilliant blue (590 nm). The intensity of absorbance at 595 nm can be used to quantify the protein concentration based on a protein standard (albumin). The dye favours binding to basic amino groups in protein structures, typically associated with amino acids such as arginine and lysine. The Coomassie dye also binds to aromatic amino acids, such as histidine, phenylalanine, tryptophan, and tyrosine, but to a lesser extent. It is also important to note a limitation of this dye is that it only binds to protein residues containing these amino acids, not free amino acids or peptides smaller than 3 kDa in size³¹¹. Further a significant uncertainty in Bradford-Assay analysis appears at high concentrations of protein. The calibration curve produced during Bradford assay analysis becomes heavily uncertain at concentrations above 750 $\mu\text{g mL}^{-1}$ (Figure 22), which is equivalent to around 30% protein content (considering the concentration of the samples is 2500 $\mu\text{g mL}^{-1}$). Sample dilution was performed to minimise the protein concentration below this threshold.

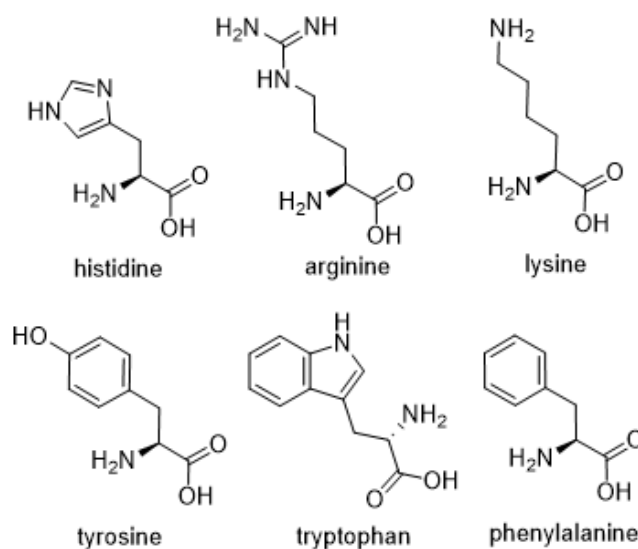


Figure 114: Chemical structure of amino acids that bind to the Coomassie dye and are recognised by Bradford Assay.

In these works, Bradford assay indicated protein presence around 10-30 % across the retentate samples obtained from ALG01 and EPA-spent ALG01. Protein extractions using water alone, exhibited the lowest protein contents at 10 % for both algal biomasses. The highest contents (28-29 %) were obtained from ALG01 biomass treated with mechanical grinding or homogenisation. Ultrasonication and microwave assisted extraction caused a poorer increase in protein content (15-25 %). Ultrasonication appeared to extract/produce the highest quantity of low weight protein molecules according to SDS-PAGE visualisation, which explains the low Bradford assay protein content but high nitrogen content, as Bradford assay has difficulty recognising these small peptides ³¹¹. This is also evident in the EPA-spent samples. However, in these samples only homogenisation appears to cause an increase in the protein content (20 %) but to a much lesser extent than extractions from ALG01. These results contrast with protein contents determined by a nitrogen-to-protein conversion ratio of 6.25, specifically the samples obtained via ultrasonication. The nitrogen content of both ALG01 and EPA-spent ALG01 derived retentates using ultrasound assisted extraction equates to 43 and 24 % protein content, respectively. Bradford assay indicates 25 and 12 % for these samples, respectively. This could be attributed to multiple reasons:

overestimation of nitrogen content protein due to non-protein nitrogen, or an underestimation of Bradford assay protein due to proteolysis, or proteins of low arginine and lysine content.

Bradford assay of permeate samples determined protein contents of less than 2%, which indicates successful protein/sugar fractionation. However, the protein content in the permeates is likely small proteins (<10kDa), peptides, and amino acids, which once again are often unrecognised by Bradford assay.

4.4.4. ATR-IR spectroscopy

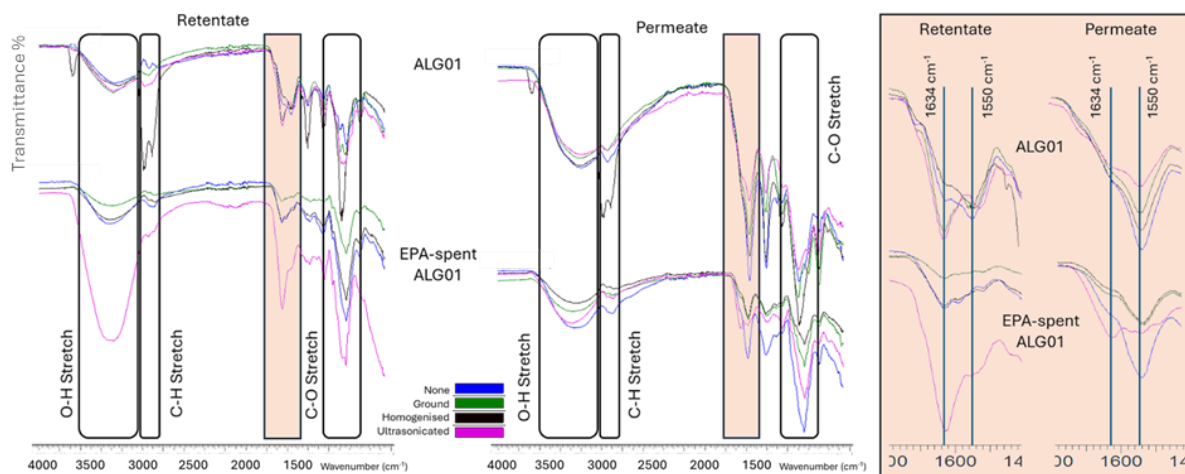


Figure 115: ATR-IR spectroscopy of ultrafiltration obtained retentate and permeates extracted ALG01 and EPA-spent ALG01 following various cell disruption methods.

Retentate and permeate samples from both biomasses exhibit O-H or N-H stretching around 3300 cm^{-1} and C-O stretching around 1050 cm^{-1} . These are features present in both protein and polysaccharide compounds. Two overlapping bands at 1630 and 1560 cm^{-1} attributable to amide I and amide II vibrations. Amide I arises mainly due to C=O stretching, however, because of hydrogen bonding between amide bonds in folded proteins the N-H bond also contributes to this vibration²²³. The same is true for Amide II which arises mainly due to N-H bending, but with contribution from the C=O bond. In the retentates, the 1630 cm^{-1} band is typically more prominent, whereas the reverse is true for the permeates. An additional carbonyl stretch at 1720 cm^{-1} in some samples suggests some acid/ester presence too. These could be attributed to aspartic or glutamic acid known to be present in *Nannochloropsis* protein extracts, accounting for approximately 10% of the total amino acid content each in literature¹⁴⁵.

4.4.5. HPLC analysis of ultrafiltration permeate

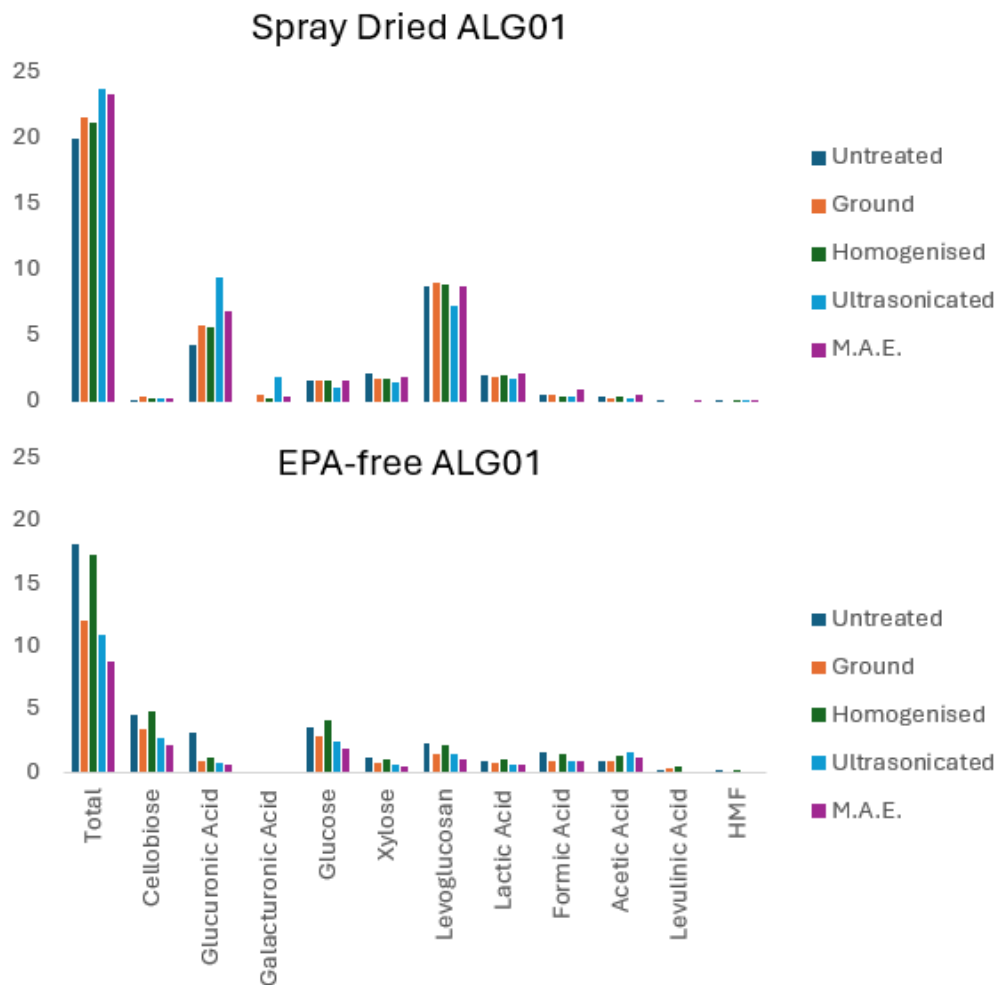


Figure 116: HPLC determined carbohydrate content of ALG01 and EPA-spent ALG01 ultrafiltration permeates.

HPLC sugar analysis of the permeates found an average carbohydrate content of 20.0% and 18.1% for the spray dried and EPA-spent algal permeates, respectively. The carbohydrate composition for the spray dried permeate was determined to mainly be composed of levoglucosan (44%), a product of thermal degradation, indicating the effect of the high temperature drying process. Other components include glucuronic acid, glucose, and xylose which accounted for 40% of the carbohydrate content. The composition of the spent algal permeate differed slightly. The main component was cellobiose (26%), a

hydrolysis product of cellulose ³¹². This further indicates the effect of the EPA extraction process. Similar to the spray dried algal permeate, glucuronic acid, glucose, and xylose still accounted for almost 40% of the carbohydrate content.

Cell disruption did not appear to have a significant effect on the carbohydrate content of the permeates. Cell disruption treatment of ALG01 appeared to slightly increase the total carbohydrate content. Specifically ultrasonication, which liberated a greater quantity of uronic acids, which indicates further breakdown of the hemicellulose content. The opposite was observed in the EPA-spent permeate samples (except homogenisation which was almost equivalent to the 'untreated' biomass).

4.5. Chapter summary

This chapter has explored green valorisation techniques: supercritical CO₂ extraction, microwave hydrothermal defibrillation of cellulose, and the extraction and enrichment of proteins using green cell disruption technologies.

In these works it was recognised that co-solvent-free supercritical CO₂ extraction is a suitable method of affording extracts containing high-value polyunsaturated fatty acids, pigments and phenolics from microalgae, ALG01. A factorial approach indicated selectivity regarding pigment and lipid content, with carotenoids favouring 300 bar pressure, chlorophylls/pheophytins favouring 400 bar pressure, and EPA favouring 35 °C temperature and pressures above 300 bar. These extracts had significant antioxidant power due to their PUFA, carotenoid, and phenolic content. The maximum achieved via a 300 bar and 50 °C extraction. These oils were thermally stable for 3 cycles between -30 and 150 °C, with only 2 samples exhibiting decomposition (SC30050 & SC40040). These results offer potential applications for these oils as nutritional supplements^{313,314}. With further research these oils could have a more novel application as a coating in edible films, providing protection against food oxidation/spoilage whilst adding nutritional value³¹⁵⁻³¹⁷.

In literature microwave hydrothermal defibrillation of cellulose has been recognised as a suitable green method of valorising cellulose-rich biomass residues. Successful defibrillation of microalgal cellulose has been achieved in these works using microwave treatment above 200 °C. Microwave-induced hydrolysis of hemicellulose material within ALG01 cell walls, afforded highly crystalline defibrillated cellulose material which is capable of retaining approximately 5 times its weight in water and forms weak gels. This valorisation technique was applied to supercritical CO₂ deoiled residues with a degree of success. Defibrillated cellulose was obtained following microwave treatment at 220 °C, this deoiled biomass exhibited a preventative effect which appeared to slow the defibrillation process. It is unclear as to why this effect takes place. In contrast to literature, which proposes supercritical fluids as a promising pretreatment or cell disruption method³¹⁸, the results of

this study could suggest this pretreatment caused a pseudo-hornification of hemicellulose and cellulose fibrils ³¹⁹. This effect, however, had minimal effect on the defibrillated cellulose water holding or gelling capacity and therefore these materials have various applications as films, coatings, rheological modifiers, and more ¹⁶².

EPA production and extraction from the microalgae, ALG01, is already at a commercial scale. This chapter has successfully valorised the EPA-free ALG01 residue, affording a protein enriched fraction using only water and green cell disruption and ultrafiltration technologies. Base-catalysed extraction of EPA liberated a fraction of the protein content via hydrolysis, which resulted in double the retentate yields in comparison to intact ALG01. Compared with similar approaches in literature, the total protein recovered is relatively low in this research. One article achieved 12 % total protein yield and almost 85 % retentate protein content ³²⁰. SDS-PAGE and Bradford Assay confirmed protein presence and identified proteins of 37 and 10 kDa in weight, however, these methods also indicated protein degradation. The addition of ultrasonication or microwave assisted extraction cell disruption, increased the retentate yield by 2 or 1.5 times the untreated EPA-free ALG01, respectively. Cell disruption technologies also enabled the liberation of larger proteins around 100-150 kDa in weight. Permeate fractions were recognised to contain high carbohydrate and protein content, however, the success of ultrafiltration limited the size of the proteins to less than 15 kDa.

Chapter 5. Future work & conclusions

5.1. Future work

Due to time constraints and availability of equipment over the duration of COVID lockdown several ideas that were initially explored had to be stopped. The following section highlights these ideas as potential for future work.

5.1.1. Carbonisation of microwave-assisted carrageenan extracts

The extraction of carrageenan from Irish Moss by microwave-assisted extraction followed by the sequential pyrolysis of the polysaccharide and production of ISPCs would be a useful piece of future work. In literature, microwave-assisted extraction has been used for the extraction of carrageenan. Ponthier et al. reported that carrageenan was successfully extracted from the red algae, *Mastocarpus stellatus*, using microwave irradiation (70-190 °C, 3-6 min) and water alone. Isolation via antisolvent precipitation (acetone), revealed a maximum yield of 60 % after a 6 minute extraction at 150 °C. Ponthier et al. also reported that the extraction temperature could selectively influence the molecular weight distribution and gelling properties of the carrageenan extract, and stated that “microwave heating temperature should be increased up to 170 °C whenever it is sought to promote the strength of the hydrogels”¹⁸³.

Our preliminary studies of microwave-assisted extraction afforded similar carrageenan extracts to conventional heating. Methodologies included in appendix 5.1. Equivalent yields, appearance, and characteristic TGA and VT NMR data, was obtained at 100 °C and 50 °C microwave runs compared to conventional hot water extraction (figure 113). Microwave-assisted extraction also produced more consistent yields.

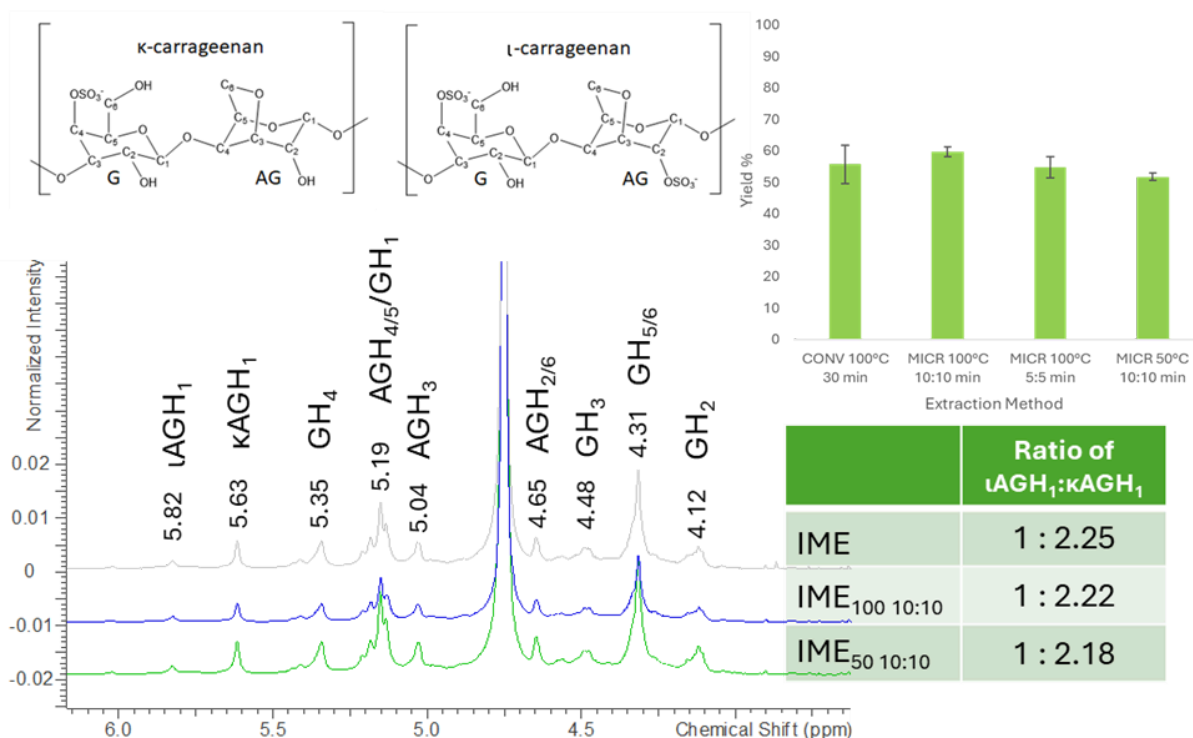


Figure 117: A zoomed region (3.5-6.0 ppm) comparing the 80 °C ¹H NMR spectra of IME obtained using conventional and microwave assisted extraction methods. Labels are pyranose proton environments of kappa carrageenan and the ratio of kappa and iota carrageenan for each sample determined by the ratio of the anomeric protons. Yields of Irish Moss extract (IME) using microwave assisted extraction methods compared to conventional heating (timings indicate ramp:hold).

Examining the residual Irish Moss biomass also indicated that microwave extraction resulted in a higher efficiency of carrageenan extraction. Following a 20 min 100 °C microwave extraction, complete carrageenan removal was achieved according to the TGA of the residues (figure 114). Conventional and low temperature (50 °C) microwave extraction, exhibited carrageenan presence in the residue by the DTG peak around 210-220 °C. Despite identical behaviour between microwave and conventionally obtained Irish Moss carrageenan, a measure of polysaccharide hydrolysis is important. HPLC of this highly viscous gel is difficult, instead the application of size exclusion chromatography (SEC) would

be beneficial to understand polysaccharide chain length distribution and obtain any indication of carrageenan oligosaccharides.

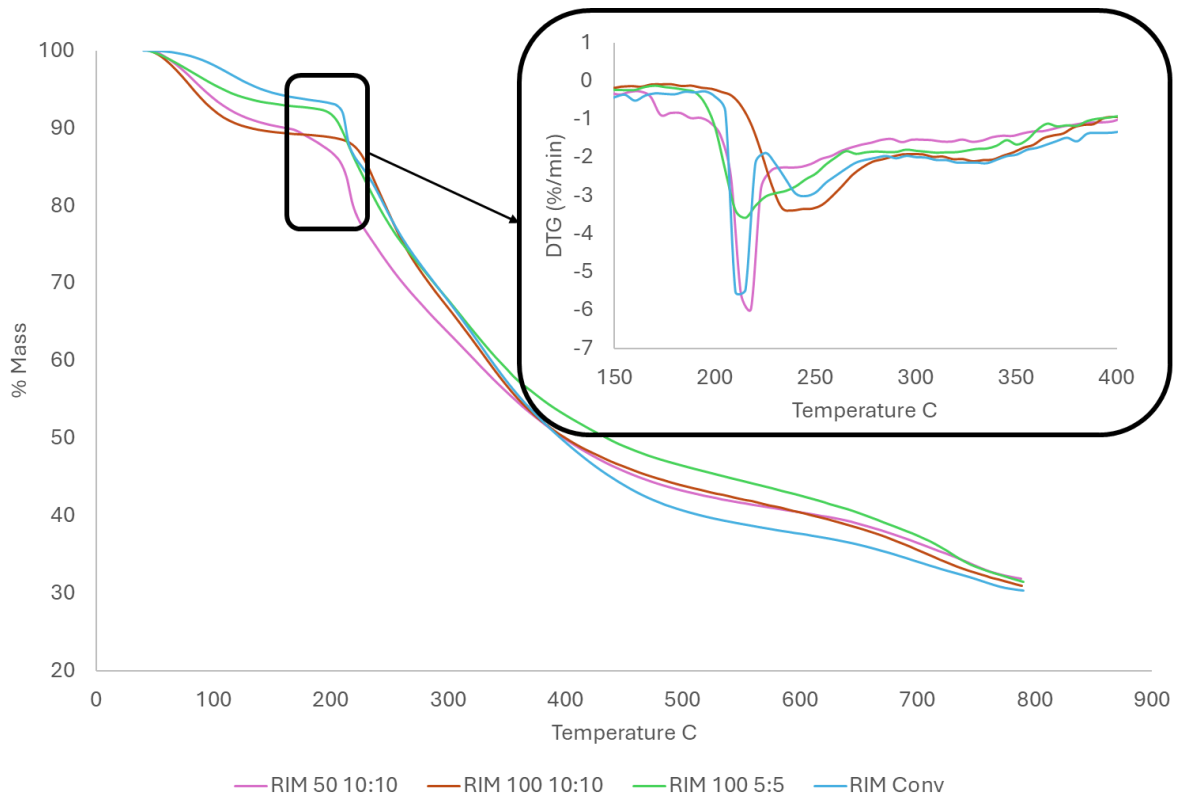


Figure 118: Thermogravimetric analysis of RIM biomass from conventional or microwave extraction processes.

Preliminary studies have proven that hydrothermal microwave processing is a faster and less energy intensive technique for carrageenan extraction compared to conventional hot water extraction. Future work now needs to explore the carbonisation and application of these materials compared with those reported in chapter 3. It is envisaged the properties of these carbonised materials will behave in a similar manner.

5.2.2. Optimisation and tuning the methodology of carrageenan-derived sulfur-containing porous carbons

The method of producing IME ISPCs in this thesis involved the formation of carrageenan aerogels directly from the extract, sequential pyrolysis of these aerogels, and aqueous washings. These chars obtained from carrageenan had sufficient properties for copper(II) adsorption, however, further development of the production methodology could be applied to attempt to enhance the porosity, sulfur content, etc. As a result, the rate of adsorption or the adsorption capacity of copper may increase. A preliminary study applied different carrageenan gel concentrations, gel preparation methods, and acid washing to afford the next generation of IMECs.



Figure 119: Carrageenan aerogels produced from freeze-drying gels of different loadings (2.5%-25%)

Gels of Irish Moss carrageenan ranging from 2.5% to 25% were produced and freeze-dried. The average concentration of carrageenan in solution immediately after extraction from the biomass was 2.5 %; the other concentrations required additional steps to produce the different aerogels. These aerogels were carbonised at 300 °C and washed with aqueous HCl (10 M) for 48h. These new chars were labelled Carr300 to signify their

difference to IMECs. N₂ adsorption porosimetry of these Carr300 carbons exhibited an increased surface area and pore volume in comparison to IMECs. Carr300 materials ranged from 300-600 m²/g surface area, 0.1-0.2 cm³/g pore volume, and average pore diameter of 2.3-2.6 nm. Surface area appeared to positively correlate with gel loading between 5 and 20%, however, at 25% the porosity of the material decreases potentially due to incomplete dissolution of carrageenan (due to approaching saturation). This relationship is visible in figure 116, and shows no apparent trend in the pore volume. This figure also shows SEM images of Carr300 particles, where a decreasing macropore size is visible over an increasing gel load; from ~20 μm at 2.5 % to ~2 μm at 20 %. Macroporosity could be further measured via NMR cryoporometry ³²¹.

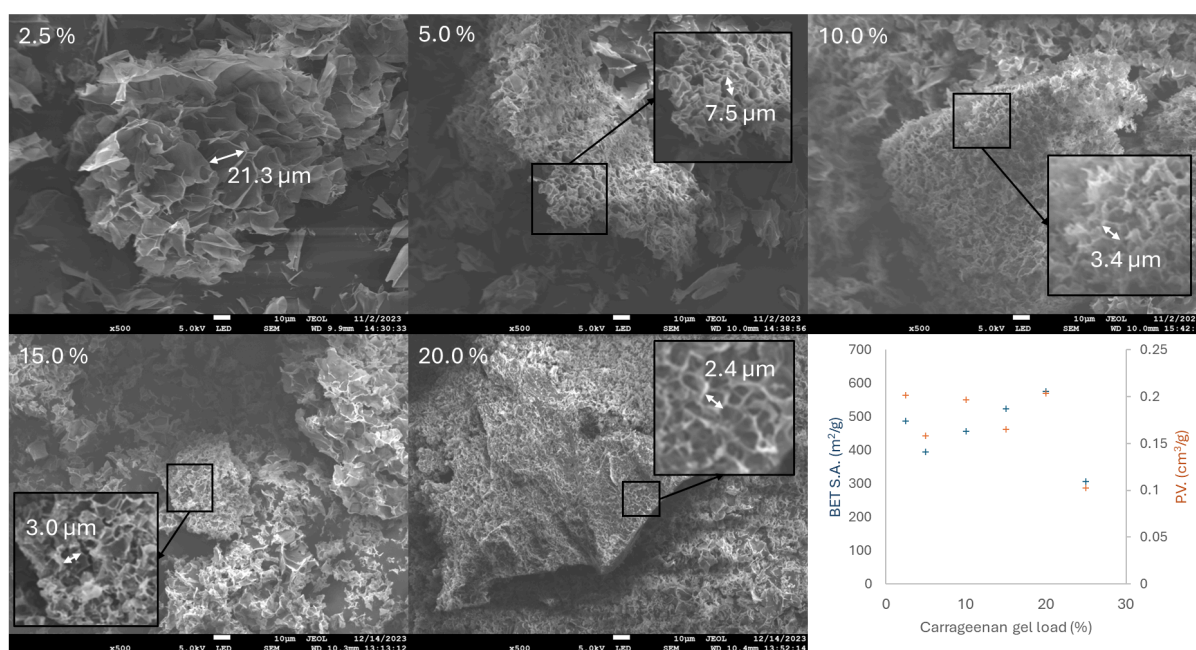


Figure 120: SEM images of Carr300 materials (2.5-20.0% Gel loading) at x500 magnification and the size of material macropores. The relationship between gel loading and the N₂ adsorption porosimetry measured surface area and pore volume is also included.

Starbons are well developed mesoporous carbons and their production stems from expanded starch, alginic acid, or pectin ²⁴⁴. Expanded aerogels are achieved by solvent

exchange with ethanol, acetone, or t-butanol, followed by a drying method such as supercritical CO₂ drying or freeze-drying. Ethanol expanded carrageenan aerogels (10 % Carrageenan loading) were treated as above to produce another generation of Carr300 materials. The expanding method seems to have introduced a different pore structure in these chars. Mesopores between 20-80 nm are seen in these materials which in turn have increased the pore volume (see figure 117). Further characterisation and application of these further developed carrageenan-derived carbons would be a useful piece of future research.

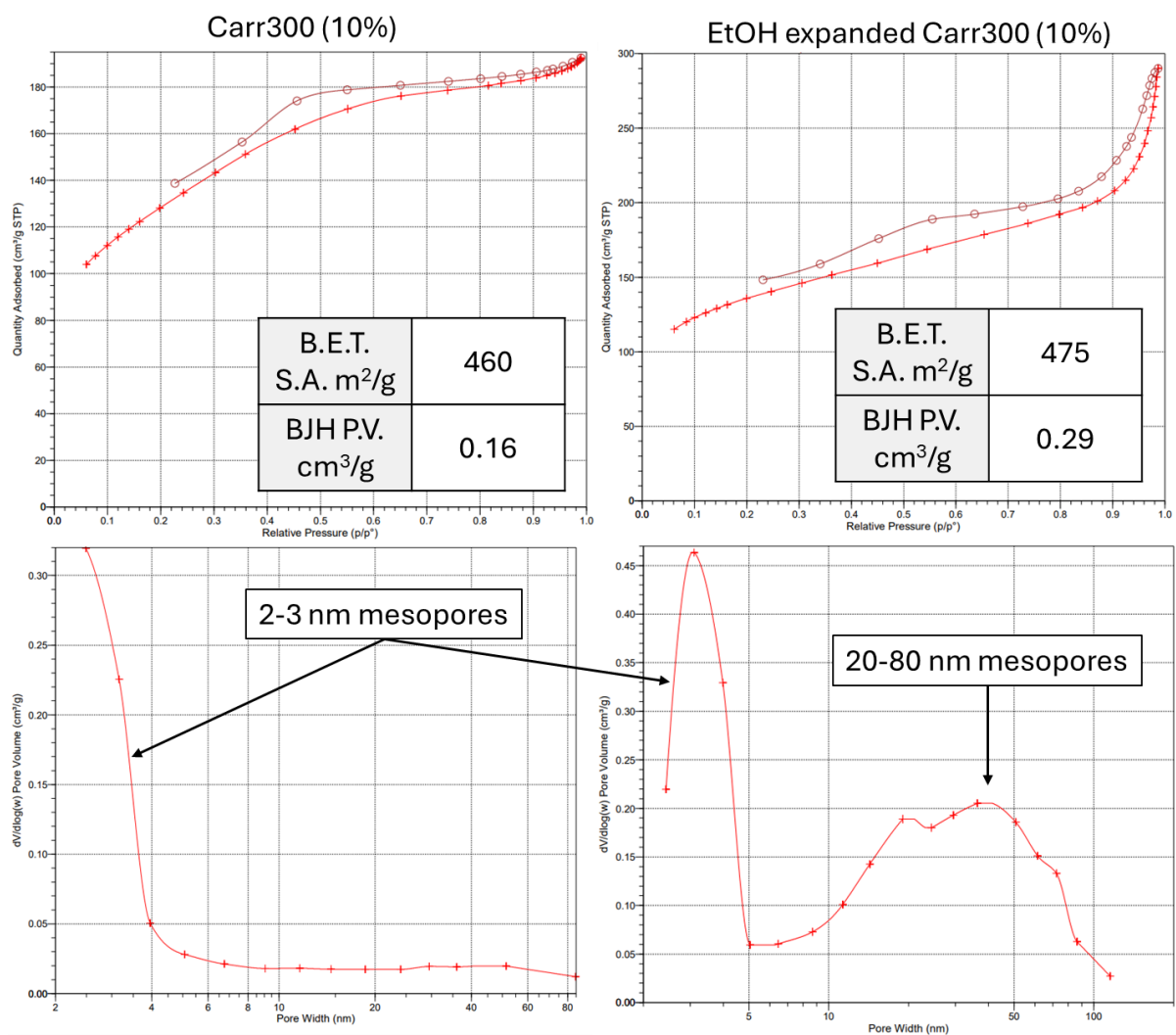


Figure 121: N₂ adsorption porosimetry adsorption isotherms and pore distribution plots of unexpanded Carr300 (10%) vs expanded Carr300 (10%).

Preliminary studies have proven that prior ethanol assisted expansion of carrageenan derives sulfur-containing carbon materials with appreciable porosity of approximately twice the surface area of the materials produced in chapter 3, and enhanced mesoporosity. Future work now needs to explore the application of these materials to metal adsorption similar to those reported in chapter 3. It is envisaged that these carbonised materials will have enhanced adsorption capabilities and with the possibility of desorption.

5.2.3. Pyrolytic bio-oils from Irish Moss

Gases evolved from the pyrolysis of Irish moss and carrageenan were analysed using TG-GCMS (section 3.1.5.1). The contents of these gases included primarily levoglucosenone and furfural compounds. Future work should explore the condensation of these gases to afford valued bio-oils. The isolation of levoglucosenone for the production of Cyrene™ (dihydrolevoglucosenone) could be a potential alternative to the pyrolysis of wood chips/sawdust²¹⁷. Further, residual furfural compounds may offer applications as biofuels³²², platform molecules³²³ or monomers in poly furans³²⁴.

5.2.4. Further metal adsorption onto inherent sulfur-containing porous carbons

Copper(II) adsorption has been explored as an application for these sulfur-containing chars. In future work, more variables for adsorption should be explored to ensure the behaviour of these ISPCs is understood. Copper(II) adsorption at a wider range of pH values would be beneficial for the application of these materials to a range of effluent streams. Competitive adsorption should be applied to compare the affinity of these materials to different metal cations. The affinity of this material to copper also implies the potential affinity to pollutant transition metals and heavy metals (nickel, cobalt, cadmium, mercury, etc.), and valuable critical elements (silver, gold, and platinum group metals (PGMs))³²⁵.

5.2.5. Additional applications of inherent sulfur-containing porous carbons

A novel application would be the development of metal sulfide or metal oxide catalysts from carrageenan. IMEC800 have been shown to produce a porous surface containing magnesium oxide and calcium sulfide salt composites. Carrageenan cation exchange is possible through dissolution in salt solutions. Metal sulfide-doped carbons have been achieved from Iron, cobalt, nickel, copper, zinc, and cadmium-carrageenans. These materials have been applied to sodium ion storage in literature ¹²⁷. However, doping porous carbon materials with metal sulfides/metal oxides also allow the material to act as a catalyst. For example, molybdenum oxide-doped Starbon materials have been recognised as an effective catalyst for the reduction of 4-nitrophenol and DPPH radical quenching for use in waste-water treatment ³²⁶. Further, bismuth sulfides/oxides supported on a porous carbon have also been shown to have catalytic activity. This bismuth(III) sulfide and bismuth(III) oxide doped carbonaceous material is capable of CO₂ conversion to formic acid due to its electrochemically reducing metal salt layered surface ³²⁷. Further alkali metal-containing carbons derived from seaweed have been used for carbon capture. Specifically magnesium oxide played a key role in CO₂ sorption ³²⁸. The chars produced in this work exhibit a combination of magnesium oxide and calcium sulphide bound to a porous carbon surface, which could be an effective material for carbon capture and conversion.

5.2.6. Advancing microalgal supercritical CO₂ extraction

Supercritical extracts from the microalgae, ALG01, have been shown to contain a heavy mixture of lipid material, including identified fatty acids: EPA, myristic, palmitic, and palmitoleic acids, and phytosterols: cholesterol and sitosterol. Varying extraction conditions have been shown to manipulate the composition of the extractives.

Although certain extraction conditions favour certain biomolecules, these extracts were complex mixtures of materials as evidenced by DSC and GC-MS analysis. In future

work, supercritical fractionation of the extracts should be attempted to isolate EPA, carotenoids, or other highly valued extractives. Supercritical CO₂ fractionation is a technique which involves passing the extract/solvent mixture through several vessels set at varying temperature and pressure, enabling the selective deposition of certain metabolites in separate vessels. Isolation of valued omega-3 fatty acids without expensive distillation of lipid material is desired. Fractionation of omega-3 fatty acids from fish oils has been achieved in literature ³²⁹. These microalgal extracts showed potential for fractionation. Figure 118 shows deposits of dark red material (likely carotenoid rich) at the top of the vessel, which indicates an immediate deposition of this material as the pressure decreases. Yellow oils can be seen at a much greater depth into the vessel suggesting they are carried by the depressurising solvent for longer. Applying several vessels at a gradient of decreasing pressures would likely produce fractions of concentrated metabolites.



Figure 122: Supercritical CO₂ extraction vessel containing microalgal extract following an extraction under 300 bar and 35 °C.

5.2.7. Applications of microalgal lipid extracts

Antioxidants and oils have been recently infused within biodegradable food packaging films and edible films to reduce the permeability of the films and to provide an antioxidant layer that prevents oxygenation and loss of nutritional quality of the food^{78,316,317}. The microalgal supercritical extracts produced in this thesis have moderate antioxidant properties. Infusing these extracts with biodegradable films may afford a material containing a built in oxidation barrier and potential pigment indicator of spoilage/poor handling. Figure 119 shows the colour change of an ALG01 lipid extract following 'mistaken handling' where the sample was not refrigerated. Applied to food films, this colour change could indicate a spoiled food product, or improper food storage within the chain of safe food handling. This could potentially be a novel research area.

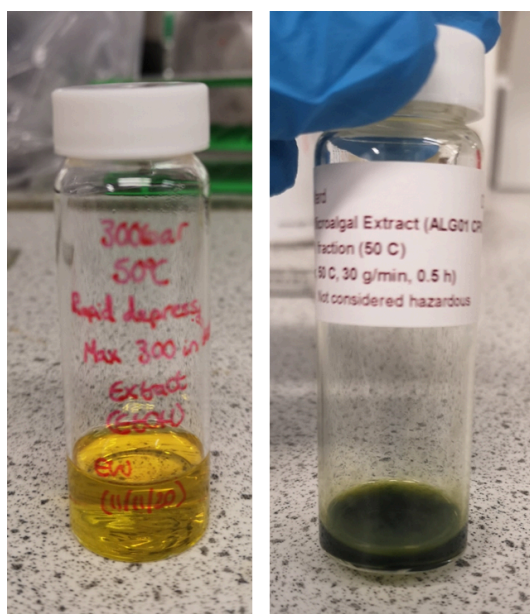


Figure 123: ALG01 supercritical CO₂ extracts (300 bar, 50 °C) in ethanol, after 24h refrigerated (left) and at room temperature (right).

5.2.8. Oil/protein-depleted ALG01 processing for bio-oil and biochar using hydrothermal liquefaction and microwave pyrolysis

Pyrolysis should be considered a last resort for a feedstock rich in high value materials. However, following EPA extraction, cell disruption, and protein extraction, the remaining residues are likely stripped of any extractable high value materials due to the destructive nature of some of the extraction and cell disruption techniques. In some cases hydrothermal liquefaction has been applied to valorise these residues. Biller *et al* used hydrothermal liquefaction (300 °C) on defatted and microwave processed *Nannochloropsis* microalgae to afford bio-crude with a HHV of ~40 MJ kg⁻¹ ²⁹⁰. Hydrothermal microwave processing was applied as a pre-treatment for lipid extraction but also to reduce the ash and nitrogen content of the bio-crude products. In the case of *Nannochloropsis*, this effect was limited ²⁹⁰. However, deoiled and protein-depleted ALG01 residues may exhibit reduced nitrogen contents following protein extraction and could afford bio-crude products with increased HHVs.

Microwave-assisted pyrolysis (MAP) is a green technology used to convert biomass into bio-oils and biochars. In a study by Du *et al*, *Chlorella* was converted to bio-oil via 500-1250 W MAP and afforded long chain aliphatic and aromatic hydrocarbons ³³⁰. Budarin *et al* achieved similar bio-oils at higher sample sizes (mass) but also recognised lower sample sizes offered a varied bio-oil rich in dehydrated sugars ³³¹. Applying varied microwave pyrolysis approaches to ALG01 residues may be another valuable piece of future work to complete the holistic biorefinery.

5.2. Conclusions

This thesis has explored green chemistry technologies to obtain materials and chemicals from renewable algal biomasses. Chapter 3 has shown the successful production of inherent sulfur-containing porous carbons from Irish Moss carrageenan which have an affinity towards aqueous copper(II); a common toxic waste stream. The production of these materials required minimal chemicals and steps, and is as follows:

1. Hot water extraction from Irish Moss.
2. Centrifugation for separation of supernatant and pellet.
3. Freeze-dry supernatant to afford carrageenan aerogel.
4. Pyrolyse carrageenan aerogels at desired temperature for specific characteristics.
5. Aqueous wash of pyrolysed char materials.

This method offered beneficial results in contrast to pyrolysing the macroalgae without treatment. Extracting the porous aerogel-forming carrageenan content enabled IMEC materials to exhibit increased porosity in contrast to IMC and RIMC. The higher carrageenan purity also afforded chars containing a higher, but also sole sulfur content in contrast to the sulfur and nitrogen content of IMC and RIMC. These IMEC materials then exhibited a higher copper(II) adsorption capacity compared with IMC materials under mildly acidic (pH 4) and strongly acidic conditions (pH 1). The presence of sulfur and high surface area of IMEC materials appeared to be a significant aspect to copper(II) adsorption under these conditions. These results should prompt the further development of carrageenan-derived inherent sulfur containing carbons for metal adsorption.

Chapter 4 provided potential holistic biorefinery approaches for the microalgal biomass ALG01. These methods afforded lipid and protein-based extracts with potential applications in nutritional supplements and novel defibrillated cellulose materials. The main aim of this work was to explore valorisation techniques in order to develop a zero waste biorefinery. These results offer two approaches to ALG01:

1. Supercritical CO₂ isolation of lipids, pigments and phenolics, followed by the microwave hydrothermal treatment for defibrillated cellulose and sugar rich hydrolysates.
2. Industrial Algaecytes EPA extraction for EPA and lipid content, followed by cell disruption combined protein extraction and tangential ultrafiltration for protein rich retentate and sugar rich permeate.

In conclusion this research has proven that both micro and macroalgae can serve as viable renewable feedstocks in the context of a zero-waste third generation biorefinery using green technologies, that produces novel sulfur-containing biochars, lipid extracts, enriched protein extracts, and defibrillated celluloses. These chemicals and materials have potential applications as metal adsorbents for waste-water treatment, antioxidants, proteins for renutrition, and rheology modifiers, respectively. A potential zero-waste algal biorefinery is summarised in figure 120.

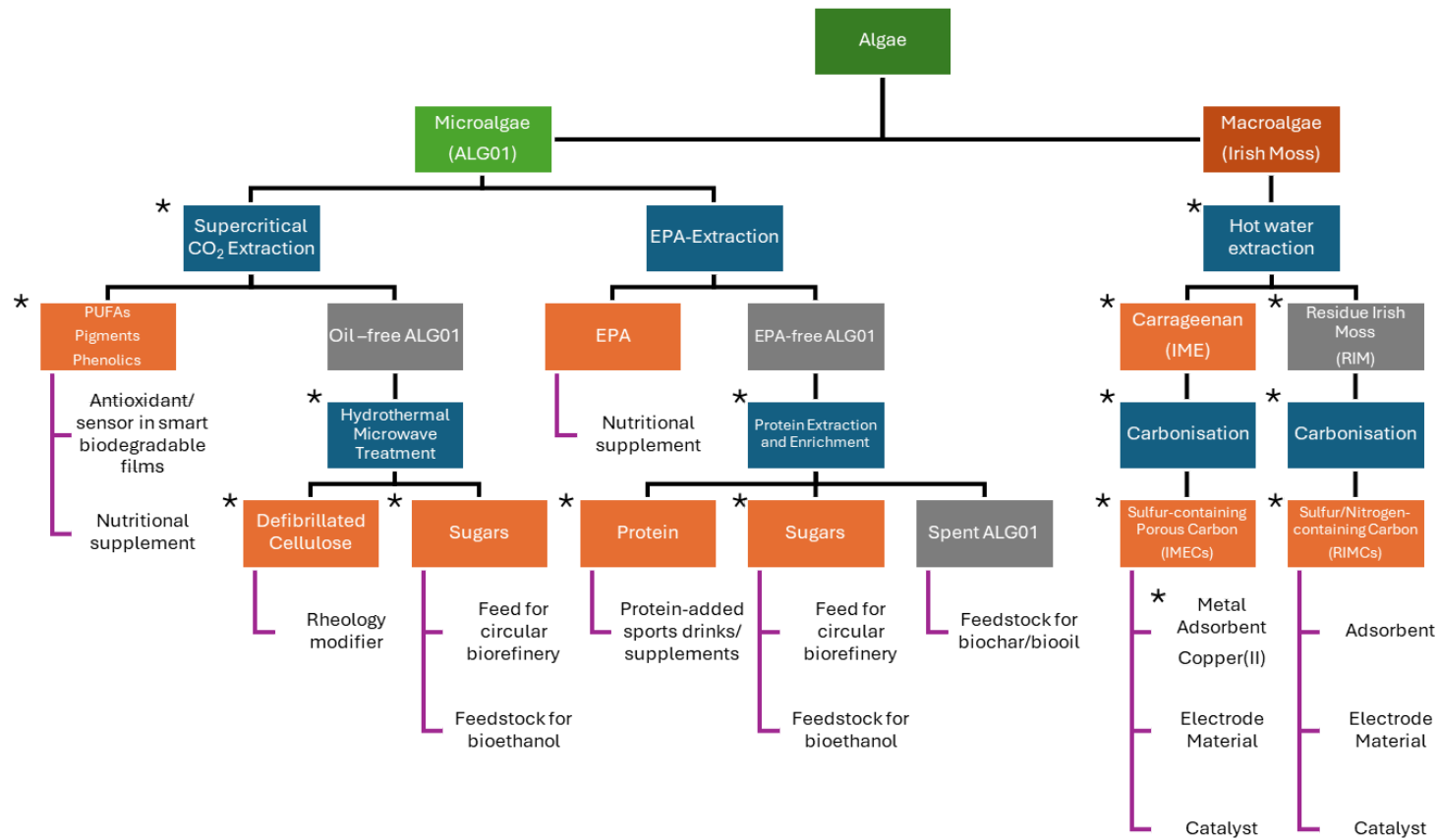


Figure 124: Proposed zero-waste biorefinery approaches for ALG01 microalgae and Irish Moss macroalgae including potential applications for all side products. Work completed in this thesis have been highlighted using *.

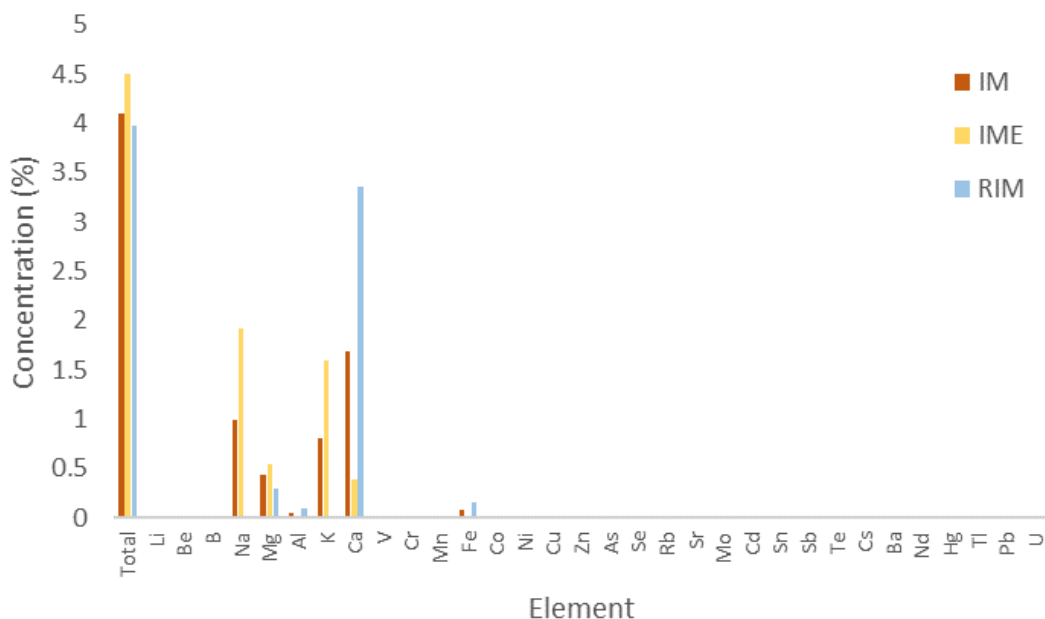
Appendices:

Chapter 1:

Appendix 1.1. 12 green chemistry principles ¹⁸⁶

Green Chemistry Principle	Description
1. Prevention	Waste prevention is preferable to waste treatment or cleaning up waste after its production.
2. Atom Economy	Efficient synthesis of products by maximising the incorporation of every aspect of reagents into the final product.
3. Less Hazardous Chemical Synthesis	Synthetic processes should be designed to use and generate materials that have minimal toxicity to human or environmental health.
4. Designing Safer Chemicals	Chemicals should be designed to be less hazardous and have minimal toxicity, while retaining functionality and efficacy.
5. Safer Solvents and Auxiliaries	The use of auxiliary substances such as, solvents and separation agents, should be made unnecessary wherever possible and, innocuous when used.
6. Design for Energy Efficiency	Energy requirements should be associated with their environmental and economic impact and should be minimised. Ambient conditions are preferable.
7. Use of Renewable Feedstocks	Feedstocks should be renewable rather than depleting to ensure the sustainability of the industries.
8. Reduce Derivatives	Unnecessary derivatization should be minimised or avoided if possible, because such steps require additional reagents and can generate waste.
9. Catalysis	Selective catalytic reagents are superior to stoichiometric reagents.
10. Design for Degradation	Products and waste if unavoidable should be designed to safely degrade and not persist in the environment.
11. Real-time Analysis for Pollution Prevention	Analytical methodologies need to be developed to allow for real-time, in-process monitoring and control prior to the formation of hazardous substances.
12. Inherently Safer Chemistry for Accident Prevention	Substances used in chemical processes should be selected to minimise the risk of chemical accidents.

Chapter 3:

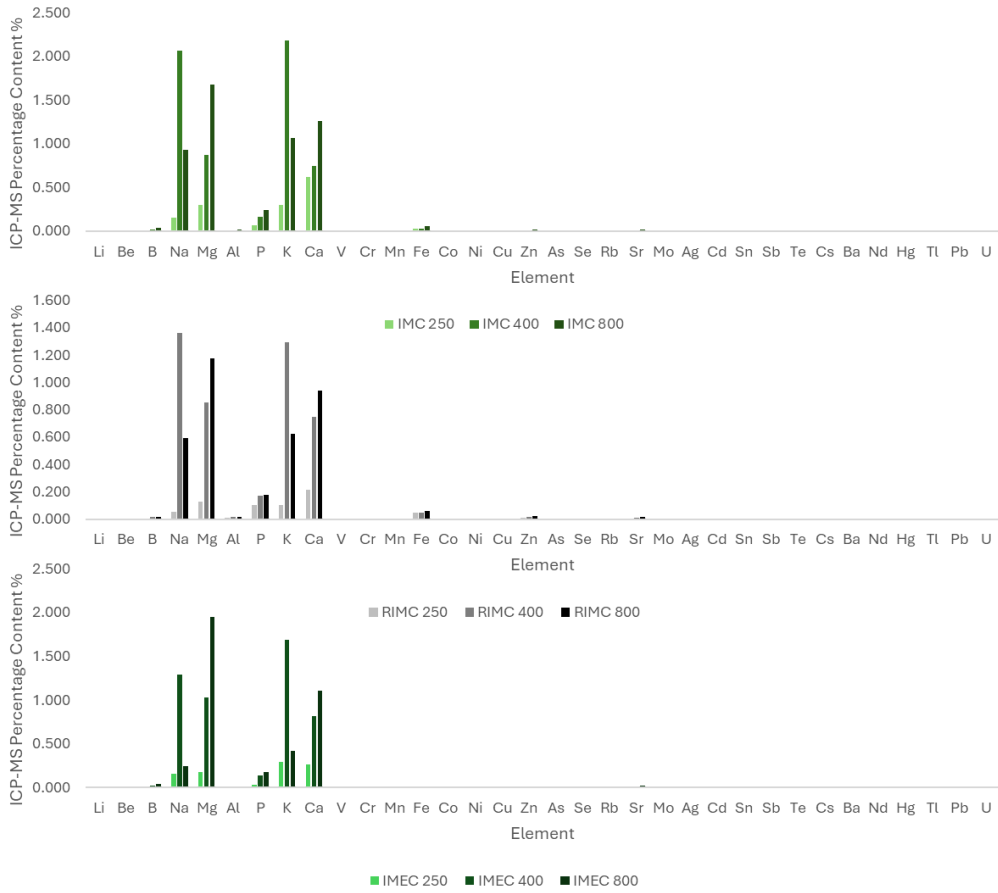


Appendix 3.1. Full ICP-MS measured mineral concentrations for IM, IME, and RIM.

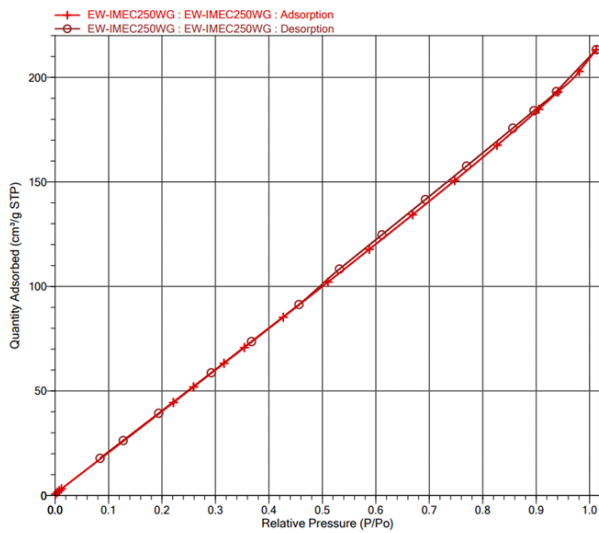
Appendix 3.2: Table of CHNS contents for IM, IME, and RIM at various pyrolysis temperatures before and after washing with hot water and acetone.

Material		Pyrolysis Temperature						
		0 °C	250 °C	250 °C Washed	400 °C	400 °C Washed	800 °C	800 °C Washed
IM	C%	29.4 ±0.04	45.8 ±0.09	55.2 ±0.10	51.3 ±0.25	57.0 ±0.12	57.6 ±0.06	63.3 ±0.07
	H%	4.8 ±0.16	3.5 ±0.06	5.0 ±0.04	2.3 ±0.14	3.1 ±0.05	1.6 ±0.08	1.69 ±0.07
	N%	2.2 ±0.04	3.2 ±0.10	4.1 ±0.08	3.6 ±0.07	3.1 ±0.07	3.0 ±0.03	3.1 ±0.02
	S%	1.6 ±0.13	4.4 ±0.08	2.1 ±0.04	3.7 ±0.23	3.3 ±0.06	1.7 ±0.23	2.5 ±0.26
	R%	62.1	43.1	33.7	39.1	33.6	36.1	29.4
IME	C%	25.4	39.3	53.9	46.2	59.4	51.0	62.9

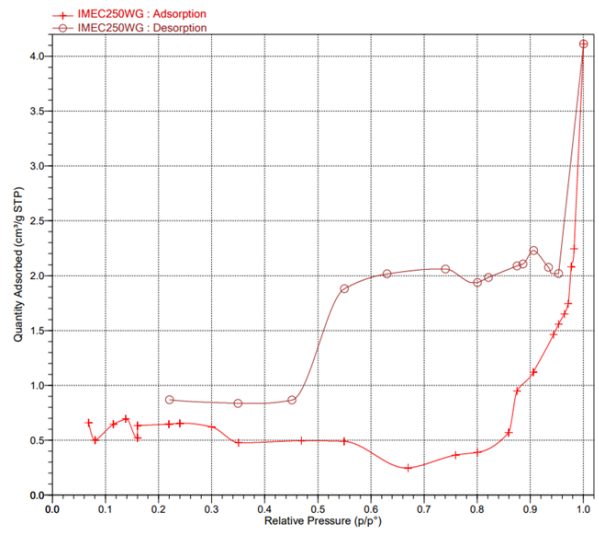
		±0.07	±0.05	±0.08	±0.09	±0.06	±0.16	±0.25
	H%	4.3 ±0.01	1.8 ±0.04	3.4 ±0.08	2.5 ±0.05	1.2 ±0.08	0.4 ±0.06	0.8 ±0.09
	N%	N.D	N.D	N.D	0.5 ±0.06	N.D	N.D	N.D
	S%	4.9 ±0.23	7.5 ±0.25	7.6 ±0.09	3.5 ±0.13	3.9 ±0.16	3.7 ±0.11	4.3 ±0.21
	R%	65.4	51.4	35.1	47.3	35.5	44.9	32.0
RIM	C%	40.5 ±0.37	46.9 ±0.09	54.4 ±0.26	58.1 ±0.04	60.7 ±0.13	64.4 ±0.05	61.3 ±0.14
	H%	6.8 ±0.38	3.4 ±0.09	4.7 ±0.05	3.0 ±0.04	2.9 ±0.01	1.0 ±0.13	1.2 ±0.10
	N%	4.2 ±0.16	4.4 ±0.10	5.8 ±0.06	5.0 ±0.13	4.2 ±0.11	5.7 ±0.09	5.5 ±0.08
	S%	2.3 ±0.23	5.0 ±0.10	2.0 ±0.08	2.98 ±0.13	2.1 ±0.06	3.3 ±0.09	2.6 ±0.11
	R%	46.1	40.2	33.1	30.9	30.1	25.6	29.4



Appendix 3.3. ICP-MS measured mineral contents of IM, IME, and RIM chars from pyrolysis at 250, 400, and 800 °C.

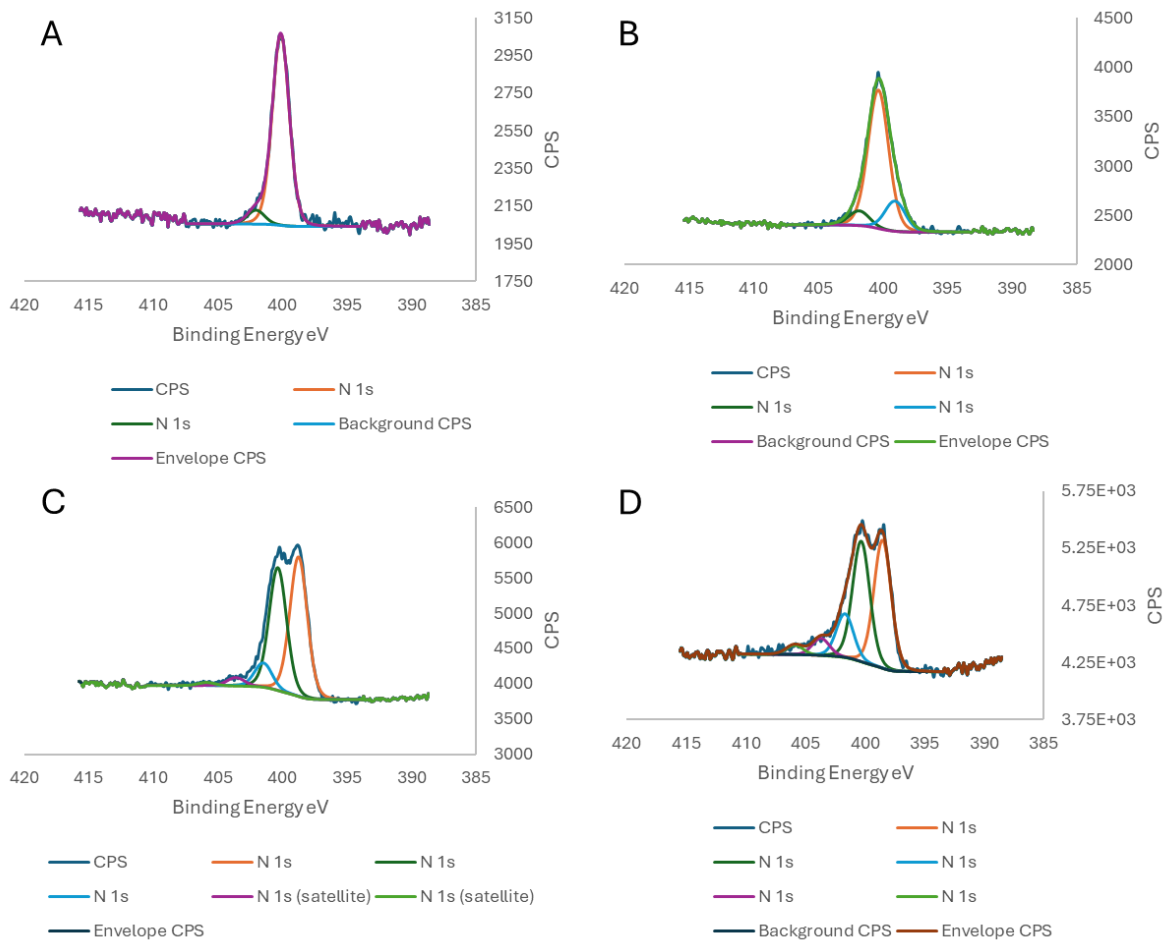


Micromeritics Tristar II



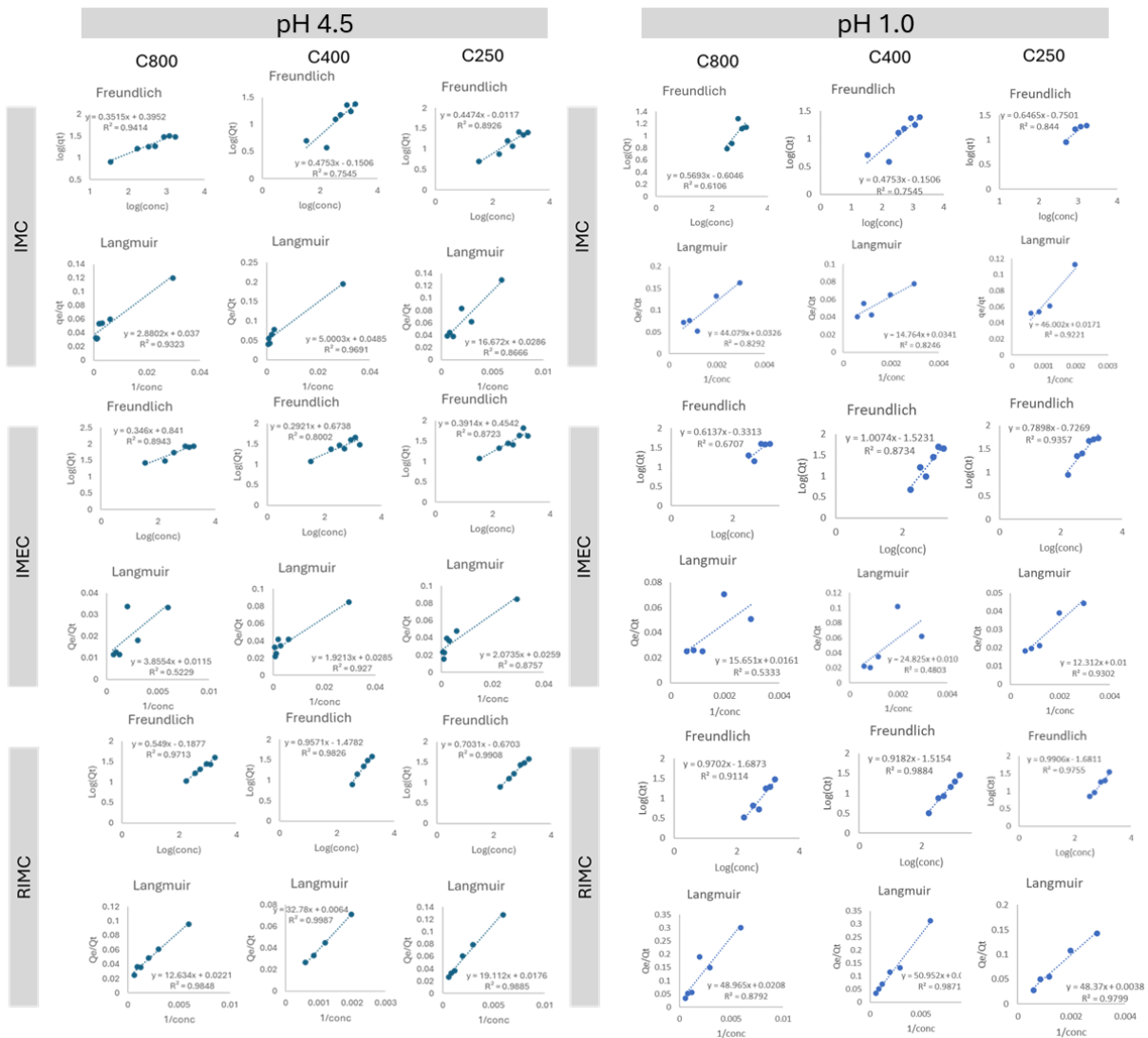
Micromeritics ASAP 2020

Appendix 3.3. N₂ adsorption porosimetry isotherms of IMEC250 from two different instruments Micromeritics Tristar and ASAP 2020.



RIM (A), RIMC250 (B), RIMC400 (C), and RIMC800 (D)

Appendix 3.4. XPS spectra of RIM and RIMC materials showing the N 1s region.



Appendix 3.5. Freundlich and Langmuir linearised copper(II) adsorption isotherm plots

Linearised Langmuir:

$$\frac{1}{q_c} = \frac{1}{q_m} + \frac{1}{q_m K_L} \cdot \frac{1}{C}$$

Linearised Freundlich:

$$\log(q_c) = \log(K_f) + \frac{1}{n} \cdot \log(C)$$

Appendix 3.6. Table of linear regression R^2 values, χ^2 errors, and sum square errors

(ERRSQ) for the fit between Freundlich and Langmuir isotherm models and the adsorption isotherm of copper(II) onto IM, IME, and RIM chars at a pH of 4.5.

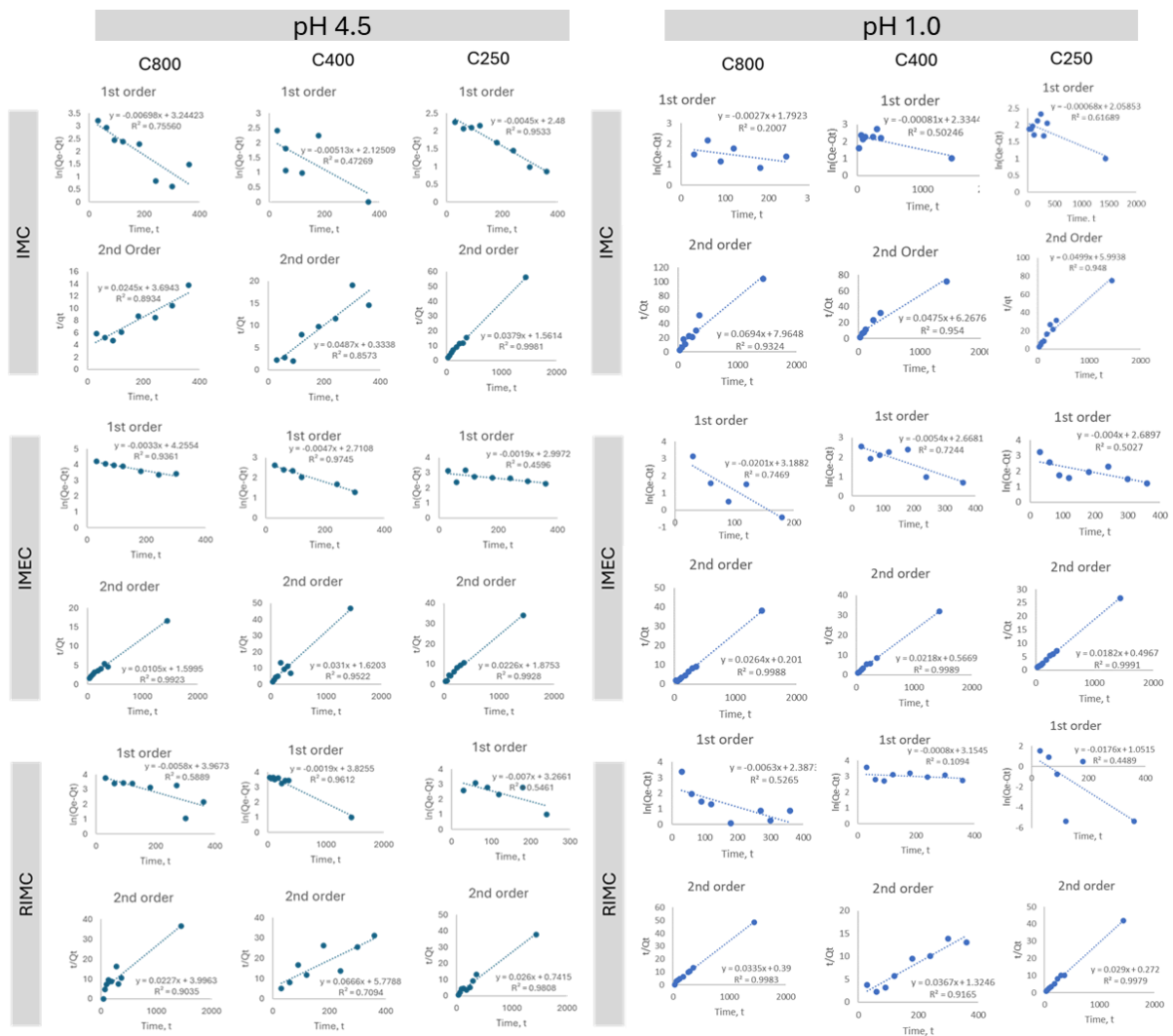
Material	Freundlich			Langmuir		
	Linear regression R^2	χ^2	ERRSQ	Linear regression R^2	χ^2	ERRSQ
IMC250	0.893	3.97	72.0	0.867	5.46	72.3
IMC400	0.755	7.39	68.5	0.969	24.12	146.6
IMC800	0.941	2.02	52.3	0.932	5.50	147.0
IMEC250	0.872	10.37	528.0	0.876	19.22	1010.3
IMEC400	0.800	7.85	256.0	0.927	6.76	252.1
IMEC800	0.894	38.06	1285.7	0.523	43.36	1882.5
RIMC250	0.991	0.42	12.1	0.989	0.80	23.1
RIMC400	0.983	23.45	29.7	0.999	31.14	27.3
RIMC800	0.971	8.19	134.5	0.985	11.79	208.7

Appendix 3.7. Table of linear regression R^2 values, χ^2 errors, and sum square errors

(ERRSQ) for the fit between Freundlich and Langmuir isotherm models and the adsorption isotherm of copper(II) onto IM, IME, and RIM chars at a pH of 1.

Material	Freundlich			Langmuir		
	Linear regression R^2	χ^2	ERRSQ	Linear regression R^2	χ^2	ERRSQ
IMC250	0.844	15.84	70.7	0.922	10.28	48.8
IMC400	0.755	7.39	68.5	0.825	8.28	59.2
IMC800	0.611	4.19	94.8	0.829	3.85	80.4
IMEC250	0.936	5.49	247.8	0.930	2.88	83.7
IMEC400	0.873	10.27	278.0	0.480	14.21	428.8

Material	Freundlich			Langmuir		
	Linear regression R ²	χ^2	ERRSQ	Linear regression R ²	χ^2	ERRSQ
IMEC800	0.671	30.20	264.4	0.533	21.83	235.5
RIMC250	0.976	0.84	30.3	0.980	1.07	40.1
RIMC400	0.988	0.26	2.5	0.987	0.34	3.6
RIMC800	0.911	3.14	27.8	0.879	7.25	142.8



Appendix 3.8. Pseudo-first and second order linearised copper(II) adsorption kinetic plots

Linearised forms of pseudo-first and second order models are expressed below, respectively. In both equations boundary conditions have been applied where at $t = 0$, $q_t = 0$ and $t = t$, $q_t = q_e$.

Linearised pseudo-first:
$$\ln(q_e - q_t) = \ln q_e - k_1 t$$

Linearised pseudo-second:
$$\frac{t}{q_t} = \frac{1}{k_2 q_e^2} + \frac{1}{q_e} t$$

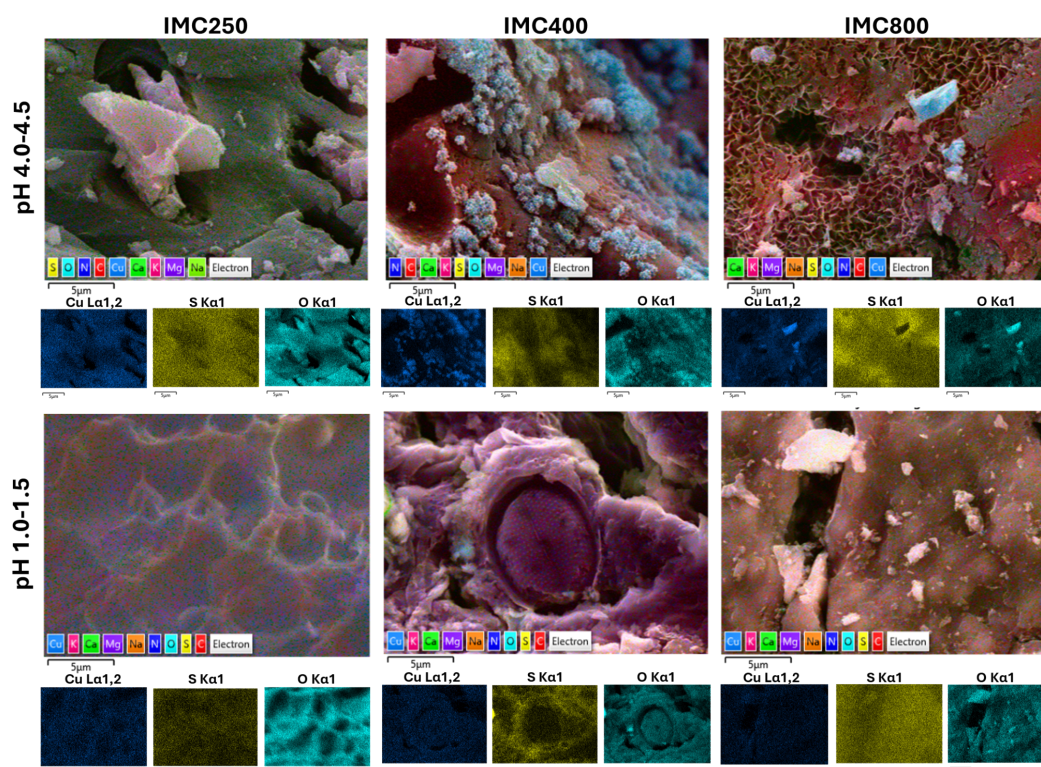
Appendix 3.9. Table of linear regression R^2 values, χ^2 errors, and sum square errors (ERRSQ) for the fit between Pseudo-first and second order kinetic models and the adsorption kinetics of copper(II) onto IM, IME, and RIM chars at a pH of 4.5.

Material	Pseudo-first order			Pseudo-second order		
	Linear regression R^2	χ^2	ERRSQ	Linear regression R^2	χ^2	ERRSQ
IMC250	0.953	29.37	523.3	0.998	2.65	47.2
IMC400	0.472	51.40	1725.4	0.857	25.64	742.9
IMC800	0.756	2.33	48.9	0.893	6.74	160.6
IMEC250	0.460	88.97	2480.9	0.993	11.24	312.8
IMEC400	0.975	43.34	1327.0	0.952	23.00	815.7
IMEC800	0.936	27.69	1117.4	0.992	5.57	376.2
RIMC250	0.546	65.05	2909.0	0.981	33.41	1483.2
RIMC400	0.961	14.18	140.8	0.709	44.35	421.6
RIMC800	0.589	20.24	349.8	0.904	49.05	744.5

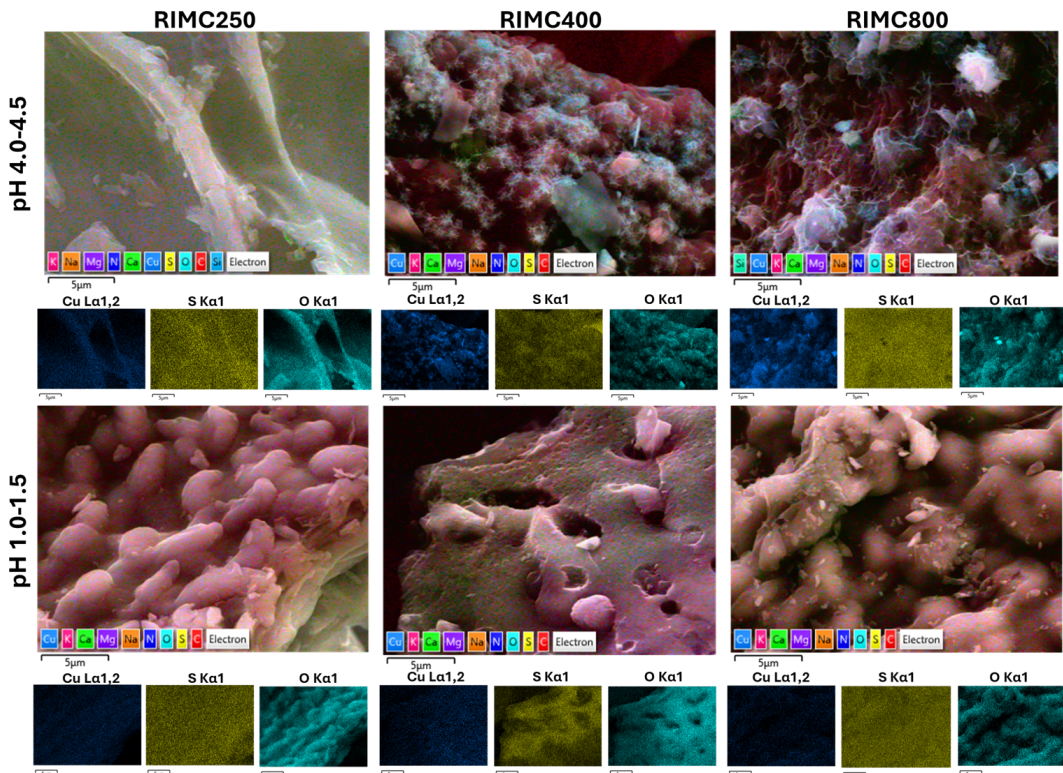
Appendix 3.10. Table of linear regression R^2 values, χ^2 errors, and sum square errors (ERRSQ) for the fit between Pseudo-first and second order kinetic models and the adsorption kinetics of copper(II) onto IM, IME, and RIM chars at a pH of 1.

Material	Pseudo-first order			Pseudo-second order		
	Linear regression R^2	χ^2	ERRSQ	Linear regression R^2	χ^2	ERRSQ
IMC250	0.617	69.81	883.1	0.948	13.90	169.5
IMC400	0.502	47.43	581.6	0.954	30.62	254.1
IMC800	0.201	25.20	272.7	0.932	13.27	142.7
IMEC250	0.503	91.99	3947.7	0.999	2.24	105.0
IMEC400	0.724	66.89	2406.6	0.999	4.16	144.6

Material	Pseudo-first order			Pseudo-second order		
	Linear regression R ²	χ^2	ERRSQ	Linear regression R ²	χ^2	ERRSQ
IMEC800	0.747	2.69	93.1	0.999	14.44	243.4
RIMC250	0.449	15.46	490.1	0.998	2.61	81.7
RIMC400	0.109	127.21	3046.0	0.917	10.13	211.3
RIMC800	0.527	21.51	564.2	0.998	0.46	471.2

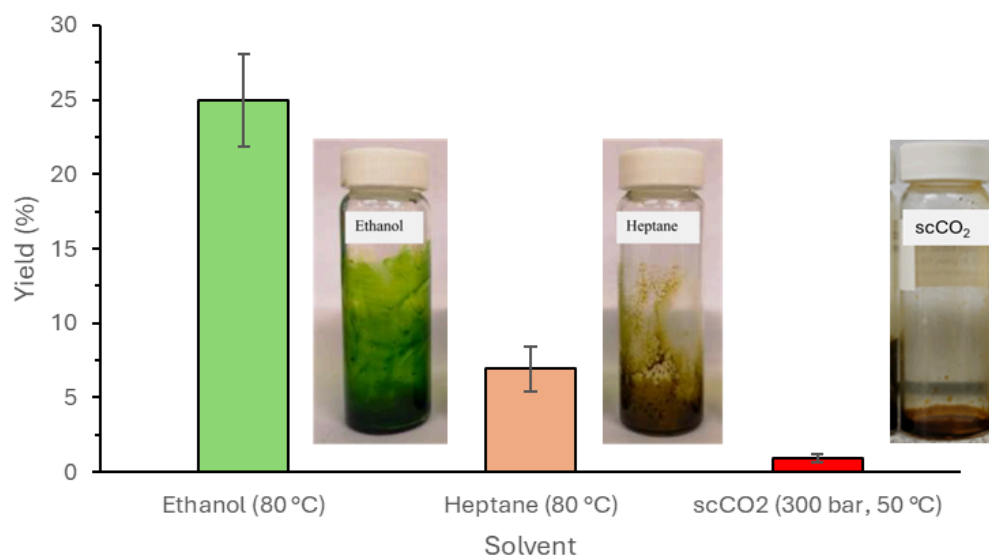


Appendix 3.11. Copper-containing IMC SEM-EDS elemental mapping images



Appendix 3.12. Copper-containing RIMC SEM-EDS elemental mapping images

Chapter 4:



Appendix 4.1. Yield comparison between ethanol and heptane solvent extractions from spray dried ALG01 and the highest yielding supercritical extraction (300 bar, 50 °C).

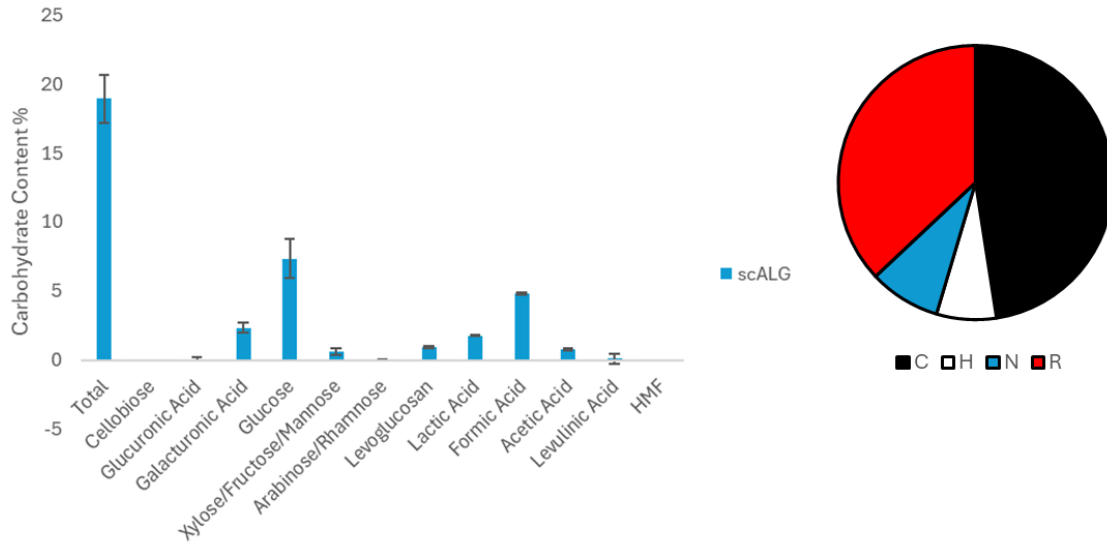
Appendix 4.2. Preliminary characterisation of ALG01 post supercritical CO₂ extraction of oils

	Composition (%)
	scCO ₂ oil-free ALG01
Carbohydrate^a	18.9 ± 1.7
Protein^b	42.8 ± 1.0
Moisture^c	N/A
Residual matter (Char)^c	N/A
Acid-insoluble content	59.2 ± 18.8
Acid-insoluble Ash	17.9 ± 6.0

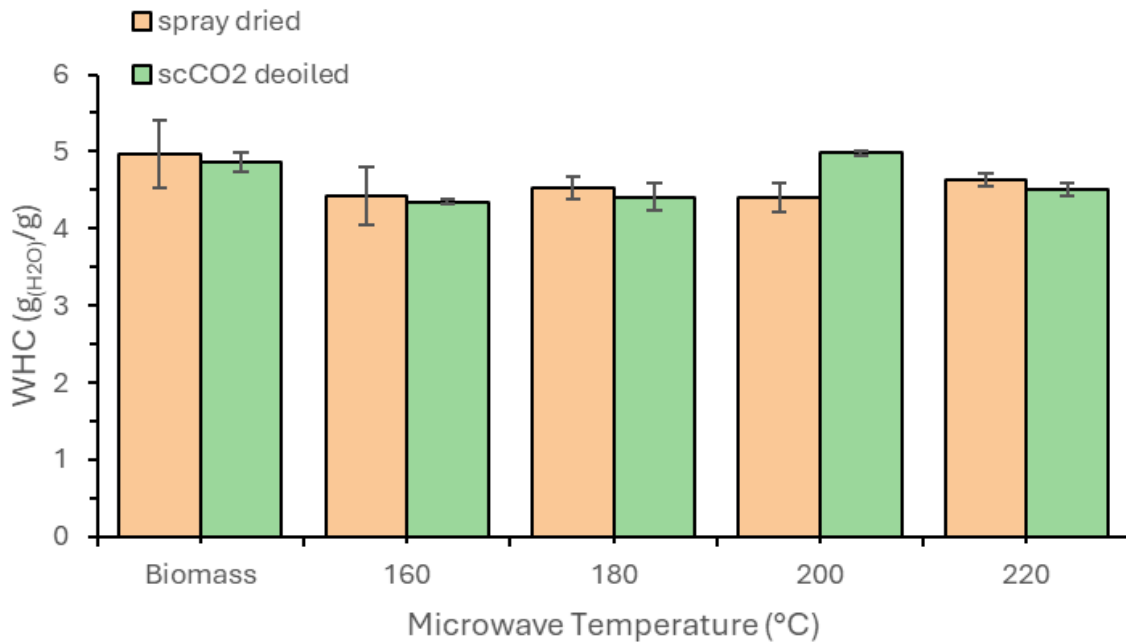
^a Derived via Klason acid-digestion and HPLC analysis

^b Estimated from CHN nitrogen content using 5.1 as a conversion factor

° Derived via TGA



Appendix 4.3. Acid-hydrolysed carbohydrate content derived via Klason analysis (left) and elemental composition (right) of scCO₂ oil-free ALG01.



Appendix 4.4: Water holding capacities (WHC) of defibrillated celluloses derived from both spray dried and scCO₂ deoiled biomass.

Chapter 5:

Appendix 5.1. Methodology for microwave assisted carrageenan extraction

Irish Moss biomass was ground by coffee grinder to a granular powder (<50 μm). This material was then immersed in deionized water (25:1 mL:g) and the contents were stirred and heated by microwave. Microwave-assisted extraction of carrageenan was carried out on a Milestone Synthwave reactor (1500 W, 2.45 GHz). The algae water mixture was added to a PTFE vessel (900 mL) and microwaved at 50 or 100 °C for a total time of 20 or 10 minutes (50:50 ramp:hold).

The resulting mixture was then immediately centrifuged using a Thermo Fisher Megafuge 4R (3000 rpm, 30 °C, 30 min) to isolate a supernatant and pellet. Both supernatant and pellet were dried using a Labylo Controlled Freeze Drier for 48h or until dry before being labelled IME and RIM respectively. Subscripts X/Y were added where MAE was applied where X is the microwave temperature and Y is the extraction duration. The aerogels were characterised by CHNS, TGA, VT NMR, ATR-IR, and gel formation. (IME_{100/20}: 59.6 \pm 1.49%, IME_{100/10}: 54.8 \pm 3.33%, IME_{50/20}: 51.7 \pm 1.29%).

Appendix 5.2. Methodology for next generation Carr300 carbons

Dried IME materials were dissolved in distilled water at concentrations of 2.5 - 25.0 % (w/v) and maintained at 80 °C for 30 minutes to ensure complete dissolution. Gels were cooled and refrigerated for 24 h. The retrograded hydrogels were rapidly frozen in liquid N₂ and freeze-dried using a Labylo Controlled Freeze Drier for 48h.

Expanded carrageenan aerogels were produced from 10 % retrograded gels by mixing the gel with ethanol (1:1 ratio by volume) for 30 minutes. The now alcogels were freeze-dried as above.

Aerogels (10 g) were loaded into a quartz flask and placed under vacuum (~30 mbar) and heated using the following program: the samples were initially heated to 100 °C at a rate of 5 °C min⁻¹, and held at this temperature for 60 min. The samples were then heated to 300

°C at a rate of 0.3 °C min⁻¹. The chars were subsequently washed with HCl (10 M) (50 mL) for 48h, filtered, and rinsed with hot water (2x 50 mL) and dried by vacuum oven at 80 °C overnight.

Chapter 6. References

- 1 A. K. Koyande, P.-L. Show, R. Guo, B. Tang, C. Ogino and J.-S. Chang, *Bioengineered*, 2019, **10**, 574–592.
- 2 D. Ravelli and C. Samori, *Biomass valorization: Sustainable methods for the production of chemicals*, Blackwell Verlag, Berlin, Germany, 2021.
- 3 C. S. Julie Chandra, S. Sasi, T. K. Bindu Sharmila and J. R. Varghese, in *Handbook of Biomass*, eds. S. Thomas, M. Hosur, D. Pasquini and C. Jose Chirayil, Springer Nature Singapore, Singapore, 2023, pp. 1–31.
- 4 F. Cherubini, *Energy Convers. Manag.*, 2010, **51**, 1412–1421.
- 5 R. Chandra, H. M. N. Iqbal, G. Vishal, H.-S. Lee and S. Nagra, *Bioresour. Technol.*, 2019, **278**, 346–359.
- 6 M. Court, Blue-green algae: How to spot in UK water and why is it harmful?, <https://www.greatbritishlife.co.uk/things-to-do/23590025.blue-green-algae-spot-uk-water-harmful/>, (accessed 4 November 2024).
- 7 R. Kassinger, *Slime: How algae created us, plague us, and just might save us*, Mariner Books, USA, 2019.
- 8 Keel Labs, <https://www.keellabs.com/press/fashion-2024-knitwear-ribbons-and-other-trends-for-the-year-ahead>, (accessed 4 November 2024).
- 9 Home, <https://www.notpla.com/>, (accessed 8 November 2024).
- 10 R. P. Rastogi, D. Madamwar and A. Pandey, *Algal green chemistry: Recent Progress in Biotechnology*, Elsevier, San Diego, Netherlands, 2017.
- 11 T. Cavalier-Smith, E. E. Chao and R. Lewis, *Protoplasma*, 2018, **255**, 1517–1574.
- 12 S. Mobin and F. Alam, *Energy Procedia*, 2017, **110**, 510–517.
- 13 A. N. Smith and A. D. Barton, *Ecol. Evol.*, 2024, **14**, e10882.
- 14 N. E.-A. El-Naggar, M. H. Hussein, S. A. Shaaban-Dessuuki and S. R. Dalal, *Sci. Rep.*, 2020, **10**, 3011.
- 15 A. Molino, V. Larocca, G. Di Sanzo, M. Martino, P. Casella, T. Marino, D. Karatza and D. Musmarra, *Molecules*, 2019, **24**, 782.
- 16 F. Saliu, C. Magoni, A. Torelli, R. Cozza, M. Lasagni and M. Labra, *Food Chem.*, 2021, **337**, 127745.
- 17 M. M. Allaf, PhD Thesis, Western University, 2013.
- 18 *Dunaliella salina* Teodoresco ssp. *salina*, <https://ccala.butbn.cas.cz/en/dunaliella-salina-teodoresco-ssp-salina>, (accessed 6 March 2024).
- 19 A. Oren, *Saline Systems*, 2005, **1**, 2.
- 20 L. Pereira, *Encyclopedia (Basel, 2021)*, 2021, **1**, 177–188.
- 21 M. L. Wells, P. Potin, J. S. Craigie, J. A. Raven, S. S. Merchant, K. E. Helliwell, A. G. Smith, M. E. Camire and S. H. Brawley, *J. Appl. Phycol.*, 2017, **29**, 949–982.
- 22 W. Wijaya, A. R. Patel, A. D. Setiowati and P. Van der Meeren, *Trends Food Sci. Technol.*, 2017, **68**, 56–69.
- 23 USPTO, 20200047927:A1, *US Patent*, 2020.
- 24 A. Frearson, London Marathon offers edible seaweed drinks capsules as alternative to plastic bottles, <https://www.dezeen.com/2019/04/29/london-marathon-ooho-edible-drinks-capsules-sea-weed/>, (accessed 4 November 2024).
- 25 News Center, <https://www.notpla.com/news-center>, (accessed 4 November 2024).
- 26 *Laminaria digitata*, https://www.seaweed.ie/descriptions/Laminaria_digitata.php, (accessed 4 November 2024).
- 27 Ooho, <https://www.notpla.com/ooho>, (accessed 4 November 2024).
- 28 S. Nara, What is Dashi? Everything You Need to Know About Japanese Soup Stock, <https://thejapanstore.us/dashi/what-is-dashi/>, (accessed 4 November 2024).
- 29 P. Geada, V. Vasconcelos, A. Vicente and B. Fernandes, in *Algal Green Chemistry*, eds. R. P. Rastogi, D. Madamwar and A. Pandey, Elsevier, Amsterdam, 2017, pp. 257–284.
- 30 K. Brindhadevi, T. Mathimani, E. R. Rene, S. Shanmugam, N. T. L. Chi and A. Pugazhendhi, *Fuel (Lond.)*, 2021, **284**, 119058.

- 31 M. Massa, S. Buono, A. L. Langellotti, A. Martello, G. L. Russo, D. A. Troise, R. Sacchi, P. Vitaglione and V. Fogliano, *N. Biotechnol.*, 2019, **53**, 9–15.
- 32 S. K. Bhatia, S. Mehariya, R. K. Bhatia, M. Kumar, A. Pugazhendhi, M. K. Awasthi, A. E. Atabani, G. Kumar, W. Kim, S.-O. Seo and Y.-H. Yang, *Sci. Total Environ.*, 2021, **751**, 141599.
- 33 H. Onyeaka, T. Miri, K. Obileke, A. Hart, C. Anumudu and Z. T. Al-Sharif, *Carbon Capture Science & Technology*, 2021, **1**, 100007.
- 34 S. Banerjee, A. Ray and D. Das, *Sci. Total Environ.*, 2021, **762**, 143080.
- 35 B. Zhao and Y. Su, *Algal Res.*, 2020, **51**, 102066.
- 36 D. Vandamme, I. Foubert and K. Muylaert, *Trends Biotechnol.*, 2013, **31**, 233–239.
- 37 A. L. Ahmad, N. H. Mat Yasin, C. J. C. Derek and J. K. Lim, *Environ. Technol.*, 2014, **35**, 2244–2253.
- 38 T. M. M. Bernaerts, L. Gheysen, I. Foubert, M. E. Hendrickx and A. M. Van Loey, *Biotechnol. Adv.*, 2019, **37**, 107419.
- 39 M. J. Scholz, T. L. Weiss, R. E. Jinkerson, J. Jing, R. Roth, U. Goodenough, M. C. Posewitz and H. G. Gerken, *Eukaryot. Cell*, 2014, **13**, 1450–1464.
- 40 R. Zhang, O. Parniakov, N. Grimi, N. Lebovka, L. Marchal and E. Vorobiev, *Bioprocess Biosyst. Eng.*, 2019, **42**, 173–186.
- 41 L. Liu, G. Pohnert and D. Wei, *Mar. Drugs*, 2016, **14**, 191.
- 42 T. Ischebeck, H. E. Krawczyk, R. T. Mullen, J. M. Dyer and K. D. Chapman, *Semin. Cell Dev. Biol.*, 2020, **108**, 82–93.
- 43 Y. Chisti, *Biotechnol. Adv.*, 2007, **25**, 294–306.
- 44 T. Suganya, M. Varman, H. H. Masjuki and S. Renganathan, *Renew. Sustain. Energy Rev.*, 2016, **55**, 909–941.
- 45 A. K. Sharma, P. Ghodke, P. K. Sharma, S. Manna, A. Pugazhendhi, L. Matsakas and A. Patel, *Biomass Convers. Biorefin.*, 2024, **14**, 5261–5274.
- 46 A. Molino, M. Martino, V. Larocca, G. Di Sanzo, A. Spagnoletta, T. Marino, D. Karatza, A. Iovine, S. Mehariya and D. Musmarra, *Mar. Drugs*, 2019, **17**, 132.
- 47 R. Siahbalaei, G. Kavooosi and M. Noroozi, *Phycological Res.*, 2021, **69**, 116–123.
- 48 T. H. Pham, V. T. A. Nguyen, T. T. T. Do, A. D. Do, D. T. Dam, T. T. Van Tran, Q. L. Pham and T. T. Le, *J. Chem.*, 2020, **2020**, 1–10.
- 49 J. B. Svenning, L. Dalheim, T. Vasskog, L. Matricon, B. Vang and R. L. Olsen, *Sci. Rep.*, 2020, **10**, 22229.
- 50 S. S. Aveiro, T. Melo, A. Figueiredo, P. Domingues, H. Pereira, I. B. Maia, J. Silva, M. R. Domingues, C. Nunes and A. S. P. Moreira, *Biomolecules*, 2020, **10**, 1434.
- 51 J. Masojidek, G. Torzillo and M. Koblížek, in *Handbook of Microalgal Culture*, John Wiley & Sons, Ltd, Oxford, UK, 2013, pp. 21–36.
- 52 R. Yadavalli, H. Ratnapuram, J. R. Peasari, C. N. Reddy, V. Ashokkumar and C. Kuppam, *Biomass Convers. Biorefin.*, 2022, **12**, 881–889.
- 53 K. Chen and M. Roca, *Food Chem.*, 2018, **266**, 368–374.
- 54 M. Martins, A. P. M. Fernandes, M. A. Torres-Acosta, P. N. Collén, M. H. Abreu and S. P. M. Ventura, *Sep. Purif. Technol.*, 2021, **254**, 117589.
- 55 M. D. Macías-Sánchez, C. Mantell Serrano, M. Rodríguez Rodríguez, E. Martínez de la Ossa, L. M. Lubián and O. Montero, *J. Sep. Sci.*, 2008, **31**, 1352–1362.
- 56 R. Zhang, A. K. L. Yuen, R. de Nys, A. F. Masters and T. Maschmeyer, *Algal Res.*, 2020, **52**, 102092.
- 57 Carotenoids Market Size, Share, Revenue, Forecast, 2032, <https://www.fortunebusinessinsights.com/industry-reports/carotenoids-market-100180>, (accessed 4 November 2024).
- 58 N. Singh, A. H. Batghare, B. J. Choudhury, A. Goyal and V. S. Moholkar, *Bioresour. Technol. Rep.*, 2020, **11**, 100440.
- 59 N. Miękus, A. Iqbal, K. Marszałek, C. Puchalski and A. Świergiel, *Molecules*, 2019, **24**, 4339.
- 60 R. V. Singh and K. Sambyal, *Food Biosci.*, 2022, **47**, 101717.
- 61 G. L. Parker, L. K. Smith and I. R. Baxendale, *Tetrahedron*, 2016, **72**, 1645–1652.

- 62 A. Mouahid, K. Seengeon, M. Martino, C. Crampon, A. Kramer and E. Badens, *J. Supercrit. Fluids*, 2020, **165**, 104934.
- 63 C. Latsos, J. van Houcke, L. Blommaert, G. P. Verbeeke, J. Kromkamp and K. R. Timmermans, *J. Appl. Phycol.*, 2021, **33**, 729–741.
- 64 Y. Xu, Q. Wang and Y. Hou, *Mar. Drugs*, 2020, **18**, 618.
- 65 P. Ardiles, P. Cerezal-Mezquita, F. Salinas-Fuentes, D. Órdenes, G. Renato and M. C. Ruiz-Domínguez, *Processes (Basel)*, 2020, **8**, 1628.
- 66 B. D. Ribeiro, D. W. Barreto and M. A. Z. Coelho, *Food Bioproc. Tech.*, 2011, **4**, 693–701.
- 67 J. Cotas, A. Leandro, P. Monteiro, D. Pacheco, A. Figueirinha, A. M. M. Gonçalves, G. J. da Silva and L. Pereira, *Mar. Drugs*, 2020, **18**, 384.
- 68 S. M. Zakaria, S. M. Mustapa Kamal, R. Harun, R. Omar and S. I. Siajam, *Sains Malays.*, 2020, **49**, 765–774.
- 69 J. Jofre, P. S. M. Celis-Plá, F. L. Figueroa and N. P. Navarro, *Mar. Drugs*, 2020, **18**, 75.
- 70 S. Kraan, in *Carbohydrates - Comprehensive Studies on Glycobiology and Glycotechnology*, ed. C.-F. Chang, InTech, Rijeka, 2012.
- 71 E.-S. Biris-Dorhoi, D. Michiu, C. R. Pop, A. M. Rotar, M. Tofana, O. L. Pop, S. A. Socaci and A. C. Farcas, *Nutrients*, 2020, **12**, 3085.
- 72 C. O. Pandeirada, É. Maricato, S. S. Ferreira, V. G. Correia, B. A. Pinheiro, D. V. Evtuguin, A. S. Palma, A. Correia, M. Vilanova, M. A. Coimbra and C. Nunes, *Carbohydr. Polym.*, 2019, **222**, 114962.
- 73 M.-J. Chanda, N. Merghoub and H. El Arroussi, *World J. Microbiol. Biotechnol.*, 2019, **35**, 177.
- 74 K. Alba and V. Kontogiorgos, in *Encyclopedia of Food Chemistry*, eds. L. Melton, F. Shahidi and P. Varelis, Elsevier, Oxford, 2019, pp. 240–250.
- 75 Carrageenan Market Size, Share & Trends Analysis Report By Processing Technology (Semi-refined, Gel Press, Alcohol Precipitation), By Function, By Product Type, By Application, By Region, And Segment Forecasts, 2023 - 2030, <https://www.grandviewresearch.com/industry-analysis/carrageenan-market>, (accessed 4 November 2024).
- 76 Market Data Forecast, Carrageenan Market Size, Share, Growth Report | 2024 To 2032, <https://www.marketdataforecast.com/market-reports/carrageenan-market>, (accessed 4 November 2024).
- 77 A. Niccolai, G. Chini Zittelli, L. Rodolfi, N. Biondi and M. R. Tredici, *Algal Res.*, 2019, **42**, 101617.
- 78 P. Thiviya, A. Gamage, A. Liyanapathirana, M. Makehelwala, R. S. Dassanayake, A. Manamperi, O. Merah, S. Mani, J. R. Koduru and T. Madhujith, *Food Chem.*, 2023, **405**, 134903.
- 79 J. O' Connor, S. Meaney, G. A. Williams and M. Hayes, *Molecules*, 2020, **25**, 2005.
- 80 N. Phusunti and B. Cheirsilp, *Algal Res.*, 2020, **48**, 101918.
- 81 O. Yulianti, T. J. Kiat Kavis and N. J. Yi, *J. Food Eng.*, 2021, **288**, 110138.
- 82 H. K. Maehre, G. K. Edvinsen, K.-E. Eilertsen and E. O. Elvevoll, *J. Appl. Phycol.*, 2016, **28**, 581–590.
- 83 S. H. M. Gorissen, J. J. R. Crombag, J. M. G. Senden, W. A. H. Waterval, J. Bierau, L. B. Verdijk and L. J. C. van Loon, *Amino Acids*, 2018, **50**, 1685–1695.
- 84 S.-J. Park, A. Sharma and H.-J. Lee, *Mar. Drugs*, , DOI:10.3390/md22010047.
- 85 S. Udayakumar, A. Girigoswami and K. Girigoswami, *Curr. Pharmacol. Rep.*, 2023, **10**, 12–26.
- 86 J. Olsson, G. B. Toth and E. Albers, *J. Appl. Phycol.*, 2020, **32**, 3305–3317.
- 87 E. G. Young and D. G. Smith, *J. Biol. Chem.*, 1958, **233**, 406–410.
- 88 T. Rudtanatip, S. A. Lynch, K. Wongprasert and S. C. Culloty, *Fish Shellfish Immunol.*, 2018, **75**, 284–290.
- 89 T. Melo, E. Alves, V. Azevedo, A. S. Martins, B. Neves, P. Domingues, R. Calado, M. H. Abreu and M. R. Domingues, *Algal Res.*, 2015, **8**, 181–191.
- 90 M. G. Tasende, *Sci. Mar.*, 2000, **64**, 421–426.

- 91 K. Koch, W. Hagen, M. Graeve and K. Bischof, *Helgol. Mar. Res.*, 2017, **71**, 1–16.
- 92 *Chondrus crispus* ou *Mastocarpus stellatus* ?, <https://biologie.ens-lyon.fr/biologie/ressources/Biodiversite/Documents/image-de-la-semaine/2011/semaine-38-19-09-2011/>, (accessed 4 November 2024).
- 93 M. García Tasende, M. Cid and M. I. Fraga, *J. Appl. Phycol.*, 2012, **24**, 941–951.
- 94 A. Q. Hurtado, A. T. Critchley and I. C. Neish, *Tropical seaweed farming trends, problems and opportunities: Focus on Kappaphycus and Eucheuma of commerce*, Springer International Publishing, Basel, Switzerland, 1st edn., 2017.
- 95 A. Bahari, K. Moelants, J. Wallecan, G. Mangiante, J. Mazoyer, M. Hendrickx and T. Grauwet, *Algal Res.*, 2021, **58**, 102371.
- 96 N. Rhein-Knudsen, M. T. Ale and A. S. Meyer, *Mar. Drugs*, 2015, **13**, 3340–3359.
- 97 Y. Dong, Z. Wei and C. Xue, *Trends Food Sci. Technol.*, 2021, **112**, 348–361.
- 98 L. Gu, D. J. McClements, J. Li, Y. Su, Y. Yang and J. Li, *Food Hydrocoll.*, 2021, **112**, 106349.
- 99 P. Ezati, Z. Riahi and J.-W. Rhim, *ACS Sustain. Chem. Eng.*, 2021, **9**, 9300–9307.
- 100 M. Morokutti-Kurz, M. Fröba, P. Graf, M. Große, A. Grassauer, J. Auth, U. Schubert and E. Prieschl-Grassauer, *PLoS One*, 2021, **16**, e0237480.
- 101 Y. Jang, H. Shin, M. K. Lee, O. S. Kwon, J. S. Shin, Y.-I. Kim, C. W. Kim, H.-R. Lee and M. Kim, *Sci. Rep.*, 2021, **11**, 821.
- 102 K. Véliz, N. Chandía, U. Karsten, C. Lara and M. Thiel, *J. Appl. Phycol.*, 2019, **31**, 665–682.
- 103 A. C. Mathieson and E. Tveter, *Aquat. Bot.*, 1975, **1**, 25–43.
- 104 V. Budarin, J. H. Clark, J. J. E. Hardy, R. Luque, K. Milkowski, S. J. Tavener and A. J. Wilson, *Angew. Chem. Int. Ed Engl.*, 2006, **45**, 3782–3786.
- 105 Z. AlOthman, *Materials (Basel)*, 2012, **5**, 2874–2902.
- 106 W. Al-Hajri, Y. De Luna and N. Bensalah, *Energy Technol.*, 2022, **10**, 2200498.
- 107 G. Ma, G. Ning and Q. Wei, *Carbon N. Y.*, 2022, **195**, 328–340.
- 108 W. Chen, M. Wan, Q. Liu, X. Xiong, F. Yu and Y. Huang, *Small Methods*, 2019, **3**, 1800323.
- 109 S. V. Sawant, A. W. Patwardhan, J. B. Joshi and K. Dasgupta, *Chem. Eng. J.*, 2022, **427**, 131616.
- 110 W. Kiciński, M. Szala and M. Bystrzejewski, *Carbon N. Y.*, 2014, **68**, 1–32.
- 111 A. Ilnicka, M. Skorupska, M. Szkoda, Z. Zarach, P. Kamedulski, W. Zielinski and J. P. Lukaszewicz, *Sci. Rep.*, 2021, **11**, 18387.
- 112 G. Wang, Y. Liu, X. Dong and X. Zhang, *J. Hazard. Mater.*, 2022, **437**, 129357.
- 113 B. Jin, J. Li, Y. Wang, Z. Yang, X. Yao, W. Sun, Y. Lu, X. Zhu and T. Zhang, *Chemical Engineering Journal Advances*, 2022, **10**, 100276.
- 114 Y. Cui, H. Wang, X. Xu, Y. Lv, J. Shi, W. Liu, S. Chen and X. Wang, *Sustainable Energy Fuels*, 2018, **2**, 381–391.
- 115 J. Attard, PhD Thesis, University of York, 2018.
- 116 J. Chen, X. Wang, Y. Huang, S. Lv, X. Cao, J. Yun and D. Cao, *Eng. Sci.*, 2018, **5**, 30–38.
- 117 Z. Zhao, C. Ma, F. Chen, G. Xu, R. Pang, X. Qian, J. Shao and X. Hu, *Biomass Bioenergy*, 2021, **145**, 105969.
- 118 J. Dai, J. Yuan and P. Giannozzi, *Appl. Phys. Lett.*, 2009, **95**, 232105.
- 119 J.-S. M. Lee, D. J. Parker, A. I. Cooper and T. Hasell, *J. Mater. Chem. A Mater. Energy Sustain.*, 2017, **5**, 18603–18609.
- 120 C. Mena Duran, PhD Thesis, University of York, 2014.
- 121 Y. Peng, F. Zhang, Y. Zhang, X. Luo, L. Chen and Y. Shi, *J. Colloid Interface Sci.*, 2022, **616**, 659–667.
- 122 Z. Lu, Y. Zhai, N. Wang, Y. Zhang, P. Xue, M. Guo, B. Tang, D. Huang, W. Wang, Z. Bai and S. Dou, *Chem. Eng. J.*, 2020, **380**, 122455.
- 123 R. Guo, D. Li, C. Lv, Y. Wang, H. Zhang, Y. Xia, D. Yang and X. Zhao, *Electrochim. Acta*, 2019, **299**, 72–79.
- 124 R. Zhang, Y. Zhou and C. Hu, *J. Appl. Phycol.*, 2021, **33**, 91–99.

- 125 W. Wei, Y. Zheng, M. Huang, J. Shi, L. Li, Z. Shi, S. Liu and H. Wang, *Nanoscale*, 2021, **13**, 4911–4920.
- 126 D. Li, Y. Sun, S. Chen, J. Yao, Y. Zhang, Y. Xia and D. Yang, *ACS Appl. Mater. Interfaces*, 2018, **10**, 17175–17182.
- 127 D. Li, D. Yang, X. Yang, Y. Wang, Z. Guo, Y. Xia, S. Sun and S. Guo, *Angew. Chem. Int. Ed Engl.*, 2016, **55**, 15925–15928.
- 128 J. Nogueira, M. António, S. M. Mikhalev, S. Fateixa, T. Trindade and A. L. Daniel-da-Silva, *Nanomaterials (Basel)*, 2018, **8**, 1004.
- 129 D. Lv, Y. Li and L. Wang, *Int. J. Biol. Macromol.*, 2020, **148**, 979–987.
- 130 D. Saha, S. Barakat, S. E. Van Bramer, K. A. Nelson, D. K. Hensley and J. Chen, *ACS Appl. Mater. Interfaces*, 2016, **8**, 34132–34142.
- 131 C. Saka, İ. Teğın and K. Kahvecioğlu, *Diam. Relat. Mater.*, 2023, **131**, 109542.
- 132 Copper, <https://www.iea.org/reports/copper>, (accessed 4 November 2024).
- 133 D. Lei, S. Li, L. Gao, M. Hu, N. Chai and J. Fan, *Environ. Sci. Pollut. Res. Int.*, 2023, **30**, 115543–115555.
- 134 J. Zhang, X. Tian, W. Chen, Y. Geng and J. Wilson, *Environ. Impact Assess. Rev.*, 2022, **96**, 106855.
- 135 Y. Liu, H. Wang, Y. Cui and N. Chen, *Int. J. Environ. Res. Public Health*, 2023, **20**(5), 3885.
- 136 L. Zanella and F. Vianello, *J. Funct. Foods*, 2020, **68**, 103919.
- 137 E. T. Chua and P. M. Schenk, *Bioresour. Technol.*, 2017, **244**, 1416–1424.
- 138 L. Rodolfi, G. Chini Zittelli, N. Bassi, G. Padovani, N. Biondi, G. Bonini and M. R. Tredici, *Biotechnol. Bioeng.*, 2009, **102**, 100–112.
- 139 G. Benvenuti, P. P. Lamers, G. Breuer, R. Bosma, A. Cerar, R. H. Wijffels and M. J. Barbosa, *Biotechnol. Biofuels*, 2016, **9**, 64.
- 140 T. Harayama and H. Riezman, *Nat. Rev. Mol. Cell Biol.*, 2018, **19**, 281–296.
- 141 L. M. Lubián, O. Montero, I. Moreno-Garrido, I. E. Huertas, C. Sobrino, M. González-del Valle and G. Parés, *J. Appl. Phycol.*, 2000, **12**, 249–255.
- 142 R. K. Saini, P. Prasad, X. Shang and Y.-S. Keum, *Int. J. Mol. Sci.*, 2021, **22**, 13643.
- 143 N. Castejón and D. Marko, *Molecules*, 2022, **27**, 3710.
- 144 P. Imbimbo, L. D’Elia, D. Liberti, G. Olivieri and D. M. Monti, *Appl. Microbiol. Biotechnol.*, 2020, **104**, 9067–9077.
- 145 S. M. Tibbetts, W. J. Bjornsson and P. J. McGinn, *Anim. Feed Sci. Technol.*, 2015, **204**, 62–71.
- 146 C. J. Hulatt, R. H. Wijffels, S. Bolla and V. Kiron, *PLoS One*, 2017, **12**, e0170440.
- 147 T. H. Coale, V. Loconte, K. A. Turk-Kubo, B. Vanslebrouck, W. K. E. Mak, S. Cheung, A. Ekman, J.-H. Chen, K. Hagino, Y. Takano, T. Nishimura, M. Adachi, M. Le Gros, C. Larabell and J. P. Zehr, *Science*, 2024, **384**, 217–222.
- 148 A. León-Vaz, I. Giráldez, I. Moreno-Garrido, J. Varela, J. Vígara, R. León and J. P. Cañavate, *Algal Res.*, 2023, **74**, 103181.
- 149 J. Martin and A. Sawyer, *Biotechniques*, 2019, **66**, 167–170.
- 150 M. S. Bretscher, *Sci. Am.*, 1985, **253**, 100–108.
- 151 S. Y. Lee, J. M. Cho, Y. K. Chang and Y.-K. Oh, *Bioresour. Technol.*, 2017, **244**, 1317–1328.
- 152 O. Spain and C. Funk, *J. Agric. Food Chem.*, 2022, **70**, 9711–9721.
- 153 I. L. Ross, S. Shah, B. Hankamer and N. Amiralian, *Trends Plant Sci.*, 2021, **26**, 924–939.
- 154 Z. Zhang and J. K. Volkman, *Org. Geochem.*, 2017, **104**, 1–7.
- 155 P.-H. Baudalet, G. Ricochon, M. Linder and L. Muniglia, *Algal Res.*, 2017, **25**, 333–371.
- 156 F. Gelin, J. K. Volkman, J. W. De Leeuw and J. S. Sinninghe Damsté, *Phytochemistry*, 1997, **45**, 641–646.
- 157 P. Blokker, S. Schouten, H. van den Ende, J. W. de Leeuw, P. G. Hatcher and J. S. Sinninghe Damsté, *Org. Geochem.*, 1998, **29**, 1453–1468.
- 158 T. M. Attard, PhD Thesis, University of York, 2015.
- 159 J. Yang, H. Lian, W. Liang, V. P. Nguyen and Y. Chen, *Int. J. Rock Mech. Min. Sci.*

- (1997), 2018, **107**, 233–242.
- 160 K. Kitada, S. Machmudah, M. Sasaki, M. Goto, Y. Nakashima, S. Kumamoto and T. Hasegawa, *J. Chem. Technol. Biotechnol.*, 2009, **84**, 657–661.
- 161 M. De Luca, I. Pappalardo, A. R. Limongi, E. Viviano, R. P. Radice, S. Todisco, G. Martelli, V. Infantino and A. Vassallo, *Cosmetics*, 2021, **8**, 52.
- 162 A. A. B. Omran, A. A. B. A. Mohammed, S. M. Sapuan, R. A. Ilyas, M. R. M. Asyraf, S. S. Rahimian Kolor and M. Petrù, *Polymers (Basel)*, 2021, **13**, 231.
- 163 H.-R. Lee, K. Kim, S. C. Mun, Y. K. Chang and S. Q. Choi, *Carbohydr. Polym.*, 2018, **180**, 276–285.
- 164 E. M. de Melo, J. H. Clark and A. S. Matharu, *Green Chem.*, 2017, **19**, 3408–3417.
- 165 Y. Gao, M. Z. Ozel, T. Dugmore, A. Sulaeman and A. S. Matharu, *J. Hazard. Mater.*, 2021, **401**, 123400.
- 166 Y. Gao, H. Xia, A. P. Sulaeman, E. M. de Melo, T. I. J. Dugmore and A. S. Matharu, *ACS Sustain. Chem. Eng.*, 2019, **7**, 11861–11871.
- 167 S. Liu, Z. Li, B. Yu, S. Wang, Y. Shen and H. Cong, *Adv. Colloid Interface Sci.*, 2020, **284**, 102254.
- 168 J. Huang, F. Wang, M. Ye and H. Zou, *J. Chromatogr. A*, 2014, **1372C**, 1–17.
- 169 S. Bleakley and M. Hayes, *Foods*, 2017, **6**, 33.
- 170 C. Safi, G. Olivieri, R. P. Campos, N. Engelen-Smit, W. J. Mulder, L. A. M. van den Broek and L. Sijtsma, *Bioresour. Technol.*, 2017, **225**, 151–158.
- 171 A.-V. Ursu, A. Marcati, T. Sayd, V. Sante-Lhoutellier, G. Djelveh and P. Michaud, *Bioresour. Technol.*, 2014, **157**, 134–139.
- 172 C. Denis, A. Massé, J. Fleurence and P. Jaouen, *Sep. Purif. Technol.*, 2009, **69**, 37–42.
- 173 H.-J. Hwang, Y. T. Kim, N. S. Kang and J. W. Han, *J. Mol. Microbiol. Biotechnol.*, 2018, **28**, 169–178.
- 174 G. Maffei, M. P. Bracciale, A. Broggi, A. Zuorro, M. L. Santarelli and R. Lavecchia, *Bioresour. Technol.*, 2018, **249**, 592–598.
- 175 R. Halim, T. W. T. Rupasinghe, D. L. Tull and P. A. Webley, *Bioresour. Technol.*, 2013, **140**, 53–63.
- 176 R. V. Kapoore, T. O. Butler, J. Pandhal and S. Vaidyanathan, *Biology (Basel)*, 2018, **7**(1), 18.
- 177 K. L. Low, A. Idris and N. Mohd Yusof, *Food Chem.*, 2020, **307**, 125631.
- 178 P. R. Postma, E. Suarez-Garcia, C. Safi, K. Yonathan, G. Olivieri, M. J. Barbosa, R. H. Wijffels and M. H. M. Eppink, *Bioresour. Technol.*, 2017, **224**, 670–679.
- 179 I. Shtein, B. Bar-On and Z. A. Popper, *Physiol. Plant.*, 2018, **164**, 56–66.
- 180 M.-R. Kula and H. Schütte, *Biotechnol. Prog.*, 1987, **3**, 31–42.
- 181 E. Günerken, E. D'Hondt, M. H. M. Eppink, L. Garcia-Gonzalez, K. Elst and R. H. Wijffels, *Biotechnol. Adv.*, 2015, **33**, 243–260.
- 182 V. Skorupskaite, V. Makareviciene, E. Sendzikiene and M. Gumbyte, *J. Appl. Phycol.*, 2019, **31**, 2349–2354.
- 183 E. Ponthier, H. Domínguez and M. D. Torres, *Algal Res.*, 2020, **51**, 102081.
- 184 M. Cooney, G. Young and N. Nagle, *Sep. Purif. Rev.*, 2009, **38**, 291–325.
- 185 L. Buchmann, I. Brändle, I. Haberkorn, M. Hiestand and A. Mathys, *Bioresour. Technol.*, 2019, **291**, 121870.
- 186 P. Anastas and N. Eghbali, *Chem. Soc. Rev.*, 2010, **39**, 301–312.
- 187 R. K. Henderson, C. Jiménez-González, D. J. C. Constable, S. R. Alston, G. G. A. Inglis, G. Fisher, J. Sherwood, S. P. Binks and A. D. Curzons, *Green Chem.*, 2011, **13**, 854–862.
- 188 N. Fairley, V. Fernandez, M. Richard-Plouet, C. Guillot-Deudon, J. Walton, E. Smith, D. Flahaut, M. Greiner, M. Biesinger, S. Tougaard, D. Morgan and J. Baltrusaitis, *Applied Surface Science Advances*, 2021, **5**, 100112.
- 189 J. Shannon, PhD Thesis, University of York, 2019.
- 190 L.-Y. Chen, C.-W. Cheng and J.-Y. Liang, *Food Chem.*, 2015, **170**, 10–15.
- 191 O. R. Alara, N. H. Abdurahman and O. A. Olalere, *J. King Saud Univ. Sci.*, 2020, **32**, 7–16.

- 192 J. O. Olugbami, M. A. Gbadegesin and O. A. Odunola, *Pharmacognosy Res.*, 2015, **7**, 49–56.
- 193 M. D. N. Meinita, B. Marhaeni, G.-T. Jeong and Y.-K. Hong, *J. Appl. Phycol.*, 2019, **31**, 2507–2515.
- 194 F. Lu, C. Wang, M. Chen, F. Yue and J. Ralph, *Green Chem.*, 2021, **23**, 5106–5112.
- 195 N. Li, X. Pan and J. Alexander, *Green Chem.*, 2016, **18**, 5367–5376.
- 196 A. Karlsson, *Carbohydr. Polym.*, 1999, **38**, 7–15.
- 197 P. T. Martone, J. M. Estevez, F. Lu, K. Ruel, M. W. Denny, C. Somerville and J. Ralph, *Curr. Biol.*, 2009, **19**, 169–175.
- 198 P. Kenrick and P. R. Crane, *Nature*, 1997, **389**, 33–39.
- 199 A. K. Khan, H. Kausar, S. S. Jaferi, S. Drouet, C. Hano, B. H. Abbasi and S. Anjum, *Biomolecules*, 2020, **10**, 1524.
- 200 S. Liu, Y. Zhu, Y. Liao, H. Wang, Q. Liu, L. Ma and C. Wang, *Applications in Energy and Combustion Science*, 2022, **10**, 100062.
- 201 E. S. Krul, *J. Am. Oil Chem. Soc.*, 2019, **96**, 339–364.
- 202 I. Biancarosa, M. Espe, C. G. Bruckner, S. Heesch, N. Liland, R. Waagbø, B. Torstensen and E. J. Lock, *J. Appl. Phycol.*, 2017, **29**, 1001–1009.
- 203 H. Tiangson, ... *of medicinal food*.
- 204 L. Mišurcová, in *Handbook of Marine Macroalgae*, John Wiley & Sons, Ltd, Chichester, UK, 2011, pp. 171–192.
- 205 R. Tuvikene, in *Handbook of Hydrocolloids*, eds. G. O. Phillips and P. A. Williams, Elsevier, 2021, pp. 767–804.
- 206 T. I. Todorov, M. M. Wolle and S. D. Conklin, *Chemosphere*, 2022, **294**, 133651.
- 207 S. Ma †, L. Chen †, X. Liu, D. Li, N. Ye and L. Wang, *Int. J. Green Energy*, 2012, **9**, 13–21.
- 208 M. Fu, Y. Wu, Q. Zhang, Z. Xue, C. Geng and Y. Xia, *Eur. Polym. J.*, 2021, **150**, 110408.
- 209 Q. Zhang, W. Zhang, C. Geng, Z. Xue, Y. Xia, Y. Qin and G. Zhang, *Carbohydr. Polym.*, 2019, **206**, 420–427.
- 210 Z. Xue, W. Zhang, M. Yan, J. Liu, B. Wang and Y. Xia, *RSC Adv.*, 2017, **7**, 25253–25264.
- 211 M. Thommes, D. R. Ely and P. Kleinebudde, *Pharm. Dev. Technol.*, 2009, **14**, 249–258.
- 212 A. B. Ross, C. Hall, K. Anastasakis, A. Westwood, J. M. Jones and R. J. Crewe, *J. Anal. Appl. Pyrolysis*, 2011, **91**, 344–351.
- 213 D. Díez, A. Urueña, R. Piñero, A. Barrio and T. Tamminen, *Processes (Basel)*, 2020, **8**, 1048.
- 214 Q.-V. Bach and W.-H. Chen, *Bioresour. Technol.*, 2017, **246**, 88–100.
- 215 P. Biller and A. B. Ross, *Algal Res.*, 2014, **6**, 91–97.
- 216 W. Rodiahwati, T. C. Brown and B. W. Greatrex, *Bioresour. Technol. Rep.*, 2023, **23**, 101576.
- 217 D. Kong and A. V. Dolzhenko, *Sustain. Chem. Pharm.*, 2022, **25**, 100591.
- 218 Q. Lu, Y. Zhang, C.-Q. Dong, Y.-P. Yang and H.-Z. Yu, *J. Anal. Appl. Pyrolysis*, 2014, **110**, 34–43.
- 219 S. Wang, Y. Hu, B. B. Uzoejinwa, B. Cao, Z. He, Q. Wang and S. Xu, *J. Anal. Appl. Pyrolysis*, 2017, **124**, 373–383.
- 220 H. Cheng, Q. Liu, M. Huang, S. Zhang and R. L. Frost, *Thermochim. Acta*, 2013, **555**, 1–6.
- 221 E. Tojo and J. Prado, *Carbohydr. Res.*, 2003, **338**, 1309–1312.
- 222 M. Robal, T. Brenner, S. Matsukawa, H. Ogawa, K. Truus, B. Rudolph and R. Tuvikene, *Food Hydrocoll.*, 2017, **63**, 656–667.
- 223 A. Barth, *Biochim. Biophys. Acta*, 2007, **1767**, 1073–1101.
- 224 F. van de Velde, S. H. Knutsen, A. I. Usov, H. S. Rollema and A. S. Cerezo, *Trends Food Sci. Technol.*, 2002, **13**, 73–92.
- 225 E. Tojo and J. Prado, *Carbohydr. Polym.*, 2003, **53**, 325–329.
- 226 F. van de Velde, *Food Hydrocoll.*, 2008, **22**, 727–734.
- 227 Elena Corina Popescu, Maria Iordan, Cristian Boscornea, *Ann. "Valahia" Univ.*

- Targoviste*, 2007, **8**, 27–32.
- 228 D. Yang, S. Gao and H. Yang, *Food Hydrocoll.*, 2020, **99**, 105317.
- 229 L. Zinke, *Nat. Rev. Earth Environ.*, 2020, **1**, 141–141.
- 230 S. A. Channiwala and P. P. Parikh, *Fuel (Lond.)*, 2002, **81**, 1051–1063.
- 231 H. Li, V. L. Budarin, J. H. Clark, M. North and X. Wu, *J. Hazard. Mater.*, 2022, **436**, 129174.
- 232 A. M. Smith and A. B. Ross, *Algal Res.*, 2016, **16**, 1–11.
- 233 N. Baccile, C. Falco and M.-M. Titirici, *Green Chem.*, 2014, **16**, 4839–4869.
- 234 B. Kartick, S. K. Srivastava and I. Srivastava, *J. Nanosci. Nanotechnol.*, 2013, **13**, 4320–4324.
- 235 A. L. Patterson, *Phys. Rev.*, 1939, **56**, 978–982.
- 236 X. Jia, Q. Wang, L. Han, L. Cheng, M. Fang, Z. Luo and K. Cen, *J. Anal. Appl. Pyrolysis*, 2017, **124**, 319–326.
- 237 B. Souza, R. Souza, I. Santos and E. Brocchi, *J. Mater. Res. Technol.*, 2020, **9**, 1847–1855.
- 238 M. Scheidema, PhD Thesis, Aalto University, 2015.
- 239 Z. Q. Li, C. J. Lu, Z. P. Xia, Y. Zhou and Z. Luo, *Carbon N. Y.*, 2007, **45**, 1686–1695.
- 240 A. N. Popova, *Coke and Chemistry*, 2017, **60**, 361–365.
- 241 L. Qie, W. Chen, X. Xiong, C. Hu, F. Zou, P. Hu and Y. Huang, *Adv. Sci. (Weinh.)*, 2015, **2**, 1500195.
- 242 N. Ayawei, A. N. Ebelegi and D. Wankasi, *J. Chem.*, 2017, **2017**, 1–11.
- 243 G. Attard and C. Barnes, *Surfaces*, Oxford University Press, 1998.
- 244 H. J. Abdoul, PhD Thesis, University of York, 2015.
- 245 F. J. Sotomayor, K. A. Cychosz, M. Thommes and Others, *Acc. Mater. Surf. Res.*, 2018, **3**, 34–50.
- 246 X. Chen, L. Zhang, W. Xu, X. Ding, S. Chen, X. She, X. Guo, C.-L. Dong, Y. Huang, L. Zhang, S. Shen and D. Yang, *Appl. Catal. B*, 2022, **313**, 121425.
- 247 M. J. Ahmed, P. U. Okoye, E. H. Hummadi and B. H. Hameed, *Bioresour. Technol.*, 2019, **278**, 159–164.
- 248 R. Hoogewijs, L. Fiermans and J. Vennik, *J. Electron Spectros. Relat. Phenomena*, 1977, **11**, 171–183.
- 249 S. Sugiyama, T. Miyamoto, H. Hayashi and J. B. Moffat, *Bull. Chem. Soc. Jpn.*, 1996, **69**, 235–240.
- 250 H. Hantsche, *Adv. Mater.*, 1993, **5**, 778–778.
- 251 X-ray Photoelectron Spectroscopy (XPS) Reference Pages, <http://www.xpsfitting.com/2009/06/sulphur.html>, (accessed 4 November 2024).
- 252 Y. Seung Kim and C. Rae Park, in *Materials Science and Engineering of Carbon*, eds. M. Inagaki and F. Kang, Elsevier, 2016, pp. 273–286.
- 253 F. Yakasai, M. Z. Jaafar, S. Bandyopadhyay and A. Agi, *J. Ind. Eng. Chem.*, 2021, **93**, 138–162.
- 254 A. T. Baker, *J. Chem. Educ.*, 1998, **75**, 98.
- 255 D. J. Pochapski, C. Carvalho Dos Santos, G. W. Leite, S. H. Pulcinelli and C. V. Santilli, *Langmuir*, 2021, **37**, 13379–13389.
- 256 S. Kalam, S. A. Abu-Khamsin, M. S. Kamal and S. Patil, *ACS Omega*, 2021, **6**, 32342–32348.
- 257 A. F. Sweeney, J. T. O'Brien, E. R. Williams and P. B. Armentrout, *Int. J. Mass Spectrom.*, 2015, **378**, 270–280.
- 258 J. D. Cuppett, S. E. Duncan and A. M. Dietrich, *Chem. Senses*, 2006, **31**, 689–697.
- 259 H. Demiral and C. Güngör, *J. Clean. Prod.*, 2016, **124**, 103–113.
- 260 L. Zhao, B. Yu, F. Xue, J. Xie, X. Zhang, R. Wu, R. Wang, Z. Hu, S.-T. Yang and J. Luo, *J. Hazard. Mater.*, 2015, **286**, 449–456.
- 261 T. Velempini and K. Pillay, *J. Environ. Chem. Eng.*, 2019, **7**, 103350.
- 262 J. M. Aguirre, A. Gutiérrez and O. Giraldo, *J. Braz. Chem. Soc.*, 2011, **22**, 546–551.
- 263 D. C. Pereira, D. L. A. de Faria and V. R. L. Constantino, *J. Braz. Chem. Soc.*, 2006, **17**, 1651–1657.

- 264 R. Weingarten, A. Rodriguez-Beuerman, F. Cao, J. S. Luterbacher, D. M. Alonso, J. A. Dumesic and G. W. Huber, *ChemCatChem*, 2014, **6**, 2229–2234.
- 265 B. W. Vogler, J. Brannum, J. W. Chung, M. Seger and M. C. Posewitz, *Algal Res.*, 2018, **36**, 152–158.
- 266 J. Rao, Z. Lv, G. Chen and F. Peng, *Prog. Polym. Sci.*, 2023, **140**, 101675.
- 267 P. A. Caetano, T. C. do Nascimento, A. S. Fernandes, P. P. Nass, K. R. Vieira, M. R. Maróstica Junior, E. Jacob-Lopes and L. Q. Zepka, *Biocatal. Agric. Biotechnol.*, 2022, **45**, 102491.
- 268 M. Zych, J. Burczyk, W. Borymska and I. Kaczmarczyk-Sedlak, *Algal Res.*, 2022, **62**, 102598.
- 269 D. W. Templeton and L. M. L. Laurens, *Algal Res.*, 2015, **11**, 359–367.
- 270 C. M. García Santander, S. M. Gómez Rueda, N. de Lima da Silva, C. L. de Camargo, T. G. Kieckbusch and M. R. Wolf Maciel, *Fuel (Lond.)*, 2012, **92**, 158–161.
- 271 S. Tzima, I. Georgiopoulou, V. Louli and K. Magoulas, *Molecules*, 2023, **28**(3), 1410.
- 272 D. Mc Gee, L. Archer, A. Paskuliakova, G. R. Mc Coy, G. T. A. Fleming, E. Gillespie and N. Touzet, *J. Appl. Phycol.*, 2018, **30**, 385–399.
- 273 George Britton, Synnøve Liaaen-Jensen, Hanspeter Pfander (Chief Operating Officer), *Carotenoids: Handbook*, Birkhauser Verlag AG, Basel, Switzerland, 1st edn., 2004.
- 274 E. Borello, D. Roncucci and V. Domenici, *Foods*, 2021, **10**, 1891.
- 275 M. Trytek, E. Janik, W. Maksymiec, J. Fiedurek, A. Lipke and M. Majdan, *J. Photochem. Photobiol. A Chem.*, 2011, **223**, 14–24.
- 276 B. Averill and P. Eldredge, *General chemistry: Principles, patterns, and applications*, Saylor Foundation, 2011.
- 277 S. Saito, N. Numadate, H. Teraoka, S. Enami, H. Kobayashi and T. Hama, *Sci. Adv.*, 2023, **9**, ead6438.
- 278 A. R. López-Rosales, K. Ancona-Canché, J. C. Chavarria-Hernandez, F. Barahona-Pérez, T. Toledano-Thompson, G. Garduño-Solórzano, S. López-Adrian, B. Canto-Canché, E. Polanco-Lugo and R. Valdez-Ojeda, *Energies*, 2018, **12**, 130.
- 279 D. Giusepponi, R. Galarini, C. Barola, P. Torquato, D. Bartolini, S. Moretti, G. Saluti, A. Gioiello, C. Libetta and F. Galli, *Free Radic. Biol. Med.*, 2019, **144**, 134–143.
- 280 L. Zhou, X. Duan, K. Li, D. R. A. Hill, G. J. O. Martin and H. A. R. Suleria, *Chem. Biodivers.*, 2023, **20**, e202300602.
- 281 A. M. Shraim, T. A. Ahmed, M. M. Rahman and Y. M. Hijji, *Lebenson. Wiss. Technol.*, 2021, **150**, 111932.
- 282 A. Del Mondo, A. Smerilli, L. Ambrosino, A. Albin, D. M. Noonan, C. Sansone and C. Brunet, *Crit. Rev. Biotechnol.*, 2021, **41**, 155–171.
- 283 I. G. Munteanu and C. Apetrei, *Int. J. Mol. Sci.*, 2021, **22**, 3380.
- 284 Y.-R. Kang, Y.-K. Lee, Y. J. Kim and Y. H. Chang, *Food Chem.*, 2019, **272**, 337–346.
- 285 G. Knothe and R. O. Dunn, *J. Am. Oil Chem. Soc.*, 2009, **86**, 843–856.
- 286 C. Park, N. Meghani, R. Loebenberg, J.-H. Cui, Q.-R. Cao and B.-J. Lee, *Eur. J. Pharm. Biopharm.*, 2020, **152**, 257–269.
- 287 P. J. Van Soest, *Nutritional Ecology of the Ruminant*, Cornell University Press, 1994.
- 288 A. T. Quitain, T. Kai, M. Sasaki and M. Goto, *Ind. Eng. Chem. Res.*, 2013, **52**, 7940–7946.
- 289 H.-Y. Wang, H. Qian and W.-R. Yao, *Food Chem.*, 2011, **128**, 573–584.
- 290 P. Biller, C. Friedman and A. B. Ross, *Bioresour. Technol.*, 2013, **136**, 188–195.
- 291 J. Iqbal and C. Theegala, *Algal Research*, 2013, **2**, 34–42.
- 292 M. Rokicka, M. Zieliński, M. Dudek and M. Dębowski, *Bioenergy Res.*, 2020, **14**, 752–760.
- 293 S. Nam, A. D. French, B. D. Condon and M. Concha, *Carbohydr. Polym.*, 2016, **135**, 1–9.
- 294 N. Terinte, R. Ibbett and K. C. Schuster, *Lenzinger Berichte*, 2011, **89**, 118–131.
- 295 P. Ahvenainen, I. Kontro and K. Svedström, *Cellulose*, 2016, **23**, 1073–1086.
- 296 M. Hajir, R. Graf and W. Tremel, *Chem. Commun.*, 2014, **50**, 6534–6536.
- 297 A. Synytsya, J. Opíková and J. Brus, *Czech Journal of Food Sciences; Prague*, 2003,

- 21, 1–12.
- 298 L. Segal, J. J. Creely, A. E. Martin and C. M. Conrad, *Text. Res. J.*, 1959, **29**, 786–794.
- 299 A. D. French and M. Santiago Cintrón, *Cellulose*, 2013, **20**, 583–588.
- 300 A. M. A. Nada and M. L. Hassan, *Polym. Degrad. Stab.*, 2000, **67**, 111–115.
- 301 L. Szcześniak, A. Rachocki and J. Tritt-Goc, *Cellulose*, 2008, **15**, 445–451.
- 302 A. A. Arnold, B. Genard, F. Zito, R. Tremblay, D. E. Warschawski and I. Marcotte, *Biochim. Biophys. Acta*, 2015, **1848**, 369–377.
- 303 A. J. Simpson, X. Zang, R. Kramer and P. G. Hatcher, *Phytochemistry*, 2003, **62**, 783–796.
- 304 S. Park, D. K. Johnson, C. I. Ishizawa, P. A. Parilla and M. F. Davis, *Cellulose*, 2009, **16**, 641–647.
- 305 G. Canelli, P. Murciano Martínez, S. Austin, M. E. Ambühl, F. Dionisi, C. J. Bolten, R. Carpine, L. Neutsch and A. Mathys, *J. Agric. Food Chem.*, 2021, **69**, 2226–2235.
- 306 A. Shchukarev, Z. Gojkovic, C. Funk and M. Ramstedt, *Appl. Surf. Sci.*, 2020, **526**, 146538.
- 307 B. Rashidi and L. M. Trindade, *Algal Research*, 2018, **35**, 152–159.
- 308 W. Jeon, C. Ban, G. Park, J. E. Kim, H. C. Woo and D. H. Kim, *Catal. Surv. Asia*, 2016, **20**, 195–209.
- 309 C. Ribeiro, E. T. Santos, L. Costa, C. Brazinha, P. Saraiva and J. G. Crespo, *Membranes (Basel)*, 2022, **12**, 401.
- 310 Y. S. Rajput and R. Sharma, *Chemical Analysis of Value Added Dairy Products and Their Quality Assurance*, 2011, **1**, 81–84.
- 311 N. J. Kruger, in *Springer Protocols Handbooks*, ed. J. M. Walker, Humana Press, Totowa, NJ, 2009, pp. 17–24.
- 312 D. B. Wilson, *Curr. Opin. Biotechnol.*, 2009, **20**, 295–299.
- 313 O. Bulut, D. Akin, Ç. Sönmez, A. Öktem, M. Yücel and H. A. Öktem, *J. Appl. Phycol.*, 2019, **31**, 1675–1683.
- 314 L. Zhou, K. Li, X. Duan, D. Hill, C. Barrow, F. Dunshea, G. Martin and H. Suleria, *Food Biosci.*, 2022, **49**, 101932.
- 315 E. Díaz-Montes and R. Castro-Muñoz, *Foods*, 2021, **10**, 249.
- 316 G. Chen, K. Wang, P. Chen, D. Cai, Y. Shao, R. Xia, C. Li, H. Wang, F. Ren, X. Cheng and Y. Yu, *Adv. Sci. (Weinh.)*, 2024, **11**, e2400826.
- 317 M. R. Khan, F. A. Di Giuseppe, E. Torrieri and M. B. Sadiq, *Food Packag. Shelf Life*, 2021, **30**, 100752.
- 318 E. L. N. Escobar, T. A. da Silva, C. L. Pirich, M. L. Corazza and L. Pereira Ramos, *Front. Bioeng. Biotechnol.*, 2020, **8**, 252.
- 319 E. Macedo de Melo, PhD Thesis, University of York, 2018.
- 320 I. Gifuni, L. Lavenant, J. Pruvost and A. Masse, *Algal Res.*, 2020, **51**, 102082.
- 321 J. B. W. Webber and H. Liu, *Magn. Reson. Imaging*, 2023, **100**, 36–42.
- 322 A. E. Eseyin and P. H. Steele, *Int. J. Adv. Chem.*, 2015, **3**, 42.
- 323 Z. Jiang, Y. Zeng, D. Hu, R. Guo, K. Yan and R. Luque, *Green Chem.*, 2023, **25**, 871–892.
- 324 A. O. C. Iroegbu and S. S. Ray, *J. Polym. Sci.*, 2024, **62**, 1044–1060.
- 325 P. R. Zalupski, R. McDowell and G. Dutech, *Solvent Extr. Ion Exch.*, 2014, **32**, 737–748.
- 326 J. Kaur, K. Kaur, S. K. Mehta and A. S. Matharu, *J. Mater. Chem. A Mater. Energy Sustain.*, 2020, **8**, 14519–14527.
- 327 X. Hu, J. Sun, W. Zheng, S. Zheng, Y. Xie, X. Gao, B. Yang, Z. Li, L. Lei and Y. Hou, *Chin. J. Chem. Eng.*, 2022, **43**, 116–123.
- 328 A. Salituro, A. Westwood, A. Ross and R. Brydson, *Sustain. Chem.*, 2020, **1**, 33–48.
- 329 L. Fiori, M. Manfrini and D. Castello, *Food Bioprod. Process.*, 2014, **92**, 120–132.
- 330 Z. Du, Y. Li, X. Wang, Y. Wan, Q. Chen, C. Wang, X. Lin, Y. Liu, P. Chen and R. Ruan, *Bioresour. Technol.*, 2011, **102**, 4890–4896.
- 331 V. L. Budarin, Y. Zhao, M. J. Gronnow, P. S. Shuttleworth, S. W. Breeden, D. J. Macquarrie and J. H. Clark, *Green Chem.*, 2011, **13**, 2330–2333.